Modelling charge and exciton transport in polymeric and molecular systems

by

Rocco Peter Fornari

A thesis submitted in partial fulfilment of the requirements for the degree of

Doctor of Philosophy in Chemistry

University of Warwick, Department of Chemistry

March 2018

Table of contents

List of Figures

Acknowledgements

I am grateful to my supervisor Prof. Alessandro Troisi for the guidance and support he provided during these years. His inventiveness and unique scientific instinct have been of fundamental importance for the research projects we undertook, as well as a valuable example for my personal development. I also would like to thank Dr. Juan Aragó, an excellent scientist whose endless availability and friendly mentorship has greatly supported me in the first part of my PhD. I am also thankful to Patrick Rowe and Daniele Padula for their friendship and valuable collaboration in one of my projects. I thank for interesting discussions and the good times together the other group members Myeong Lee, Ben Ip, Hainam Do, Alina Kuzmich, Alejandro Santana Bonilla, Yun Geng, Xiaoyu Xie and Kirsten Claridge. Finally, I am thankful to the new group members at the University of Liverpool who made me feel welcome in the final months of my PhD.

I kindly acknowledge the European Research Council (ERC) for financial support.

Declaration

This thesis is submitted to the University of Warwick in support of my application for the degree of Doctor of Philosophy. It has been composed by myself and it has not been submitted in any previous application for any degree. The work presented (including data generated and data analysis) was carried out by the author except in the cases outlined below:

In chapter 2, Dr. Juan Aragó created Figure 2.1 and performed the derivation in section 2.3.1.1.

In chapter 3, Dr. Juan Aragó created Figure 3.1, computed the intramolecular couplings in the model system with H_2-OBPc and isoindole (Figure 3.7) and computed the inter-column couplings (Figure 3.8).

In chapter 4, Patrick Rowe selected and extracted the chromophore pairs from the structures of the light-harvesting complexes, optimized their structures and computed the couplings between them.

Parts of this thesis have been published by the author:

1. R. P. Fornari and A. Troisi, Theory of charge hopping along a disordered polymer chain, *Phys. Chem. Chem. Phys.*, 2014, **16**, 9997–10007.
2. R. P. Fornari and A. Troisi, Narrower Bands with Better Charge Transport: The Counterintuitive Behavior of Semiconducting Copolymers, *Adv. Mater.*, 2014, **26**, 7627–7631.
3. R. P. Fornari, J. Aragó and A. Troisi, A very general rate expression for charge hopping in semiconducting polymers, *J. Chem. Phys.*, 2015, **142**, 184105.
4. R. P. Fornari, J. Aragó and A. Troisi, Exciton Dynamics in Phthalocyanine Molecular Crystals, *J. Phys. Chem. C*, 2016, **120**, 7987–7996.
5. R. P. Fornari, P. Rowe, D. Padula and A. Troisi, Importance and Nature of Short-Range Excitonic Interactions in Light-harvesting Complexes and Organic Semiconductors, *J. Chem. Theory Comput.*, 2017, **13**, 3754−3763.
6. R. P. Fornari, P. W. M. Blom and A. Troisi, How Many Parameters Actually Affect the Mobility of Conjugated Polymers?, *Phys. Rev. Lett.*, 2017, **118**, 86601.

Abstract

In this thesis some fundamental aspects of charge transport and exciton dynamics in organic semiconductors are explored from a theoretical and computational point of view. After a brief review of the field of organic electronics, the theoretical methods most commonly used to describe exciton dynamics and charge transport are summarised, with an emphasis on the specific methods employed in this thesis (chapter 1).

A very general kinetic rate of hopping between electronic states in the incoherent regime is then derived (chapter 2). This rate contains the most commonly used rates (Miller-Abrahams, Marcus, Marcus-Levich-Jortner) as special cases.

The excitonic couplings between molecules determine the properties of excited states in biological and artificial molecular aggregates. A large number of excitonic couplings in these systems are computed (chapters 3 and 4) including both the Coulombic and the short-range (non-Coulombic) contributions as well as the thermal fluctuation of the coupling (dynamic disorder). The effect of thermal fluctuations in crystalline materials is found to be important when evaluating exciton dynamics (chapter 3). The short-range component of the coupling needs to be included when the interacting molecules are in close contact (chapter 3).

The characteristics of charge transport in disordered polymers depend in principle on many parameters. With the aim of accounting for the complicated nature of these materials, a very general charge transport model is presented here (chapter 5). A detailed electronic structure with variable localization of the electronic states is obtained from a simple model Hamiltonian depending on just a few parameters. Using the hopping rate derived in chapter 2, the charge mobility along disordered polymer chains is computed. The proposed model includes features of both variable range hopping (VRH) and mobility edge (ME) models, but it starts from fewer assumptions. Donor-acceptor copolymers have a narrower transport band which in principle should result in lower mobility. Instead, the narrower band is found to enhance mobility if the other parameters are kept constant. By exploring the large parameter space of this model, the temperature dependence of mobility is found to follow a universal Arrhenius behaviour in agreement with experimental data (chapter 6). The activation energy for transport depends only on the effective electronic disorder of the polymer chain. When the 3D structure of the polymer chains and the role of inter-chain hopping are also considered (chapter 7), the mobility is found to be linearly dependent on the persistence length. The activation energy is found to depend only on the electronic disorder and not on chain rigidity.

List of abbreviations

1D	one-dimensional
3D	three-dimensional
ATC	atomic transition charges
BChlA	bacteriochlorophyll-a
BHJ	bulk heterojunction
B-O	Born-Oppenheimer
CAM-B3LYP	Coulomb-attenuating method Becke 3-parameter Lee-Yang-Parr exchange-correlation functional
ChlA	chlorophyll-a
CI	configuration interaction
CIS	configuration interaction singles
CT	charge transfer
DFT	density functional theory
dip-dip	dipole-dipole
DOS	density of states
DPP	diketopyrroloppyrrole
EET	electronic energy transfer
FSSH	fewest switches surface hopping
FC	Franck-Condon
FCTW	Franck-Condon and temperature weighted
FMO	Fenna-Matthews-Olson protein
GDM	Gaussian disorder model
$\hbar$	reduced Planck constant $h/2\pi$
H_2-OBPc	1,4,8,11,15,18,22,25-octabutoxy-29*H*,31*H*-phthalocyanine
HOMO	highest occupied molecular orbital
IPR	inverse participation ratio
J^{C}	Coulombic excitonic coupling
J^{TOT}	total excitonic coupling
J^{short}	short-range excitonic coupling
k_B	Boltzmann constant
kMC	kinetic Monte Carlo

LC-ωPBE long-range corrected Perdew-Burke-Ernzerhof exchange-correlation functional

LDOS local density of states

LH2 light-harvesting 2 protein

LHC light-harvesting complex

LL localization length

LUMO lowest unoccupied molecular orbital

MC Monte Carlo

MD molecular dynamics

ME mobility edge

MLJ Marcus-Levich-Jortner

MTR multiple trapping and release

NNH nearest neighbour hopping

NPT constant particle number (N), pressure (P) and temperature (T)

NVT constant particle number (N), volume (V) and temperature (T)

OBPc 1,4,8,11,15,18,22,25-octabutoxy-29*H*,31*H*-phthalocyanine

OLED organic light emitting diode

OPV organic photovoltaic

OTFT organic thin film transistor

P3HT poly(3-hexylthiophene)

PBC periodic boundary conditions

PCDTBT Poly[*N*-9'-heptadecanyl-2,7-carbazole-*alt*-5,5-(4',7'-di-2-thienyl-2',1',3'-benzothiadiazole)]

Pc phthalocyanine

PCE power conversion efficiency

PCP peridinin chlorophyll protein

PES potential energy surface

p_{esc} escape probability

PPV poly(*p*-phenynelene vinylene)

RMSD root mean square deviation

RMSE root mean square error

TDC transition density cube

TDDFT time-dependent density functional theory

VRH	variable range hopping
WLC	worm-like chain
ZPE	zero point energy
ZnPc	zinc phthalocyanine

1. Introduction

1.1 Organic electronics

The present generation is witnessing a transition from a high-energy society based on the consumption of cheap and convenient fossil fuels to a society with lower energy consumption relying more and more on renewable energy sources, or in other words on direct rather than fossil solar energy, a change already envisaged more than 100 years ago by pioneering photochemist Giacomo Ciamician.[1] During such a large scale transformation we face many different challenges such as the exhaustion of natural resources and climate change. A diverse range of new technologies and approaches is necessary for better resilience among changing conditions.

One of the most promising and active research fields of the last decades is organic electronics, whose object of study is a class of carbon-based materials named organic semiconductors, which are classified into polymers and small molecules. Polymers are very long molecules made of chemically bonded repeating units (monomers), while "small molecules" is used as a broader term including oligomers (up to a few tens of repeating units), dendrimers and smaller molecules. The chemical structures of the molecular semiconductor zinc phthalocyanine (studied in chapter 4) and of the high performance semiconducting polymer PCDTBT (Poly[*N*-9'-heptadecanyl-2,7-carbazole-*alt*-5,5-(4',7'-di-2-thienyl-2',1',3'-benzothiadiazole)]) [2–4] are shown in Figure 1.1. The common feature which makes these materials semiconducting is conjugation, i.e. the presence of π orbitals delocalized over the molecule or the polymer backbone. The energy difference between the highest occupied and the lowest unoccupied molecular orbital (HOMO-LUMO gap) is usually in the visible range and gives conjugated molecules photoactive properties such as the ability to absorb or emit light. The term "organic" is used to distinguish these prevalently carbon-based materials from conventional semiconductors based on inorganic materials such as silicon and germanium.

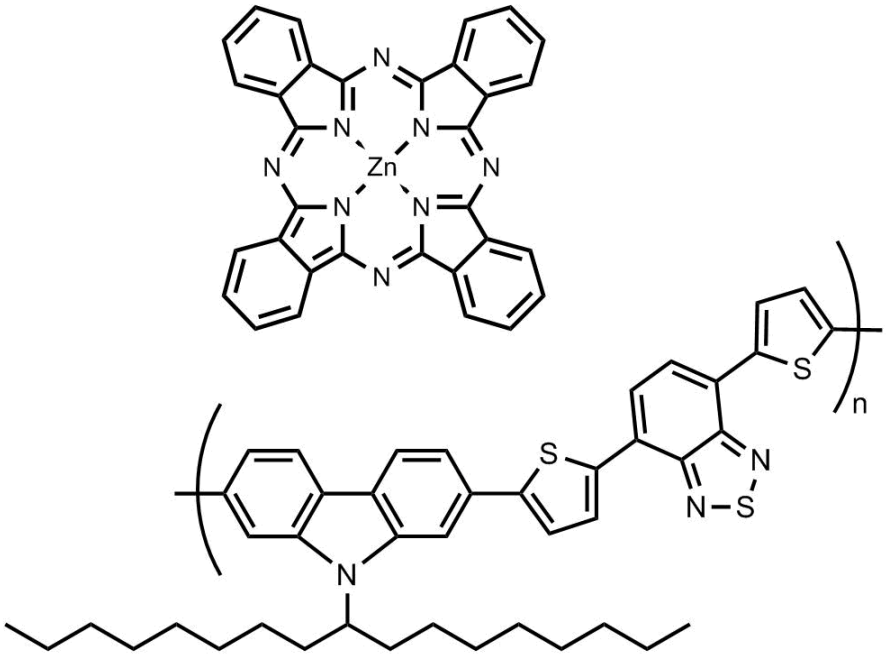

Figure 1.1. Chemical structures of the small molecule semiconductor zinc phthalocyanine (top) and of the semiconducting polymer PCDTBT (bottom).

There are many characteristics making organic materials attractive for the electronics industry: i) Fine-tunability of many properties through chemical synthesis: the molecular structure determines electronic properties such as light absorption or emission, physical and chemical properties such as solubility, stability, and the morphology at the micro- and macroscopic scale affecting the material's performance. ii) Ease of processing enabling low temperature and fast (hence low-energy and low-cost) roll-to-roll fabrication processes such as solution printing (polymers) or vacuum deposition (small molecules) on flexible substrates. iii) The unique properties of organic electronic devices, such as flexibility, transparency, and light weight, enable innovative applications such as transparent/translucent photovoltaic films, flexible/stretchable displays, and wearable electronics. These characteristics make organic semiconducting materials complementary rather than alternative to inorganic semiconductors.[5]

The semiconducting properties of conjugated molecules have been known for a long time, since in 1948 Eley first examined the conductivity of phthalocyanines [6] and other aromatic molecules and associated it with the π orbitals forming transport bands in the crystal.[7,8] Similar observations were made by Mette et al. [9] on anthracene single crystals in 1953 and by Akamatu et al. [10] on a perylene-bromide complex in 1954. Bernanose [11] managed to obtain electroluminescence by applying

a high voltage alternating current to organic compounds already in 1955, but a major breakthrough was made in 1963 when Pope et al. built the first direct current organic light emitting diode (OLED) based on anthracene.[12] These early devices required very high operating voltages due to the large thickness of the crystals. A much better performing OLED operating at low voltage was constructed much later in 1987 by Tang and VanSlyke; its active layer consisted of two thin layers of vacuum deposited molecules.[13] The history of polymer electronics traditionally begins in 1977 when Shirakawa and co-workers showed that the conductance of the conjugated polymer polyacetylene can be greatly enhanced by doping with halogens.[14] This finding opened a new chapter in the history of organic semiconductors and Shirakawa, MacDiarmid and Heeger were awarded the Nobel prize in chemistry in 2000 for this discovery. The first undoped polymer OLED, based on poly(*p*-phenynelene vinylene) (PPV), was built in 1990 by Burroughes et al.[15] OLED technology has now reached commercial maturity and is widely employed in the displays of small devices such as smartphones. Most OLED displays are currently fabricated by vacuum deposition of small molecules.[16] The realization of larger displays e.g. for television screens requires solution-processable (printable) active materials, for which polymeric materials are the best candidates.[16] Organic thin film transistors (OTFT), for which the first working examples were reported in the early 1980s,[17,18] are another important class of organic electronic devices which will enable a range of new applications such as all-organic integrated circuits, sensors, and backplanes for fully flexible OLED displays in the near future.[19,20]

Organic photovoltaic (OPV) cells represent maybe the most ground-breaking innovation enabled by organic semiconductors, as they can in principle be mass-produced at a much lower cost than conventional silicon solar panels and have a wider range of potential applications. The fundamental steps enabling a typical donor-acceptor solar cell to convert light into electricity are represented schematically in Figure 1.2: i) a photon of light is absorbed by the donor material and forms an electronically excited state (exciton), ii) the exciton diffuses towards the donor-acceptor interface (junction), iii) the exciton dissociates into a free electron in the acceptor material and a free hole in the donor material (charge separation), iii) the electron and hole travel towards the electrodes (charge transport), establishing a current.

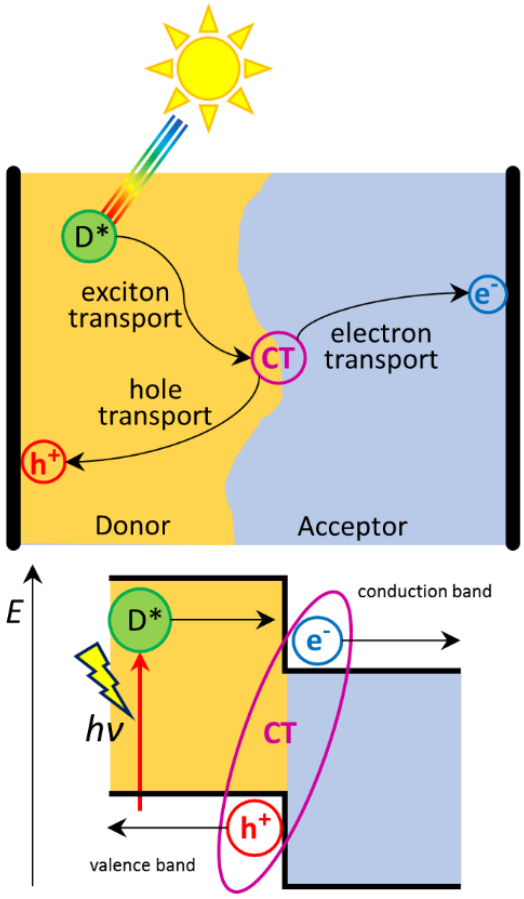

Figure 1.2. Scheme illustrating the basic working principles of a donor-acceptor organic solar cell. D* indicates an electronically excited state of the donor material. CT indicates a charge transfer state which may form at the donor-acceptor interface, leading to separation of the electron (e^-) and hole (h^+). Charge separation is facilitated by the offset between donor and acceptor energy levels.

In the early stages of development organic solar cells were based on a Shottky barrier architecture with a single layer of light-absorbing, usually hole-transporting (*p*-type) photoactive material, sandwiched between metal electrodes with different work functions. In these devices charge separation occurred at the interface between the organic material and one of the electrodes. These devices exhibited very low power conversion efficiencies (PCE) < 1 %.[21] In 1986 Tang [22] reported the first organic solar cell based on a two-layer architecture where free charges are efficiently generated at the interface between the donor and acceptor materials as depicted in Figure 1.2. Soon after Sariciftci and co-workers discovered that ultrafast photoinduced electron transfer occurs between a semiconducting polymer, as main light absorber and electron donor, and a buckminsterfullerene (C_{60}) as electron acceptor.[23] The polymer-fullerene pair has since become the standard workhorse of polymer photovoltaic cells. The importance of efficient diffusion of the excitons to

the interface was already recognized by Tang.[22] It is now widely agreed that excited states (excitons) in most organic materials can diffuse for just about 10 nm before recombining.[24] Therefore, for efficient charge separation it is necessary that a donor-acceptor interface is reached within that length scale, but ~20 nm is much too thin for a simple double layer device to absorb enough light to be efficient. A major breakthrough came again from Heeger's group: by blending together polymer and fullerene (or its derivatives) rather than depositing them in separate layers, they obtained a material where donor and acceptor materials spontaneously phase-separate at the 10-20 nm length scale, forming a bi-continuous interpenetrating network of donor and acceptor domains with a large interface area available for charge separation, a novel concept named bulk heterojunction (BHJ).[25] Thanks to the BHJ morphology and other innovations, the performance of organic solar cells has greatly improved over the recent decades,[26] reaching in February 2016 a world record PCE of 13.2 % for a multi-junction vacuum deposited small molecule device reported by Heliatek GMBH.[27] Although the PCE of OPV devices is much lower than that of inorganic solar cells (currently around 20 % for commercial panels) under standard one sun illumination, they perform better in low-light conditions [28] such as cloudy sky, diffused/reflected sunlight or indoor LED lighting, opening a range of new potential applications.[29,30] Thanks to their low material consumption and low carbon footprint, roll-to-roll manufactured OPV films are very close to become one of the leading technologies for renewable energy generation, both for large-scale solar parks [31] and for small to medium scale applications such as power sources for electronic devices [32] and flexible light-harvesting films for any type of surface such as tents, vehicles and buildings.[33]

In order to make organic electronics commercially and ecologically viable, it is important to improve many different aspects such as ease of processing, device architecture, (transparent) electrode materials, encapsulation materials (to improve ambient stability), but the most important and challenging aspects are the fundamental properties of the active material itself. Given a material with suitable energy levels for the required application, the performance of the device will strongly depend on the efficiency of the dynamical processes illustrated in Figure 1.2, namely exciton transport, charge separation and charge transport. In this thesis, we will explore some of the theoretical aspects determining the exciton transport and charge transport

properties of a given organic material. Both are multi-scale problems as they depend on the material's structure from the atomic up to the macroscopic scale. Charge separation is equally important, but it is a nanometre-scale problem regarding the donor-acceptor interface and is outside the scope of this thesis. As already mentioned above in the description of the OPV cell, efficient diffusion of the excitons to the donor-acceptor interface is fundamental to ensure that most of the absorbed photons are converted to free charges before the excitons recombine. Efficient charge transport is also very important as it determines the charge mobility, a property affecting the performance of all devices based on semiconducting materials. In an OPV cell the free charges need to travel from the interface to the electrodes and in an OLED the opposite way. The operation of an OTFT also requires materials with high charge mobility.[19]

The dynamic behaviour of charge and exciton transport depends mainly on the spatial arrangement of the subunits constituting the material (molecules or polymer segments) and on the interactions (couplings) between the relevant electronic states localized on the subunits (sites). In simple terms, the interplay between the electronic coupling strength, the degree of regularity (order) and the interactions with nuclear degrees of freedom (electron-phonon coupling) determines the transport mechanism. There are different types of disorder affecting organic materials: variations of the electronic energy levels and of the couplings between them are respectively called *on-site* and *off-site* (or *diagonal* and *off-diagonal*) disorder; *dynamic* disorder is due to fluctuations on a timescale equal or faster than that of the dynamical process under consideration, while *static* disorder indicates variability in space due to disordered morphology or to fluctuations slower than the relevant timescale.

A better theoretical understanding of the mechanisms of these fundamental dynamical processes and their dependence on structural, environmental and operational parameters is essential for interpreting and predicting experimental data and for suggesting new materials design guidelines to improve the properties of organic electronic devices. In the next three sections, some key theoretical aspects of exciton dynamics and charge transport in organic semiconductors will be outlined.

1.2 Excited states in molecular aggregates – from dimer couplings to exciton dynamics

When a photoactive material absorbs an incoming photon, or when free charge carriers associate, an electronically excited state is created. This process can be roughly described as one electron being promoted from an occupied to an unoccupied orbital. In an extended system such as a crystal or aggregate, the excitation energy can be shared between molecules or fragments, leading to delocalization of the excited state. Electronically excited states in solid materials can be described starting from two opposite limits depending on the material's structure and dielectric constant.

The electronic structure of inorganic periodic solids (such as atomic crystals), is described in terms of energy bands delocalized over the bulk of the material. Excited states are also delocalized and thanks to a high dielectric constant the electron-hole pair is weakly bound, i.e. they can readily separate into free carriers without the need for a donor-acceptor interface. Confinement due to morphology and/or defects can increase the electron-hole binding energy and cause localization of the excited state, referred to as Wannier-Mott exciton in this picture.[34]

Organic materials are generally characterised by a low dielectric constant, hence the more strongly bound electron-hole pair is better described starting from a singlet excitation spatially confined on a subunit of the aggregate. Such a localized singlet excited state is referred to as a Frenkel exciton.[35,36] The interactions between different subunits (which can be molecules, fragments or monomers, and from now on generically called chromophores) lead to delocalization of the excitons and the spectroscopy of the aggregate will differ from that of the isolated chromophore. In this framework, a molecular aggregate can be described by the (static) excitonic Hamiltonian

$$H_{\mathrm{exc}} = \sum_i E_i |i\rangle\langle i| + \sum_i \sum_{j \neq i} J_{ij} |j\rangle\langle i|, \tag{1.1}$$

written in the basis of the diabatic states $|i\rangle$ (Frenkel exciton localized on chromophore *i*), whose excitation energy is E_i. The interaction between any pair of chromophores *i* and *j* is given by the excitonic coupling J_{ij}. The eigenstates of this Hamiltonian are the adiabatic excitonic states which can be delocalized over several chromophores if the couplings between them are strong enough. The properties of the

system will therefore strongly depend on the strength of the excitonic couplings. In the next section we discuss the nature of this interaction and present a method to compute couplings between singlet Frenkel excitons with high accuracy.

1.2.1 Excitonic couplings

Excitonic couplings are important as they can affect not only the spectroscopy of aggregates, but also the dynamic electronic energy transfer (EET) processes which enable exciton transport. The mechanism of singlet EET was initially rationalized by Förster,[37] who found that the rate of energy transfer between two chromophores (energy donor and energy acceptor) depends on the spectral overlap between the donor emission and acceptor absorption spectra (i.e. resonance between their excitation energies), and on the Coulombic interaction (coupling) between their transition densities. The Coulombic coupling can be approximated by the interaction between the transition dipole moments (point dipoles placed on the chromophores' centres of mass) only when the inter-chromophore distance is very large compared to the chromophore size. The point dipole approximation is therefore rarely accurate enough for computing couplings in closely packed molecular aggregates. The full Coulombic coupling is [38–40]

$$J^{\mathrm{C}} = \int\int \frac{\rho^{a}(\mathbf{r}_i)\cdot\rho^{b}(\mathbf{r}_j)}{\left|\mathbf{r}_i-\mathbf{r}_j\right|} d\mathbf{r}_i d\mathbf{r}_j \cong \sum_{i,j}^{N_{\mathrm{grid}}} \frac{\rho_i^{a}\cdot\rho_j^{b}}{\left|\mathbf{r}_i-\mathbf{r}_j\right|}, \tag{1.2}$$

where $\rho^{a(b)}(\mathbf{r})$ is the value of the transition density of the Frenkel exciton *a* (*b*). In practice, the integral in eq. (1.2) can be evaluated numerically as a summation over a grid of points $\{\mathbf{r}_i\}$ commonly called transition density cube (TDC),[39] with $\rho_i^{a(b)} = \rho^{a(b)}(\mathbf{r}_i)$. The full Coulombic interaction J^{C} is a very good approximation of the excitonic coupling when the distances between chromophores are larger than interatomic distances.[37] Evaluating J^{C} from TDCs can be computationally demanding due to the large number of grid points needed to reach convergence. For this reason, it is often assumed that approximations based on coarser representations of the transition density are appropriate. When the distance between molecules is comparable to the molecular sizes, one can discretize the transition density, expressing it as charges centred on the atoms [41,42] (atomic transition charges, ATC), while for very distant pairs, as mentioned above, the point dipole approximation adopted by Förster [37] is often used. However, when the chromophores are in van der Waals

contact (e.g. some atoms are within π-π stacking distances < 5 Å as in the systems considered in chapters 3 and 4), the Coulombic interaction may not be accurate enough since there are other effects contributing to the excitonic coupling. These short-range contributions depend on the inter-chromophore overlap between orbitals and their nature has been investigated by Harcourt, Scholes and Ghiggino in a series of papers.[43–45] By studying the interactions between Frenkel and charge transfer (CT) excited configurations,[43] the dominant non-Coulombic short-range contributions were identified to be: i) a penetration interaction, generally reinforcing the Coulombic term,[44] and ii) a Dexter-type exchange term which opposes it but is of smaller magnitude.[45] Short-range contributions to the excitonic couplings were found to play an important role in the exciton dynamics of molecular crystals:[46,47] due to their strong dependence on intermolecular overlap, they cause the interaction to be very sensitive to small relative displacements, which can cause large fluctuations of the couplings. Therefore, the accuracy with which they are computed affects the sensitivity of the system's properties to both static and dynamic disorder.

Describing the spectroscopy and dynamics of an aggregate starting from a Hamiltonian as in eq. (1.1) requires computing a large number of excitonic couplings. In practice, the Coulombic coupling can be easily computed for many chromophore pairs using eq. (1.2) or one of its approximations (ATC, point dipoles), while the short-range contributions are not easily obtainable explicitly. However, it is possible to accurately compute the total excitonic coupling (including both Coulombic and short-range contributions) by using one of the available diabatization techniques. These techniques can be computationally more demanding as they require computing the adiabatic excited states of the chromophore pair (dimer) and the diabatic excited states of interest, i.e. the reference states between which the coupling is needed (in our case, the singlet Frenkel excitons localized on the single chromophore). A diabatization is a unitary transformation of the adiabatic Hamiltonian of the dimer so that it is expressed in the desired diabatic basis. If we choose this basis to be as similar as possible to the diabatic reference states, we will obtain a diabatic Hamiltonian which contains the couplings between these diabatic states. To find this transformation, some diabatization schemes rely on the excited state wavefunctions.[48,49] These methods are rigorous but their implementation is not easy as it depends on the choice of the level of theory. Instead, diabatization schemes based on molecular properties (which

need to be representative of the states of interest) are in principle independent of the electronic structure calculation method.

In chapters 3 and 4 of this thesis, excitonic couplings between chromophores in close (van der Waals) contact will be considered. For these molecular pairs, the Coulombic couplings obtained from eq. (1.2) cannot always be considered of sufficient accuracy so they will be compared with the total coupling computed with the diabatization method described in the next section.

1.2.1.1 Diabatization between multiple excited states

The diabatization scheme recently presented by Aragó et al. [50] allows to compute the full excitonic couplings between multiple excited states in molecular pairs. The ability to consider multiple excited states is particularly useful in situations where the lowest Frenkel states are quasi-degenerate (as in porphyrins, phthalocyanines or polymeric systems) or where inter-molecular charge transfer states or other dark states are close in energy to the lowest Frenkel states, so that their interactions should not be neglected. The procedure followed in this diabatization scheme can be explained as follows. Considering a dimer system, we can calculate with any suitable computational method a set of *n* adiabatic singlet excited states $\left\{\psi_1^{\mathrm{A}},\psi_2^{\mathrm{A}},\cdots,\psi_n^{\mathrm{A}}\right\}$; their energies $\left\{E_1^{\mathrm{A}},E_2^{\mathrm{A}},\cdots,E_n^{\mathrm{A}}\right\}$ are the diagonal elements of the adiabatic Hamiltonian

$$\mathbf{H}^{\mathrm{A}}=\begin{bmatrix} E_1^{\mathrm{A}} & 0 & \cdots & 0 \\ 0 & E_2^{\mathrm{A}} & \cdots & 0 \\ \vdots & \vdots & \ddots & \vdots \\ 0 & 0 & \cdots & E_n^{\mathrm{A}} \end{bmatrix}. \tag{1.3}$$

The key passage of the diabatization is to find the orthogonal transformation matrix $\mathbf{C}=\left\{C_{ij}\right\}$ whose elements transform the adiabatic states into quasi-diabatic states: $\psi_i^{\mathrm{D}}=\sum_j C_{ij}\psi_j^{\mathrm{A}}$. In other words, **C** transforms the adiabatic Hamiltonian (eq.(1.3)) into the diabatic Hamiltonian $\mathbf{H}^{\mathrm{D}}=\mathbf{C}\mathbf{H}^{\mathrm{A}}\mathbf{C}^{T}$, where $\mathbf{C}^{T}$ is the transpose of **C**. In order to find **C**, we need to use a molecular property characterising the different excited states. The atomic transition charges (ATC), which are a reasonably fine-grained approximation of the transition density, were found to be a property suitable for the diabatization as they allow monitoring the nature of the excited states. We start by building the rectangular matrix $\mathbf{q}^{\mathrm{A}}=\left(\mathbf{q}_1^{\mathrm{A}},\mathbf{q}_2^{\mathrm{A}},\cdots,\mathbf{q}_n^{\mathrm{A}}\right)$ which contains the adiabatic

ATCs. Each column vector $\mathbf{q}_i^{\mathrm{A}}$ contains the set of ATCs (one for each atom) for the *i*-th adiabatic state. $\mathbf{q}^{\mathrm{A}}$ is related to the diabatic ATC matrix $\mathbf{q}^{\mathrm{D}}$ by the transformation matrix **C** we are looking for: $\mathbf{q}^{\mathrm{D}} = \mathbf{q}^{\mathrm{A}}\mathbf{C}^T$. Then we define, using chemical intuition, an "ideal" diabatic reference matrix $\mathbf{q}^{\mathrm{D,ref}}$ for the dimer system, which should mimic the properties of the reference states (in our case, $\mathbf{q}^{\mathrm{D,ref}}$ will contain the ATCs of the excited states localized on the isolated molecules). Now we have to find the transformation matrix **C** which, applied to $\mathbf{q}^{\mathrm{A}}$, makes the resulting $\mathbf{q}^{\mathrm{D}}$ as similar as possible to $\mathbf{q}^{\mathrm{D,ref}}$. This amounts to finding the matrix which minimizes the Frobenius norm (square root of the sum of all squared matrix elements) of the difference between the transformed charges and the reference charges:

$$\mathbf{C}^T = \arg\min_{\mathbf{R}} \left\| \mathbf{q}^{\mathrm{A}}\mathbf{R} - \mathbf{q}^{\mathrm{D,ref}} \right\|. \tag{1.4}$$

This is a linear algebra problem known as orthogonal Procrustes problem [51] whose unique solution is $\mathbf{C}^T = \mathbf{U}\mathbf{V}^T$, where **U** and $\mathbf{V}^T$ are obtained from the singular value decomposition of the matrix $\left(\mathbf{q}^{\mathrm{A}}\right)^T \mathbf{q}^{\mathrm{D,ref}} = \mathbf{U}\mathbf{\Sigma}\mathbf{V}^T$. The final result is the diabatic Hamiltonian $\mathbf{H}^{\mathrm{D}} = \mathbf{C}\mathbf{H}^{\mathrm{A}}\mathbf{C}^T$ which has the form

$$\mathbf{H}^{\mathrm{D}} = \begin{bmatrix} E_1^{\mathrm{D}} & J_{12} & \cdots & J_{1n} \\ J_{21} & E_2^{\mathrm{D}} & \cdots & J_{2n} \\ \vdots & \vdots & \ddots & \vdots \\ J_{n1} & J_{n2} & \cdots & E_n^{\mathrm{D}} \end{bmatrix}, \tag{1.5}$$

where the diagonal elements are the diabatic energies E_i^{D} (which should be similar to the energies of the reference states), and the off-diagonal elements are the excitonic couplings J_{ij} between the diabatic states ψ_i^{D} and ψ_j^{D}. In summary, the diabatization scheme described here is a general method for computing the total excitonic couplings (including short-range contributions) between multiple excited states in chromophore pairs. For medium to large molecules (>20 atoms), the computational bottleneck of this procedure is the electronic structure calculation of the excited states of each dimer. Typically, the couplings between many dimers are needed to build an excitonic Hamiltonian such as eq. (1.1), but the dimers are independent of each other so they can be simultaneously calculated by different computing nodes. When the short-range contributions can be neglected, i.e. the Coulombic couplings are sufficiently accurate, it is preferable (much faster) to compute them using eq. (1.2).

1.2.2 Exciton dynamics: regimes and theories

The description of electronically excited states was hitherto limited to static properties. The excitonic Hamiltonian in eq. (1.1) can describe the system at a given moment in time, but to study the movement of excitation energy in time (exciton dynamics of the system), one has to resort to more complex theoretical concepts and models. This area of research is thriving since the discovery of long-lived coherent phenomena in light-harvesting complexes of photosynthetic bacteria.[52] It is now believed that process coherence, defined as the persistence in time of superpositions of quantum states, plays an important role in fast exciton transport in light-harvesting complexes,[53] although the role of coherence is still up to debate.[54] Since coherent effects have also been observed in artificial systems,[55–58] it has been suggested that these concepts could be exploited to improve the performance of organic semiconductors.[59–63] We will now outline the most commonly used methods for studying exciton dynamics in open quantum systems, valid for both biological (light-harvesting complexes) and artificial systems (e.g. organic semiconductors). Depending on the parameters of the system, different transport regimes can be identified and, correspondingly, different methods have been developed for modelling exciton dynamics, depending on the approximations that can be made in these regimes.

The timescales of electronic and nuclear motions are often comparable and in principle both need to be considered as well as the interactions between them. The phenomenon of homogeneous line broadening due to interaction between electronic and vibrational levels is well known in spectroscopy and the energy difference between the absorption and emission maxima (the Stokes shift) corresponds to roughly twice the geometric relaxation energy, which is a measure of the *local* exciton-phonon coupling strength. Intuitively, the relaxation is an adaptation of the nuclear geometry to the newly adopted electronic configuration. In the context of exciton transfer between two molecules, the reorganization energy λ for the process is composed of the relaxation energies of the donor and acceptor molecules, the former going from the vibrationally relaxed excited state to the ground state and the latter from the relaxed ground state to the excited state (see section 3.2.3 and the scheme in Figure 3.2). The thermal fluctuations of the couplings J (dynamic disorder), also known as *non-local* electron-phonon coupling, are often neglected but should be taken

into account for a quantitative description of exciton dynamics and other related phenomena in molecular aggregates where the couplings can be very sensitive to small relative displacements.[47,64,65]

The relative strength of λ and of the excitonic coupling J determines the regime of exciton transport. In the two opposite limiting regimes (weak and strong excitonic coupling) for the separability of electronic and nuclear degrees of freedom, the Born-Oppenheimer (B-O) approximation, is valid. When $J \ll \lambda$ (incoherent regime), the local electron-phonon coupling is strong enough for the exciton to be localized on one molecule, and the B-O separability applies to the individual molecules.[53] The exciton transfer process can be described as a nonadiabatic reaction between donor and acceptor molecule with a barrier of $\approx \lambda/4$, hence a rate for the reaction can be defined and the transport proceeds by a hopping mechanism. In this regime the Förster theory of EET,[37] its generalized version,[66] or non-adiabatic rate theories [47] are suitable to describe exciton dynamics (the rate expression used in ref. [47] is discussed in chapter 2). In the incoherent regime, larger couplings lead in general to faster transition rates and consequently faster exciton transport. Dynamic disorder does not alter the physics of the transport in this regime but needs to be considered as it can affect the hopping rates quantitatively.[47]

In the opposite limit of very large coupling ($J \gg \lambda$), excitons are delocalized, and the B-O separability applies to the whole system, i.e. the vibrations are normal modes of the delocalized eigenstates.[53] The dynamics of the system in this regime are commonly described by Redfield theory:[67] in addition to the electronic Hamiltonian (eq. (1.1)) further terms are introduced which describe the classical nuclear motion and the local exciton-phonon coupling. The time evolution of the system is described by the coherent evolution of the reduced density matrix and by a perturbation due to weak local exciton-phonon coupling which allows transitions between the electronic eigenstates. In section 2.3.1.1 we will show that, starting from Redfield theory, a kinetic rate expression for transitions between electronic states promoted by weak coupling to phonon modes can be derived.

The approximations and methods valid in the regimes just described are in general not valid in the intermediate regime where J and λ are of comparable magnitude. This is the so-called coherent regime where the energy transfer is predicted to be fastest.[53] The B-O approximation is no longer valid here since the

timescales of energy transfer and nuclear motions are comparable. On the contrary, the strong interaction (mixing) between electronic and (in some cases non-equilibrium) vibrational degrees of freedom plays a fundamental role in the time evolution of the system. The Markov approximation (valid in Redfield theory), which assumes that vibrational modes relax faster than the excitation transfer, is usually not valid in this intermediate regime. Out-of-equilibrium modes interacting with the electronic states can give rise to memory effects which cannot be ignored. The coherent oscillations observed experimentally, sometimes interpreted as supporting fast exciton transport, can be of electronic, vibrational or vibronic (mixed) origin.[53] The broad range of different phenomena observed is due to a complicated interplay between unitary evolution of the wavefunction and dissipation due to phonon modes, which makes realistic theoretical models difficult to solve. The exact solution of the Schrödinger equation for the whole system is usually beyond reach due to the large number of degrees of freedom. Only for systems with very few degrees of freedom it can be solved exactly using for example the multi-configuration time dependent Hartree method.[68] The system is therefore usually partitioned into an electronic part, the *subsystem*, consisting of just the chromophores' electronic energy levels and a few other relevant degrees of freedom, while the remaining variables are treated collectively as the *bath*, which can include intra- and intermolecular vibrations as well as the surrounding environment with various degrees of simplification. One of the major challenges in developing simplified theoretical methods is correctly accounting for the effects of the bath on the dynamics of the subsystem (and vice versa).

One class of approaches is based on the Nakajima-Zwanzig generalized quantum master equation [69,70] describing the time evolution of the reduced density matrix. The hierarchical equations of motion methods [71,72] provide a formally exact solution for the time evolution of a reduced system coupled with a bath of quantum oscillators. Non-Markovian effects are accounted for by a memory kernel and system-bath correlations (often neglected) can be described by an inhomogeneous term. Due to difficulties in the treatment of the bath modes, often they are assumed to relax faster than the system and weak system-bath coupling is assumed (effectively reducing to Redfield theory). Of course, such approximations come at the cost of not accounting for solvation dynamics and bath memory effects. The approach proposed

in ref. [73], where the memory kernel and inhomogeneous term can obtained for any system-bath coupling strength, overcomes these limitations.

Among the wavefunction-based methods it is worth mentioning the surrogate Hamiltonian method, where an exactly solvable system-bath Hamiltonian is built with a finite number of bath modes. This finite system can reproduce the true dynamics of an infinite (open) system at short times. The advantage of this method is that one does not need to assume weak system-bath interaction and separation of timescales. Lee et al. recently proposed a vibronic version of the surrogate Hamiltonian method, where the relevant vibrational modes are part of the main system.[74] This method made it possible to evaluate the strong influence of both local and non-local exciton-phonon coupling (intra- and inter-molecular relaxation, or respectively reorganization energy and thermal fluctuations of the couplings) on exciton dynamics.[65]

Mixed quantum-classical approaches, where only the electronic part and a few effective vibrations are treated quantum mechanically and the remaining degrees of freedom are treated classically, have the advantage of a much-reduced computational cost. In the mean field approach (Ehrenfest method) the motions of the classical subsystem are restricted to a single potential energy surface (PES), obtained from a weighted average over quantum states. A similar approach is adopted in section 3.3.5, where the exciton motion along a stack of phthalocyanine molecules is described by propagating a semiclassical model Hamiltonian (eq. (3.2)), which includes electronic and electron-phonon coupling parameters obtained from classical and quantum calculations. The shortcoming of mean field methods is that due to inconsistencies between classical and quantum descriptions the decoherences are not taken into account and the equilibrium populations at long times can be incorrect.[75] Surface hopping methods, where stochastic transitions (hops) between PESs are introduced, are more suitable to situations where the quantum and classical parts are strongly coupled, and they can approximately reproduce the Boltzmann populations of quantum states. The standard surface hopping algorithm is the fewest switches surface hopping (FSSH): [76] its essential steps are i) classical motion of the nuclei (as in molecular dynamics), ii) quantum evolution of the wavefunction, iii) surface hopping (accepted if the nuclei have enough kinetic energy), and iv) adjustment of the nuclear velocities to the new PES. Many surface hopping trajectories generate a statistical ensemble which can provide useful insights into the system's population dynamics. A

recent implementation of the FSSH method allows the treatment of populations and coherences on equal footing.[77]

Dynamic disorder, i.e. the fluctuation of electronic energies and couplings on timescales equal or faster than those of the relevant transport process, is mainly due to intra- and inter-molecular vibrations. The role of dynamic disorder is often neglected in exciton dynamics models, but in the intermediate to strong coupling regime it can strongly influence exciton dynamics if the fluctuation of the coupling is large compared to its magnitude.[47] In order to select an appropriate method and correctly describe exciton dynamics in molecular aggregates, it is important to compute the excitonic couplings *J* with high accuracy and to fully account for their fluctuations in space and time. As discussed in section 1.2.1, the Coulombic interaction does not capture the full coupling at short intermolecular distances. The role of dynamic disorder in a phthalocyanine molecular crystal is investigated in chapter 3 and the relative importance of short-range contributions for the couplings in a wide range of molecular aggregates is presented in chapter 4.

1.3 Charge transport in disordered polymers

The transport of electrical charges is one of the most important processes limiting the performance of organic semiconducting materials. In a photovoltaic device, for example, efficient charge transport is essential from the nanometre-scale, e.g. to avoid recombination of freshly separated charges, up to the macroscopic device scale (μm to cm), to allow efficient charge collection enabling large currents. The charge mobility is in general a 3 x 3 tensor $\bar{\boldsymbol{\mu}}$ and is defined as the charge carrier's velocity response to an externally applied (or built-in) electric field **F**:

$$\mu_{\alpha\beta} = \frac{\langle v_\alpha \rangle}{F_\beta}, \tag{1.6}$$

where α, β are the spatial coordinates *x*, *y*, *z* and $\langle v_\alpha \rangle$ is the time-averaged carrier velocity along one direction. For vanishing field, it is more appropriate to use the Einstein-Smoluchowski equation valid when the transport is diffusive

$$\mu_{\alpha\beta} = \frac{qD_{\alpha\beta}}{k_{\mathrm{B}}T}, \tag{1.7}$$

where *q* is the charge and $D_{\alpha\beta}$ is the element of the diffusion tensor.

The highest mobilities in organic semiconductors are achieved in highly ordered materials, e.g. ultra-pure single crystals of small molecules such as pentacene and rubrene, where the transport mechanism is now believed to be essentially diffusion limited by dynamic disorder,[78] a scenario named transient localization [75] which is not too different from the intermediate regime of exciton transport described in the previous section. This regime will not be discussed here as the treatment of charge transport in this thesis is focused on incoherent transport in disordered polymers.

Decades of research in semiconducting polymers have led to a wide variety of chemical structures and morphologies. If we also consider the large number of degrees of freedom determining the structure of these macromolecules, the task of rationalising the charge transport properties can appear rather complicated. Polymeric materials can have ordered domains but can never be completely crystalline due to their large number of conformational degrees of freedom. The different types of morphology of polymeric materials are schematically represented in the top panels of Figure 1.3. After the introduction of poly(3-hexylthiophene) (P3HT), a semicrystalline polythiophene exhibiting highly ordered lamellar crystalline domains and fairly high mobility (0.1 compared to the 10^{-5} $cm^2V^{-1}s^{-1}$ of amorphous polymers at that time), [79,80] the research community focused on designing more long-range ordered polymers with larger crystallites and higher fraction of crystallinity, resulting in another order of magnitude increase in mobility.[81] However, the recent introduction of a new class of donor-acceptor polymers, most notably of the diketopyrroloppyrrole (DPP) family,[82] challenged this idea since materials with very low crystallinity or no long-range order exhibited even higher mobilities. The data from ref. [83] reported in the bottom panel of Figure 1.3 shows that some of these newly reported poorly ordered polymers can perform better than semicrystalline materials (see caption). It is now believed that non-crystalline short-range aggregation [84], tolerance to disorder [85,86], and efficient transport along disordered chains which ensure connectivity between ordered domains,[83] are much more successful design strategies leading to higher mobility semiconducting polymers.[87–90] This approach also has a technological advantage, since thin films without big crystallites are more homogeneous and are therefore more easily processable and yield a more uniform film morphology.[91,92] In summary, the ideal semiconducting polymer is well soluble and has good photophysical characteristics; its aromatic backbone is

rather rigid, minimising effective electronic disorder and ensuring efficient transport along the chain; the microstructure is homogeneous and is essentially a network of disordered chains with small, but well interconnected, aggregates where inter-chain hopping can take place ensuring sufficient connectivity for efficient charge transport.

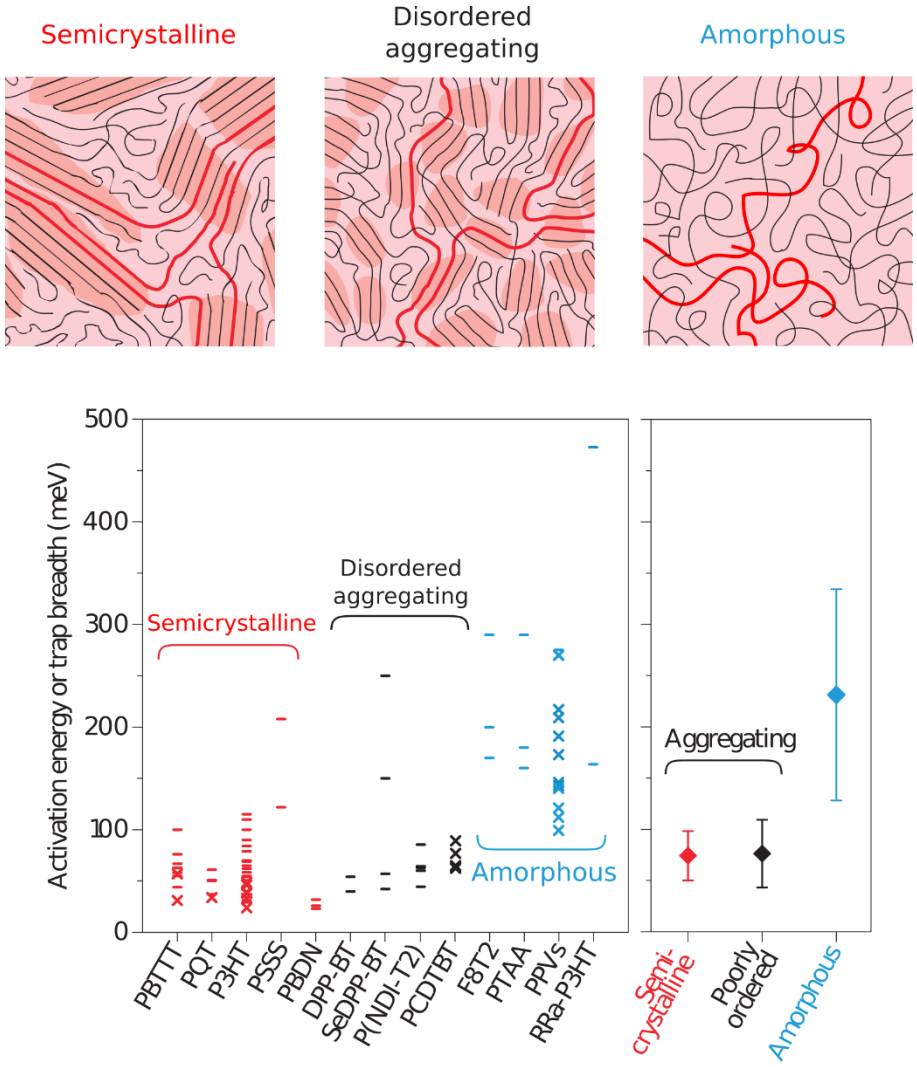

Figure 1.3. (Top) Schematic representations of the different morphologies of semiconducting polymers. Long chains connect the ordered domains (darker colour) where the charge can more easily hop to other chains. The light colour indicates amorphous regions. (Bottom) Activation energy for charge transport in polymers with different classes of morphologies. Lower activation energy corresponds to less effective electronic disorder and higher mobility. Figure adapted from ref. [83].

With the exception of few examples of devices with extremely well aligned polymer fibres directly connecting the electrodes,[93] band transport is rarely observed in polymeric semiconductors. Thermally activated transport is generally accepted as evidence for a transport mechanism based on incoherent hopping between localized states.[94] The primary cause of charge localization is believed to be structural disorder due to the static conformation of the polymer chains (Anderson

localization [95]) rather than electron-phonon coupling.[96–98] Therefore it is important to understand how molecular and electronic structure affects the disordered landscape where charge hopping takes place.

There are a number of theoretical models which can accurately describe hopping transport in disordered organic solids. Most of them are based on kinetic rates for the electron transfer between molecular units or sites. For a given set of sites, once the rates connecting them are known the mobility can be computed by solving the master equation of the system. The Gaussian disorder model (GDM), rooted in solid state physics, starts from the assumption that charges hop between sites localized on a lattice and that the density of states (DOS) can be approximated by a Gaussian distribution of the energy levels.[99] Mott's variable range hopping (VRH) concept,[100] according to which carriers can hop over a short distance with large energy difference ΔE or over a longer distance with a smaller ΔE, was combined with percolation theory by Vissenberg and Matters to describe charge transport in disordered organic materials: the temperature dependence of transport was explained by activation of carriers, i.e. promotion to a transport energy where the higher density of available states with smaller ΔE facilitates transport.[101] The coexistence of delocalized states and localized traps in partially ordered materials such as polycrystalline polymer films was taken into account by the multiple trapping and release (MTR) model [102] and later by the conceptually similar mobility edge (ME) model.[103,104] In these models transport is described by hopping between localized trap states below a fixed or adjustable energy threshold (the ME), and increasing temperature or carrier density allows carriers to reach the ME where delocalized transport with constant mobility takes place. The models just described usually assume that transport takes place on a grid of sites evenly distributed in space, but they fail to capture the complex microstructure of polymer films. The approach proposed by the Spakowitz group, based on the worm-like chain model for the conformation of polymer chains, allows to investigate the multiscale character of charge transport, which appears to be dominated by fast transport along the chains at short timescales, while inter-chain transport becomes more relevant at the macroscopic (device) scale.[105–107]

The models just summarized have the advantage of providing easily computable expressions for mobility and they have been very successful at explaining

experimental observations of electrical properties of devices.[108] However, the underlying assumptions about the shape of the DOS and the localization of states, as well as the parameters entering these models, are not obtained from chemical details of the material but from phenomenological fitting to experimental measurements. On the other hand, atomistic simulations and electronic structure methods (usually classical molecular dynamics combined with quantum chemistry) are now able to describe the local structure of specific semiconducting polymers.[85,98,109–111] The results of these studies often contrast with the assumptions made by phenomenological models in one crucial point: localization of states is energy-dependent and there is not a sharp energy threshold separating localized and delocalized states. One consequence is that the charge carrier can cover longer distances along a polymer chain by hopping into a more delocalized state and back into a localized state many monomers away. This situation is intermediate between GDM and ME models, but both fail to describe its complexity due to the assumptions they are based on. Therefore, it would be desirable to build a more general model able to bridge between the material-specific details offered by atomistic studies and a simplified transport model. With such a model, the mobility could be easily computed starting from a set of parameters that can be obtained from atomistic studies. The dependence of mobility on these parameters would then offer more insight into structure-property relationships compared to phenomenological models where the parameters are fitted to experimental data but have little relation with chemical details. A general model with these characteristics, derived starting from the minimum required amount of assumptions, and the results obtained by feeding it with a realistic range of parameters, are presented in chapters 5, 6 and 7.

A further motivation for a more general transport model is represented by the long-standing debate [112] about the temperature dependence of mobility: the GDM model predicts that $\log(\mu)$ is proportional to $1/T^2$,[99] while the ME model predicts an Arrhenius dependence ($\log(\mu) \propto 1/T$).[104] A set of experimental low charge density mobility measurements from a wide range of semiconductors [113] strongly suggests a universal Arrhenius temperature dependence, while the $1/T^2$ dependence would be valid only in the limit of zero carrier density.[114]

Finally, another key ingredient for modelling incoherent transport is the hopping rate between localized sites, often assumed to be either of the Miller-Abrahams [115]

or of the Marcus [116] type in the models summarised so far. However, when the details about charge localization and reorganization energy are known (e.g. from atomistic calculations), there is no need to resort to such simplified rate expressions. With the aim of clarifying the hidden assumptions that come with the choice of a particular rate expression, we present in chapter 2 a more general rate expression for the hopping between electronic states localized by disorder, which is also valid in the context of incoherent electronic energy transfer.

1.4 Scope and structure of this thesis

This chapter serves as an introduction to the field of organic electronics, providing the background and motivation of this thesis and an overview of the theoretical methods commonly used to describe charge and exciton transport in organic semiconductors. In the first instance, this thesis will consider an expression for the rate of charge or exciton hopping between electronic states localized by static disorder (chapter 2). This rate expression considers both local and non-local electron-phonon coupling and is very general, i.e. it can be reduced to the rates most used in literature when the appropriate limits are taken.

The central part of this work (chapters 3 and 4) deals with some aspects of exciton transport in molecular aggregates, with a focus on the interactions between excited states localized on individual molecules (excitonic couplings). Specifically, in chapter 3 the thermal fluctuations of the excitonic couplings, and their influence on exciton transport in a phthalocyanine crystal, are investigated. In chapter 4 a large number of excitonic couplings in biological and artificial aggregates are analysed with the aim of assessing the relative importance of long-range (Coulombic) and short-range interactions.

The final part of this thesis (chapters 5, 6 and 7) focuses on the theory of charge transport in semiconducting polymers. First, a very general model is presented (chapter 5), where a realistic electronic structure with variable localization of the electronic states is obtained from a simple model Hamiltonian depending on just a few parameters determining the amount of static disorder. Using the rate expression described in chapter 2, the dependence of intra-chain charge mobility on various system parameters is investigated. In chapter 5, the model is compared to existing analytical charge transport models (GDM, VRH, ME, see section 1.3) and the focus

of the analysis is the influence of the electronic structure parameters (off-site disorder and donor-acceptor structure) on charge transport along a single polymer chain. A more comprehensive exploration of the parameter space of the model (including the parameters entering the rate expression) is presented in chapter 6. Here, the model is used to rationalise the experimental observation of a universal Arrhenius temperature dependence of mobility in a wide range of semiconducting materials. Finally, the role of chain rigidity (considering the 3D structure of the polymer chains) and the interplay between intra- and inter-chain hopping, representing a further generalization of the model, are investigated in chapter 7.

2. Hopping rate between electronic states promoted by electron-phonon coupling*

Summary: In this chapter we propose an expression of the hopping rate between localized states in semiconducting disordered polymers that contains the rates most used in the literature as special cases. Although derived in the context of electron transfer, the rate is also valid to describe excitation energy transfer in the incoherent regime.[47] We stress that these rates cannot be obtained directly from electron transfer rate theories as it is not possible to define diabatic localized states if the localization is caused by disorder, as in most polymers, rather than nuclear polarization effects. After defining the separate classes of accepting and inducing nuclear modes in the system, we obtain a general expression of the hopping rate. We show that, under the appropriate limits, this expression reduces to (i) single-phonon rate expression or (ii) the Miller-Abrahams rate or (iii) a multi-phonon expression. The description of these limits from a more general expression is useful to interpolate between them, to validate the assumptions of each limiting case, and to define the simplest rate expression that still captures the main features of the charge transport. When the rate expression is fed with a range of realistic parameters the deviation from the Miller-Abrahams rate is large or extremely large, especially for hopping toward lower energy states, due to the energy gap law.

2.1 Introduction

The expression used to compute the hopping rate between two different electronic states is crucial for all types of hopping transport models. In the literature, different rate expressions, usually derived from different branches of physics, are adopted, and their validity is discussed on the basis of the comparison between computed and experimental results. In this chapter, we derive a more general expression for the hopping rate that includes the most commonly used hopping rates as limiting cases. The first advantage of having such a general expression is that it makes it easy to understand the relationships between the different rate expressions and the assumptions needed to make each of them valid. Furthermore, such a general

* The content of this chapter is published in R. P. Fornari, J. Aragó and A. Troisi, *J. Chem. Phys.*, 2015, **142**, 184105. Dr. Juan Aragó created Figure 2.1 and performed the derivation in section 2.3.1.1.

expression allows one to interpolate between limiting cases, i.e. study how the assumptions of a particular limiting expression influence the final results. If one is interested in a more "universal" behaviour of semiconducting polymers, it would be desirable to start from a general rate expression that contains the minimum number of assumptions. Finally, a more general expression is typically best suited to incorporate the details of atomistic calculations and can therefore be used to create the link between detailed electronic structure calculations and larger scale models.

When looked at individually, the hopping rate expressions that have been recently used seem to be in contradiction with each other and with other theories. The most used rate expression to study charge transport in polymers is the Miller-Abrahams rate k_{12} for the hopping between two electronic states (say 1 and 2): [115]

$$k_{12} = \begin{cases} k^0 & for\ \Delta E_{12} < 0 \\ k^0 \exp\left(-\Delta E_{12}/k_{\mathrm{B}}T\right) & for\ \Delta E_{12} > 0 \end{cases} \tag{2.1}$$

k^0 is a function that depends on the distance and localization of the states (not relevant for this discussion), ΔE_{12} is the energy of the final state minus the energy of the initial state and $k_{\mathrm{B}}T$ is the thermal energy. According to this expression, the downhill rate is independent of ΔE_{12}. This contradicts what is known in photophysics as the energy gap law,[117,118] i.e. an exponential decrease of the non-radiative transition rate between two states with the increase of the energy gap between them. The rate expressions based on Marcus theory [116] or alternative formulations with a similar dependence on the energy gap [119] seem to err in the opposite direction, making $k_{12} \propto \exp\left(-(\Delta E_{12}+\lambda)^2/4\lambda k_{\mathrm{B}}T\right)$, i.e. the rate decreases too rapidly (as a Gaussian) for very negative ΔE_{12}. In a series of recent works, Vukmirovic et al. [120–123] have used an alternative expression where the hopping between states is promoted via electron-phonon coupling by a phonon matching the energy difference between them. The results depend strongly on the phonon spectrum, unlike the other two models mentioned above. The main objective of this paper is to reconcile the various models proposed and describe the relation between them in a simple fashion.

Aspects that will not be discussed here include the effect of the distance between the states, their relative localization, and the possibility that stronger or weaker coupling between them can result from the details of the electronic structure. These

are also extremely important effects. It was shown for example that the distance dependence normally included in the Miller-Abrahams rate is too approximate.[121] This will be addressed in chapters 5, 6 and 7 where the importance of variable localization of states will be highlighted. The rest of this chapter, however, will consider only the hopping between two states, with arbitrary localization and distance between them.

2.2 Theory

2.2.1 Two electronically coupled manifolds of vibronic states

To define more clearly the notation and compare with well-known results from the literature, we start by reconsidering the classical problem of non-adiabatic electron transfer between two manifolds of vibronic states. We will explain in the next section why this framework is *not* appropriate for the problem of charge hopping in polymeric systems but, as we will see, there is a component of this theory that can be transferred to the case of charge hopping in polymeric systems and there are relevant similarities between the results under certain conditions. We indicate with $\{|1,w\rangle\}$ and $\{|2,w'\rangle\}$ two sets of vibronic states localized on two different sites (see Figure 2.1). The indexes 1 and 2 label the two electronic states and the indexes *w* and *w*' are the vibrational quantum numbers (we treat them as scalar but, in the presence of many nuclear modes, they can represent the vectors of the quantum numbers). We assume that the vibrational degrees of freedom are described by quantum harmonic oscillators. The sets of harmonic oscillators in states 1 and 2 have the same frequencies but they can be displaced with respect to each other, i.e. the equilibrium position along certain modes is different in electronic states 1 and 2.

A very general Hamiltonian can be written as:

$$H = \sum_{w} \varepsilon_{1,w} |1,w\rangle\langle 1,w| + \sum_{w'} \varepsilon_{2,w'} |2,w'\rangle\langle 2,w'| + \sum_{w,w'} H_{12,ww'} |1,w\rangle\langle 2,w'| + h.c. \tag{2.2}$$

$\varepsilon_{1,w}$ (or $\varepsilon_{2,w'}$) is the energy of the unperturbed vibronic state. According to the Condon approximation, one can separate the matrix element $H_{12,ww'}$ into an electronic component V_{12} and the Franck-Condon overlap $\mathrm{FC}_{ww'}$ between the vibrational states *w* and *w*' in electronic states 1 and 2, respectively:

$$H_{12,ww'} = \langle 1, w | H | 2, w' \rangle = \langle 1 | H^{el} | 2 \rangle \langle w | w' \rangle = V_{12} \mathrm{FC}_{ww'} \tag{2.3}$$

The hopping rate k_{12} from any state in the manifold $\{|1, w\rangle\}$ to any state in the manifold $\{|2, w'\rangle\}$ can be given by the Fermi Golden Rule, if the coupling is sufficiently weak:

$$\begin{aligned} k_{12} &= \frac{2\pi}{\hbar} \sum_{w,w'} P_T(w) \left| H_{12,ww'} \right|^2 \delta(\varepsilon_{2,w'} - \varepsilon_{1,w}) \\ &= \frac{2\pi}{\hbar} |V_{12}|^2 \sum_{w,w'} P_T(w) \left| \mathrm{FC}_{ww'} \right|^2 \delta(\varepsilon_{2,w'} - \varepsilon_{1,w}) \\ &= \frac{2\pi}{\hbar} |V_{12}|^2 \rho_{\mathrm{FCTW}}(\Delta E_{12}) \end{aligned} \tag{2.4}$$

where $P_T(w)$ is the probability that vibronic state *w* on electronic state 1 is occupied at temperature *T* and δ is the Dirac delta function. The summation in the second equality is written more compactly as $\rho_{\mathrm{FCTW}}(\Delta E_{12})$, a density of states weighted by the Franck-Condon factor and temperature (FCTW), where $\Delta E_{12} = \varepsilon_{2,0} - \varepsilon_{1,0}$ is the energy difference between the lowest vibronic states of each manifold.

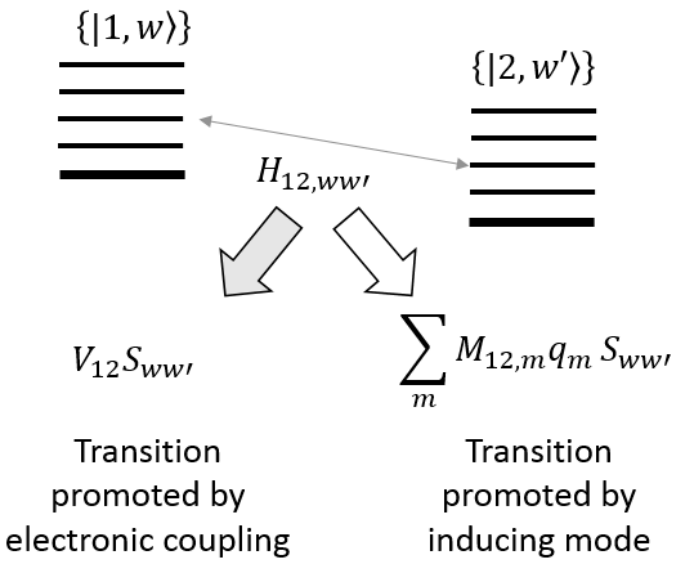

Figure 2.1. Schematics of the interacting manifold of vibronic states. If the two sets are coupled by a common electronic coupling term V_{12}, we obtain the general structure of most non-adiabatic electron transfer theories. Here we discuss a general rate in the case where the electronic coupling between the two manifolds is promoted by nuclear modes $\{q_m\}$ and would be otherwise zero in the absence of these modes.

The function $\rho_{\mathrm{FCTW}}(\Delta E_{12})$ depends on the Franck-Condon factors, which are in turn determined by the relative displacement from the equilibrium position in going from state 1 to state 2. An analytical expression for $\mathrm{FC}_{ww'}$ is available if one assumes that the vibrational modes are harmonic. Two limiting cases are particularly useful. If one assumes that the all nuclear modes can be treated classically, the function ρ_{FCTW} can be written as [124]

$$\rho_{\mathrm{FCTW}}^{\mathrm{Marcus}}(\Delta E)=\sqrt{\frac{1}{4\pi\lambda^{(\mathrm{C})}k_{\mathrm{B}}T}}\exp\left[-\frac{(\Delta E+\lambda^{(\mathrm{C})})^2}{4\lambda^{(\mathrm{C})}k_{\mathrm{B}}T}\right] \tag{2.5}$$

where the effect of the different equilibrium geometry between states 1 and 2 is parameterized by the classical reorganization energy $\lambda^{(\mathrm{C})}$ (see also sections 3.2.3 and 5.1.1). The combination of eq. (2.4) and (2.5) gives the same charge hopping rate derived by Marcus.[116]

If one assumes that a single vibrational mode should be treated quantum mechanically and all the others classically, the function ρ_{FCTW} can be written as

$$\begin{aligned}\rho_{\mathrm{FCTW}}^{\mathrm{MLJ}}(\Delta E)=&\sqrt{\frac{1}{4\pi\lambda^{(\mathrm{C})}k_{\mathrm{B}}T}}\sum_{w}P(w)\sum_{w'}\left|\mathrm{FC}_{ww'}\right|^2\\&\times\exp\left[-\frac{(\Delta E+\lambda^{(\mathrm{C})}+(w'-w)\hbar\omega^{A})^2}{4\lambda^{(\mathrm{C})}k_{\mathrm{B}}T}\right],\end{aligned} \tag{2.6}$$

where the Franck-Condon integrals $\mathrm{FC}_{ww'}$ are calculated as:[125]

$$\begin{aligned}\mathrm{FC}_{ww'}=&\exp\left(-\frac{G}{2}\right)\sum_{u=0}^{w}\sum_{u'=0}^{w'}\frac{(-1)^{u'}\left(\sqrt{G}\right)^{u+u'}}{u!u'!}\\&\times\sqrt{\frac{w!w'!}{(w-u)!(w'-u')!}}\delta_{w-u,w'-u'}.\end{aligned} \tag{2.7}$$

G is the Huang-Rhys factor, which describes the relative displacement along the quantum normal mode with energy $\hbar\omega^{A}$ and is related to the quantum component of the reorganization energy as $\lambda^{(\mathrm{Q})}=G\hbar\omega^{A}$. The rate given by the combination of eq. (2.4) and eq. (2.6) is very similar to that known as Marcus-Levich-Jortner (MLJ) rate,[126] which is more commonly evaluated with the further simplification $P(w=0)=1$ and $P(w>0)=0$ valid when $\hbar\omega^{A}\gg k_{\mathrm{B}}T$. We have used above the notation more common in chemical physics. However, expressions equivalent to eq.

(2.5) and eq. (2.6) respectively have been derived in the context of small polaron hopping in solid state physics by Holstein[127] and Emin.[128]

2.2.2 Hopping promoted by inducing vibrational modes

The theoretical framework described in the previous section cannot be used to describe hopping between states localized by disorder in polymeric semiconductors. States 1 and 2 are obtained by diagonalizing the electronic Hamiltonian and, by construction, the matrix element V_{12} is null. It is not easy to decompose the states of polymeric semiconductors into weakly interacting pairs (diabatic states) as many of them overlap considerably in space [110] (see also section 5.1.3). The natural generalization of the theory is to consider that the electronic coupling between states is modulated by vibrational modes that induce the transition. The electronic coupling between states 1 and 2 is therefore zero *on average* but the displacement of certain nuclear modes may induce a coupling proportional to the displacement.[129] This linear non-local coupling is known in other areas of chemical physics as the Herzberg-Teller coupling (responsible for the intensity of optically forbidden electronic transitions),[130] non-adiabatic coupling (responsible for (photo)chemical dynamics involving multiple potential energy surfaces)[76] or non-local electron-phonon coupling (used in the solid state physics of molecular crystals).[131] In the original paper by Miller and Abrahams,[115] it was assumed that acoustic modes were responsible for this coupling, while here we have not made any assumption on their nature. To describe this situation the Hamiltonian in eq. (2.2) needs to be modified as follows:

$$\begin{aligned} H = & \sum_{w} \varepsilon_{1,w} \left|1,w\right\rangle\left\langle 1,w\right| + \sum_{w'} \varepsilon_{2,w'} \left|2,w'\right\rangle\left\langle 2,w'\right| \\ & + \sum_{m} M_{12,m} q_m \sum_{w.w'} \mathrm{FC}_{ww'} \left|1,w\right\rangle\left\langle 2,w'\right| \\ & + \sum_{m} \hbar\omega_m^I \left(-\frac{1}{2}\frac{\partial^2}{\partial q_m^2} + \frac{1}{2} q_m^2 \right) + h.c. \end{aligned} \tag{2.8}$$

With respect to the Hamiltonian in eq. (2.2) we have substituted the matrix element V_{12} with the electron-phonon coupling term $M_{12,m} q_m$. q_m is the (adimensional) displacement along mode *m* that modulates the coupling between states 1 and 2. As these modes induce the transition we denote them as *inducing* modes, each with energy $\hbar\omega_m^I$. An approximation implicit in the Hamiltonian above is that the accepting

modes (those associated with the quantum numbers *w* or *w*') and the inducing modes are separate. The accepting modes have different equilibrium geometries in states 1 and 2 but do not affect the coupling between 1 and 2, whereas the inducing modes influence the coupling between states 1 and 2 but their equilibrium position is not affected by the electronic states of the system. This separation is rigorous in systems with symmetry elements where the accepting modes are always totally symmetric and the inducing modes are non-totally symmetric.[132] In general, it is a (very reasonable) approximation as only a small fraction of all modes are important accepting or inducing modes and it is unlikely that they coincide. Understanding the different role played by the two classes of nuclear modes is essential to compare and discuss the different rate expressions given in the literature. Many authors discuss the role of the electron-phonon coupling but refer to just one of the classes of electron-phonon couplings, which can be confusing when we wish to compare different results, as in this case. Accepting modes are often discussed in the context of small polaron theories and are determined by local electron-phonon coupling, i.e. stabilization of the on-site energy along a nuclear mode. Inducing modes are those responsible for the breakdown of the Born-Oppenheimer approximation (non-adiabatic effects) and are associated with the non-local electron-phonon coupling.

If we indicate with $|v_m\rangle$ the eigenstates of $\hbar\omega_m^I\left(-\frac{1}{2}\frac{\partial^2}{\partial q_m^2}+\frac{1}{2}q_m^2\right)$, where v_m is the quantum number of the oscillator *m*, we have $\langle v'_m|v_m\rangle=\delta_{v'_m,v_m}$, and we can write the unperturbed wavefunction of the Hamiltonian in eq. (2.8) as $|1,w\rangle|v_1\rangle...|v_m\rangle...$ and $|2,w'\rangle|v'_1\rangle...|v'_m\rangle....$

The matrix element $M_{12,m}q_m$ promotes the transition between the manifold $|1,w\rangle$ and the manifold $|2,w'\rangle$ where all the vibrational quantum numbers of the inducing modes except v_m remain unchanged. To simplify the notation for a few steps we can evaluate the transition between electronic states 1 and 2 as

$$k_{12}=\sum_m k_{12}^m, \tag{2.9}$$

where k_{12}^m is the rate resulting only from the coupling $M_{12,m}q_m\sum_{w.w'}\mathrm{FC}_{ww'}|1,w\rangle\langle 2,w'|$, i.e. considering only one inducing mode *m*. The rate can be expressed as a sum over

all the initial and final vibronic states with thermal averaging of the population of the initial states:

$$k_{12}^{m} = \sum_{v_m, v'_m} P_T(v_m) \sum_{w,w'} P_T(w) k^{m}_{12, wv_m \to w'v'_m}, \tag{2.10}$$

where $P_T(v_m)$ is the probability that the state with quantum number v_m is occupied at a given temperature, and $k^{m}_{12, wv_m \to w'v'_m}$ is the rate for the transition between state $|1,w\rangle|v_m\rangle$ and state $|2,w'\rangle|v'_m\rangle$. The latter can be expressed by a Golden Rule expression (note the energy conservation relation in the delta function):

$$\begin{aligned} k^{m}_{12, wv_m \to w'v'_m} = & \frac{2\pi}{\hbar} \left| \langle v_m | \langle 1,w | H | 2,w' \rangle | v'_m \rangle \right|^2 \\ & \times \delta\left(\varepsilon_{2,w'} - \varepsilon_{1,w} + \hbar\omega_m^I (v'_m - v_m) \right) \end{aligned} \tag{2.11}$$

From our Hamiltonian (eq. (2.8)), we have $\left| \langle v_m | \langle 1,w | H | 2,w' \rangle | v'_m \rangle \right|^2 = \left| M_{12,m} \right|^2 \left| \langle v_m | q_m | v'_m \rangle \right|^2 \left| \mathrm{FC}_{ww'} \right|^2$ and we can use the harmonic oscillator relation

$$\left| \langle v_m | q_m | v'_m \rangle \right|^2 = \tfrac{1}{2} \left(v_m \, \delta_{v_m, v'_m - 1} + (v_m + 1) \delta_{v_m, v'_m + 1} \right) \tag{2.12}$$

to express

$$\begin{aligned} k_{12}^{m} = \frac{\pi}{\hbar} \left| M_{12,m} \right|^2 \Bigg[& \sum_{v_m} P_T(v_m) v_m \sum_{w,w'} P_T(w) \left| \mathrm{FC}_{ww'} \right|^2 \delta\left(\varepsilon_{2,w'} - \varepsilon_{1,w} - \hbar\omega_m^I \right) \\ & + \sum_{v_m} P_T(v_m)(v_m + 1) \sum_{w,w'} P_T(w) \left| \mathrm{FC}_{ww'} \right|^2 \delta\left(\varepsilon_{2,w'} - \varepsilon_{1,w} + \hbar\omega_m^I \right) \Bigg]. \end{aligned} \tag{2.13}$$

The terms in the last summation are identical to those defining the function ρ_{FCWT} (eq. (2.4)), so

$$\begin{aligned} k_{12}^{m} = \frac{\pi}{\hbar} \left| M_{12,m} \right|^2 \Bigg[& \sum_{v_m} P_T(v_m) v_m \; \rho_{\mathrm{FCWT}}\left(\Delta E_{12} - \hbar\omega_m^I \right) \\ & + \sum_{v_m} P_T(v_m)(v_m + 1) \rho_{\mathrm{FCWT}}\left(\Delta E_{12} + \hbar\omega_m^I \right) \Bigg]. \end{aligned} \tag{2.14}$$

Moreover, $\sum_{v_m} P_T(v_m) v_m$ is just the phonon occupation number $N(\omega_m) = \left(\exp(\hbar\omega_m^I / k_B T) - 1 \right)^{-1}$. The resulting rate for a single inducing mode *m* is therefore:

$$k_{12}^{m} = \frac{\pi}{\hbar}\left|M_{12,m}\right|^2 \Big[N(\omega_m^I)\rho_{\mathrm{FCWT}}\left(\Delta E_{12} - \hbar\omega_m^I\right) + \left(N(\omega_m^I)+1\right)\rho_{\mathrm{FCWT}}\left(\Delta E_{12} + \hbar\omega_m^I\right)\Big]. \tag{2.15}$$

Our final and main result is obtained by summing over the inducing modes *m* (eq. (2.9)):

$$k_{12} = \frac{\pi}{\hbar}\sum_m \left|M_{12,m}\right|^2 \Big[N(\omega_m^I)\rho_{\mathrm{FCWT}}\left(\Delta E_{12} - \hbar\omega_m^I\right) + \left(N(\omega_m^I)+1\right)\rho_{\mathrm{FCWT}}\left(\Delta E_{12} + \hbar\omega_m^I\right)\Big] \tag{2.16}$$

The expression above is essentially a generalization of several existing models and the best way to explore its meaning is to take few limits to show that it can be reduced to any of the expressions that have been proposed so far to discuss charge transport in semiconducting polymers.

2.3 Limiting cases

2.3.1 Absence of active accepting modes

In this limit, there are no vibrations with different equilibrium positions in electronic states 1 and 2. Thus, only transitions where $w = w'$ can take place and the function $\rho_{\mathrm{FCWT}}\left(\Delta E_{12}\right)$ simply becomes the Dirac delta function $\delta\left(\Delta E_{12}\right)$. One can obtain the same expression also by taking the limit $\lambda \to 0$ of eq. (5), which highlights the nature of accepting modes as "broadening" of the electron donor and acceptor levels, as noticed for example by Gerisher's formulation of Marcus theory.[133]

The hopping rate in this limit becomes simply

$$k_{12} = \frac{\pi}{\hbar}\sum_m \left|M_{12,m}\right|^2 \Big[N(\omega_m^I)\delta\left(\Delta E_{12} - \hbar\omega_m^I\right) + \left(N(\omega_m^I)+1\right)\delta\left(\Delta E_{12} + \hbar\omega_m^I\right)\Big]. \tag{2.17}$$

This is the rate that has been extensively used by Vukmirović et al. [120] in their exploration of the charge transport in polymeric systems from atomistic calculations. Note that we have been using dimensionless nuclear modes whereas Vukmirović et al. have used mass weighted coordinates. This changes the definition of the electron-phonon coupling and eq. (2.17) is apparently different but in fact identical to the equation used, e.g., in ref. [120]. This derivation highlights that eq. (2.17) is valid in the limit of vanishing reorganization energy (or local electron-phonon coupling). Good polymers supporting very delocalized states have indeed very low

reorganization energy (the latter is inversely proportional to the delocalization of the orbital) [134] and it is therefore expected that eq. (2.17) should be a good approximation if the important transitions do not involve very localized trap states. Obviously, in this limit there is a vanishing rate between states whose energy difference is larger than any inducing vibration present in the system. This can be a problem if the transitions to and from deep traps in the polymer are important, a situation possibly encountered at low temperature and charge density.[114]

2.3.1.1 Derivation from Redfield theory

An alternative way to interpret eq. (2.17) is to assume that there is a set of electronic states weakly coupled with a thermal bath (the inducing phonons). Indeed, eq. (2.17) can be also derived using the language of quantum dynamics of open systems, where the electronic states of interest are considered the "system" and the inducing phonons represent the "bath". The weak nature of the system-bath interaction only allows single phonon transitions to take place. In this limit, the total Hamiltonian can be alternatively written as:

$$H = H^S + H^B + H^{SB} \tag{2.18}$$

where H^S, H^B, and H^{SB} denote the system, bath, and system-bath Hamiltonian, respectively, and can be expressed as:

$$H^S = \sum_{\mu} \varepsilon_{\mu} |\mu\rangle\langle\mu| \tag{2.19}$$

$$H^B = \sum_{m} \hbar\omega_m^I \left(-\frac{1}{2}\frac{\partial^2}{\partial q_m^2} + \frac{1}{2} q_m^2 \right) \tag{2.20}$$

$$H^{SB} = \sum_{\mu\nu} \sum_{m} M_{\mu\nu,m} q_m |\mu\rangle\langle\nu| + h.c. \tag{2.21}$$

In eq. (2.19), $|\mu\rangle$ and ε_{μ} represent the eigenstates of the system Hamiltonian and their corresponding energies. In the bath Hamiltonian (eq. (2.20), identical to the last term in eq. (2.8)), a set of inducing harmonic oscillators, $\hbar\omega_m^I$ and q_m are the frequency and the dimensionless normal mode coordinate of the *m*th normal mode. In eq. (2.21) (system-bath Hamiltonian) $M_{\mu\nu,m}$ corresponds to the electron-phonon coupling strength.

Now, we assume the electronic states as the relevant system while the inducing phonon degrees of freedom constitute the thermal bath responsible for the energy fluctuations of the states and the relaxation between them. An appropriate description

of the electron transfer dynamics can be given by the reduced density operator ρ, which is obtained by taking the partial trace of the total density operator ρ^{tot} over the irrelevant phonon degrees of freedom: $\rho = \text{Tr}_{\text{ph}}\left\{\rho^{\text{tot}}\right\}$. We will make use of ρ in its eigenstates (rather than site) representation; that is, the reduced density matrix is given by $\rho_{\mu\nu} = \langle\mu|\rho|\nu\rangle$.

In the case of weak system-bath coupling (vanishing reorganization energy), this coupling can be treated perturbatively and the electron transfer dynamics can be adequately described by the Redfield equation in the adiabatic representation,

$$\frac{\partial}{\partial t}\rho_{\mu\nu}(t) = -i\omega_{\mu\nu}\rho_{\mu\nu}(t) + \sum_{\mu',\nu'} R_{\mu\nu,\mu'\nu'}\rho_{\mu'\nu'}(t)\,, \tag{2.22}$$

where the Markovian approximation has been invoked.[125,135] The first term of eq. (2.22) represents the coherent evolution governed by the system Hamiltonian, where $\hbar\omega_{\mu\nu} = E_\nu - E_\mu$ is the energy gap between the electronic states. The second term describes the phonon-induced relaxation process. $R_{\mu\nu,\mu'\nu'}$ is the element of a tetradic matrix, known as the Redfield tensor, and can be seen as a transfer rate from $\mu'\nu' \to \mu\nu$. The Redfield tensor is expressed as [67]

$$R_{\mu\nu,\mu'\nu'} \equiv \Gamma_{\nu'\nu,\mu\mu'} + \Gamma^*_{\mu'\mu,\nu\nu'} - \delta_{\nu\nu'}\sum_\kappa \Gamma_{\mu\kappa,\kappa\mu'} - \delta_{\mu\mu'}\sum_\kappa \Gamma^*_{\nu\kappa,\kappa\nu'} \tag{2.23}$$

where

$$\Gamma_{\nu'\nu,\mu\mu'} = \frac{1}{\hbar^2}\int_0^t dt \left\langle \langle\nu|H^{SB}(t)|\nu'\rangle\langle\mu|H^{SB}(t)|\mu'\rangle \right\rangle_B e^{i\Delta E_{\mu'\mu}t/\hbar}\,. \tag{2.24}$$

In eq. (2.24), $\langle\cdots\rangle_B$ denotes a thermal average over the bath phonons. By using eq. (2.21), we can express eq. (2.24) as

$$\Gamma_{\nu'\nu,\mu\mu'} = \frac{1}{\hbar^2}\int_0^t dt \sum_m M_{\nu\nu',m}M_{\mu\mu',m}\langle q_m(0)q_m(t)\rangle_B e^{i\Delta E_{\mu'\mu}t/\hbar}\,. \tag{2.25}$$

At this point, it is useful to introduce the bath time correlation function as:[124]

$$\begin{aligned} C_{mm}(t) &= \sum_m M_{\nu\nu',m}M_{\mu\mu',m}\langle q_m(0)q_m(t)\rangle_B \\ &= \frac{1}{2}\sum_m M_{\nu\nu',m}M_{\mu\mu',m}\left[\left(N(\omega_m^I)+1\right)e^{-i\omega_m^I t} + N(\omega_m^I)e^{i\omega_m^I t}\right] \end{aligned} \tag{2.26}$$

where $N(\omega_m^I) = \left(\exp(\hbar\omega_m^I/k_BT)-1\right)^{-1}$ is the phonon occupation number. Substituting eq. (2.26) into eq. (2.25) and replacing $t \to \infty$ (stationary approximation), we obtain

$$\Gamma_{\nu'\nu,\mu\mu'} = \frac{1}{2\hbar^2}\sum_m M_{\nu\nu',m}M_{\mu\mu',m}\left[\left(N(\omega_m^I)+1\right)\int_0^\infty dt e^{i\Delta E_{\mu'\mu}t/\hbar}e^{-i\omega_m^I t} + N(\omega_m^I)\int_0^\infty dt e^{i\Delta E_{\mu'\mu}t/\hbar}e^{i\omega_m^I t}\right]. \tag{2.27}$$

The integrals in eq. (2.27) can be analytically evaluated since

$$\int_0^\infty dt e^{\pm i(\Delta E_{\mu'\mu}\mp\hbar\omega_m)t/\hbar} = \hbar\pi\delta(\Delta E_{\mu'\mu}\mp\hbar\omega_m) \pm iP\frac{1}{\Delta E_{\mu'\mu}\mp\hbar\omega_m}\ , \tag{2.28}$$

where *P* denotes the Cauchy principal part. Therefore, eq. (2.27) can be rewritten as

$$\Gamma_{\nu'\nu,\mu\mu'} = \frac{1}{2\hbar^2}\sum_m M_{\nu\nu',m}M_{\mu\mu',m} \times\left[\left(N(\omega_m^I)+1\right)\left(\hbar\pi\delta(\Delta E_{\mu'\mu}-\hbar\omega_m^I)+iP\frac{1}{\Delta E_{\mu'\mu}-\hbar\omega_m^I}\right) + N(\omega_m^I)\left(\hbar\pi\delta(\Delta E_{\mu'\mu}+\hbar\omega_m^I)-iP\frac{1}{\Delta E_{\mu'\mu}+\hbar\omega_m^I}\right)\right]. \tag{2.29}$$

So far, the derivation has been as general as possible, but if we focus on the particular case of a two electronic state system surrounded by a thermal bath of inducing harmonic oscillators, the k_{12} rate expression of interest can be written as

$$\begin{aligned} k_{12} &= R_{22,11} = \Gamma_{12,21} + \Gamma^*_{12,21} \\ &= \frac{\pi}{\hbar}\sum_m\left(M_{12,m}\right)^2\left[\left(N(\omega_m^I)+1\right)\delta\left(\Delta E_{12}-\hbar\omega_m^I\right)\right. \\ &\left. + N(\omega_m^I)\delta\left(\Delta E_{12}+\hbar\omega_m^I\right)\right], \end{aligned} \tag{2.30}$$

which is identical to that previously derived under the same approximation (eq. (2.17)).

2.3.2 The Miller-Abrahams limit

The Miller-Abrahams limit is obtained in the same limit of eq. (2.17) with further (and fairly stringent) conditions. In the original Miller-Abrahams paper,[115] the inducing modes were assumed to be acoustic modes (below the Debye cut-off) and no accepting modes were included. To recover the Miller-Abrahams limit we rewrite eq. (2.17) with an integral instead of a summation as we wish to describe the continuum of acoustic modes:

$$J(\omega) = \sum_m\left|M_{ij,m}\right|^2\delta\left(\omega-\omega_m^I\right) \tag{2.31}$$

$$k_{12} = \frac{\pi}{\hbar}\int_0^\infty J(\omega)\Big[N(\omega)\delta\left(\Delta E_{12} - \hbar\omega\right) + \left(N(\omega)+1\right)\delta\left(\Delta E_{12} + \hbar\omega\right)\Big] d\omega \tag{2.32}$$

$J(\omega)$ is a spectral density, measuring how strongly the inducing modes promote the electronic transition at a given frequency. Using the properties of the delta function we have

$$k_{12} = \begin{cases} \frac{\pi}{\hbar} J(-\Delta E_{12}/\hbar)\left(N(-\Delta E_{12}/\hbar)+1\right) & \textit{for } \Delta E_{12} < 0 \\ \frac{\pi}{\hbar} J(\Delta E_{12}/\hbar) N(\Delta E_{12}/\hbar) & \textit{for } \Delta E_{12} > 0 \end{cases}, \tag{2.33}$$

or, more explicitly,

$$k_{12} = \begin{cases} \frac{\pi}{\hbar} J(-\Delta E_{12}/\hbar)\frac{\exp\left(-\Delta E_{12}/k_{\mathrm{B}}T\right)}{\exp\left(-\Delta E_{12}/k_{\mathrm{B}}T\right)-1} & \textit{for } \Delta E_{12} < 0 \\ \frac{\pi}{\hbar} J(\Delta E_{12}/\hbar)\frac{1}{\exp\left(\Delta E_{12}/k_{\mathrm{B}}T\right)-1} & \textit{for } \Delta E_{12} > 0 \end{cases} \tag{2.34}$$

The equations above have the form of the Miller-Abrahams expression (eq. (2.1)) as a limit for $\Delta E_{12} >> k_{\mathrm{B}}T$ and $J(\omega) \sim$ constant. It was already noted [128] that the Miller-Abrahams rate is a (very) low temperature limit. The fact that *J* becomes a constant for sufficiently large frequencies is acceptable in the original formulation of the theory, where localized impurities are coupled by acoustic modes. If the wavelength of the acoustic phonon is shorter than the distance between interacting sites (which happens at large ΔE), the relative displacement between the two sites is little dependent on the wavelength. Also, in the opposite limit of $\omega \to 0$ the electron-phonon coupling should vanish for acoustic phonons because the inter-site distance is not changed by the phonon displacements. In summary, for acoustic phonon coupling and localized impurities the rate expression becomes *similar* to the Miller-Abrahams rate. The expression becomes *exactly* the Miller-Abrahams rate (eq. (2.1)) if the following spectral density is used

$$J(\omega) = A\frac{\exp\left(\hbar\omega/k_{\mathrm{B}}T\right)-1}{\exp(\hbar\omega/k_{\mathrm{B}}T)}. \tag{2.35}$$

The conditions required for the Miller-Abrahams rate to be valid are very difficult to justify in the context of charge hopping in polymeric materials. Computations have

revealed the importance of optical modes and, very often, the hopping takes place between sites that are very close in space, while the original theory is developed for well separated (diluted) impurities.[115] On the other hand, only by comparing the rate computed under more lenient conditions with the Miller-Abrahams rate is it possible to establish whether the differences are important for the description of the material's properties.

2.3.3 Classical inducing modes

We consider now the case where accepting modes play a role and we consider the limit where inducing modes can be assumed to be classical, i.e. $\hbar\omega_m^I \ll k_B T$. In this limit we have $N(\omega_m^I) = k_B T / \hbar\omega_m^I \gg 1$ and eq. (2.16) becomes

$$k_{12}^{\{\omega_m\}\to 0} = \frac{2\pi}{\hbar} \sum_m \left| M_{12,m} \right|^2 \frac{k_B T}{\hbar\omega_m} \rho_{FCWT}\left(\Delta E_{12}\right). \tag{2.36}$$

In the classical limit, $\frac{k_B T}{\hbar\omega_m}$ is the average squared displacement $\left\langle q_m^2 \right\rangle$ of an oscillator with potential energy $\frac{1}{2}\hbar\omega_m q_m^2$. The rate can be rewritten as

$$k_{12}^{\{\omega_m\}\to 0} = \frac{2\pi}{\hbar} \rho_{FCWT}\left(\Delta E_{12}\right) \sum_m \left| M_{12,m} \right|^2 \left\langle q_m^2 \right\rangle. \tag{2.37}$$

The quantity in the summation has a very intuitive meaning in the classical limit: this is the thermal fluctuation of the electronic coupling between electronic states 1 and 2 and can be written as $\left\langle |V_{12}|^2 \right\rangle$. The final rate in this limit takes a particularly simple form:

$$k_{12}^{\{\omega_m\}\to 0} = \frac{2\pi}{\hbar} \left\langle |V_{12}|^2 \right\rangle \rho_{FCWT}\left(\Delta E_{12}\right). \tag{2.38}$$

This is just like the electron-transfer rate where the electronic coupling is replaced by its average value (see eq. (2.4)). In this way it is particularly easy to "visualize" the role of inducing modes in the hopping process: thermal fluctuations mix initial and final states and the hopping rate is related to the magnitude of this mixing. Eq. (2.38) will be used for the study of charge transport in polymers in chapter 5 and different derivations that can be reduced to eq. (2.38) have also been proposed.[136,137] The same result has often been used in the context of electron transfer in donor-bridge-acceptor systems or in biological systems.[138–140] When comparing eq. (2.38) with

the more general eq. (2.16) it becomes easier to understand the general process of charge hopping in polymeric systems. The static disorder in the polymer generates localized states with a given ΔE_{12}. The accepting modes generate an effective Gaussian "broadening" of these states, allowing transitions also when initial and final energy are far off-resonance. The coupling between states is zero by construction but there are fluctuations around the equilibrium position that promote the transition between the states.

2.4 Discussion

The main advantage of our formulation of the hopping rate is that it is possible to build a model that continuously interpolates between the various limiting cases. This is useful to appreciate under what conditions a particular limit is invalid or, equivalently, what is the minimal model with the desired qualitative features. The drawback of a general formulation is that the parameter space is extremely large. In fact, it is essentially impossible to start with something as general as eq. (2.16) to build a phenomenological model because the model would depend on too many choices that one has to make. To use eq. (2.16) for interpreting realistic data, it is essential to feed the equation with detailed computational results on the electron-phonon coupling terms so that the adjustable parameters are kept to a minimum. The relative importance of the parameters entering this rate and their influence on charge mobility in a general transport model are discussed in detail in chapter 6.

In this chapter, we wish to study the main qualitative differences of the general rate expression (eq. (2.16)) with respect to the other expressions used in the literature. A rather surprising property of the Miller-Abrahams rate is that it does not decrease as ΔE_{12} becomes more negative. Such behaviour would be expected for non-radiative transitions involving molecular levels and it is well documented in the photophysics literature (energy gap law).[118] We therefore express the hopping rate as a function of ΔE_{12} for various choices of the system parameters at a constant temperature of 300 K.

We consider a system with four inducing modes and all matrix elements $M_{12,m}$ = 10^{-3} eV (coupling strengths) set to give plausible rates. We consider a Model 1 where the inducing modes are low energy (i.e. comparable to $k_B T$) and fixed at 0.01, 0.02,

0.03 and 0.04 eV. Then we consider a Model 2 where two of the modes are at low energies, 0.01 and 0.03 eV, and two at intermediate/high energies (0.10 and 0.18 eV). We further consider a Model 3 where the inducing modes are at high energy (0.16, 0.17, 0.18, 0.19 eV). Model 1 is in line with the assumption made in chapter 5 that low frequency modes, mostly hindered torsions, are the main inducing modes. Model 2 samples more uniformly across the vibrational spectrum of a typical material. Model 3 is more unrealistic but useful to see the effect of quantum inducing modes, otherwise hidden in the other models.

For ρ_{FCTW} we consider a case with a single quantum oscillator (eq. (2.6)), whose energy is set to 0.186 eV, the energy of the C=C bond stretching as a representative quantum mode in conjugated molecules. The function ρ_{FCTW} can be fully determined by the total reorganization energy, $\lambda = \lambda^{(\mathrm{Q})} + \lambda^{(\mathrm{C})}$, and the fraction *f* determining the partition of the reorganization between the classical and quantum component ($\lambda^{(\mathrm{Q})} = f\lambda$ and $\lambda^{(\mathrm{C})} = (1-f)\lambda$). We consider the cases of $\lambda =$ 0.06, 0.2, 0.6 eV, corresponding to small, intermediate and extremely large reorganization energies using electronic structure calculations as a reference,[141] and *f* = 0.15 (close to the Marcus limit of fully classical reorganization energy), *f* = 0.50 (closer to what emerges from electronic structure calculations [142]) and *f* = 0.85 (a more extreme case where the quantum mode is dominating).

The results are provided in Figure 2.2, where each panel reports the rate as a function of ΔE_{12} for three different fractions *f* of quantum reorganization energy. In the panels we have added the Miller-Abrahams rate (dashed line) for comparison purposes. The curves are reported in a broader energy range, to better see the trends, however it is unlikely that hopping between states whose energy difference is larger than 0.3 eV would be relevant in realistic polymers. The results for Model 1 are very simple to interpret, because they are qualitatively similar to the behaviour of standard non-adiabatic rate theory given the relation we have shown in (eq. (2.36)) for low energy inducing modes. The maximum rate is observed for $\Delta E_{12} = -\lambda$. The rate decreases more steeply than the Miller-Abrahams limit and the difference between the two rates is particularly remarkable for negative ΔE_{12}. It is coincidental that the curve that most resembles the Miller-Abrahams limit is that for high reorganization energy

and strong quantum component of the reorganization energy. Large values of reorganization energy are in fact found in the opposite limit with respect to the Miller-Abrahams limit and the weak energy dependence for negative ΔE_{12} is due to multi-phonon transitions involving the quantum mode (also absent in the Miller-Abrahams theory).

When inducing modes at higher frequency are introduced in going from Model 1 to Model 2, the differences are qualitatively modest. For this reason one may argue that, to define an appropriate charge transport model with a limited number of parameters, it may not be necessary to have a very detailed set of electron-phonon couplings $M_{12,m}$. A similar conclusion was achieved with different arguments in ref. [121]. Moreover, if quantum inducing modes are not too important, one can neglect them altogether using the equation valid in the classical limit of inducing modes (eq. (2.38)) where there is only one coupling parameter incorporating the effect of all inducing modes, which is the approach adopted in chapter 5. However, it can be instructive to consider also the situation with only high energy inducing modes, i.e. our Model 3. At low reorganization energy, the hopping rate is reduced at $\Delta E_{12} = 0$, because the ρ_{FCTW} functions are very narrowly peaked at the origin and the closest maxima in the rates are found near $\Delta E_{12} \sim \pm\hbar\omega_m^I$. The anomaly of k_{12} increasing as ΔE_{12} increases disappears when the reorganization energy becomes comparable with the inducing mode energy.

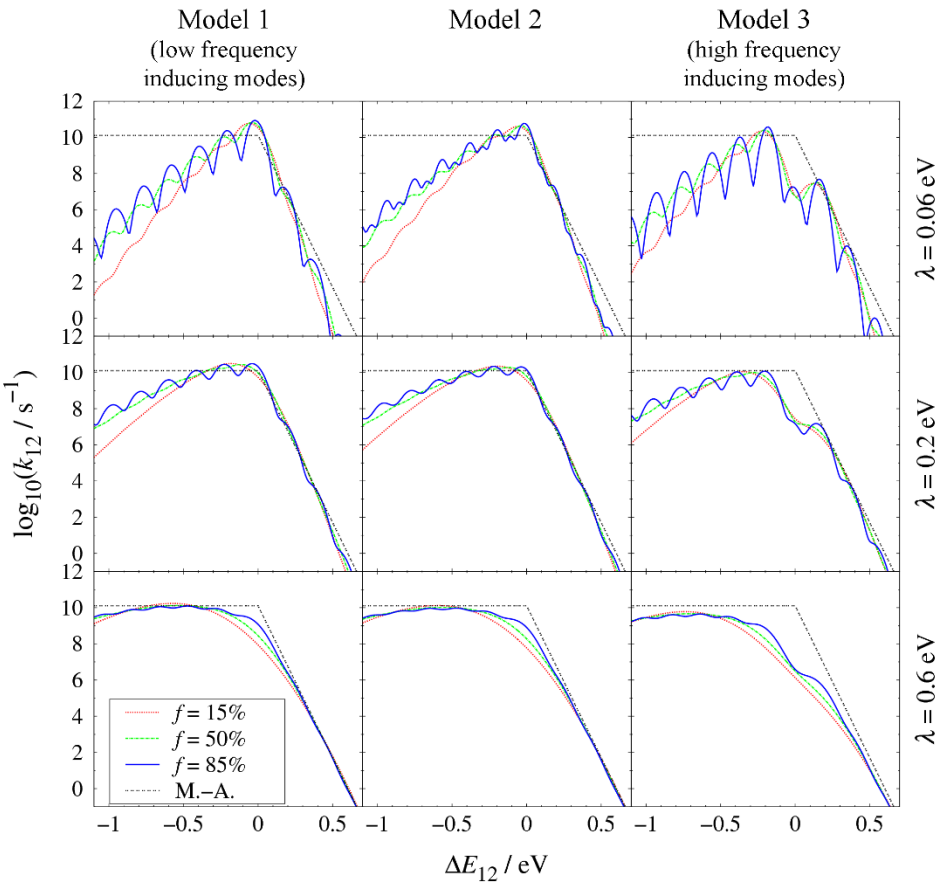

Figure 2.2. Charge hopping rates as a function of the energy difference ΔE_{12} for different parameter sets. Moving from top to bottom row the total reorganization energy is increased from 0.06 to 0.6 eV. Moving from left to right column the importance of quantum (high frequency) inducing modes is increased (see text for the definition of Model 1, 2, 3). The curves in each panel correspond to the rate with the same total reorganization energy but a different fraction (15% red, 50% green, 85% blue) of the quantum high frequency mode contributing to the reorganization energy. The dashed grey line (for reference) is the Miller-Abrahams rate.

It seems not possible to approach the Miller-Abrahams limit using a reasonable choice of parameters. Nevertheless, for the development of a phenomenological theory, in the limit of small reorganization energy (the same where the Miller-Abrahams rate was developed), it seems possible to substitute the expression in eq. (2.1) with the following empirical variant:

$$k_{12} = \begin{cases} k^0 \exp\left((\alpha - 1)\Delta E_{12}/k_B T\right) & \text{for } \Delta E_{12} < 0 \\ k^0 \exp\left(-\alpha \Delta E_{12}/k_B T\right) & \text{for } \Delta E_{12} > 0 \end{cases} \tag{2.39}$$

which would reproduce the behaviour of the realistic rates at the cost of only one additional parameter $\alpha > 1$ that re-establishes the energy gap law.

Finally, and very importantly, this work was concerned with the evaluation of the correct rate expression and did not explore the effect on the coupling matrix

elements of the distance between sites. It has been noted that k^0 is not a simple function of the distance between states 1 and 2 and this may have a dramatic effect on the global theory. Thereby, if one is interested in exploring the effect of different rate expressions on the charge carrier mobilities of polymers, it is essential to consider a rate expression that not only includes the correct dependence on the energy difference (energy gap law) but also the correct distance dependence. As the latter depends on a number of further assumptions, it will not be explored here. In section 5.1.3 we will show how the coupling M_{12} (and consequently the hopping rate) depends on the overlap between eigenstates of the electronic Hamiltonian, thereby including a very detailed distance dependence.

Several assumptions implicit in the use of the Fermi Golden rule to obtain rates (coupling should be weak, hopping rate should be slower than thermal relaxation rate, i.e. the process is always incoherent) have not been described in detail as they are common to all other models discussed here. However, it is important to stress that the Hamiltonian we started with is based on the assumption that initial and final states are obtained by diagonalizing the electronic Hamiltonian of the system and they are localized by the disorder in such Hamiltonian. If the polaronic effects are stronger than the disorder effect, i.e. if the charge is localized more by polarization than by disorder, this treatment is invalid. There is some consensus that charge carriers in most polymers are localized by disorder [83,143] but it should be mentioned that some more recent experimental and theoretical works suggested that, in the best available polymers, the disorder is not very effective in localizing the carriers and the polarization effect can effectively compete with the disorder effects. [144] This could be the effect in action in the recently reported Hall effects in polymeric semiconductors.[145]

In summary, we have established a relation between various hopping rate expressions proposed in the literature to study charge hopping in semiconducting polymers by building a more general rate expression from a Hamiltonian that should capture the main physics of charge hopping in various situations. We have stressed the different roles played by vibrations associated with polarization effects (accepting modes) and vibrations that promote the electron transfer via non-adiabatic coupling (inducing modes). The final rate expression can incorporate the effect of any number of modes with any frequency and it is therefore suitable to be used in conjunction with

atomistic models that provide the appropriate parameters for the simulation of realistic polymers. Like in many physical problems, it is very difficult to establish the best level of simplification for any given model so that only the details that are essential are kept in the description. The formulation of the hopping rate proposed here will allow a more systematic study of the level of detail that needs to be included to understand incoherent charge (or exciton) transport in organic semiconductors.

3. Influence of thermal fluctuations on exciton dynamics in a molecular crystal*

Summary: In this chapter, the exciton transport properties of an octa(butyl)-substituted metal-free phthalocyanine (H_2-OBPc) molecular crystal are explored by means of a combined computational (molecular dynamics and electronic structure calculations) and theoretical (model Hamiltonian) approach. The excitonic couplings between phthalocyanine molecules, where multiple quasi-degenerate excited states are present, are computed using the multistate diabatization scheme described in section 1.2.1.1, which is able to capture both short- and long-range excitonic coupling effects. Thermal motions in phthalocyanine molecular crystals at room temperature cause substantial fluctuation of the excitonic couplings between neighbouring molecules (dynamic disorder). The average values of the excitonic couplings are found to be not much smaller than the reorganization energy for the excitation energy transfer and the commonly assumed incoherent regime for this class of materials cannot be invoked. A simple but realistic model Hamiltonian is proposed to study the exciton dynamics in phthalocyanine molecular crystals or aggregates beyond the incoherent regime.

3.1 Introduction

Efficient exciton diffusion in molecular materials or aggregates over long distances is crucial for the performance of photosynthetic light-harvesting systems and photovoltaic applications.[146–149] Two limiting transport regimes (coherent and incoherent) are commonly invoked to describe the exciton diffusion in molecular materials or aggregates [125] (see also section 1.2.2). In the coherent regime, the exciton wavefunction is delocalized over several molecular units or, in some cases, over the whole molecular aggregate, whereas in the opposite (incoherent) regime, the exciton wavefunction is localized on a molecular unit. Although coherent transport would be highly desirable in terms of efficiency, exciton diffusion in most molecular materials used for optoelectronic applications takes place via a series of hopping events between neighbouring molecules, with exciton diffusion lengths that rarely exceed 10 nm.[148] Recent studies, however, have shown that an efficient singlet

* The content of this chapter is published in R. P. Fornari, J. Aragó and A. Troisi, *J. Phys. Chem. C*, 2016, **120**, 7987–7996. The following figures and the corresponding calculations have been made by Dr. Juan Aragó: Figure 3.1, Figure 3.7 (intramolecular couplings in the model system with H_2-OBPc and isoindole), Figure 3.8 (inter-column couplings).

exciton migration can occur in highly ordered supramolecular materials.[58,150,151] In particular, Sung et al. have shown by ultrafast transient fluorescence spectroscopy that in helical π-stacks of perylene bisimides delocalized excitons are initially formed and move coherently along the chain in tens of femtoseconds prior to the excimer formation.[58] Haedler et al. have demonstrated that one-dimensional self-assembled nanofibers, based on carbonyl-bridged triarylamine building blocks, are able to efficiently transport singlet excitons over more than 4 μm at room temperature by means of a predominantly coherent mechanism.[150] Park et al. have obtained a tunable light-harvesting material, based on a self-assembled chromophore network controlled by a genetically-engineered virus template, which has exhibited enhanced exciton transport via a partially coherent regime.[151] These recent examples clearly highlight the growing interest for obtaining controllable molecular materials for potential nanophotonic and quantum information applications where excitons move beyond the incoherent transport regime. In this sense, it would be useful to consider model systems for studying partially coherent exciton propagation with a good level of detail.

Phthalocyanine (Pc) derivatives are promising candidates as organic semiconductors for artificial photosynthesis and optoelectronic applications.[152–155] Inspired by their photosynthetic homologues (e.g., bacteriochlorophyll chromophores), different representative examples of self-assembled molecular materials based on Pc building blocks have been synthesized to investigate their exciton transport properties.[156] In contrast to the field of photosynthesis,[53,59,157] in the field of organic electronics a hopping (incoherent) mechanism is generally assumed when the exciton/charge dynamics in Pc-based self-assembled materials is investigated.[148,158,159] However, this assumption is not completely justified in this class of Pc systems since they may present quite large excitonic couplings (20−100 meV) and small exciton-phonon couplings (reorganization energies can be as small as 37 meV).[158,160] A few examples in related self-assembled systems (porphyrins) have shown that exciton diffusion can efficiently occur by means of a coherent mechanism.[161]

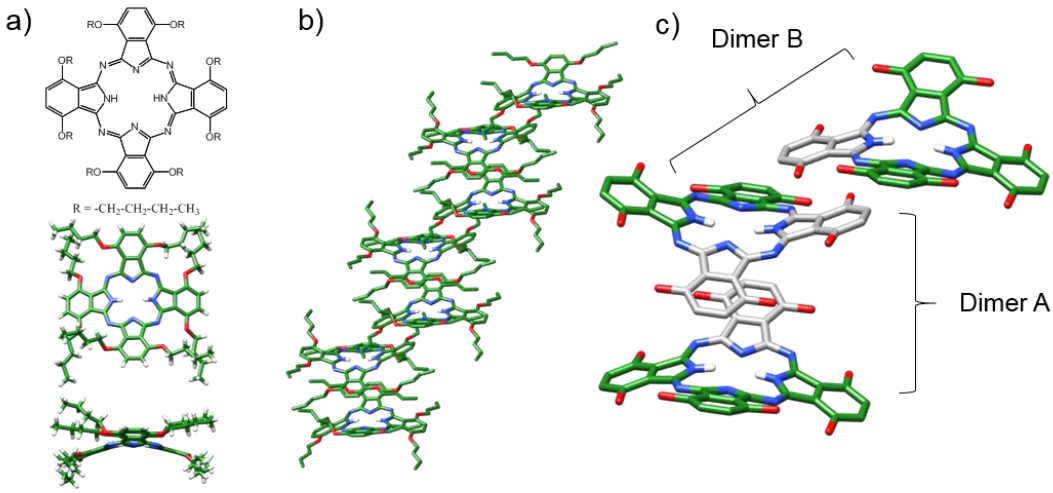

Figure 3.1. a) Chemical structure and geometry of the H_2-OBPc molecule in the crystal, b) packing of the molecules along the crystalline axis 110 and c) magnification of the three central molecules in b to show the structure of the two relevant molecular dimers (A and B) for the exciton transport. The interacting isoindole groups with the shortest intermolecular contacts are depicted in gray, hydrogens (in b and c) and octabutoxy chains (in c) have been omitted for clarity.

Recently, an octa(butyl)-substituted metal-free phthalocyanine, H_2-OBPc (1,4,8,11,15,18,22,25-octabutoxy-29*H*,31*H*-phthalocyanine, see Figure 3.1a) has been synthesized and exhibited good crystallinity properties (1D π-stacked arrangements, see Figure 3.1b) in thin films.[162,163] The high degree of crystallinity of the solution-processed thin films allowed Rawat et al. to investigate the correlation between long-range order and the nature of the lowest exciton states of the aggregate.[163] The H_2-OBPc compound is therefore an excellent molecular crystal model to study exciton diffusion at room temperature in the absence of amorphous phase (static) disorder and grain boundaries. The only source of disorder would stem from the intrinsically thermal nuclear motions (dynamic disorder), which needs to be taken into account for a proper description of the exciton transport.[46,47]

Regardless of the exciton diffusion mechanism invoked, the transport of molecular excitons is mainly governed by the excitonic coupling (J) between the excited states localized on the molecular units (Frenkel excited states).[125,164] In Pc systems, the two lowest-energy singlet excited states (commonly known as Q-bands [165]) are almost degenerate in energy and, thus, both may participate in the exciton transport of Pc molecular crystals or aggregates. Diabatization techniques are particularly suited for evaluating excitonic couplings between several excited states.[49,166–168] In particular, the diabatization scheme developed by Aragó et al.

[50], summarized in section 1.2.1.1, allows to compute the excitonic couplings between excited states in molecular crystal pairs beyond the two-level approximation. The great advantage of diabatization schemes is that they capture the full excitonic couplings, including both the short-range (overlap and exchange) and long-range (Coulombic) contributions.

The Coulombic coupling is often the only term considered to study exciton transport in molecular aggregates.[169] However, in organic molecular aggregates and crystals (including Pc derivatives) short intermolecular distances in the 3.5–5.5 Å range can be commonly found and, thus, short-range excitonic coupling contributions might become relevant.[170,171] Furthermore, short-range excitonic interactions, unlike the long-range counterpart, are extremely sensitive to the mutual position of the interacting molecular units and, therefore, can undergo significant fluctuations owing to the thermal molecular motions.[46] The thermal fluctuation of the excitonic couplings (also known as non-local exciton-phonon coupling) must be taken into account for a quantitative description of the exciton diffusion and other related phenomena in molecular crystals.[47,64]

In this chapter, we investigate the exciton transport properties of the H_2-OBPc molecular crystal (Figure 3.1). First, using the multistate diabatization scheme described in section 1.2.1.1 we compute the total excitonic couplings between all the relevant excited states in the molecular crystal dimers belonging to the 1D stack (Figure 3.1c) and analyse the behaviour of the couplings as a function of the intermolecular distance. Second, we evaluate the amount of thermal fluctuation of the excitonic couplings in the most relevant molecular crystal dimers. Third, the plausible exciton transport regimes are discussed: starting from the parameters computed for this material we determine the most appropriate transport regime. The exciton dynamics are finally studied with an appropriate theoretical approximation where the thermal excitonic coupling fluctuations have been properly taken into account.

3.2 Methods

3.2.1 Excitonic couplings from two-state diabatization

The excitonic couplings between the lowest two singlet excited states in each molecular pair (dimer) are computed using the scheme described in section 1.2.1.1, using the Mulliken atomic transition charges (ATC) as the reference property. The

ATC were computed from a transition density Mulliken population analysis[50,172] taking into account the full configuration interaction (CI) vectors obtained from the time-dependent density functional theory (TDDFT) calculations of the single molecules and dimers. It should be stressed that the phase of the wavefunction (which can affect the sign of the coupling) can be easily kept constant by controlling the sign of the ATC, so that couplings have a self-consistent sign independent of the (arbitrary) sign of the wavefunction. This is of great relevance when one wishes to calculate the time evolution of excitonic couplings along a molecular dynamics simulation as we will do here.

3.2.2 Molecular dynamics simulation of the thermal motion of the crystal

To model the thermal nuclear motions in the H_2-OBPc molecular crystal, we have performed a molecular dynamics (MD) simulation. A 3 × 3 × 3 supercell of the H_2-OBPc crystal was built by replicating the unit cell along each crystallographic axis. The MD simulation was run at room temperature (300 K) and constant volume using the Tinker package.[173]

The standard MM3 force field [174–176] was modified to match the equilibrium structure of H_2-OBPc computed quantum mechanically at the LC-ωPBE/6-31G** level (see section 3.2.4). In particular, in order to ensure that the electronic structure of the frontier orbitals, which depends largely on the geometry of the aromatic backbone of the H_2-OBPc molecule, remained consistent along the molecular dynamics (MD) simulation, the MM3 force field has been modified as follows. The bond orders of the bonds involved in the π-system have been i) optimized to match the equilibrium bond lengths obtained from a quantum chemical geometry optimization and ii) kept constant during the MD simulation, with the additional advantage of speeding up the simulation. The optimization was performed as follows. The first guess for the bond orders B, and the corresponding bond lengths L, were obtained from the Tinker *optimize* program using the standard MM3 force field. The reference bond lengths L_{ref} were obtained from a geometry optimization performed at the LC-ωPBE/6-31G** level of theory. Since the bond lengths depend linearly on the bond orders ($L = L_0 + mB$), we obtained the proportionality constant m and the intercept L_0 from a linear fitting. The C-C and C-N aromatic bonds were fitted separately as they have different values of m and L_0. The corrected bond orders were then calculated for each set of bonds as $B_{corr} = B + (L_{ref} - L) / m$ and used to obtain a

new set of bond lengths from the force field. The procedure was repeated until the root mean square of the length difference, $\sqrt{\left\langle \left(L_{\text{ref}} - L \right)^2 \right\rangle}$, fell below 0.01 Å. The largest length difference at convergence was $7.2 \cdot 10^{-3}$ Å.

3.2.3 Reorganization energy

The intramolecular reorganization energy (λ) for an excitation energy transfer reaction between two molecules can be estimated from their ground state (S_0) and excited state (S_1) potential energy surfaces, schematically represented in Figure 3.2. Q_0 and Q_1 are the equilibrium (relaxed) geometries of the ground and excited state along a generic reaction coordinate Q. The reorganization energy for the energy transfer process is $\lambda = E_a - E_d = \lambda_{S_0}^{(d)} + \lambda_{S_1}^{(a)}$, where *d* and *a* stand for donor and acceptor molecules. The difference between the acceptor's absorption and the donor's emission energy (the Stokes shift $E_a - E_d$) corresponds to the sum of the two geometry relaxation energies $\lambda_{S_0}^{(d)} = E(S_0, Q_1) - E(S_0, Q_0)$ and $\lambda_{S_1}^{(a)} = E(S_1, Q_0) - E(S_1, Q_1)$ as indicated in the left and right panels of Figure 3.2 respectively. In practice, these relaxation energies can be obtained from four single point energy calculations once the equilibrium geometries Q_0 and Q_1 are known.

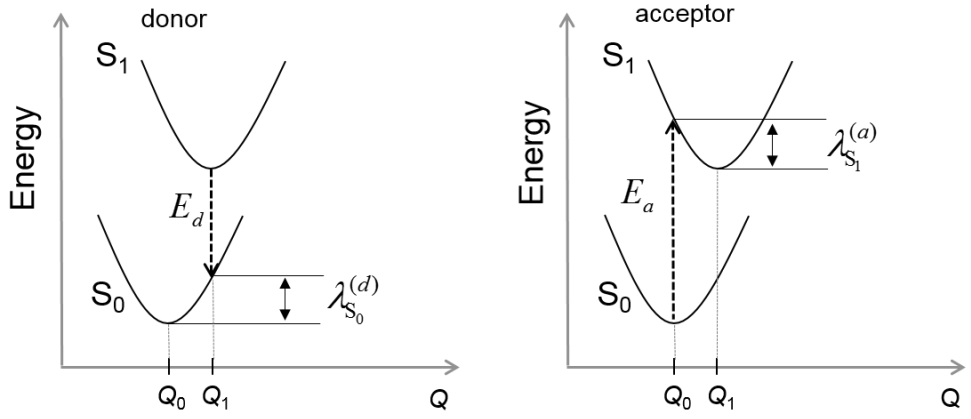

Figure 3.2. Schemes of the potential energy surfaces of the ground state and the first excited state in the monomeric representation for two molecules (donor and acceptor) involved in the exciton transfer process. $\lambda_{S_0}^{(d)}$ and $\lambda_{S_1}^{(a)}$ are the two relaxation energies contributing to the total reorganization energy λ.

3.2.4 Quantum chemical calculations

To estimate the reorganization energy λ of the energy transfer process, the optimized equilibrium geometries as well as the excitation energies of the ground state and first two excited states of the H_2-OBPc monomer were calculated in the framework of the density functional theory (DFT) and time-dependent density functional theory (TDDFT) by using the long-range corrected LC-ωPBE [177] density functional and the 6-31G** basis set.[178] The LC-ωPBE functional has been selected because it should be able to provide an accurate and balanced description of valence and charge-transfer excitations and avoids the typical underestimation of the charge-transfer excitations found in standard hybrid density functionals.[179] A ω value of 0.3 a_0^{-1} for the long-range corrected functional has been employed because it has been found to be an optimal value that provides a root mean square error (RMSE) of 0.3 eV for both localized and charge-transfer excitations in a large set of medium-sized molecules.[179]

250 snapshots from the MD simulation were taken at time intervals of 50 fs. A cluster of three H_2-OBPc molecules was extracted from each snapshot to compute the excitonic couplings for dimers A and B (see Figure 3.1). To be able to calculate the excitation energies and the atomic transition charges (the molecular properties needed for the diabatization) for 500 dimers (180 atoms per dimer), the calculations were performed at the TDDFT/LC-ωPBE/3-21G* level. This approximation was validated by comparing the intermolecular distance dependence of the excitonic couplings obtained at this level of theory with those computed at the TDDFT/LC-ωPBE/6-31G** level. As shown in Figure 3.3, the distance dependence is qualitatively similar when using the two basis sets. Finally, it should be noted that in the quantum chemical calculations of both the monomer and the dimer of H_2-OBPc the butoxy chains have been replaced by methoxy groups to alleviate the computational cost since they do not have a significant impact on the electronic structure of H_2-OBPc. All quantum chemical calculations have been performed with the NWChem 6.6 program package.[180]

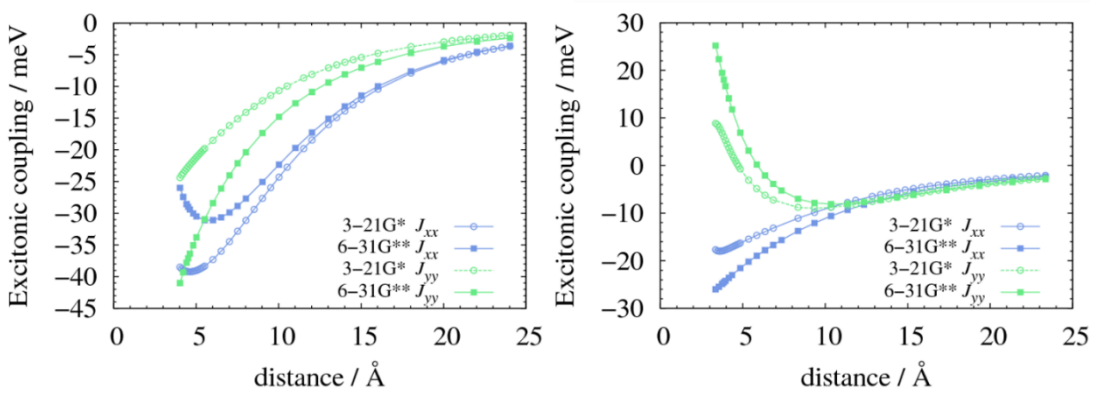

Figure 3.3. Intermolecular excitonic couplings (see section 3.3.1 for the definition of the couplings) as a function of the intermolecular π-π stacking distance between the planes formed by the isoindole rings for dimers A (left) and B (right) at the TDDFT/LC-ωPBE level with the 3-21G* and 6-31G** basis sets. The dimers are A and B are defined in Figure 3.1.

3.3 Results and discussion

3.3.1 Excitonic couplings between multiple excited states in H_2-OBPc

The H_2-OBPc crystal presents a pronounced 1D crystal packing along a particular crystalline direction (Figure 3.1b) with short π-π intermolecular distances in the 3.5–4.5 Å range between nearest neighbours (see ref. [162] for further crystallographic details). Along the 1D packing direction (column) two different molecular pairs (dimers A and B) with the closest intermolecular contacts can be defined (Figure 3.1c). Both dimers interact through the isoindole groups by means of π-π interactions; specifically, dimer A interacts through the hydrogen-free isoindole-like groups whereas dimer B through the isoindole-like groups. It should be noted that the geometry of the H_2-OBPc molecule in the crystal structure is not planar and, therefore, the position of the central hydrogens can be unambiguously inferred from the geometry of the central cavity (the opposite nitrogen atom pairs connected to H atoms are more distant).

The first two excited states S_1 and S_2 of the H_2-OBPc molecule in the crystal geometry were found to be 1.73 and 1.74 eV above the ground state and can be described as one-electron promotions from the highest occupied molecular orbital (HOMO) to the lowest unoccupied molecular orbitals (LUMO and LUMO+1); their transition dipole moments are polarized in almost perpendicular directions with similar oscillator strengths (see Figure 3.4). These computed excited states correspond to the experimental peaks recorded at 1.64 and 1.68 eV in solution (commonly known as the Q_x and Q_y electronic transitions).[163] Higher excited states belonging to the

so-called B-band are found to be at least 1.67 eV higher in energy than the S_2 excited state. Therefore, the subspace formed by the first two excited states (Q_x and Q_y) localized on each molecule would be enough to study the exciton dynamics in the H_2-OBPc crystal and the excitonic couplings in dimers A and B would stem mainly from the interactions between these localized Q_x and Q_y states, giving rise to four intermolecular excitonic couplings (J_{xx}, J_{xy}, J_{yx}, and J_{yy}, *vide infra*).

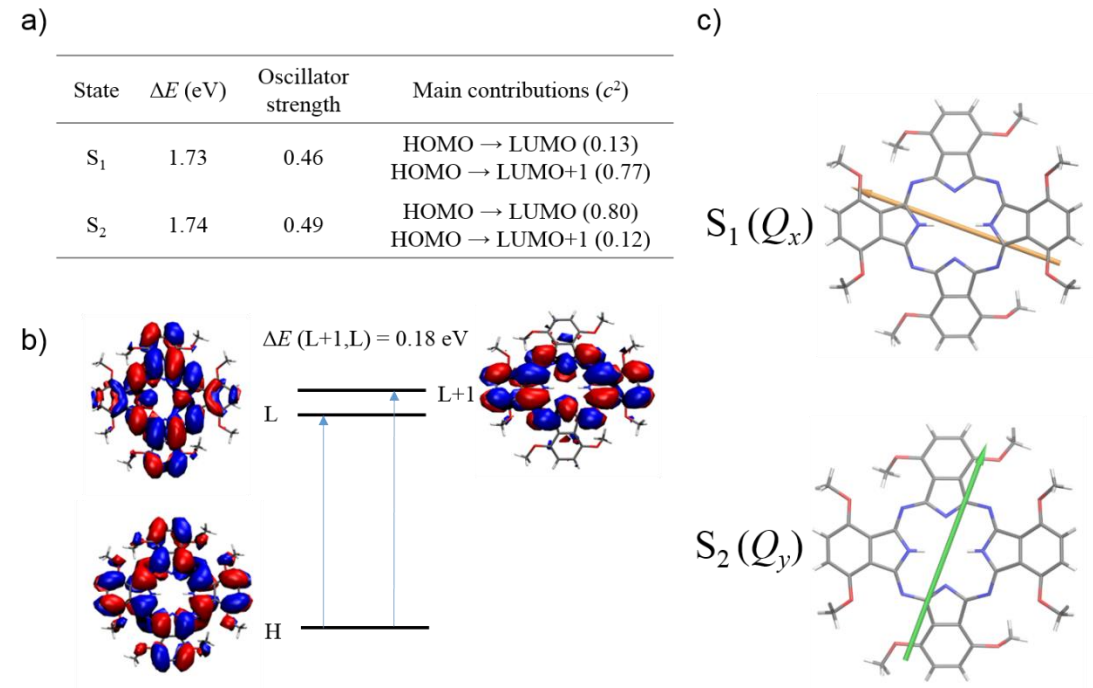

Figure 3.4. (a) Excitation energy, oscillator strength and character of the first two excited states S_1 and S_2 of H_2-OBPc. (b) Molecular orbitals contributing most to the first two excited states. H and L denote HOMO and LUMO. (c) Orientation of the transition dipole moments of S_1 and S_2. Level of theory LC-ωPBE/6-31G**.

The total excitonic couplings (which include short- and long-range interactions) in dimers A and B have been computed first at the crystal structure equilibrium geometry. For each dimer, a 4 × 4 diabatic Hamiltonian matrix is obtained (using the diabatization procedure described in section 1.2.1.1) with six off-diagonal excitonic couplings elements (see also diagram in Figure 3.5):

$$\mathbf{H}^{\mathrm{D}} = \begin{bmatrix} E_1^{D,1} & J_{1xy} & J_{xx} & J_{xy} \\ & E_2^{D,1} & J_{yx} & J_{yy} \\ & & E_1^{D,2} & J_{2xy} \\ & & & E_2^{D,2} \end{bmatrix}. \tag{3.1}$$

The off-diagonal elements of $\mathbf{H}^{\mathrm{D}}$ correspond to the intramolecular (J_{1xy} and J_{2xy}) and intermolecular (J_{xx}, J_{xy}, J_{yx}, and J_{yy},) excitonic couplings between the diabatic excited states Q_x and Q_y. The intramolecular excitonic couplings J_{1xy} and J_{2xy} should be in

principle close to zero and will be discussed below. The intermolecular couplings J_{xx}, J_{xy}, J_{yx}, and J_{yy} for dimer A (dimer B) are computed to be −38.51, −8.77, −8.71, and −24.40 meV, respectively (−17.68, 18.12, 18.12, and 8.86 meV, respectively). In general, dimer A presents slightly stronger excitonic couplings than dimer B, especially the J_{xx} coupling.

Figure 3.5 displays the evolution of all the intermolecular (J_{xx}, J_{yy} and $J_{xy} = J_{yx}$) and intramolecular (J_{1xy}) excitonic couplings as a function of the intermolecular distance between the planes formed by the isoindole groups. All the excitonic couplings approach to zero with the increase of the intermolecular distance between the monomers. Nevertheless, at long distances (> 20 Å) the largest J_{xx} and J_{yy} couplings in both dimers A and B still present significant values (absolute values in the 5–10 meV range) as a consequence of the long-range Coulombic coupling effects.

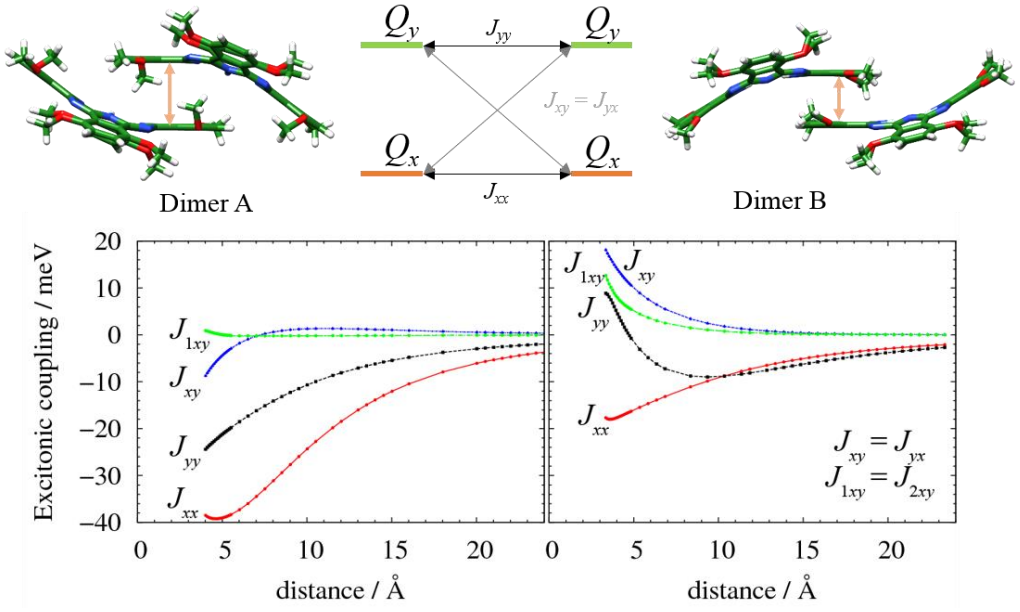

Figure 3.5. Excitonic couplings as a function of the intermolecular π-π stacking distance between the planes formed by the isoindole rings for dimers A and B at the LC-ωPBE/3-21G* level. The shortest distance shown corresponds to the crystal equilibrium distance.

Short-range interactions are also evident from the non-monotonous behaviour of some of the excitonic coupling with the intermolecular distance. To analyse this further, we have compared the total intermolecular excitonic couplings with the purely Coulombic excitonic couplings J^C as a function of the intermolecular distance between the planes formed by the isoindole groups (Figure 3.6). J^C is computed using eq. (1.2) from the ATCs of the isolated molecules. At long intermolecular distances the total excitonic couplings are, as expected, almost identical to the Coulombic

couplings. Only at short/intermediate intermolecular distances, the non-Coulombic short-range effects are not negligible. At 4.0 Å for dimer A (i.e., crystal structure), the short-range coupling component, calculated as the difference between the total and Coulombic coupling, is −11.27, −8.54, and −7.92 meV for J_{xx}, J_{xy}, and J_{yy}, respectively. For dimer B, a similar short-range coupling component for the J_{xx}, J_{xy}, and J_{yy} couplings is found (−12.36, 9.36, and 2.24 meV at crystal structure, 3.35 Å). These results highlight the importance of the short-range excitonic coupling component at short intermolecular distances in agreement with other authors [170,171] and, thus, the necessity of computing the excitonic couplings with proper diabatization schemes able to capture the global effect of short- and long-range interactions. Additionally, the short-range interactions are of great relevance since they determine the fluctuation of excitonic couplings owing to thermal nuclear motions.[46] A thorough analysis of short-range interactions in a large set of molecular dimers is presented in chapter 4.

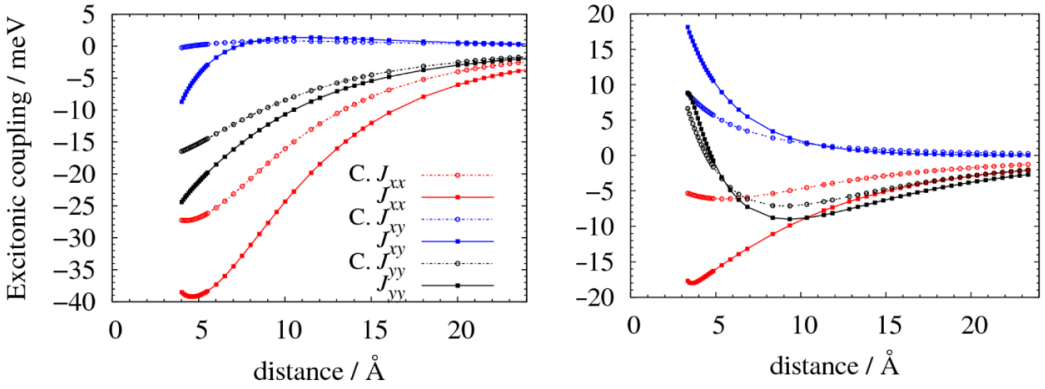

Figure 3.6. Total (full symbols) and Coulombic (empty symbols) excitonic couplings as a function of the intermolecular π-π stacking distance between the planes formed by the isoindole rings for dimers A and B at the LC-ωPBE/3-21G* level.

A further inspection of Figure 3.5 reveals that the intramolecular J_{1xy} and J_{2xy} excitonic couplings for dimers A and B are not completely negligible at short intermolecular distances, especially in dimer B where it presents significant values around 12 meV. As mentioned above, the intramolecular excitonic couplings should be close to zero because they come from the interactions between the Q_x and Q_y states located in the same molecule and with almost perpendicular transition dipole moments. However, in a dimer, the excited states localized on the same molecule may now be mixed owing just to the presence of the other molecule (i.e., an electrostatic perturbation). To explore this in more detail, we have computed the excitonic

couplings between the first two excited states in a model system that consists of one whole H_2-OBPc molecule and only the interacting isoindole group of the other molecule (Figure 3.7(Top)). Now, we only focus on the excitonic coupling between the first two excited states localized on the phthalocyanine molecule. The excited states in the isoindole group are found to be higher in energy. The couplings J_{1xy} for the models at the geometries of dimers A and B are 1.89 and 12.36 meV, respectively, and are in good agreement with the values computed for the whole dimers (0.97 and 12.66 meV, shown in Figure 3.7(Bottom)). Therefore, these findings clearly show that the non-negligible intramolecular coupling values are not an artefact of the diabatization process but arise as a consequence of the perturbation caused by the adjacent molecule.

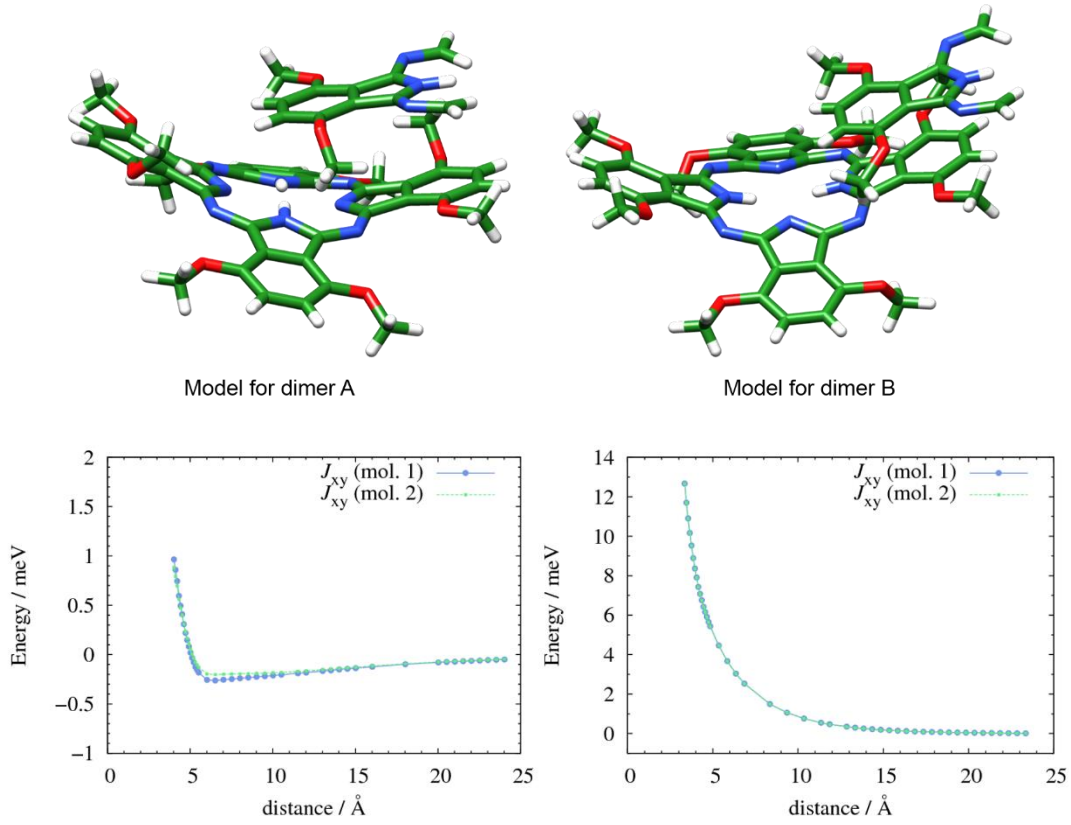

Figure 3.7. (Top) Molecular structure of the model systems used to analyse the intramolecular J_{1xy} and J_{2xy} excitonic couplings. (Bottom) Distance dependence of the intramolecular couplings in the whole dimers A (left) and B (right).

Finally, we assess the importance of the interactions between different columns in the bulk crystal. The three intercolumnar (C, D and E) dimers with the closest intermolecular contacts, shown in Figure 3.8, exhibit excitonic couplings smaller (see Table 3.1) than those found for the intracolumnar dimers A and B. It is therefore

expected that exciton transport is more important along the 1D crystal packing direction and therefore the intercolumnar dimers have not been taken into account.

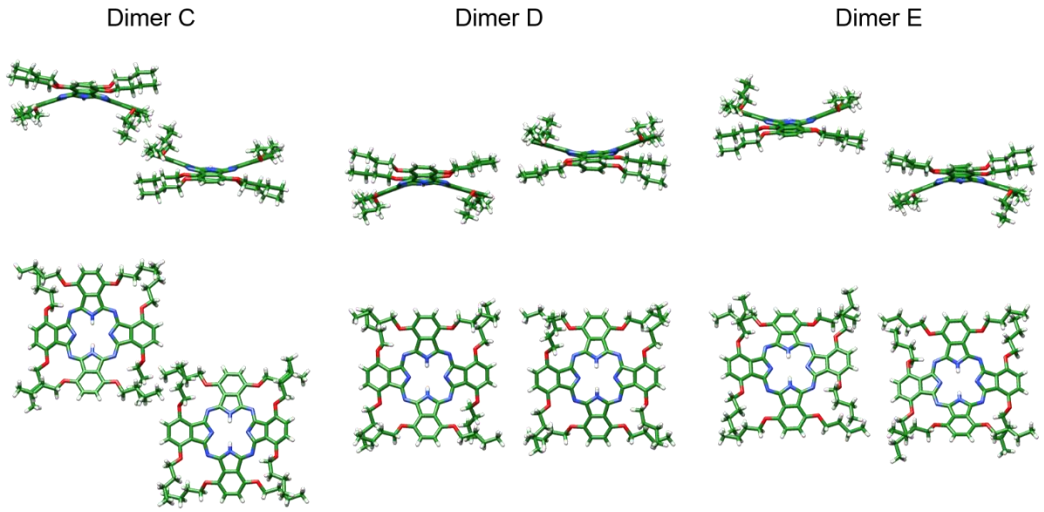

Figure 3.8. Molecular structure of the three intercolumnar dimers (C, D and E) with the closest intermolecular contacts and comparison of the excitonic couplings (meV) between intracolumnar dimers A and B and the intercolumnar dimers C, D, and E computed at LC-ωPBE/3-21G*.

Table 3.1. Excitonic couplings at the crystal geometry for all dimers considered.

Dimer	J_{xx}	J_{xy}	J_{yx}	J_{yy}
A	−38.51	−8.77	−8.71	−24.40
B	−17.68	18.12	18.12	8.86
C	9.23	7.06	7.06	−4.23
D	13.96	−2.65	−2.65	−6.21
E	7.18	−1.64	−1.65	−5.88

3.3.2 Thermal fluctuations of the excitonic couplings

Figure 3.9 displays the time evolution and distributions of the relevant (intermolecular) excitonic couplings (J_{xx}, J_{xy}, J_{yx}, and J_{yy}) for dimers A and B and Table 3.2 collects the average and standard deviation of each excitonic coupling computed for a total of 250 snapshots separated by 50 fs. All excitonic couplings seem to be normally distributed. The thermally averaged excitonic couplings J_{xx} and J_{yy} for dimer A are found to be −39.25 and −24.29 meV, respectively; i.e., very similar to the couplings computed at the equilibrium crystal structure reported in the previous section, while the average cross-couplings J_{xy} and J_{yx} are larger (in absolute value) than the crystal values. Unlike dimer A, dimer B presents similar average excitonic

couplings around 18 meV for J_{xx} and the cross-couplings, whereas the average of J_{yy} is larger than the crystal value. Both dimers exhibit significant standard deviations (σ_{ii}) of approximately one fifth of the average coupling values, in agreement with standard deviations found for other molecular crystals.[46,47]

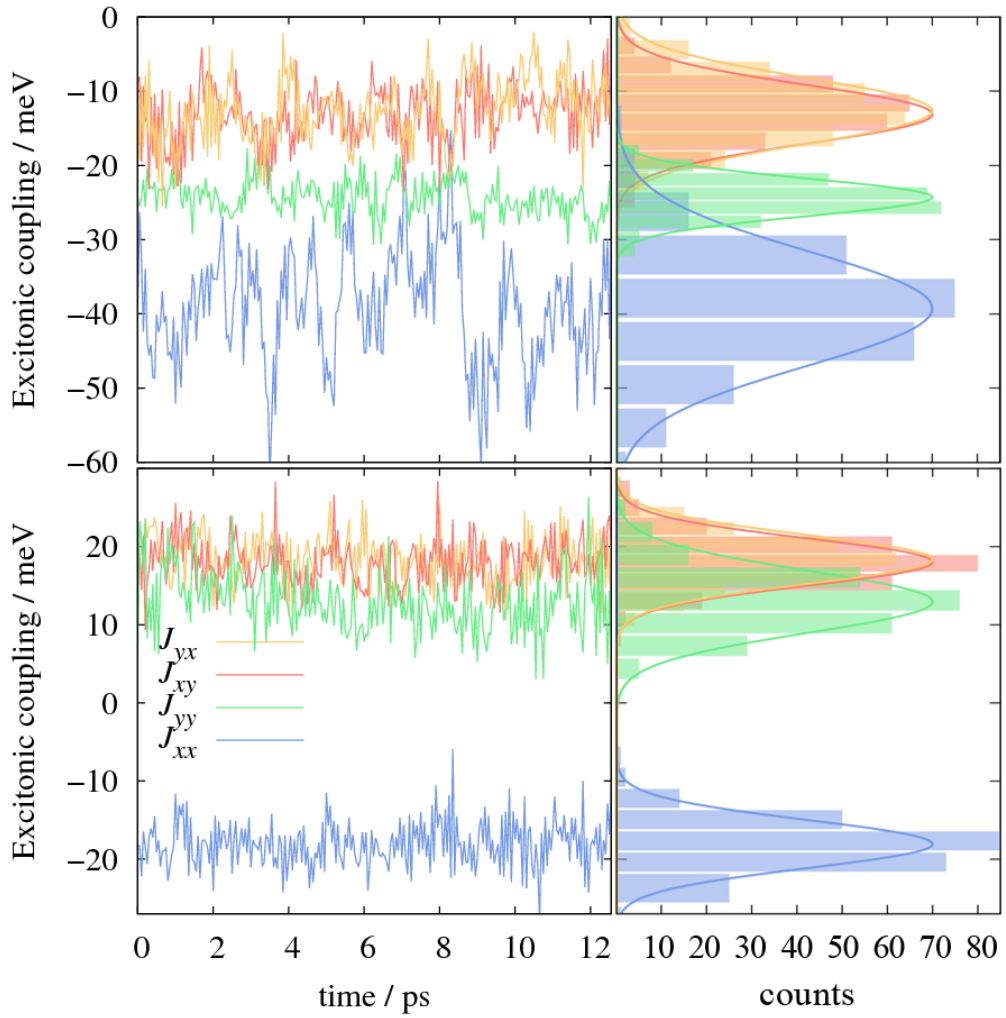

Figure 3.9. Time evolution (left) and distributions (right) of the excitonic couplings computed at 300 K for the dimers A (top) and B (bottom).

Table 3.2. Average and standard deviation in meV for all the intermolecular excitonic couplings computed for dimers A and B.

States	Dimer A		Dimer B	
	$\langle J_{ij} \rangle$	σ_{ij}	$\langle J_{ij} \rangle$	σ_{ij}
xx	−39.25	7.71	−18.07	3.07
xy	−13.11	3.92	18.03	3.01
yx	−12.64	4.40	18.35	3.12
yy	−24.29	2.53	12.94	3.98

In order to identify the vibrations responsible for the excitonic coupling fluctuations, the autocorrelation function $\left\langle \delta J_{ij}(0)\delta J_{ij}(t)\right\rangle$ was computed, where $\delta J_{ij}(t) = J_{ij}(t) - \left\langle J_{ij}(t)\right\rangle$ is the deviation from the time-averaged coupling. Two examples of the time evolution of $\left\langle \delta J_{ij}(0)\delta J_{ij}(t)\right\rangle$ are shown in Figure 3.10. Using the same procedure as in ref. [46], the Fourier transformation of the autocorrelation function was computed for each coupling to identify which frequencies contribute most to the fluctuations. Despite the low resolution of the resulting spectral densities, shown in Figure 3.11, the findings seem to suggest that low frequency vibrations below 100 cm^{-1} are mainly responsible for the modulation of the couplings, while a vibration just above 300 cm^{-1} is also present but has a much smaller amplitude as visible in Figure 3.10. These results would be in agreement with higher-resolved spectral densities computed for other molecular crystals in the context of charge and exciton transport where only low-frequency vibrations were identified to be responsible for the modulation of the excitonic couplings.[46,47,181]

Finally, we investigate the possible correlations between the excitonic couplings in dimers A and B, which share one molecule as they are consecutive in the 1D column (see Figure 3.1). For each couple of intermolecular couplings $\left(J_{ij}^{A}, J_{ij}^{B}\right)$ we computed the statistical correlation factor $cor\left(J_{ij}^{A}, J_{ij}^{B}\right) = \dfrac{\left\langle J_{ij}^{A} J_{ij}^{B}\right\rangle - \left\langle J_{ij}^{A}\right\rangle \left\langle J_{ij}^{B}\right\rangle}{\sigma_{J_{ij}^{A}} \sigma_{J_{ij}^{B}}}$, where $\langle \ldots \rangle$ denotes averaging over the MD simulation. The results are collected in Table 3.3 and show that none of the correlations is particularly strong. The largest correlation (−0.248) is found between the couplings J_{xx} and J_{xy}. The scatter plot for this pair of couplings for all MD snapshots, reported in Figure 3.12, clearly shows that there is no significant correlation between them. We can therefore safely assume that the role of correlations in time between different couplings can be neglected. The correlation values are similar to those found for charge transfer integrals (electronic couplings) between dimers in the family of oligoacenes.[181]

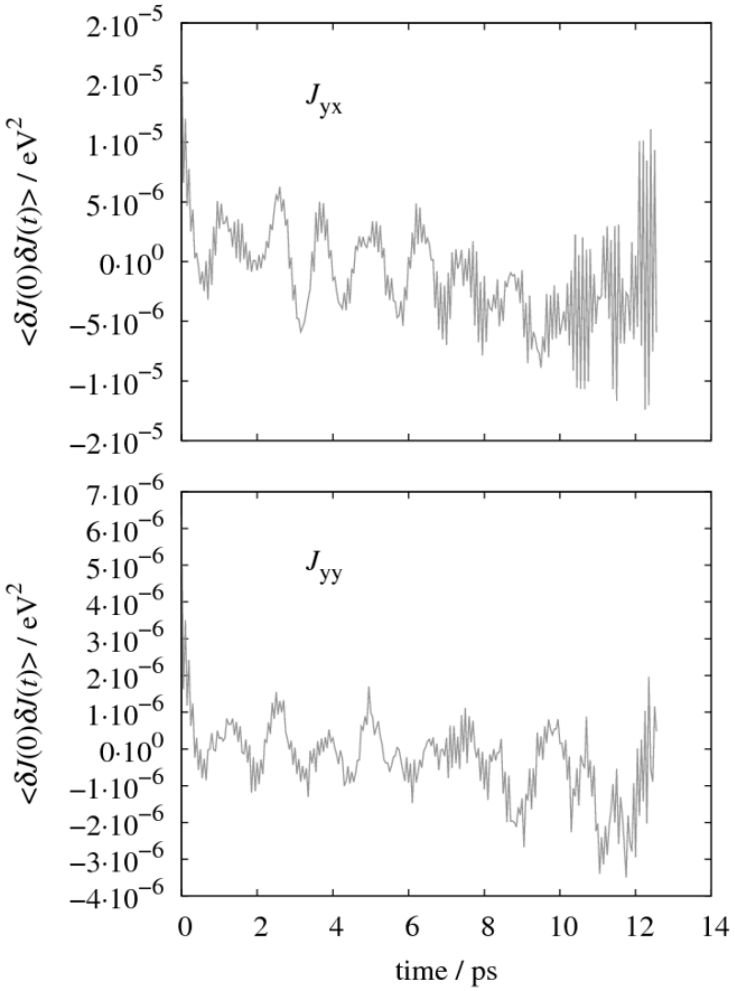

Figure 3.10. Time evolution of the autocorrelation function of two of the couplings in dimer A, obtained from the data shown in Figure 3.9.

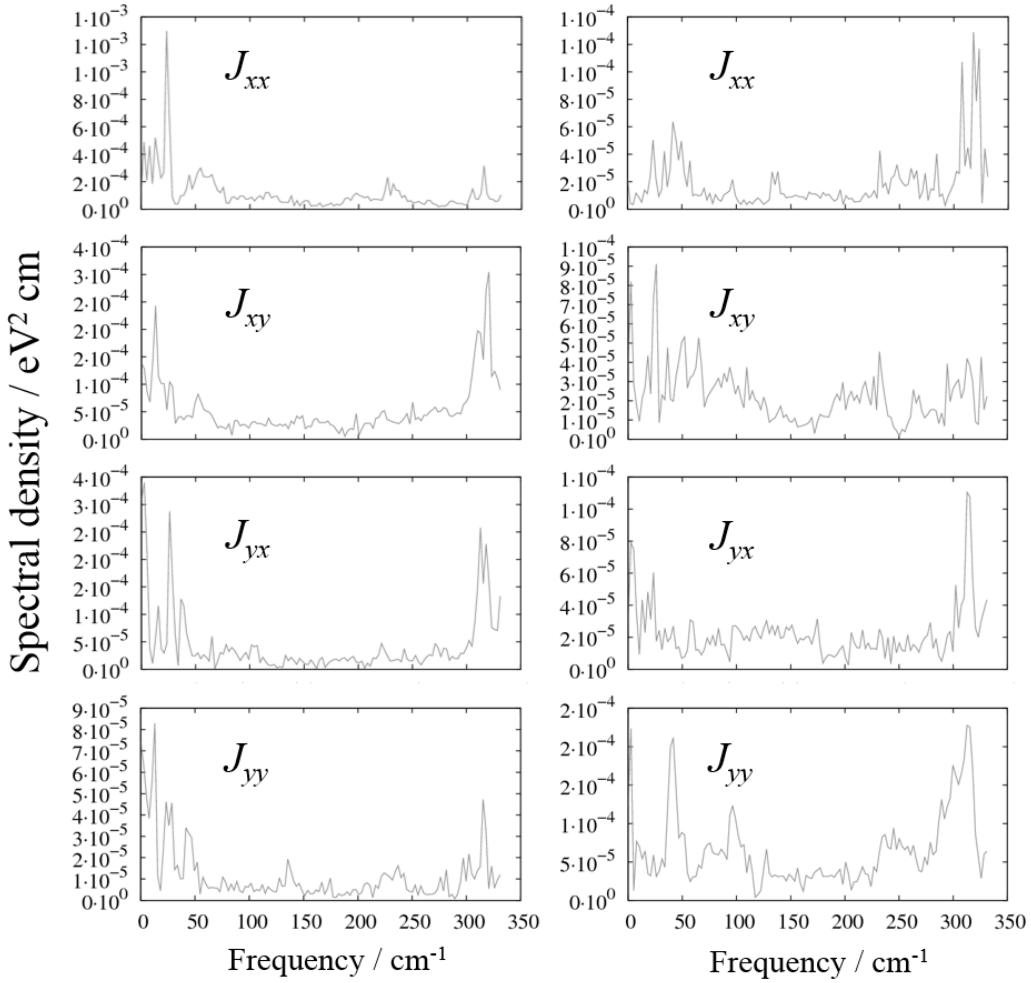

Figure 3.11. Spectral density obtained from the fourier transformation of the autocorrelation function of the four intermolecular excitonic couplings in dimers A (left) and B (right), obtained from the data shown in Figure 3.9.

Table 3.3. Correlations between the excitonic couplings in dimers A and B.

$cor\left(J_{ij}^{A}, J_{ij}^{B}\right)$	J_{xx}	J_{xy}	J_{yx}	J_{yy}
J_{xx}	−0.034	−0.248	0.007	0.038
J_{xy}		0.185	−0.024	−0.208
J_{yx}			−0.088	0.020
J_{yy}				−0.116

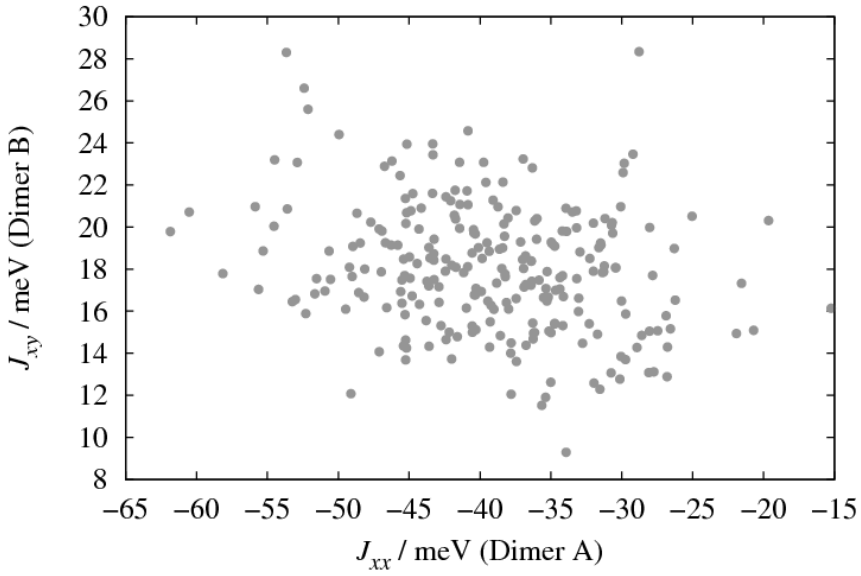

Figure 3.12. Scatter plot of the intermolecular couplings J_{xx} and J_{xy} (the most correlated pair in Table 3.3) in dimers A and B for all 250 snapshots of the MD simulation.

3.3.3 Local exciton-phonon coupling

In addition to the excitonic coupling between the electronic excited states (discussed above), the coupling between the electronic excited states and the vibrations localized on the molecular moieties (generally known as local exciton-phonon coupling) is also crucial for exciton transport. In an excitation energy transfer, the strength of the local exciton-phonon coupling can be evaluated by means of the reorganization energy λ defined in section 3.2.3. The total reorganization energy λ for an excitation energy transfer between two H_2-OBPc molecules (respectively undergoing the $S_0 \rightarrow S_1$ and $S_1 \rightarrow S_0$ electronic transitions) is computed to be 110.89 meV at the LC-ωPBE/6-31G** level. As mentioned in section 3.2.3, the reorganization energy stems from the two energy relaxation contributions λ_{S_1} and λ_{S_0}, where we dropped the (*d*) and (*a*) labels. These can be decomposed into the individual energy contributions from each normal mode *k*, e.g. $\lambda_{S_1} = \sum_k S_k \hbar\omega_k$, where S_k (in italics) denotes the Huang-Rhys factor, not to be confused with S_0, S_1, … denoting electronic states. The Huang-Rhys factors are computed by projecting the difference between the equilibrium geometries of the two electronic states involved (e.g., S_0 and S_1) on each normal mode of the ground state, assuming similar normal modes and frequencies in the ground and excited states (displaced undistorted harmonic oscillator model, see for instance ref.

[182] for further details). Figure 3.13 (top) displays the individual relaxation energy contributions of each vibration ($S_k\hbar\omega_k$) computed from the S_1 state of the H_2-OBPc molecule and clearly reveals that the relaxation energies are mainly dominated by the contribution of the vibration at 1660 cm^{-1}, which can be described as a collective stretching of the C=N/C=C/C−C bonds of the π-conjugated backbone. The strongest coupling of the high-frequency vibration at 1660 cm^{-1} between S_0 and S_1 is in reasonable agreement with the energy spacing of the vibronic progression (~1500 cm^{-1}) experimentally observed in the absorption spectrum of the metal-free Pc with and without peripheral chains for the Q_x and Q_y bands.[183,184] The similar progressions observed for both bands suggest that the same exciton-phonon coupling pattern is expected for the two first electronic transitions ($S_0 \rightarrow S_1$ and $S_0 \rightarrow S_2$). This is confirmed by the analysis of the Huang-Rhys factors computed for the $S_0 \rightarrow S_2$ electronic transition (Figure 3.13, bottom), where the relaxation energy λ_{S_2} is also dominated by the contribution of the vibration at 1660 cm^{-1}. The total λ for the excitation energy transfer involving S_0 and S_2 is calculated to be 158.73 meV. The analysis of the exciton dynamics is significantly simplified if one defines a single effective reaction coordinate with vibrational frequency $\hbar\omega_{eff} = \sum_k S_k\hbar\omega_k \Big/ \sum_k S_k$ with the total associated Huang-Rhys factor $S_{eff} = \sum_k S_k$. The effective vibration frequencies for the relaxation energies λ_{S_1} and λ_{S_2} are calculated to be 1164 and 1192 cm^{-1}, respectively.

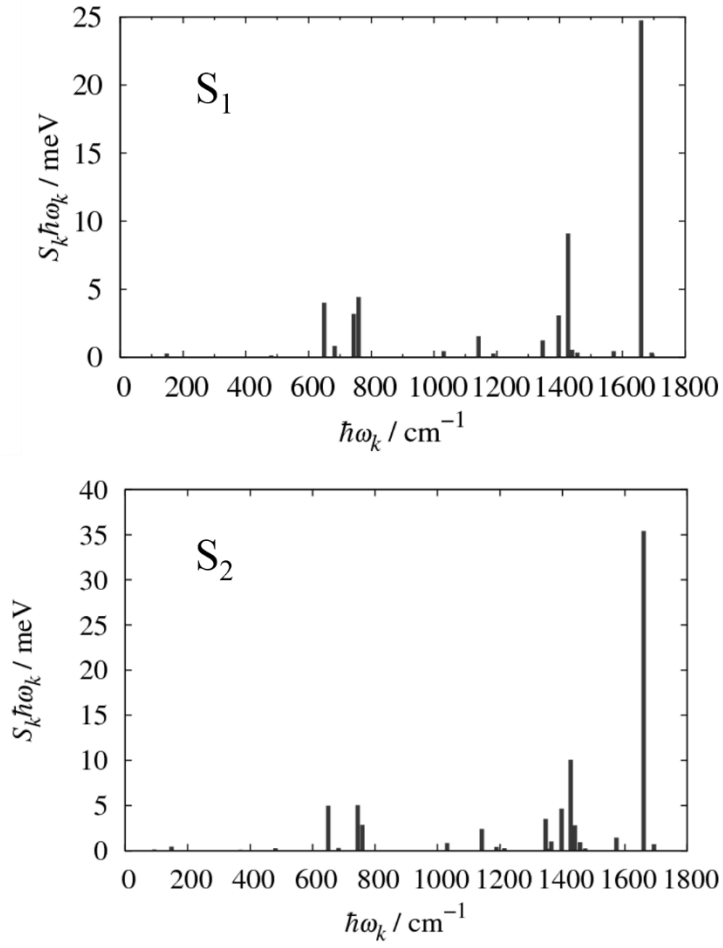

Figure 3.13. Individual relaxation energy contribution from each normal mode in the first (top) and second (bottom) excited state.

3.3.4 Identification of the appropriate transport regime

The interplay between the excitonic coupling and the strength of the local exciton-phonon coupling determines the regime for the exciton transport in a molecular crystal or aggregate. When λ is much larger than the (average) excitonic coupling J, the exciton is localized on an individual molecular unit and the exciton transport occurs by means of a sequence of (incoherent) hops with a specific exciton transfer rate. Conversely, when λ is smaller or similar to the excitonic coupling, excitons can be delocalized over several molecules. Evaluating J and λ is therefore a requirement to identify the plausible regimes of exciton transport in a given molecular crystal.

Figure 3.14 shows the diabatic and adiabatic potential energy surfaces (PES) computed for the excitation energy transfer reaction in dimers A and B along an effective reaction coordinate q. With the parameters previously computed for the

states S_1 in dimer A ($\left|\langle J_{xx} \rangle\right|$ = 39.25 meV and λ = 110.89 meV), the adiabatic PES shows two minima separated by a very small energy barrier (2.37 meV). The thermal energy ($k_B T$ = 25.85 meV) and the zero point energy (E_{ZPE}), estimated as E_{ZPE} = $1/2\hbar\omega_{eff}$ = 72.16 meV, are also included for comparison purposes. The exciton is therefore clearly delocalized between the two molecular units. It is also interesting to analyse the adiabatic PES computed with the parameters calculated for dimer B ($\left|\langle J_{xx} \rangle\right|$ = 18.07 meV and λ = 110.89 meV) in the bottom panel of Figure 3.14. In this case, two well-defined minima are found, separated by an energy barrier (12.60 meV) higher than that obtained in dimer A. Nevertheless, it is important to stress that even the thermal energy $k_B T$ would already be enough to overcome the energy barrier between the two adiabatic minima and the exciton can also be delocalized in both molecular moieties in dimer B. In this context, it seems difficult to be able to assume an incoherent regime for the exciton transport and, therefore, the use of a nonadiabatic transfer rate such as the popular Förster [37] or Marcus [116] rates or even the more sophisticated Marcus–Levich–Jortner (MLJ) rate.[126] For example, by using the general rate expression derived in chapter 2 and applied in the context of excitation energy transfer,[47] the exciton transfer rates between the Q_x excited states for dimer A and B (i.e., only the $\langle J_{xx}^2 \rangle$ coupling is used) are calculated to be 2.690×10^{13} and 5.649×10^{12} s^{-1}, respectively. These rates are faster than any plausible vibrational relaxation rate [184,185] and are therefore inconsistent with the existence of a rate constant for the process. Similar values of reorganization energy (λ = 99 meV) and electronic coupling (45 meV) in the context of charge transport for a nonperipheral octahexyl substituted Pc in its crystal and liquid crystal phase have been recently reported.[159] The authors investigated the charge-transport properties of this Pc derivative but invoked directly an incoherent regime for the transport, which seems to be inconsistent with the parameters (λ and the electronic coupling) of this problem. In the next section, we will describe a model able to describe the exciton dynamics in the H_2-OBPc molecular crystal where the incoherent regime does not apply.

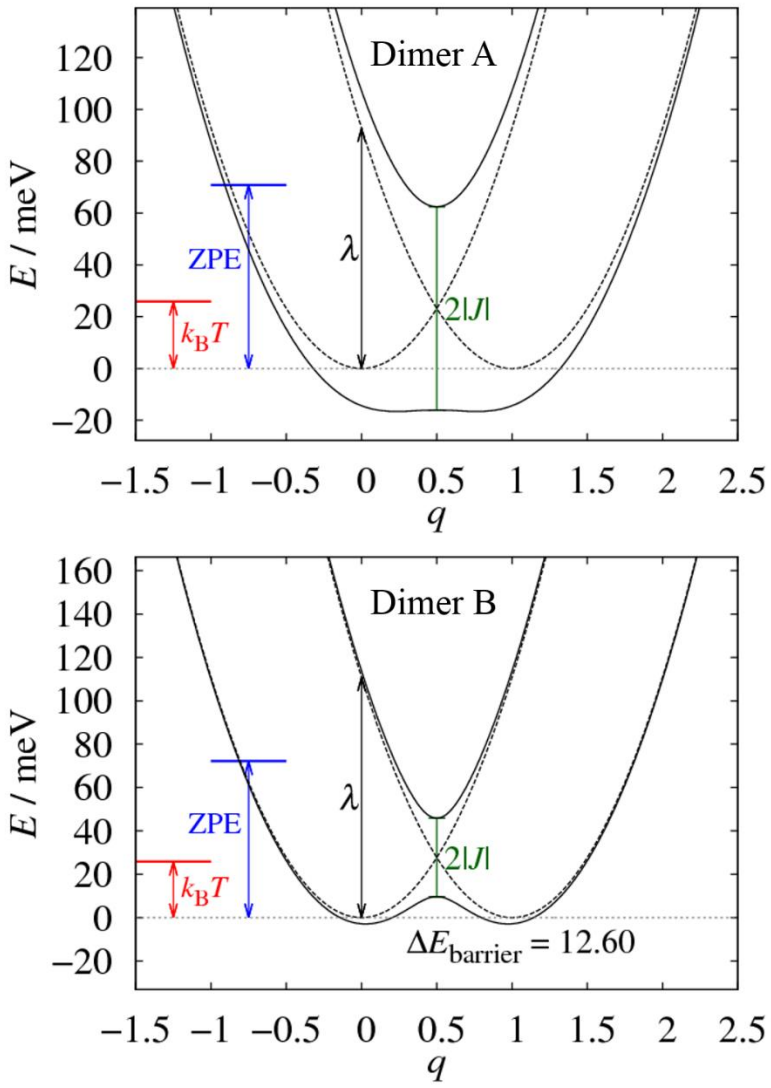

Figure 3.14. Representation of the diabatic (dotted lines) and adiabatic (solid lines) potential energy surfaces computed with the average excitonic coupling $|\langle J_{xx} \rangle|$ and the total reorganization energy λ previously computed for dimers A (top) and B (bottom). The thermal energy (k_BT) and zero point energy (E_{ZPE}) are also given.

3.3.5 Exciton dynamics

The transport in the H_2-OBPc crystal can be assumed to take place mainly along the 1D columns with the two alternating dimers A and B (see the cartoon in Figure 3.15a). In this situation, a model Hamiltonian able to incorporate the different physical ingredients for the exciton transport but with a low number of degrees of freedom can be derived. This model Hamiltonian is written as: [47]

$$
\begin{aligned}
H = & \sum_{jp}\left(E_{jp} + \sum_{k} g_{jp}^{(k)} q_{j}^{(k)} \right) \left| j_p \right\rangle \left\langle j_p \right| \\
& + \sum_{jpp'}\left(J_{jpp'} + \sum_{k} a_{jpp'}^{(k)} \left(q_{j}^{(k)} - q_{j+1}^{(k)} \right) \right) \left| j_p \right\rangle \left\langle \left(j+1 \right)_{p'} \right| + h.c. \\
& + \sum_{j}\sum_{k}\left(\frac{1}{2} m^{(k)} \left(\dot{q}_{j}^{(k)} \right)^2 + \frac{1}{2} m^{(k)} \left(\omega^{(k)} q_{j}^{(k)} \right)^2 \right)
\end{aligned}
\tag{3.2}
$$

The index *j* runs over the molecular sites in the 1D assembly (Figure 3.15a) where the odd and even *j* sites are not equivalent. *p* runs over the excited states of each site. On each molecule, only two singlet excited states ($p = 2$) and several harmonic nuclear vibration modes (indexed by *k*, with displacement $q_j^{(k)}$, effective mass $m^{(k)}$, and frequency $\omega^{(k)}$) are considered. At equilibrium position ($q_j^{(k)} = 0$), E_{jp} and $J_{jpp'}$ denote the energy of the *p*-th singlet excited state at site *j* and the excitonic couplings between the *p* and *p*' excited states at adjacent molecular sites *j* and *j*+1. The nuclear vibrations in this model Hamiltonian are coupled to the exciton carriers in two different ways. They modify the energy of the *p*-th exciton at site *j* according to the linear local exciton-phonon coupling (Holstein coupling [127]) term $g_{jp}^{(k)} q_j^{(k)} \left| j_p \right\rangle \left\langle j_p \right|$, where $g_{jp}^{(k)}$ is the local exciton-phonon constant and is related to the reorganization energy. Moreover, the relative displacements between $q_j^{(k)}$ and $q_{j+1}^{(k)}$ modulate the excitonic coupling between the states $\left| j_p \right\rangle$ and $\left| \left(j+1 \right)_{p'} \right\rangle$ through the term $a_{jpp'}^{(k)} \left(q_j^{(k)} - q_{j+1}^{(k)} \right)$ where $a_{jpp'}^{(k)}$ quantifies the nonlocal electron-phonon coupling and is related to the magnitude of the thermal fluctuation.

E_{j1} and E_{j2} are set to 0 and 10 meV for all the sites, from the first two excited states computed for the isolated H_2-OBPc molecule in the crystal geometry. The local Holstein exciton-phonon constant $g_{jp}^{(k)}$ is independent from *j* but it is different for the two excited states per molecule ($g_{jp}^{(k)} = g_p^{(k)}$). The analysis of the Huang-Rhys factors computed for H_2-OBPc (Figure 3.13) allowed us in section 3.3.3 to define a single effective vibration for each $S_0 \rightarrow S_1$ and $S_0 \rightarrow S_2$ excitation of H_2-OBPc associated with the total reorganization energy (111 and 159 meV, respectively). The frequencies of these two effective modes ($k = 1$ and $k = 2$) are set to $\omega^{(1)} = 1164$ and $\omega^{(2)} = 1192$ cm^{-1} (144 and 148 meV) and the mass $m^{(1)} = m^{(2)} = 6$ amu (the reduced mass of the

C-C/C=C bonds that gives the main contribution to these modes). Note that the vibration mode $k = 1$ ($k = 2$) only modulates the diagonal energy E_{j1} (E_{j2}). The local Holstein exciton-phonon constants are therefore computed as $g_1^{(1)} = \omega^{(1)}\sqrt{m^{(1)}\lambda_{S_0 \to S_1}} =$ 1821 and $g_2^{(2)} = \omega^{(2)}\sqrt{m^{(2)}\lambda_{S_0 \to S_2}} =$ 2231 meV Å^{-1}. It should be mentioned that the external contribution due to neighbouring molecules on the site fluctuation in molecular crystals (external reorganization energy) is expected to be much smaller than the fluctuation due to intramolecular vibrations [186,187] and, thus, this environmental effect has not been included.

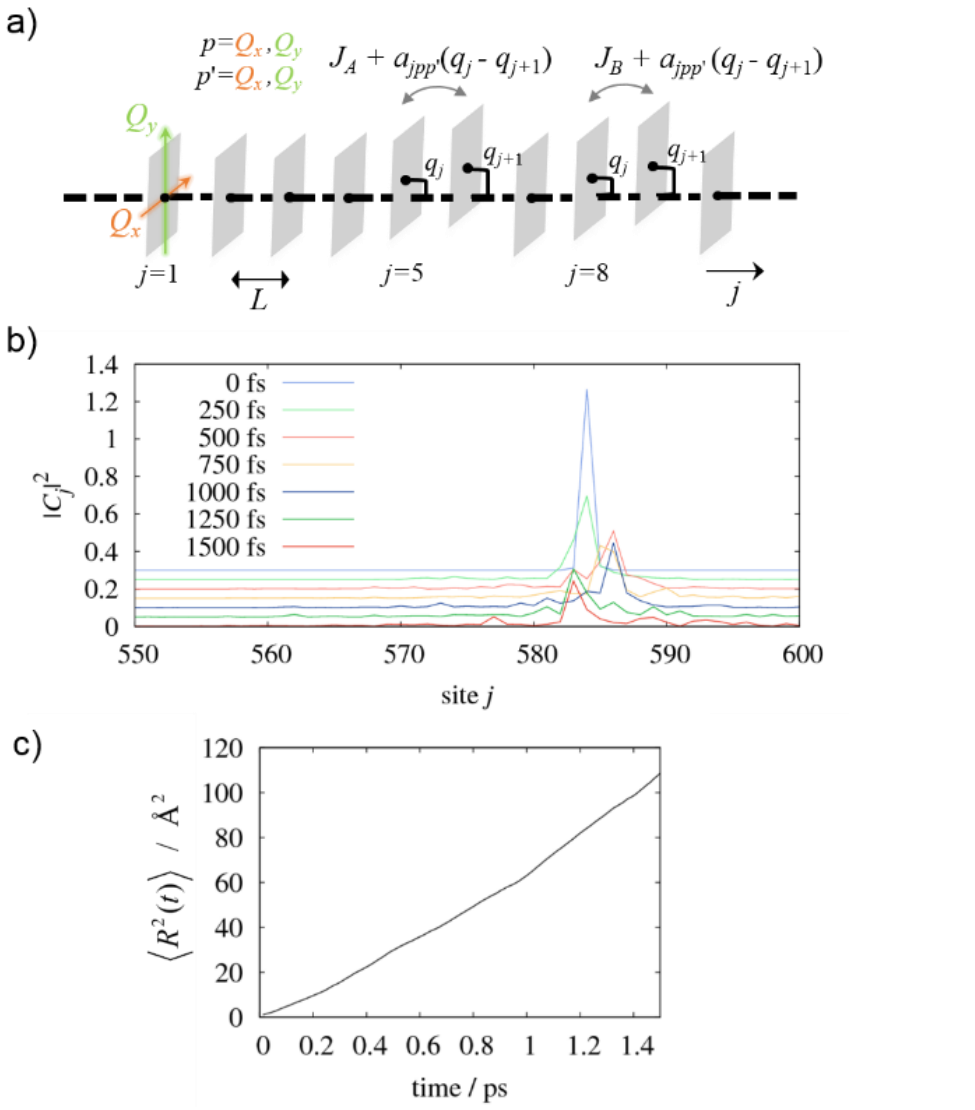

Figure 3.15. a) Scheme of the 1D model used to describe the exciton transport in the H_2-OBPc molecular crystal. b) Time evolution of the exciton wavefunction evaluated from the model Hamiltonian using the parameters reported in Table 3.4. Populations on each site (vertically off-set for clarity) are reported from t = 0 to t = 1500 fs every 250 fs. Site j represents molecules in the model. c) Plot of the temperature averaged square displacement $\langle R^2(t) \rangle$ versus time.

For the off-diagonal elements, the $J_{jpp'}$ couplings when j is an odd (even) site are set to be the average excitonic couplings computed for dimers A (B) (see Figure 3.15a). Similar to the local exciton-phonon coupling, it is also convenient to select an effective mode (or at least a few effective modes) that can capture the overall effect of the low-frequency vibrations on the excitonic coupling fluctuations in the model Hamiltonian (eq. (3.2)). Based on the low-resolved spectral densities shown in Figure 3.11 and high-resolved spectral densities computed for other molecular crystals in the context of charge and exciton transport,[46,47,181] low-frequency vibrations in the

10–100 cm^{-1} range seem to be mainly responsible for the modulation of the excitonic coupling. Correlations between the excitonic couplings fluctuations between dimers A and B were found to be very small (see Table 3.3 and Figure 3.12). It is therefore reasonable to assume four independent low-frequency vibrations (k = 3, 4, 5 and 6) as the effective modes coupled strongly to each excitonic coupling. The frequencies of these effective modes can be tentatively estimated from a weighted average of the low-frequency vibrations (< 100 cm^{-1}) of the spectral density (Figure 3.11) and are found to be very similar ($\omega^{(3)} = \omega^{(4)} = \omega^{(5)} = \omega^{(6)} = 5$ meV). Note that a precise assignment of the frequency of these effective modes is not essential for the exciton transport model. The mass for these effective vibrations is set to be $m^{(3)} = m^{(4)} = m^{(5)} = m^{(6)} =$ 754 amu, which corresponds to the mass of the H_2-OBPc molecule. A specific value for the non-local exciton-phonon coupling constant $a_{jpp'}^{(k)}$ can be calculated if it is assumed that only the k-th effective mode couples with $J_{jpp'}$. Using the standard deviations previously computed for the excitonic couplings (Table 3.2), $a_{jpp'}^{(k)}$ can be then computed as $\sigma_{J_{jpp'}} = a_{jpp'}^{(k)} \sqrt{2k_B T \Big/ m^{(k)} \left(\omega^{(k)}\right)^2}$. Table 2 summarizes all the parameters used for the model Hamiltonian (eq. (3.2)).

Table 3.4. Parameters used for the H_2-OBPc crystal exciton transport model Hamiltonian (eq. (3.2)).

Parameter	Value
N	600
E_{jp}	0 (p = 1) and 10 (p = 2) meV
J_{j11}, J_{j12}, J_{j21}, and J_{j22} (j odd)	−39, −13, −13, and −24 meV
J_{j11}, J_{j12}, J_{j21}, and J_{j22} (j even)	−18, 18, 18, and 13 meV
$g_1^{(1)}$ and $g_2^{(2)}$	1821 and 2231 meV $Å^{-1}$
$\omega^{(1)}$ and $\omega^{(2)}$	144 and 148 meV
$m^{(1)} = m^{(2)}$	6 amu
$a_{j11}^{(3)}$, $a_{j12}^{(4)}$, $a_{j21}^{(5)}$, and $a_{j22}^{(6)}$ (j odd)	71, 36, 41, and 23 meV $Å^{-1}$
$a_{j11}^{(3)}$, $a_{j12}^{(4)}$, $a_{j21}^{(5)}$, and $a_{j22}^{(6)}$ (j even)	29, 28, 29, and 37 meV $Å^{-1}$
$\omega^{(3)} = \omega^{(4)} = \omega^{(5)} = \omega^{(6)}$	5 meV
$m^{(3)} = m^{(4)} = m^{(5)} = m^{(6)}$	754 amu

Recently, Schröter and Kühn have analysed the interplay between local nonadiabatic deactivation effects and Frenkel exciton transfer in molecular perylene bisimide aggregates.[188] To do so, they adopted a Frenkel Hamiltonian model in the

diabatic representation which was extended to incorporate nonadiabatic couplings between the excitonic bands (adiabatic representation). Although the nonadiabatic effects can be relevant when two excited states are close in energy as is the case here, our model is able to partially capture these effects because we are allowing for the mixing between the Q_x and Q_y diabatic states (or Q_y and Q_x) localized on each molecular site by the non-zero cross excitonic couplings (J_{xy} and J_{yx}). Note that Schröter and Kühn set these cross couplings to be zero.

As noted in ref. [47], the model proposed is able to include both diagonal (on-site energies) and off-diagonal (excitonic couplings) fluctuations of the electronic Hamiltonian on equal footing, the two terms being respectively the second and fourth term in eq. (3.2). In fact, the model Hamiltonian was constructed to reproduce the amplitude and the timescale of the fluctuations of the excitonic coupling computed from the MD/quantum chemistry procedure. The masses and force constants determine the timescale of the fluctuations and the non-local exciton-phonon coupling constants determine their strength.

The time evolution of the exciton wavefunction can be computed by integrating the model Hamiltonian (eq. (3.2)) within an Ehrenfest dynamics scheme, where the nuclear modes are treated classically. Further details of the numerical integration can be found for example in ref. [78]. The Ehrenfest scheme has some important limitations extensively discussed in literature,[75] mainly, the absence of decoherences and erroneous thermal equilibration at long times. However, it is preferable over surface hopping methods [76] when a quasi-continuum of electronic states is present, as in this case.[189,190]

The initial nuclear positions, $q_j^{(k)}(0)$, and velocities, $\dot{q}_j^{(k)}(0)$, for the simulation at temperature T = 300 K were randomly selected from the Boltzmann distribution. The non-local exciton-phonon couplings have been chosen so that the distribution of the instantaneous excitonic couplings at 300 K has the same mean and standard deviation of that computed for the atomistic system at the same temperature (Table 3.2). In the semiclassical evolution of the system, the classical modes oscillate around their equilibrium position with random phases and a thermal distribution of amplitudes, modulating the excitonic coupling and reproducing the dynamic disorder observed computationally.

Figure 3.15b displays the time evolution of the exciton wavefunction. The initial wavefunction, which is selected to be in one of the excitonic eigenstates of the Hamiltonian at the beginning of the simulation (only the lowest-energy wavefunction is shown in Figure 3.15b), is localized on just a few sites (< 4) at 300 K. The initial localization of the exciton wavefunction is induced by disorder in the diagonal and off-diagonal terms of the electronic Hamiltonian. Nevertheless, the exciton wavefunction spreads as a consequence of the time dependence of the excitonic couplings. The exciton diffusion coefficient along the columns of the H_2-OBPc system can be quantitatively calculated by monitoring

$$R_n^2(t) \equiv \langle \psi_n(t) | r^2 | \psi_n(t) \rangle - \langle \psi_n(t) | r | \psi_n(t) \rangle^2 \tag{3.3}$$

which measures the time-dependent spread of the wavefunction. $R_n^2(t)$ is computed from 300 different initial wavefunctions $\psi_n(0)$ (and energies E_n) and averaged (with Boltzmann weight) to give the temperature-averaged $\langle R^2(t) \rangle$. The initial wavefunctions $\psi_n(0)$ included in the Boltzmann average have been chosen to be those that can be thermally accessible with energies above the lowest-energy eigenstate in the 260 meV range. In this way, different degrees of localization found to be relevant in molecular crystals are taken into account for the estimate of the exciton diffusion coefficient.[191,192]

Figure 3.15c displays the temperature-averaged squared displacement $\langle R^2(t) \rangle$ versus time. $\langle R^2(t) \rangle$ increases linearly with time which is indicative of a diffusive behaviour. The exciton diffusion coefficient is then evaluated from the relationship $D = \lim_{t \to \infty} \langle R^2(t) \rangle / 2t$ (in practice D is evaluated from the longest simulated time of 1.5 ps). The distance between molecules is set to 8.64 Å (distance between the centers of mass averaged over dimers A and B). A value of D = 0.324 $cm^2\ s^{-1}$ is obtained for the H_2-OBPc crystal. It should be also noted that the exciton diffusion coefficient computed from the model Hamiltonian with two electronic states per site is larger than the exciton diffusion coefficient (D = 0.095 $cm^2\ s^{-1}$) computed with a similar model but with only one electronic state per site (Figure 3.16). The comparison between the two models clearly reveals that the incorporation of the two electronic excited states close in energy (Q_x and Q_y) gives rise to an enhanced exciton transport pathway.

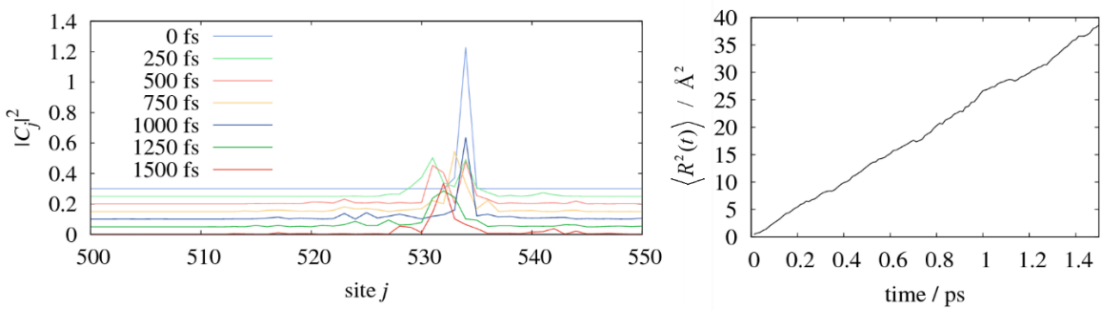

Figure 3.16. Time evolution of the exciton wavefunction (left) and plot of the temperature averaged square displacement $\langle R^2(t) \rangle$ versus time (right). In this case only a single excited state per site is considered in the model Hamiltonian.

The predicted exciton diffusion coefficient (0.324 cm^2 s^{-1}) is of the same order of magnitude as that reported for a zinc Pc (ZnPc) derivative aggregate (D = 0.43 cm^2 s^{-1}) derived from exciton-exciton annihilation measurements [193] although larger than exciton diffusion coefficients of other Pc-based amorphous materials.[194] However, the diffusion coefficient of the ZnPc aggregate was estimated by assuming an incoherent regime with an exciton transfer rate of ~1.0 × 10^{13} s^{-1}, which is close to the limit of validity of a first order rate process in a molecular system. The agreement between the theoretical and experimental exciton diffusion coefficients suggests that the model proposed here is able to correctly describe exciton diffusion, but without assuming an incoherent regime, which would be incompatible with the J and λ parameters of this system (see Figure 3.14 and the discussion in section 3.3.3). It seems therefore very likely that in Pc aggregates with efficient exciton transport properties at room temperature the exciton diffusion regime (beyond the incoherent) is that limited by the thermal fluctuation of the excitonic couplings (dynamic disorder).

3.4 Conclusions

In this chapter we have investigated the exciton transport properties of an octa(butyl)-substituted metal-free phthalocyanine (H_2-OBPc) molecular crystal using a combination of classical molecular dynamics, quantum chemical electronic structure calculations, a multi-state diabatization scheme and a model Hamiltonian with semiclassical time evolution of the exciton.

We have shown that the multi-state diabatization scheme described in section 1.2.1.1 is particularly suited for computing the excitonic couplings in molecular dimers of phthalocyanines where multiple quasi-degenerate excited states are present

in the isolated chromophore. Short-range excitonic interactions, included in the couplings computed with this approach, were shown to be potentially significant between molecules in close contact, and their role in a wide range of molecular aggregates (including H_2-OBPc) will be analysed in detail in chapter 4.

The fluctuation of the excitonic couplings owing to thermal nuclear motions was found to be significant in this molecular crystal, in agreement with other molecular crystals. Low-frequency vibrations were shown to be responsible for the excitonic coupling fluctuation. The average values of the excitonic couplings were found to be significant in the 40–18 meV range and not much smaller than the reorganization energy associated with the exciton energy transfer. In this situation, the exciton is delocalized, the commonly assumed incoherent regime for self-assembled phthalocyanine-based molecular aggregates is not valid, and a simple nonadiabatic exciton transfer rate cannot be derived. The results clearly suggest that phthalocyanine-based molecular aggregates may be good candidates for efficient excitation energy transport in the coherent regime (see section 1.2.2) beyond the Förster (incoherent) mechanism.

A simple but realistic model Hamiltonian able to incorporate multiple excited states per site and fluctuations of the excitonic couplings has been proposed to interpret the exciton dynamics of the H_2-OBPc molecular crystal. The fluctuation of the excitonic couplings (dynamic disorder) causes the initial localization of the exciton wavefunction in just a few molecules but also assists its quick spread. This transport regime, where the off-diagonal fluctuations are of great relevance, is completely different than the transport regimes generally assumed in the context of exciton transport (incoherent) and seems to be adequate for Pc aggregates with efficient exciton transport properties at room temperature. Although the theoretical model proposed can capture the essential behaviour of the exciton transport, there are some challenging but missing features (going beyond the 1D model, including quantum vibronic effects and introducing decoherences) that should be incorporated in fully quantitative models.

4. Short distance interactions can strongly affect excitonic couplings in biological and artificial molecular aggregates*

Summary: In chapter 3 we have seen how the fluctuation of the couplings can affect exciton transport in a molecular crystal and how the inclusion of short-range interactions can influence the computed coupling strength (see Figure 3.6). In this chapter, we will analyse in more detail the relative importance of the short-range (exchange, overlap, orbital) and long-range (Coulombic) components of the excitonic coupling in a large database of structures: three different light-harvesting complexes (LHCs) and two organic semiconductors (one disordered and one crystalline). We find that Mulliken atomic transition charges (ATC) can introduce systematic errors in the Coulombic coupling and that the dipole-dipole interaction fails to capture the true Coulombic coupling even at intermolecular distances of up to 50 Å. The non-Coulombic short-range contribution to the excitonic coupling is found to represent up to ~70% of the total value for molecules in close contact, while, as expected, it is found to be negligible for dimers not in close contact. For the face-to-face dimers considered here, the sign of the short-range interaction was found to correlate with the sign of the Coulombic coupling, i.e. reinforcing it when it is already strong. The results confirm that, for a quantitative description of the exciton dynamics in aggregates of closely packed molecules (in van der Waals contact), the total couplings including the short-range effects should be computed, especially since it is often important to capture the full extent of the thermal fluctuation as discussed in chapter 3.

4.1 Introduction

The excitonic coupling between localized Frenkel excitons determines the dynamics of electronic energy transfer in a variety of molecular systems, including biological light-harvesting complexes[195,196] and organic semiconductors.[146,197] For the study of the quantum mechanical evolution of excited states it has become commonplace to evaluate the excitonic coupling for a large number of structures, e.g.

* The content of this chapter is published in R. P. Fornari, P. Rowe, D. Padula and A. Troisi, *J. Chem. Theory Comput.*, 2017, **13**, 3754−3763. Patrick Rowe selected and extracted the chromophore pairs from the structures of the light-harvesting complexes, optimized their structures and computed the couplings between them.

those deriving from a molecular dynamics simulation[46,158,198–204] or representing the interaction between chromophores in an amorphous system.[205–211] To perform these large scale simulations efficiently, to rationalize the observed properties and to design new materials it is important to identify the main components of the excitonic coupling and assess their relative importance.

The excitonic coupling is conventionally separated into a Coulombic contribution, which dominates interactions at large distances and a number of short range contributions, which are important for molecules in close contact.[170,196] The Coulombic coupling defined in eq. (1.2) is the electrostatic interaction between the transition densities of the Frenkel excitons localized on the chromophores. The short-range contributions, which are essentially overlap and exchange interactions as summarized in section 1.2.1, can be captured by diabatization techniques such as the one described in section 1.2.1.1. In these approaches, the adiabatic electronic Hamiltonian of the system is transformed into a diabatic Hamiltonian where the off-diagonal elements are the couplings between diabatic excited states. Although the different short-range contributions to the couplings cannot be distinguished when obtained from a diabatization, the non-Coulombic short-range interaction can be evaluated indirectly as the difference between the total coupling and the purely Coulombic coupling.

For a number of problems in the fields of biophysics and materials science it has become particularly important to be able to understand and quantify the effect of short-range interactions. In organic semiconductors, where the most important couplings are between molecules in contact, it is important to know whether the dominant interaction is still Coulombic, i.e. computable from eq. (1.2), in which case it can still be treated by approximate representations of the transition density like atomic transition charges (ATC) or point dipole, or if the short range component must also be included. This is a crucial question since the excitonic couplings determine the static and dynamic properties of molecular aggregates. As discussed in sections 1.2.2 and 3.3.3, the regime of exciton transport (coherent or incoherent) is determined by the relative strength of the excitonic coupling and the exciton-phonon coupling.[47,125] Furthermore, short range interactions at finite temperature cause strong fluctuations in the excitonic coupling [46,197] which in some instances can influence or limit the energy transfer dynamics.[47,212,213] The role of coupling

fluctuations in the case of a phthalocyanine crystal was investigated in chapter 3. In photosynthesis, light absorption and efficient transport of the excitation energy is achieved by clusters of chromophores in proteins commonly called light-harvesting complexes (LHCs).[196] Generally, the majority of chromophore pairs are sufficiently distant that their interaction is reasonably well described by expressions like (1.2). This has been shown to be true, for example, for most pairs in the well-studied Fenna-Matthews-Olson (FMO) protein.[200] On the other hand, some LHCs such as light-harvesting 2 (LH2) contain chromophore pairs for which the intermolecular separation is small enough that short range interactions may play an important role.[214] A highly debated point in the literature is the role of quantum mechanical coherence in the evolution of excited states in LHCs.[52,53,215] Any fluctuation of the excitonic couplings due to short range interactions coupled to thermal motion is expected to decrease the coherence and affect the exciton dynamics.[65,213,216]

The aim of the study presented in this chapter is to evaluate the excitonic coupling between pairs of chromophores in three different LHCs and in two organic semiconductors (one amorphous and one crystalline), to achieve a broader understanding of the importance of short range interactions valid for most of the problems under current consideration. This large database of structures is used to assess the role of short range interactions with respect to the Coulombic one. The results will be also used to establish criteria for using approximate methods to evaluate the Coulombic interaction.

4.2 Systems investigated

Among the astounding variety of LHCs that have been discovered, we have selected a few with the intent of covering a broad range of different chromophore arrangements: the Fenna-Matthews-Olson protein (FMO) from *Chlorobium Tepidum*,[217] the light-harvesting 2 protein (LH2) from *Rhodopseudomonas Acidophila*[218] and the peridinin chlorophyll protein (PCP) from *Amphidinium carterae*.[219] The FMO protein has become the model system for much research into exciton transport in LHCs since the initial report of coherent energy transfer.[52,220] Comprising of three identical subunits containing 8 bacteriochlorophyll-a (BChlA) chromophores each, FMO is relatively simple from a chemical perspective, but is

topologically complex, with no symmetry to the spatial arrangement of chromophores in space within a monomeric unit. LH2 is of great interest for the opposite reason: it is comprised of both BChlA and rhodopin glucoside (carotenoid) chromophores arranged in a C_9 symmetric structure giving rise to very peculiar effects such as spectral shifts and exciton delocalization[221] which may affect the coherent evolution of excitons.[39,214,215,222] We include PCP in our study as a representative LHC containing two different type of chromophores: two pseudo-twofold symmetric sets of peridinin chromophores (carotenoids) and a pair of chlorophyll-a (ChlA) chromophores.[219,223] The arrangement of chromophores in these structures is illustrated in Figure 4.1.

To illustrate the role of short range contributions to excitonic coupling in molecular materials, we have considered two examples with different morphologies, an ordered material (with dynamic disorder) and a partially disordered molecular solid. In both cases phthalocyanines have been chosen as they are widely studied and well performing semiconductors and because of their structural and spectroscopic similarity to natural chlorophylls.

The ordered material is the H_2-OBPc molecular crystal analysed in chapter 3, where we investigated the effect of thermal fluctuations of the couplings on exciton dynamics. The couplings in the two closely packed dimers of H_2-OBPc (see Figure 4.1) were evaluated for 250 snapshots, separated by 50 fs, taken from a molecular dynamics (MD) simulation at 300 K. The data presented in chapter 3 are analysed here with the purpose of characterizing and quantifying the role of the short-range component in presence of thermal fluctuations.

Disordered phases in organic semiconductors are of great interest as they make up a significant fraction of polycrystalline thin films, not to mention amorphous films. While the morphology of the crystalline phase is usually well characterized, this is not the case for the disordered regions, which are believed to be of crucial importance for charge and exciton transport as they connect crystalline regions.[224–226] To provide a plausible example of a partially disordered structure we have simulated the rapid thermal annealing from high temperature of the well-studied zinc phthalocyanine (ZnPc). The resulting solid, shown in Figure 4.1, is a sample of non-crystalline phase where the molecules are preferentially stacked in columns with π-π intermolecular distances in the 3.0-3.8 Å range. There is disorder both in the intra-column rotational

angles and in the tilt angles of adjacent columns, making this an interesting and statistically varied example for the comparison of long and short range excitonic interactions.

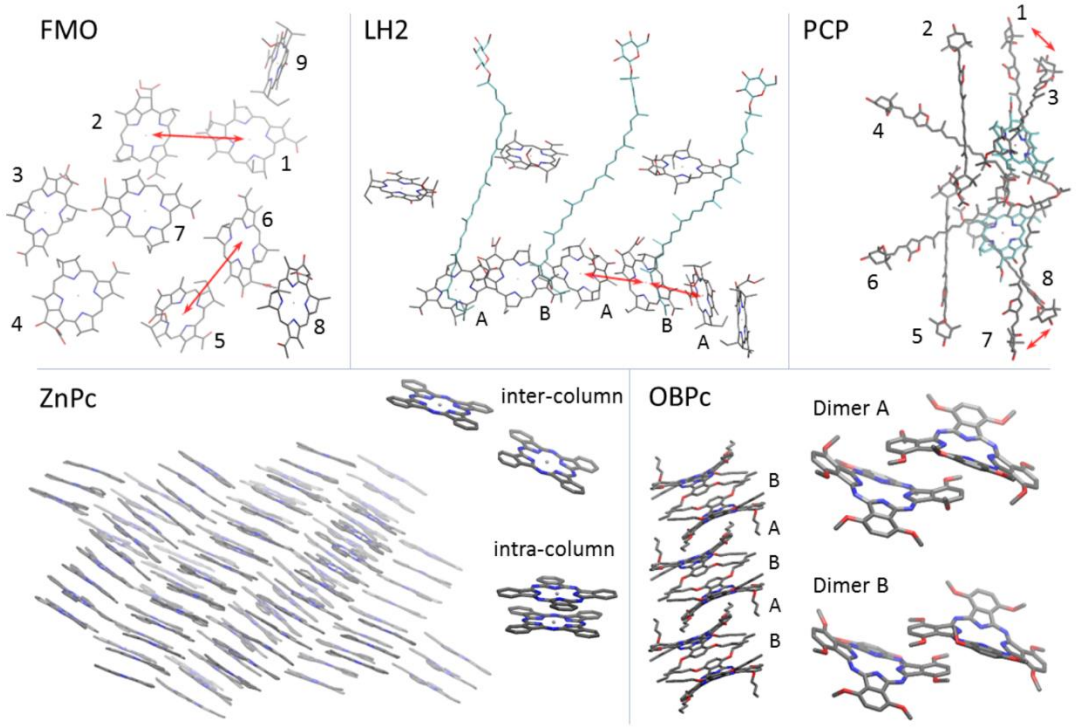

Figure 4.1. Structures of the LHCs (top) and molecular materials (bottom) considered. Hydrogens are omitted in all structures. Top: Only the chromophores are shown. One third of the LH2 complex is considered. The phytyl chain of BChlA and ChlA is replaced by methyl. The red arrows indicate the pairs with the strongest short-range interactions. Bottom left: Disordered sample of 90 ZnPc molecules and examples of inter- and intra-column dimers. Bottom right: stacking of the molecules in the H_2-OBPc (OBPc) crystal and detail of the two dimers (with butoxy replaced by methoxy). Numeric labels indicate chromophores while letters indicate equivalent pairs. The structure figures were generated with VMD.[227]

4.3 Methods

4.3.1 Molecular structures

The structures of the LHCs were obtained from the Protein Data Bank entries 3BSD[228] (FMO), 1NKZ[229] (LH2) and 1PPR[219] (PCP). All pairs of identical chromophores (*homo-dimers*) were considered, for which the role of charge transfer states and the effect of the relative alignment of excitation energy levels on the couplings can be neglected. This is not the case for *hetero-dimers* (i.e. chlorophyll-carotenoid), which were therefore excluded from this study. In FMO we have considered the 8 BChlA belonging to one of the subunits and, due to its proximity, one BChlA from the neighbouring subunit. In LH2 we have considered all homo-dimers within one third of the complex as shown in Figure 4.1, thereby avoiding the

calculation of the weaker couplings. The phytyl chain of BChlA and ChlA was substituted with a methyl group since its effects on the excited state properties are not large enough to justify the additional computational cost of including it.[230]

A plausible structure of the disordered phase of zinc phthalocyanine (ZnPc) was obtained from a molecular dynamics simulation performed with the GROMACS 5.0.5 software[231] using a force field parametrized for ZnPc.[232] A sample of 90 molecules starting from the experimental crystalline phase[233] was first equilibrated at 300 K (for 5 ns), then heated (over 5 ns) and equilibrated at 700 K (for 30 ns) under NVT conditions using a Nose-Hoover thermostat. Then it was repeatedly kept at 700 K for 10 ns and quenched to 300 K (over 5 ns) under NPT conditions using a Berendsen barostat, obtaining after 6 such annealing cycles (and 204 ns total simulation time) a partially disordered phase stable at 300 K consisting of closely spaced columns. From the final snapshot at 300 K (shown in Figure 4.1) two sets of molecular pair configurations were extracted. The *intra-column dimers* are defined as those where the distance between the centres of mass is less than 6 Å and the *inter-column dimers* are those where this distance is between 6 and 15 Å. The dimers where the molecules are within 15 Å but they are in the same column (i.e. they are second or third neighbours) are not considered. In summary, our data set consists of all homo-dimers from the LHCs, 90 intra-column dimers and 10 inter-column dimers from the ZnPc sample and 250 MD snapshots for each dimer of H_2-OBPc.

Since we are more interested in comparing long and short-range interactions in a large set of structures, rather than in the absolute accuracy of the couplings, it is desirable to exclude from our analysis the uncertainties in the experimental data (for the LHCs) and the uncertainties in the MD force field (for ZnPc). Therefore, all couplings (excluding H_2-OBPc) were computed using the same rigid molecular geometry, superposed on the original geometry with a root mean square distance minimization procedure using the *superpose* program included in Tinker 7.1.[173] In the LHCs the rigid geometry was obtained by optimizing the chromophore in vacuum at the LC-ωPBE/6-31G** level. For ZnPc, the experimental crystal structure[233] was used as the rigid geometry.

4.3.2 Excited states and couplings

The singlet excited states of all molecules and dimers were computed with TDDFT at the LC-ωPBE/6-31G** level of theory (3-21G for H_2-OBPc) using the NWChem 6.6

software.[180] The long-range corrected density functional LC-ωPBE,[177] with the parameter $\omega = 0.3\, a_0^{-1}$, was chosen as it was shown to correctly describe both localized and charge transfer excitations.[179] The effect of this choice was assessed by comparing the results with those obtained from two other range separated density functionals (LC-PBE and CAM-B3LYP) in a subset of dimers (*vide infra*). The Mulliken atomic transition charges (ATC) were computed as explained in section 3.2.1.

In most of the molecules considered, the lowest singlet excited states S_1 and S_2 were found to be relatively close in energy (ΔE_{12} = 0.5 eV in BChlA, 0.6 eV in ChlA, 0.8 eV in rhodopin, 0.02 eV in ZnPc and 0.03 eV in H_2-OBPc), while S_3 was found to be higher (ΔE_{23} = 0.6-1.5 eV). Considering that the laser pulses used to excite the system in pump-probe experiments usually have a duration of 10-50 fs,[234] resulting in an excitation bandwidth of 0.08-0.4 eV, it seems likely that S_2 plays an important role in the ultrafast dynamics of the lowest excitons in these systems[235,236] and it may influence the coupling between S_1 states at close separations.[230] The importance of considering S_2 has been recognized for phthalocyanines[158] and porphyrins[237] although often only S_1 of BChlA is considered in studies of excitons in FMO[200] and LH2.[201] Therefore, with the exception of peridinin (where ΔE_{12} = 1.1 eV and ΔE_{23} = 0.3 eV), all intermolecular excitonic couplings J_{11}, J_{22}, J_{12} and J_{21} were considered.

The Coulombic couplings were evaluated from eq. (1.2) using the TDC obtained from the TDDFT calculation. In order to avoid discontinuities due to grid points at short distances, which may occur for interpenetrating transition densities, we introduced at each volume element a Gaussian distribution of the charge density as in eqs. 2 and 3 of ref.[238] We verified that the results were converged with respect to the chosen grid size of 0.2 Å. The dielectric effect of the different mediums (protein, molecular solid) was neglected by setting the relative permittivity (dielectric constant) to 1, as the aim was to compare the relative importance of short- and long-range interactions, rather than the effect of the environment on these. As suggested in the literature, the effect of the environment could be taken into account by scaling the Coulombic coupling by an effective screening factor[239–242] derived from explicit or approximate inclusion of the polarizability of the protein, or by the optical dielectric constant of the bulk material.[42] However, the dielectric is likely to play a more

complex role as it can also change the excitation energies and transition dipole moments.[243] The overall effect of the dielectric can be approximated as a simple scaling factor of the coupling in the 0.5-0.9 range[42,240,244] in the Coulombic regime and as a negligible or very small strengthening of the short range interactions.[50] Therefore, the dielectric is expected not to affect our qualitative conclusions and its inclusion is beyond the scope of this work.

The total excitonic couplings between the localized Frenkel excitons S_1 and S_2 were computed for each molecular pair (dimer) using the diabatization procedure described in section 1.2.1.1. In this chapter we are only interested in the intermolecular couplings J_{11}, J_{22}, J_{12} and J_{21} which mainly determine the properties of the aggregate. The mixing between S_1 and S_2 on the same molecule due to electrostatic perturbation effects, as shown in section 3.3.1, can determine small intramolecular couplings. Since this is an environmental effect, it is outside the scope of this work, so we consider the intramolecular couplings negligible due to orthogonality of the transition dipole moment vectors $\boldsymbol{\mu}_1$ and $\boldsymbol{\mu}_2$ in the chlorophylls and phthalocyanines.

4.4 Results

The importance of short range excitonic interactions was evaluated by comparing the Coulombic coupling and the total coupling for all molecular pairs at long and short intermolecular distance. It is customary to describe the total excitonic coupling $J^{TOT} = J^{C} + J^{short}$ as the sum of a Coulombic term, prevalent at intermediate to long distance, and a short range contribution.[170,196] The sign of the excitonic coupling is determined by the signs of the wavefunctions in the basis set used for the excited state energy calculations. Since the transition densities of the localized excitations are used both for computing J^{C} with eq. (1.2) and as the reference property in the diabatization (see section 1.2.1.1) for computing J^{TOT}, their signs are guaranteed to be consistent with each other. In order to have a consistent value of J^{short} and understand if it is strengthening or weakening J^{TOT} with respect to J^{C}, we arbitrarily choose the sign of the wavefunction which makes J^{C} positive and report J^{TOT} with a consistent sign, i.e. with the same sign of the wavefunction.

Before comparing the couplings computed with different methods, it is essential to quantify their associated uncertainties and inaccuracies, addressed in the next

section. Relative differences much smaller than these deviations will not form a good basis for quantitative predictions.

4.4.1 Systematic errors in the evaluation of the Coulombic coupling

In this section we discuss a number of systematic errors that can affect the evaluation of the Coulombic coupling and that, consequently, may influence the assessment of the importance of short range interactions. We start by reporting on the variability of the Coulombic excitonic couplings due to the use of different density functionals in all 36 BChlA dimers from FMO and in 20 ZnPc dimers (10 intra-column and 10 inter-column). We report deviations between the properties obtained from two other range-separated functionals (LC-PBE and CAM-B3LYP) with respect to the functional chosen for this work (LC-ωPBE). For the excited states of BChlA we found variations on the norms of the transition dipole moments, $|\boldsymbol{\mu}_1|$ and $|\boldsymbol{\mu}_2|$, of 0.80 % and −0.31 % (LC-PBE), 2.4 % and −3.6 % (CAM-B3LYP). For ZnPc we found smaller variations of −0.29 % and −0.25 % (LC-PBE), 0.019 % and 0.19 % (CAM-B3LYP). For the Coulombic couplings J^{C} (from TDCs) we found RMS deviations (normalized by $\left\langle J^{\mathrm{C}}_{\text{LC-}\omega\text{PBE}} \right\rangle$) of 6.4 % (LC-PBE) and 12 % (CAM-B3LYP) for BChlA, 2.2 % (LC-PBE) and 3.8 % (CAM-B3LYP) for ZnPc. These variations represent a first estimate of the uncertainty on J^{C} and will be taken into account when discussing the relative difference between J^{TOT} and J^{C}.

Next, it is necessary to evaluate the accuracy of computing J^{C} using approximate representations of the transition density (ATC and point dipole) compared with the full coupling computed from transition density cubes (TDC, (eq. (1.2)). A preliminary examination found that in the roughly disc-shaped chlorophylls and phthalocyanines, the ATC obtained from Mulliken population analysis overestimate by about 3% the value of $|\boldsymbol{\mu}|$ with respect to the evaluation from the full TDDFT wavefunction, while this error is, expectedly, lower than 0.5% when the transition density is described by a TDC. The error is even more striking in the carotenoids examined (rhodopin glucoside in LH2 and peridinin in PCP) where the ATCs overestimate $|\boldsymbol{\mu}|$ by up to 20% as they fail to capture the transition density in the regions further away from the atoms, an effect amplified by the elongated shape and the large basis set. The TDC are much more accurate, giving errors of 0.13% (rhodopin) and 0.05% (peridinin). When the ATC are rescaled to reproduce the TDDFT transition dipole moment, the

root mean square relative error between the Coulombic couplings obtained from ATC compared to TDCs is reduced from 69% to 10% for peridinin. ATC obtained by fitting to the electrostatic potential (TrEsp method,[230] not considered in this study) have also been shown to represent the transition density of chlorophylls with accuracy comparable to TDC.[245] In summary, we observe that in some cases, such as elongated molecules, the Mulliken ATC do not describe the transition density with sufficient accuracy. Therefore, for the purpose of evaluating the short range contributions with high accuracy, the Coulombic couplings J^{C} are computed from TDC using eq. (1.2) in the remainder of this chapter.

The behaviour of the different methods in the intermediate to long range was then investigated by building a symmetric model dimer of two BChlA molecules arranged face-to-face (with an inversion point) and computing the couplings as a function of the distance between the centres of mass in the range 6-50 Å, measured along the vector normal to the molecular plane. First, we assessed the difference between the couplings computed using the dipole-dipole approximation and TDC by computing $J^{\mathrm{C}}_{\text{dip-dip}} \big/ J^{\mathrm{C}}_{\mathrm{TDC}}$ as a function of distance and fitting the data with the following polynomial function of the distance d obtained from the ratio between dipole-dipole and multipole (up to hexadecapoles) interaction:

$$\frac{U_{\text{dip-dip}}}{U_{\text{multipole}}}(d) = \left(1 + c_1 \cdot d^{-1} + c_2 \cdot d^{-2} + c_3 \cdot d^{-3} + c_4 \cdot d^{-4} + c_5 \cdot d^{-5} + c_6 \cdot d^{-6}\right)^{-1}. \tag{4.1}$$

The results, reported in the top panel of Figure 4.2, show that the multipole (higher than dipole) terms, captured by the TDC, make up a large fraction (67% at 6 Å and 6% at 50 Å for J_{11}) of the electrostatic interactions between the transition densities in the intermediate to long distance range, calling into question the validity of the point dipole approximation for an accurate evaluation of the Coulombic couplings in LHCs. $J^{\mathrm{C}}_{\text{dip-dip}}$ converges to within 4% of $J^{\mathrm{C}}_{\mathrm{TDC}}$ at 100 Å, while at larger distance the two methods diverge since the summation in eq. (1.2) over a large number of grid points of the TDC becomes more prone to accumulation of numerical errors.

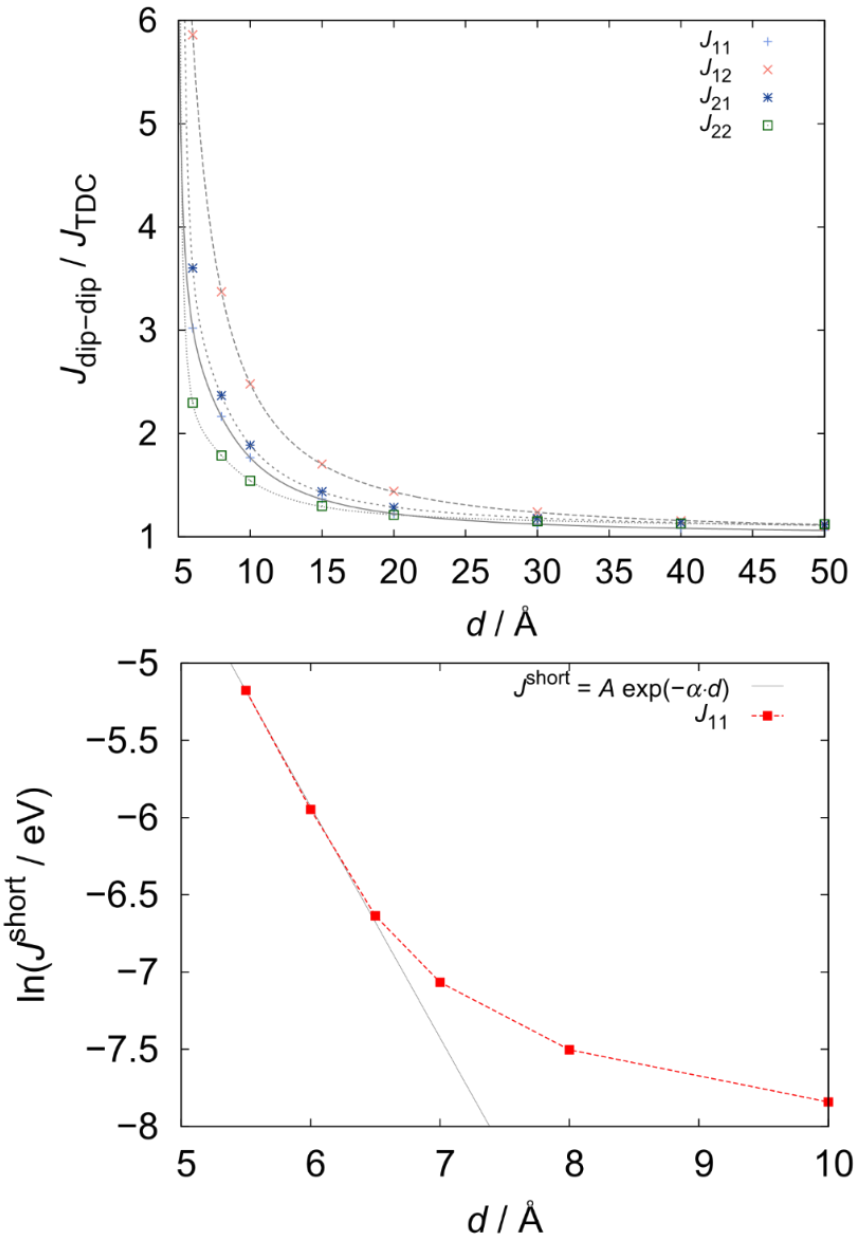

Figure 4.2. (Top) Ratio between dipole-dipole[37] and TDC (eq. (1.2)) Coulombic couplings as a function of distance. The grey lines are obtained from fitting the data points with eq. (4.1). (Bottom) Distance dependence of the short-range component. The solid line is obtained by fitting the data to the equation shown in the figure between 5.5 and 6.5 Å. The fitting parameters are A = 21.4 eV and α = 1.50.

Finally, using the same symmetric model system we assessed the relative accuracy of the Coulombic coupling J^{C} (eq. (1.2)) by comparing it to the total coupling J^{TOT} obtained from the diabatization procedure. At short distance, the short range component $J^{short} = J^{TOT} - J^{C}$ follows an overlap-dependent exponential attenuation as shown in the bottom panel of Figure 4.2, in agreement with ref. [44]. At long distance, although the interaction is expected to be purely Coulombic, we found a residual deviation between J^{TOT} and J^{C} (3 % for J_{11}, 13 % for J_{22}, 11 % for $J_{12} = J_{21}$), which is

nearly constant between 20 and 50 Å. The discrepancy can be attributed to an intrinsic difference between the two approaches. The coupling J^{C} is computed perturbatively between two reference unperturbed wavefunctions, while J^{TOT} is extracted from the variational solution of the dimer, which includes the relaxation of the orbitals and all the excited state CI coefficients. For this reason, and considering the uncertainty on J^{C} due to the DFT functional, the discrepancy between J^{TOT} and J^{C} can be interpreted more safely as a short-range interaction only when it exceeds 10-15 %.

4.4.2 Short range interactions in light-harvesting complexes

The spatial arrangements of the chromophores are more heterogeneous in LHCs than in molecular materials (see Figure 4.1), with a few closely spaced chromophore pairs interacting much more strongly than the others. In Figure 4.3 we compare J^{TOT} and J^{C} separately for the three light-harvesting complexes. Different symbols are used for different pairs of identical chromophores. We have separated the data of short distance chromophore pairs (i.e. those within a minimum intermolecular distance D = 7 Å) from the more distant ones.

For pairs not in close contact (D > 7 Å), we observe that the couplings are in general smaller than 10 meV, showing root mean square deviation (RMSD) between J^{C} and $|J^{TOT}|$ smaller than 1 meV, and RMS relative error of ~12 %. In other words, in pairs separated by long distances the deviations do not significantly exceed the uncertainty attributable to different computational methods and the excitonic couplings are described reasonably well by the Coulombic interaction.

Conversely, the chromophore pairs with short distance contacts (D < 7 Å) have significantly larger RMSD (by one order of magnitude), and in a few pairs the short-range components represent a substantial fraction of the total coupling. The couplings with the largest short-range contributions are reported in Table 4.1. These chromophore pairs are strongly coupled due to significant intermolecular overlap, such as the neighbouring BChlA in the B850 ring of LH2, a few BChlA pairs in FMO and peridinin pairs in PCP (see also Figure 4.1). The values of J^{TOT} and J^{short} for dimers A and B in LH2 obtained by Scholes and co-workers [214] are reported in Table 4.1 for comparison. The differences are mainly due to the well-known overestimation of $|\boldsymbol{\mu}|$ by the CIS method (see [214] and references therein), which results in a factor of ~2 overestimation of the splitting between the two lowest excited states in the dimer compared to our TDDFT calculation. The resulting J^{TOT} and J^{C}

couplings obtained by Scholes et al. are therefore overestimated by a factor of ~2, but the short-range component is found to be of similar relative importance.

It is also worth noting that in FMO and LH2 some of the strongest short-range interactions are those which enhance the otherwise rather weak J_{22}, J_{12} and J_{21} Coulombic couplings. If one limits the analysis to the J_{11} couplings,[200,201] the Coulombic interaction may offer a sufficiently accurate description of the excitonic couplings, but this is not necessarily the case if the couplings involving S_2 have to be included in the exciton dynamics, as discussed in section 4.3.2. Finally, it was verified that including S_2 of BChlA in the diabatization procedure does not significantly affect the J_{11} couplings: the RMSD between the J_{11} couplings obtained without and with S_2 was found to be 0.056 meV in FMO and 0.010 meV in LH2.

These results have two major implications to consider when studying the excitonic properties of LHCs. First, short range effects need to be included when studying their exciton dynamics, since the properties of the excitonic Hamiltonian are determined by the strongest couplings between closely spaced chromophores rather than by the average couplings. Moreover, including the second excited state and computing the cross-couplings may be crucial for a complete and accurate description of these systems.

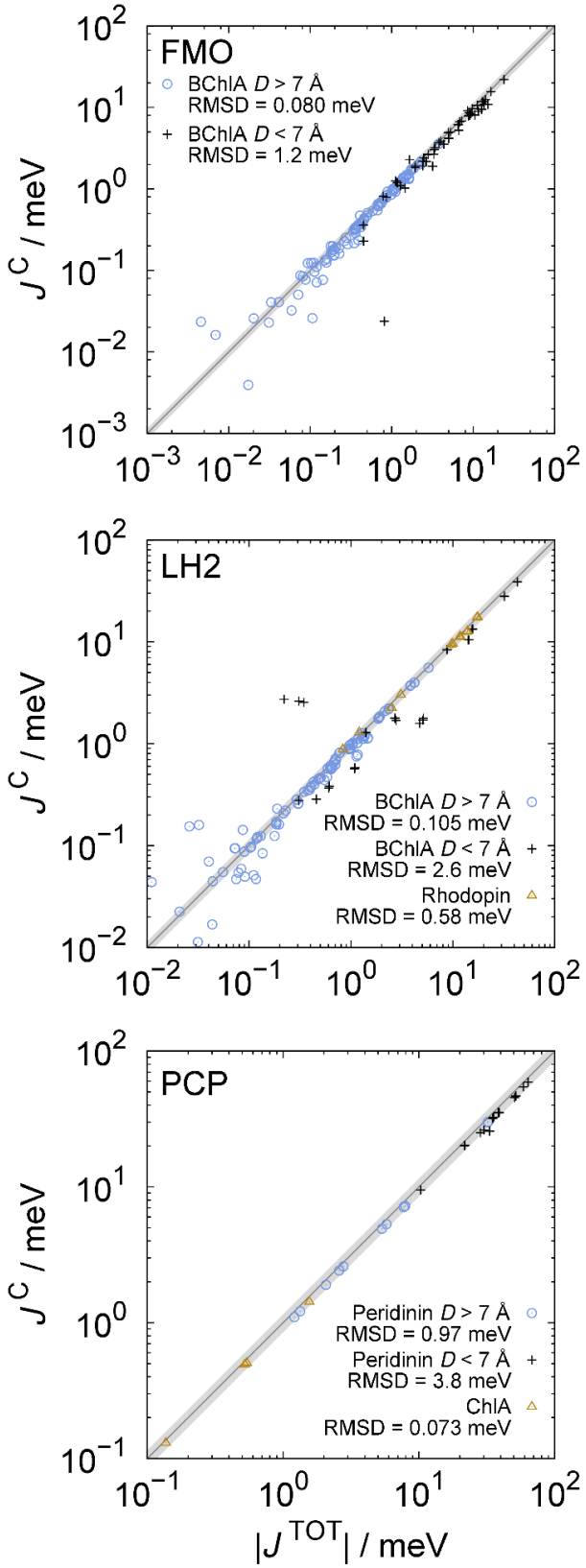

Figure 4.3. Coulombic couplings (from TDCs) plotted against total excitonic couplings between chromophore pairs in LHCs. The shaded area corresponds to a ± 15% deviation from the $J^{C} = |J^{TOT}|$ line.

Table 4.1. Couplings with the largest short-range contributions J^{short} for each of the LHCs. All couplings are in meV. In LH2 each value is averaged over all equivalent pairs (three of type A and two of type B in the B850 ring as indicated in Figure 4.1).

System	Pair	D / Å	Coupled states	J^{TOT}	$J^{short}\left(\frac{J^{short}}{J^{TOT}}\right)$
FMO	1-2	2.26	1,2	15.2	4.29 (28%)
	5-6	2.61	1,2	12.6	3.19 (25%)
	5-6	2.61	2,1	13.6	2.61 (19%)
	4-7	2.58	1,2	11.5	2.59 (22%)
	3-7	2.18	1,2	10.5	2.41 (23%)
LH2	A[a]	-	1,1	90.5	6.8 (7.5%)
	B[a]	-	1,1	68.2	7.4 (11%)
	A	1.90	1,1	42.9	4.31 (10%)
	B	1.71	1,1	32.0	4.12 (13%)
	A	1.90	2,2	14.3	3.82 (27%)
	A	1.90	1,2	4.98	3.30 (66%)
	B	1.71	2,2	15.5	2.24 (14%)
PCP	4-7	0.98	1,1	33.1	7.41 (22%)
	1-3	2.53	1,1	50.7	5.16 (10%)
	7-8	2.65	1,1	51.8	5.08 (10%)
	2-4	2.40	1,1	63.6	4.50 (7.1%)
	5-6	2.98	1,1	58.7	4.24(7.2%)

[a] Results from ref. [214].

4.4.3 Short range interactions in molecular semiconductors

We will now examine the role short range interactions in the molecular solids considered. In the disordered ZnPc model we consider separately a set of 10 inter-column dimers and 90 intra-column dimers (first neighbours), reported in the top and bottom panels of Figure 4.4 respectively.

The interactions between molecules in adjacent columns in ZnPc are characterized by moderate couplings in the 1-30 meV range and small short-range contributions are easily rationalized in terms of very small intermolecular overlap. This results in a small systematic shift corresponding to a relative short-range contribution $J^{short} / J^{TOT} = 7.5$ % as quantified by a linear fit to the data (see top panel of Figure 4.4). As this does not significantly exceed the deviation due to the methods, we conclude that for inter-column dimers J^{C} is a good approximation of J^{TOT}.

On the other hand, in the intra-column dimers, where there is significant orbital overlap between molecules, the excitonic couplings are dominated by the short-range interactions J^{short}, which are found to be very large: up to 195 meV (66% of J^{TOT}). The set of couplings in this disordered sample has very peculiar characteristics, as is

evident in the bottom panel of Figure 4.4. For J^{C} smaller than 70 meV, occurring when the transition dipoles are not well-aligned, the sign of J^{short} is not correlated with J^{C}, i.e. the short-range effects can either enhance or diminish $|J^{TOT}|$ with respect to J^{C}. Surprisingly, when J^{C} is larger than 70 meV J^{short} always has the same sign as J^{C}, resulting in J^{TOT} always being stronger than J^{C}. In the range of couplings found in this system, where the strongest J^{C} are around 100 meV but J^{TOT} can be as high as 290 meV. A correct consideration of the short range interactions may make the difference between incoherent (or intermediate) and coherent exciton transport regime since the reorganization energy of ZnPc is ~40 meV.[160]

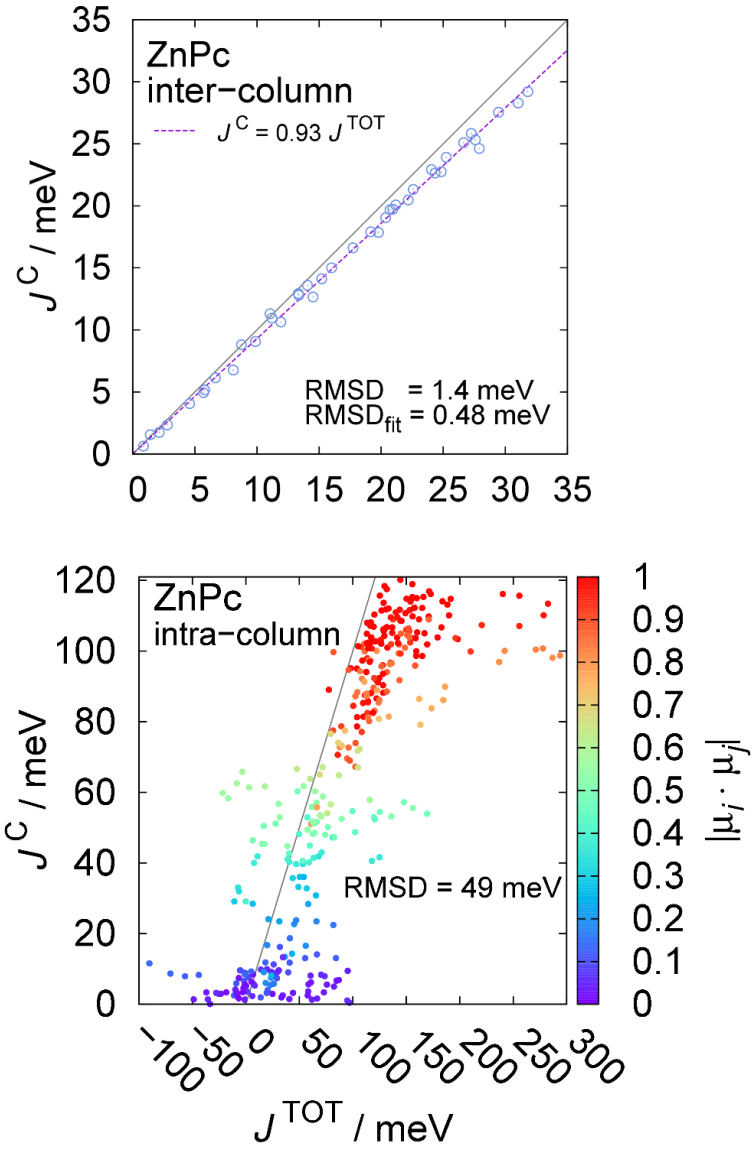

Figure 4.4. Coulombic couplings (from TDCs) plotted against total excitonic couplings in disordered ZnPc. (Top) The dashed line is a linear fit to the data points. (Bottom) Data from neighbouring intra-column dimers. The colour of the data points is proportional to the absolute value of the dot product between the transition dipole moments of the localized excitations.

Further insight into the role of short-range interactions is given by examining the couplings between neighbouring molecules in the H_2-OBPc crystal subject to thermal fluctuations. The spectroscopy and exciton dynamics of this system are mainly determined by the couplings in the intra-column dimers A and B.[163] The very short π-π intermolecular distances in the 3.5-4.5 Å range (see Figure 4.1) make these couplings very sensitive to thermal fluctuations. The values of J^C and J^{TOT} for 250 MD snapshots are shown in Figure 4.5. We first note that the short-range contributions J^{short} can make up a significant fraction (up to 60%) of J^{TOT}, and in this

case can also influence the regime of exciton transport since the reorganization energy was found to be of the same order of magnitude (~100 meV, see section 3.3.3). Furthermore, for all couplings the distributions of J^{TOT} are significantly wider than those of J^{C}, confirming the primary role of short-range effects in determining the thermal fluctuations of the couplings and consequently their influence on exciton dynamics. Finally, as is evident from Figure 4.5, the short-range component in dimer A tends to have the same sign as the Coulombic coupling, while in dimer B there appears to be no correlation at all. This striking difference between the apparently similar dimers A and B can be intuitively rationalized in terms of overlap: dimer A has a prevalently face-to-face arrangement with overlap extending over more than half of the molecular surface, while dimer B has a head-to-tail character with only one of the isoindole units overlapping (see right panel of Figure 4.5). In general, one would not expect to observe such strong correlation between the signs of Coulombic and short range interactions.[196] However, in some specific cases with large intermolecular overlap, such as dimer A of H_2-OBPc or the most strongly coupled intra-column dimers of ZnPc, the short range interaction can be strongly correlated with the Coulombic interaction, systematically reinforcing it when it is already strong. Conversely when the overlap is smaller, e.g. in head-to-tail configurations such as dimer B of H_2-OBPc, the short-range component can still be large in magnitude but the sign is not necessarily correlated with that of the Coulombic interaction. It should be noted that a similar correlation was reported for the naphthalene dimer by Scholes and Ghiggino.[44] Since this correlation effect depends on the specific wavefunctions and packing geometry of a given system, its occurrence may be difficult to predict without actually computing the couplings. In summary, we found that in some molecular dimers with favourable intermolecular geometry and large overlap the short-range effects may tend to enhance rather than being uncorrelated with the Coulombic interaction, resulting in stronger excitonic couplings.

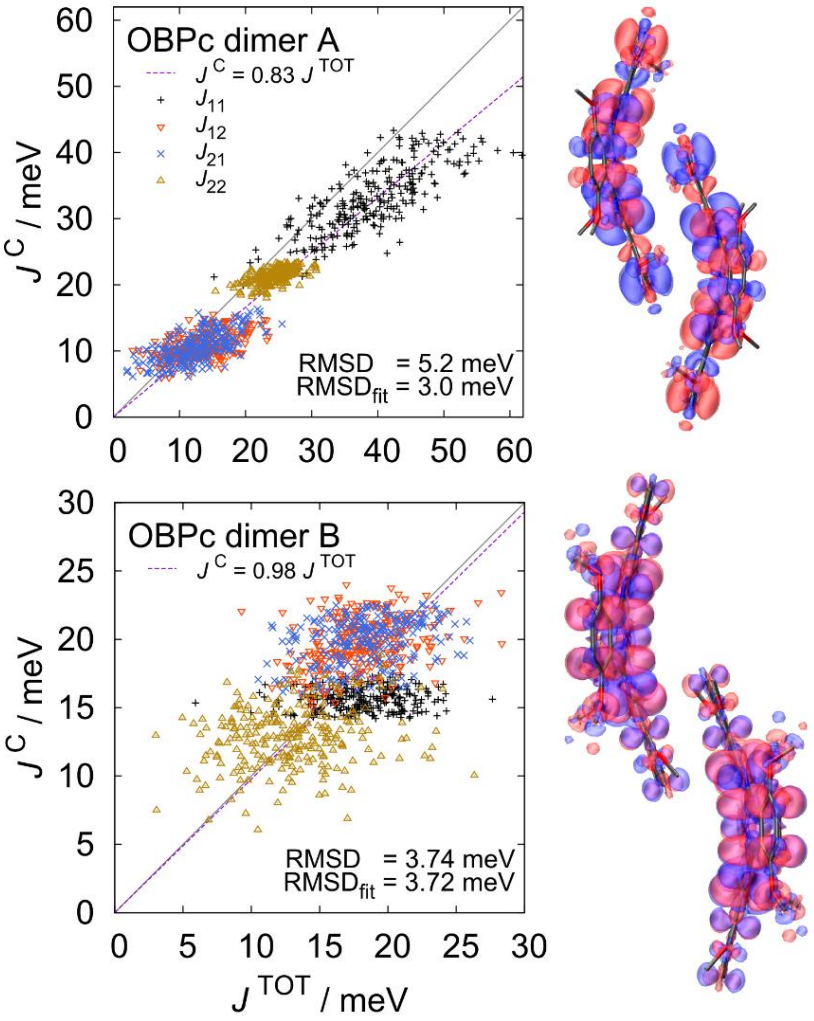

Figure 4.5. (Left) Coulombic couplings (from TDCs) plotted against the total excitonic couplings in two dimers of the H_2-OBPc molecular crystal, computed along a MD simulation (250 snapshots every 50 fs) described in section 3.2.2. The dashed lines are linear fits to the data points. (Right) Transition density plots (generated with VMD[227]) of the S_1 excited state localized on the molecules in the two dimers at the crystal geometry.

4.5 Conclusions

The importance of short range effects on excitonic couplings between chromophores in three natural light-harvesting complexes and two organic semiconductors has been investigated, comparing the total excitonic coupling (computed via a diabatization scheme) and the Coulombic component (using a fine grid representation of the transition density). For molecules not in close contact, as expected, the Coulombic coupling is comparable to the coupling obtained by diabatization. The discrepancies are typically of around 10 %, i.e. below what can be considered important for the description of excitonic physics also considering the variability among computational methods.

When the interacting molecules are in close contact, the stronger couplings can be significantly affected by short range effects. Among the natural LHCs studied, only few pairs of chromophores are strongly coupled. In FMO, the most strongly coupled dimers have short range components up to 4 meV (28 % of the total coupling). The neighbouring BChlA chromophores in the B850 ring of LH2 also exhibit significant short-range interactions of up to ~4 meV and up to 66 % of the total coupling (~3 meV out of ~5 meV). In PCP, only two of the peridinin dimers have moderate short-range components of 7 and 5 meV (22 % and 10 % of the total coupling). Although in general the couplings between chromophores are well described by the Coulombic interaction, the excitonic properties of the aggregates are expected to be dominated by the strongest couplings, i.e. those between neighbouring chromophores which require the evaluation of short range contributions.

In molecular solids, the excitonic coupling in closely packed face-to-face dimers is dominated by short range interactions which are found to be very large: up to 200 meV (70% of the total coupling). For the particular materials considered in this work we found that when the Coulombic coupling is stronger than 70 meV, the short-range component always has the same sign as the Coulombic coupling, making the total coupling even stronger when it is already large. This effect of reinforcement, which is found to be present in face-to-face but not in head-to-tail dimers, is potentially very important for the mechanism of exciton diffusion as stronger coupling favours more coherent dynamics as discussed in section 1.2.2.

5. A general model for charge transport in disordered semiconducting polymers*

Summary: Modelling charge transport in disordered semiconducting polymers is a challenging task. On the one hand, charge transport models rooted in solid state physics, some of which are summarised in section 1.3, provide a simple and reliable description of the dependence of mobility on temperature, electric field and charge density, in agreement with experimental observations. The parameters entering these models (shape of the DOS, localization, hopping rates) are obtained by fitting to observables but their significance cannot be directly linked to the microstructure of the polymer. On the other hand, atomistic simulations offer a much more detailed picture of the electronic structure (variable localization, see section 1.3) which contrasts with the assumptions made by simplified models about the localization of the states. In this chapter, we will describe a very general theoretical model for describing charge transport along a single polymer chain, starting from the minimum possible number of assumptions about electronic structure. Such a general model will depend on a large number of parameters, reflecting the wide variety of chemistries and morphologies in this class of materials. These parameters will be given arbitrary but realistic values in order to understand how they affect mobility, but in principle they could be obtained from atomistic simulations to predict the mobility of a specific polymer. After the description of the model, given in section 5.1, we will show in section 5.2.1 that it can describe a detailed and realistic electronic structure. In section 5.2.2 we will discuss the dependence of mobility on electric field, disorder and charge density, and compare the results to existing analytical models. Finally, in section 1.1.1 we will analyse how the complicated electronic structure of a donor-acceptor alternating copolymer can affect the charge transport properties. In chapter 6 we will explore the parameter space of this model (using the more general rate derived in chapter 2) to find out which parameters affect the temperature dependence of mobility in this vast class of materials. The role of inter-chain hopping has been shown to be irrelevant in the case of very rigid (straight) polymer chains,[246] so our single chain model is appropriate to describe transport in this limit. A further generalisation of this

* The content of this chapter is published in R. P. Fornari and A. Troisi, *Phys. Chem. Chem. Phys.*, 2014, **16**, 9997–10007 and R. P. Fornari and A. Troisi, *Adv. Mater.*, 2014, **26**, 7627–7631.

model, where we consider a 3D structure of the chains and take inter-chain transport into account, is presented in chapter 7.

5.1 Methodology

5.1.1 Electronic structure from a disordered tight binding Hamiltonian

Polymers are composed of very long molecules made of relatively rigid monomers (e.g. the thiophene ring in P3HT), which constitute the fundamental units (*sites*) of our model. To simplify the electronic structure, we consider for each site *n* one electronic state $|n\rangle$ which represents the frontier orbital relevant to charge transport (HOMO or LUMO for hole and electron transport respectively). The electronic Hamiltonian for a single chain of *N* sites is

$$H^{\mathrm{el}} = \sum_{n}^{N} \alpha_n |n\rangle\langle n| + \sum_{n}^{N-1} \beta_n |n\rangle\langle n+1| + \beta_N |N\rangle\langle 1| + \ h.c. \tag{5.1}$$

where α_n is the energy of state $|n\rangle$ and β_n is the electronic coupling between neighbouring sites. The third term, connecting the last and first sites, introduces a periodic boundary condition (PBC), useful to avoid finite size effects in the case of a one-dimensional (1D) chain. α_n and β_n are random variables normally distributed around the mean values α_0 and β_0 with standard deviations σ_α and σ_β, which are the parameters controlling diagonal and off-diagonal disorder respectively. α_0 can be set to 0 eV (determining the origin of the energy scale) or it can have different values in even and odd monomers to mimic a donor-acceptor structure (see section 1.1.1).

This model represents a polymer chain in a frozen configuration, and the main source of static off-diagonal disorder is the distribution of the couplings β_n depending on the dihedral angles between neighbouring monomers.[85,110,122] It is important to define more rigorously what we mean by static and dynamic disorder and whether it is generally possible to separate them. As we are mainly interested in the dynamics of the charge carrier, a component of the disorder can be considered static if it evolves on timescales much longer than the charge carrier dynamics. We will see that the hopping rates that contribute to transport are of the order of 10^9-10^{11} s^{-1} and so we can deem as "static" all disorder that evolves on a timescale slower that 10 ns. The large conformational changes of the polymer (those that cause for example changes in the

overall polymer shape in bulk) are known to be much slower and can be considered static. In fact, calculations of the molecular orbitals of amorphous polymers repeated along a molecular dynamics trajectory show that they maintain the same shape and localization for hundreds of nanoseconds.[110] Conversely, essentially all oscillations of the polymer chain around its equilibrium position are faster than the charge carrier dynamics (~10^{11} s^{-1} correspond to a vibrational frequency of 3 cm^{-1}). Thus, for the specific problem of charge transport in amorphous polymers, the separation between static and dynamic disorder is relatively uncontroversial.

From the diagonalization of H^{el} we obtain *N* one-electron states (eigenstates) with energies E_i and wavefunctions $|\psi_i\rangle = \sum_n c_{ni}|n\rangle$ (E_i are the eigenvalues and c_{ni} are the eigenvectors of H^{el}). The mean position of the charge in each state (centroid) is computed as $\langle r_i \rangle = \sum_n c_{ni}^2 r_n$, where r_n is the position of monomer *n*.

Starting from a few realistic parameters (energies, couplings, and disorder), this model Hamiltonian naturally provides a detailed energy landscape of electronic states localized by static disorder and a realistic DOS (see Figure 5.1 and Figure 5.2). Charge transport along the chain is then described as a series of hopping events between these electronic states, with hopping rates discussed in the next section.

5.1.2 Polaronic effects

Before moving on, it is necessary to discuss the role of polaronic effects, i.e. the self-localization of the charge due to local electron-phonon coupling, distinct from the localization due to static disorder. For polymeric chains, there is some consensus that the localization is largely induced by the structural disorder and not by the formation of small polarons.[94,96–98,247] Experimentally, whenever is it possible to control the disorder of the polymer it was shown that electronic states are more localized when the disorder is increased, i.e. the localization is determined by the disorder, not by polaronic effects.[248] This is a consequence of a very large electronic coupling β_0 between monomers (of the order of ~1 eV) in comparison with the monomer's reorganization energy (typically lower than the inter-monomer electronic coupling), a characteristic shared by all high mobility polymeric semiconductors.

To quantify the reorganization energy for the electron transfer, we need to add to the Hamiltonian in (5.1) two more terms: H^{nucl} describing the nuclear motion and

the local electron-phonon coupling $V^{\text{el-nucl}}$. The third additional term $V^{\text{el}}(t)$ is the time-dependent electronic coupling which will be discussed in the next section.

$$\begin{aligned} H &= H^{\text{el}} + H^{\text{nucl}} + V^{\text{el-nucl}} + V^{\text{el}}(t) \\ &= H^{\text{el}} + \sum_n^N \frac{p_n^2}{2m} + \frac{1}{2} m\omega^2 x_n{}^2 + \sum_n^N g x_n |n\rangle\langle n| + V^{\text{el}}(t) + h.c. \end{aligned} \tag{5.2}$$

The nuclear motions in H^{nucl} are described by harmonic oscillators of mass *m* and frequency ω, with x_n being a nuclear degree of freedom localized on site *n*. A linear Holstein-type electron-phonon coupling $V^{\text{el-nucl}}$ is assumed, with strength determined by the parameter *g*, and we can treat it as a perturbation since the reorganization energy is small compared to β_0. To the first order of perturbation theory each eigenstate $|\psi_i\rangle = \sum_n c_{ni}|n\rangle$ can be therefore used to compute the nuclear potential energy for that state:

$$U_i(x_n) = \sum_n^N \frac{1}{2} m\omega^2 x_n{}^2 + \sum_n^N g x_n c_{ni}^* c_{ni} \tag{5.3}$$

Each oscillator x_n, perturbed by the potential $\sum_n^N g x_n c_{ni}^* c_{ni}$, will have in state $|\psi_i\rangle$ the new equilibrium position $x_n^{\text{eq},i} = -\frac{g c_{ni}^* c_{ni}}{m\omega^2}$ and the equilibrium potential energy $-\frac{g^2 \left(c_{ni}^* c_{ni}\right)^2}{2m\omega^2}$. The reorganization energy[57] for the removal of an electron from state $|\psi_i\rangle$ is therefore

$$\lambda_i = \sum_n^N \frac{g^2 \left(c_{ni}^* c_{ni}\right)^2}{m\omega^2} = \frac{g^2}{m\omega^2} \sum_n^N |c_{ni}|^4 = \lambda_1 \sum_n^N |c_{ni}|^4 \tag{5.4}$$

In (5.4) we have defined $\lambda_1 = \frac{g^2}{m\omega^2}$ as the reorganization energy for a system containing only one monomer. $\sum_n^N |c_{ni}|^4$ is known as the *participation ratio* and its inverse expresses how many sites share the electron. $\sum_n^N |c_{ni}|^4$ is obviously unity if state *i* is fully localized on one site and 1/*N* if the state is fully delocalized on all sites (in such a case $|c_n| = 1/\sqrt{N}$). The relation above between λ and $\sum_n^N |c_{ni}|^4$ is the basis

for the common assumption $\lambda \approx \lambda_1 / N$ used for large conjugated systems.[134,182] The reorganization energy for a charge transfer, λ_{ij}, is the sum of the reorganization energy for removing a charge from state $|\psi_i\rangle$ and that for adding a charge in state $|\psi_j\rangle$. It can be expressed as:

$$\lambda_{ij} = \lambda_1 \sum_n |c_{ni}|^4 + |c_{nj}|^4 . \tag{5.5}$$

5.1.3 Hopping promoted by dynamic disorder

The time-dependent term in eq. (5.2), $V^{\mathrm{el}}(t) = \sum_n^N \gamma_n(t) |n\rangle\langle n+1| + h.c.$, couples the eigenstates $|\psi_i\rangle = \sum_n c_{ni} |n\rangle$ of the electronic Hamiltonian H^{el} (without it they would not be coupled as they are orthogonal). $\gamma_n(t)$ is the thermal fluctuation of the coupling between neighbouring monomers and is due to oscillations (assuming one effective nuclear mode) around the equilibrium position, so it is null on average, $\langle \gamma_n(t) \rangle = 0$, but not its square, $M^2 = \langle \gamma_n(t)^2 \rangle$, where the amplitude of the fluctuation M is the parameter determining the strength of the non-local electron-phonon coupling (dynamic disorder). As long as $M \ll \sigma_\beta$, as expected in the most common polymers, the states can be considered to be localized almost exclusively by static disorder.[96,249] This non-local coupling induced by vibrations was discussed in detail in section 2.2.2. Here we introduce the dependence of the coupling on the overlap between eigenstates.

The coupling between any two eigenstates $|\psi_i\rangle$ and $|\psi_j\rangle$ due to dynamic disorder can be written as:

$$\begin{aligned} V_{ij}(t) &= \langle \psi_i | V^{\mathrm{el}}(t) | \psi_j \rangle = \sum_{nn'} c_{n,i} c_{n',j} \langle n | \hat{V}(t) | n' \rangle \\ &= \sum_n c_{n,i} c_{n+1,j} \gamma_n(t) + c_{n,i} c_{n-1,j} \gamma_{n-1}(t) \end{aligned} \tag{5.6}$$

The average coupling between these states, $\langle V_{ij}(t) \rangle$, is null because $\langle \gamma_n(t) \rangle = 0$. The average of the squared coupling can be evaluated as:

$$V_{ij}^{\ 2}(t) = \sum_n \left(c_{n.i}c_{n+1,j}\right)^2 \gamma_n^2(t) + \left(c_{n.i}c_{n-1,j}\right)^2 \gamma_{n-1}^2(t) + 2\left(c_{n.i}c_{n+1,j}\right)\left(c_{n.i}c_{n-1,j}\right)\gamma_n(t)\gamma_{n-1}(t) \tag{5.7}$$

$$\begin{aligned}\left\langle V_{ij}^{\ 2}\right\rangle &= \sum_n \left(c_{n.i}c_{n+1,j}\right)^2 \left\langle \gamma_n^2(t)\right\rangle + \left(c_{n.i}c_{n-1,j}\right)^2 \left\langle \gamma_{n-1}^2(t)\right\rangle \\ &\quad + 2\left(c_{n.i}c_{n+1,j}\right)\left(c_{n.i}c_{n-1,j}\right)\left\langle \gamma_n(t)\gamma_{n-1}(t)\right\rangle \\ &= \sum_n \left(c_{n.i}c_{n+1,j}\right)^2 \left\langle \gamma_n^2(t)\right\rangle + \left(c_{n.i}c_{n-1,j}\right)^2 \left\langle \gamma_{n-1}^2(t)\right\rangle \\ &= M^2 \sum_n \left(c_{n.i}c_{n+1,j}\right)^2 + \left(c_{n.i}c_{n-1,j}\right)^2 \\ &\approx M^2 \sum_n \left(c_{ni}c_{nj}\right)^2 = M^2 S_{ij}^2\end{aligned} \tag{5.8}$$

where we have used the further assumption that the coupling fluctuations are uncorrelated, i.e. $\left\langle \gamma_n(t)\gamma_{n-1}(t)\right\rangle = \left\langle \gamma_n(t)\right\rangle\left\langle \gamma_{n-1}(t)\right\rangle = 0$, and we have simplified the expression of the overlap. The expression in (5.8) contains the dependence of the coupling on the overlap S_{ij}^2 between the wavefunctions, and consequently on the distance between them. $\left\langle V_{ij}^{\ 2}\right\rangle$ is vanishingly small if states $\left|\psi_i\right\rangle$ and $\left|\psi_j\right\rangle$ are located in different regions of the polymer. When these states are located in the same region, $\left\langle V_{ij}^{\ 2}\right\rangle$ is still smaller than M^2.

The hopping rate is given by a combination of eqs. (2.38) and (2.5):

$$k_{ij} = \frac{2\pi}{\hbar} M^2 S_{ij}^2 \sqrt{\frac{1}{4\pi\lambda_{ij}k_B T}} \exp\left[-\frac{(\Delta E_{ij} + \lambda_{ij})^2}{4\lambda_{ij}k_B T}\right], \tag{5.9}$$

i.e. we are assuming that all accepting modes can be treated classically and that there is only one effective inducing mode also treated classically. A more general hopping rate, presented in chapter 2, is not considered here to keep the number of parameters limited, since the main focus of this chapter is the role of the electronic structure. In chapter 6 we will present results obtained from this model with the more general hopping rate. The limits of validity of the non-adiabatic hopping mechanism are discussed in section 5.2.3.

5.1.4 Parameters of the model

The main parameter investigated here is the static disorder of the polymer chain. For β_0 =1 eV (a typical coupling between chemically connected small monomers[103]),

σ_β=0.1 eV reproduces the typical Gaussian tail of density of state at the band edge that is found by fitting phenomenological models.[109] The effect of disorder is explored by changing σ_β between 0 and 0.2 eV. It should be kept in mind that, as the disorder becomes negligible, the Hamiltonian becomes closer to that of a simple 1D semiconductor with large polaron states, where the transport cannot be described by hopping but by one of the polaronic theories more appropriate for ordered polymeric chains, where different models should be adopted.[250] It is therefore expected that the methodology proposed here will break down at sufficiently small disorder as discussed below in section 5.2.3.

The reorganization energy for a single monomer is set to λ_1 = 0.45 β_0 = 0.45 eV on the basis of various available electronic structure calculations.[141,251] The distance between monomers, needed to make a connection with charge mobility, is set to d = 1 nm, i.e. of the order of magnitude of the distance between the centres of the monomers (e.g. this distance is 0.6 nm in PPV). This parameter is chosen to simplify the presentation of the results and it is not very crucial as the physical charge mobility scales simply as ~ d^2. The fluctuation of the coupling, parametrized by the variable M, was set to 0.005 β_0 estimated assuming that the fluctuation of the inter-monomer coupling is determined by the fluctuation of the dihedral angle between monomers (found to be ~15° in a recent simulation of PPV [110]). As long as M is substantially smaller than β_0, it does not play an important role on the results because M^2 appears as a pre-factor in the hopping rate eq. (5.9).

For most calculations we considered a chain of 1024 monomers with periodic boundary conditions unless indicated otherwise and many realizations of the disorder Hamiltonian have been averaged until the results converged.

In this phenomenological study the parameters are close to the typical parameters encountered in polymeric semiconductors but no specific chemical system is considered. The model is realistic in the sense that it can be generalized easily to incorporate the details encountered in realistic polymers. For example, it is possible to introduce alternating different monomers in the chain (with different on-site energy, coupling, fluctuation and reorganization energy), as shown in section 1.1.1, and one can introduce the effect of static disorder on the on-site energy if needed. However,

to keep the number of parameters under control these generalizations are not introduced here.

5.1.5 Evaluation of 1D drift mobility

The mobility of a single polymer chain is not generally observable as the experimental mobility always includes (and sometimes is dominated by) the transport across chains. On the other hand, such quantity can be evaluated theoretically and can be useful to quantify, within a single parameter, the efficiency of transport along a given chain. More importantly, several analytical and numerical models of charge transport along a 1D disordered chain exist [108] and it can be useful to compare our results, obtained from a model Hamiltonian, with the results obtained by one of these analytical models for 1D transport.[252]

All analytical models assume that the electrostatic potential varies linearly along the chain, i.e. the energy difference ΔE_{ij} appearing in the expression of the rate is modified in the presence of an applied external electric field *F* along the chain as

$$\Delta E_{ij}(F) = \Delta E_{ij}(0) - eR_{ij}F, \tag{5.10}$$

where *e* is the elementary charge and R_{ij} is the vector connecting the centroids of the initial and final state. The sign implies that we are considering negatively charged carriers which occupy the low energy edge of the band. To compute R_{ij} we assume that the monomer orbitals $\{|n\rangle\}$ are centred in position $d \cdot n$ along the direction along which the field *F* is applied. This is an excellent approximation for semi-crystalline polymers as P3HT, whose monomers are aligned for very long distances. A generalisation of the model, incorporating a 3D description of the polymer shape in relation with the applied field, is presented in chapter 7.

The kinetics of the incoherent charge hopping can be described by a standard master equation where p_i is the occupation probability (population) of eigenstate *i*:

$$\frac{dp_i}{dt} = -\sum_{j \neq i} \left[k_{ij} p_i (1 - p_j) - k_{ji} p_j (1 - p_i) \right]. \tag{5.11}$$

For sufficiently low total charge $n = \sum_i p_i$ the Coulombic repulsion between carriers can be neglected and one can seek a mean field steady state solution by setting $dp_i / dt = 0$ and obtaining the set of equations:

$$0 = \sum_{j \neq i} \left[k_{ij} p_i (1 - p_j) - k_{ji} p_j (1 - p_i) \right]. \tag{5.12}$$

This set can be solved iteratively from the following cyclic expression derived from eq. (5.12)

$$p_i = \frac{\sum_{j \neq i} k_{ji} p_j}{\sum_{j \neq i} \left[k_{ij} (1 - p_j) + k_{ji} p_j \right]}, \tag{5.13}$$

where the prescriptions of ref. [253] were used for the practical implementation of this formula.

In the limit of only one charge carrier present in the system, the master equation in (5.11) becomes simply

$$\frac{d}{dt} p_i = -\left(\sum_{j \neq i} k_{ij} \right) p_i + \sum_{j \neq i} k_{ji} p_j, \tag{5.14}$$

or in matrix form

$$\frac{d}{dt} \mathbf{p} = \mathbf{K} \mathbf{p}, \tag{5.15}$$

where $\mathbf{p} = \{p_i\}$ is the column vector of the populations and $\mathbf{K}$ is a matrix whose diagonal and off-diagonal elements are:

$$K_{ii} = -\left(\sum_{j \neq i} k_{ij} \right); \quad K_{ij} = k_{ji}. \tag{5.16}$$

The solutions of eq. (5.15) are given by

$$\mathbf{p} = e^{\mathbf{K}t} \mathbf{p}_0. \tag{5.17}$$

At the steady state, the populations do not change in time, i.e. $d\mathbf{p} / dt = \mathbf{K}\mathbf{p} = 0$. We are looking for the non-trivial solution $\mathbf{p}$, which is the eigenvector of the matrix $\mathbf{K}$ with null eigenvalue. To find it, we set the first element of $\mathbf{p}$ to an arbitrary value, e.g. $p_1 = 1$, and find the solution of the system of N-1 equations. The whole system of N equations can be written as

$$\mathbf{K}\mathbf{p} = \begin{bmatrix} K_{11} & \mathbf{k}^T \\ \mathbf{k} & \mathbf{K}_{N-1} \end{bmatrix} \begin{bmatrix} 1 \\ \mathbf{p}_{N-1} \end{bmatrix} = \begin{bmatrix} 0 \\ \mathbf{0} \end{bmatrix}, \tag{5.18}$$

where $\mathbf{k}$ ($\mathbf{k}^T$) is the first column (row) of $\mathbf{K}$ without the first element, $\mathbf{K}_{N-1}$ is the matrix $\mathbf{K}$ without the first column and the first row, and $\mathbf{p}_{N-1}$ is the eigenvector corresponding to the null eigenvalue, or the solution of the system of N-1 linear equations:

$$\mathbf{K}_{N-1} \mathbf{p}_{N-1} = -\mathbf{k}. \tag{5.19}$$

The vector $\mathbf{p} = \begin{bmatrix} 1 \\ \mathbf{p}_{N-1} \end{bmatrix}$ contains the (not normalized) steady state populations p_i of our system which are then normalized such that $\sum_i p_i = 1$. With this method, the steady state populations can be obtained analytically as the eigenvector corresponding to the null eigenvalue of the matrix of the rates.

The drift mobility is then computed as:

$$\mu = \frac{1}{n \cdot F} \sum_i \sum_j k_{ij} p_i (1 - p_j) R_{ij} \tag{5.20}$$

where F is the electric field, n is the number of charges, p_i are the steady state populations and R_{ij} is the distance between the centroids of the states i and j. The contribution of each pair of states to the total mobility is represented by the particle current $k_{ij} p_i (1 - p_j)$.

5.2 Results and discussion

5.2.1 Qualitative features of the model

Before considering the mobility results it is convenient to analyze the distribution and characteristics of the electronic states generated by the Hamiltonian in (5.1) with the choice of parameters we considered. Figure 5.1 reports the density of states (DOS), the localization length (LL) and the inverse participation ratio (IPR), all scaled by the number of monomers, for different amounts of off-diagonal disorder. The DOS is defined as usual in terms of the eigenvalues E_j of H^{el} and the Dirac delta function as:

$$\text{DOS}(E) = \sum_j \delta(E - E_j) \tag{5.21}$$

The localization length of an individual state is computed as

$$\begin{aligned} \text{LL}_j &= 2\left[\left\langle \psi_j \left| r^2 \right| \psi_j \right\rangle - \left\langle \psi_j \left| r \right| \psi_j \right\rangle^2 \right]^{1/2} \\ &= 2\left[\sum_n \left(r_n - \langle r \rangle_j \right)^2 c_{nj}^2 \right]^{1/2} \end{aligned} \tag{5.22}$$

and the energy-dependent localization length is defined as

$$\text{LL}(E) = \sum_j \text{LL}_j \delta(E - E_j) \Big/ \sum_j \delta(E - E_j) \tag{5.23}$$

The inverse participation ratio for an individual state is an alternative measure of localization and indicates the average number of monomers that share the orbital. It is defined as

$$\mathrm{IPR}_j = \left(\sum_n \left| c_{nj} \right|^4 \right)^{-1} \tag{5.24}$$

and, for a convenient representation, it is useful to consider its energy dependent counterpart:

$$\mathrm{IPR}(E) = \sum_j \mathrm{IPR}_j \delta(E - E_j) \Big/ \sum_j \delta(E - E_j) \tag{5.25}$$

The data in Figure 5.1 derive from 10 repeated diagonalizations of the Hamiltonian with different realizations of random variables and with the Dirac delta function approximated with a Gaussian of width $0.1\,\beta_0$.

In the absence of disorder (upper panel of Figure 5.1) all states are naturally delocalized and the DOS has the shape familiar for 1D chains (in this limit the hopping mechanism cannot be assumed). The introduction of disorder causes the localization of all states according to Anderson theory[95] and a broadening of the DOS. The localization is not uniform at all energies as the states at the DOS edge are more localized.[83,254] For intermediate disorder, states with a broad range of localization become accessible thermally and the increase in charge carrier density is accompanied by an increase of the localization length at the Fermi level. The presence of this energy dependent localization, together with the inclusion of a microscopic hopping rate expression, is the main innovation of this model with respect to analytical models.

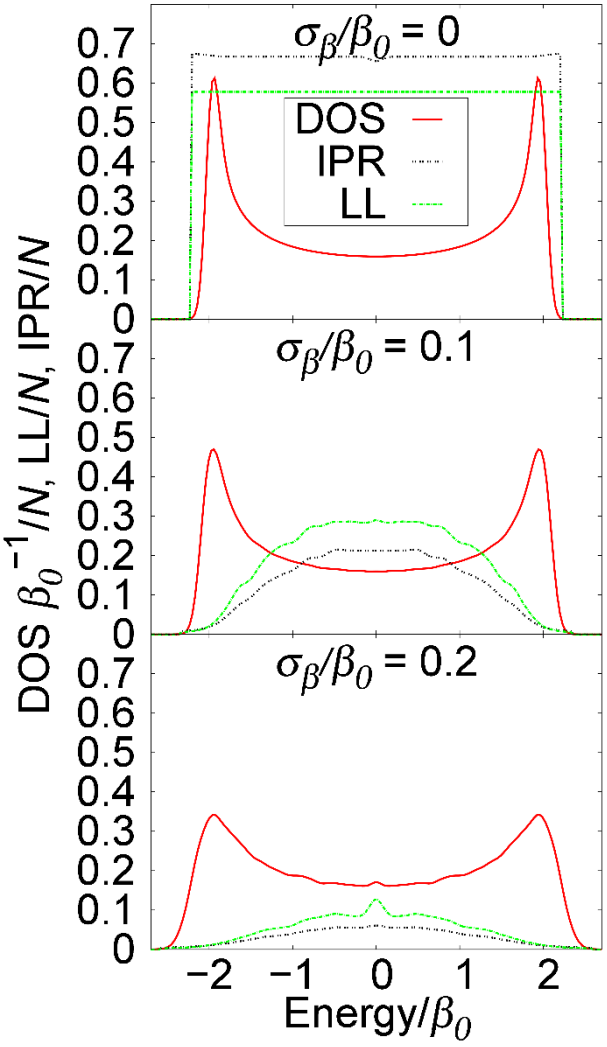

Figure 5.1. Density of states, localization length and inverse participation ratio (defined in eqs. (5.21)-(5.25)) of the eigenstates of the electronic Hamiltonian for different levels of off-diagonal disorder σ_β.

We consider next a qualitative visualization of the results that will help the following quantitative analysis. In Figure 5.2 we represent, for three levels of disorder σ_β = 0.08, 0.10 and 0.12 β_0, the spatial distribution of the eigenstates of H^{el}, their energy and their localization. We have represented only the states observed on a small portion of the polymer chain. One can observe the increase in the density of states with increasing energy and the existence of more delocalized states at higher energy. In Figure 5.2, the particle currents $k_{ij} p_i (1-p_j)$ that are not negligible in magnitude are represented by coloured lines connecting states *i* and *j* and, as expected, one observes that particle current (hopping) is appreciable only between states that are relatively close in space. The picture at high disorder is not too different from the

assumptions made in most variable range hopping models (all states are localized). However, at lower disorder more long-range hopping events are observed because the system contains relatively delocalized states that can be accessed from many initial states. These delocalized states act as intermediates for long range displacements of the charge and they are clearly not considered in standard variable range hopping models, while they consistently appear in atomistic calculations of the orbitals in polymers.[110,254]

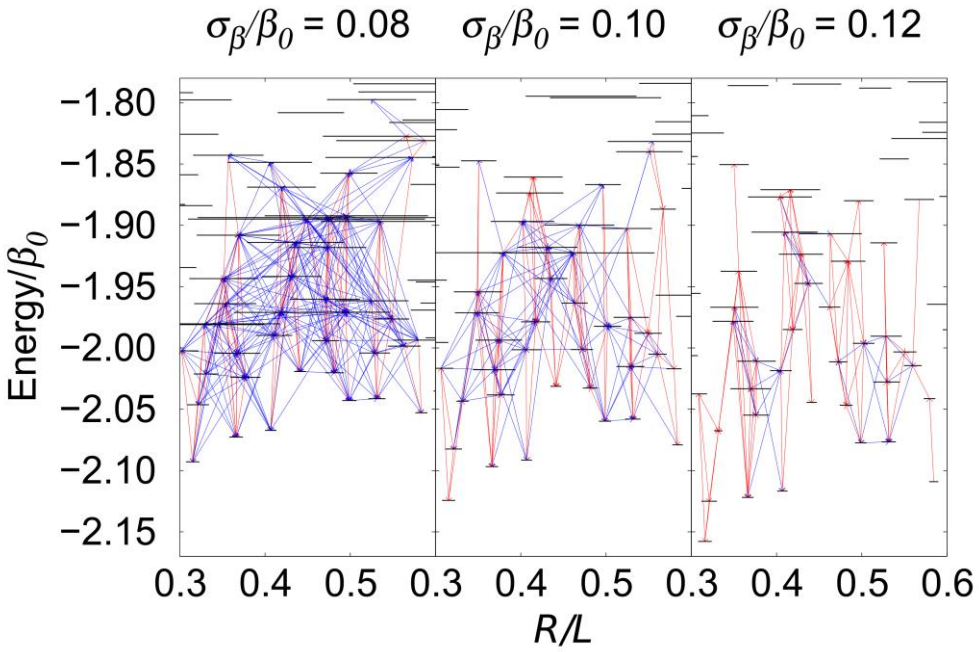

Figure 5.2. Diagram of the spatial distribution, energy and localization of the electronic eigenstates of the system. Only the energy states in the band tail are shown and only a portion of the chain is considered. The length of the chain is $L = 1024 \cdot d$. Each state is represented by a horizontal segment line whose width is the localization length, and whose central coordinate represents the energy of this state and the position along the chain on the vertical and horizontal axes respectively. The coloured arrows connecting the horizontal segments represent the particle currents $k_{ij} p_i (1 - p_j)$ between states, obtained from the steady state solution of the master equation in the limit of weak electrical field (F = 100 V/cm) and low charge density $(\langle n \rangle = 5)$. For clarity, only the particle currents which make up the 99.99% of the total particle current, calculated as $\sum_{i \neq j} k_{ij} p_i (1 - p_j) + k_{ji} p_j (1 - p_i)$, are shown. The red arrows represent jumps shorter than 0.025 L.

To better appreciate the timescale for the hopping events depicted in Figure 5.2 and their dependence on some of the system parameters, we have reported in Figure 5.3 the distribution of the particle currents at a fixed disorder for different temperatures and reorganization energies λ_1 of the monomer. Particle currents are more informative than the rates as they include only the relevant hopping processes

and, on a logarithmic scale, they are only slightly smaller (up to ~10 times) than the corresponding hopping rate. The fastest particle currents for any reasonable polymer described by our model are in the 10^9-10^{11} s^{-1} range, i.e. the description in terms of incoherent hopping is acceptable as well as the separability between static (slower than 10^9 s^{-1}) and dynamic (faster than 10^{11} s^{-1}) disorder.

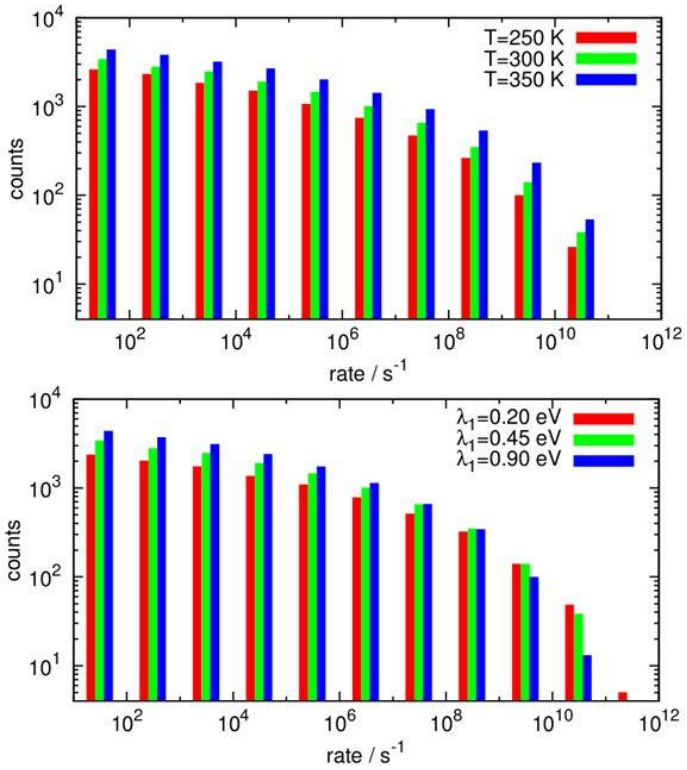

Figure 5.3. Distribution of the particle currents ($k_{ij} p_i (1-p_j)$) (for a system of 4000 monomers and σ_β / β_0=0.12) for various system parameters. In the top panel λ_1 = 0.45 eV and in the bottom panel T = 300 K. Note the logarithmic scale on both axes.

5.2.2 Mobility as a function of system parameters

In this section we compute the charge mobility along a 1D polymer chain considering the effect of applied field, disorder and charge density. We are interested in any important differences with respect to other models that are based on few assumptions on the structure of the transport master equation.

Figure 5.4 shows the dependence of the mobility on the applied electric field. The results are very similar to what is discussed in ref. [252] for nearest neighbor hopping transport along a 1D chain with Miller-Abrahams rates between localized states with a Gaussian energy distribution. At low fields, when $\left|eFR_{ij}\right| \ll \left|\Delta E^0\right|$ for all significant rates, the mobility is independent of the field. This is because we are in the linear response regime for small perturbations and the disorder is uncorrelated. As the

field is increased, the processes where $\left|\Delta E^0\right| \simeq \left|eFR_{ij}\right|$ are "activated" by the field so that the mobility grows nonlinearly, until it reaches a maximum; at higher fields, the transport enters a regime where the significant rates which were high in the weak field regime are "deactivated" by the effect of the field (when $\left|eFR_{ij}\right| \gg \left|\Delta E^0\right|$, the effective ΔE becomes so negative that the process is in the inverted Marcus region). The processes "activated" by the field are again those where $\left|\Delta E^0\right| \simeq \left|eFR_{ij}\right|$, so either very far in energy (large ΔE^0) or very close in space (small R_{ij}). In this regime the mobility decreases nonlinearly with respect to the field, with a slope becoming much steeper than $1/F$ with increasing field strength (possibly a result of using eq. (5.9) instead of Miller-Abrahams rates). However, considering the high degree of idealization in the models, we should conclude that the additional features of our model do not alter in important ways the effect of the field on the observable mobility.

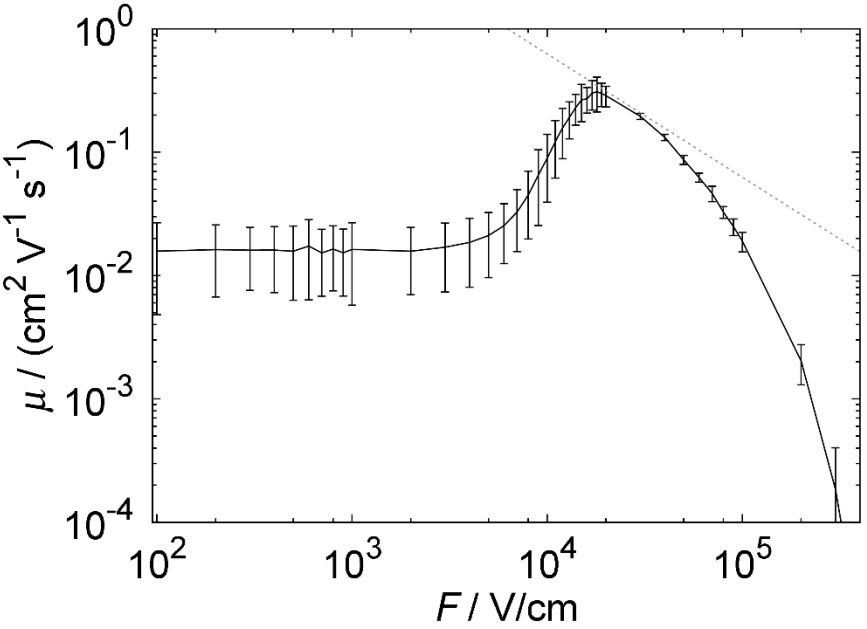

Figure 5.4. Mobility as a function of electric field along a 1024 monomer chain, obtained from our model with disorder σ_β = 0.1 β_0. Each point is obtained by averaging the mobilities of 20 realizations of the model with 1 charge per chain. The dotted line is the function $\mu = \upsilon_0 d / F$ with $\upsilon_0 = 6.25 \cdot 10^{10}\,\mathrm{s}^{-1}$ and d =10 Å = 10^{-7} cm.

We will now examine the dependence of mobility on the amount of static disorder, whose main effect is to localize the states and therefore decrease the mobility. The mobility as a function of disorder in the limit of weak field is shown in Figure 5.5. The dashed line is the analytical result obtained by Cordes et al. [252] (eq.

30 therein), for nearest neighbour hopping (NNH) along a 1D chain of localized states randomly distributed in energy (Gaussian Disorder Model, GDM). Although our results agree with this theoretical model at low disorder, the curves rapidly diverge at higher disorder. The fundamental difference is that in our model hopping is not limited to the nearest neighbours: as we will show below, even at high disorder, long range hops are still possible. Pasveer et al. [255] have shown, by means of a master equation approach to 1D transport, that the inclusion of distant hops (VRH) yields drastically higher mobilities than the NNH model.

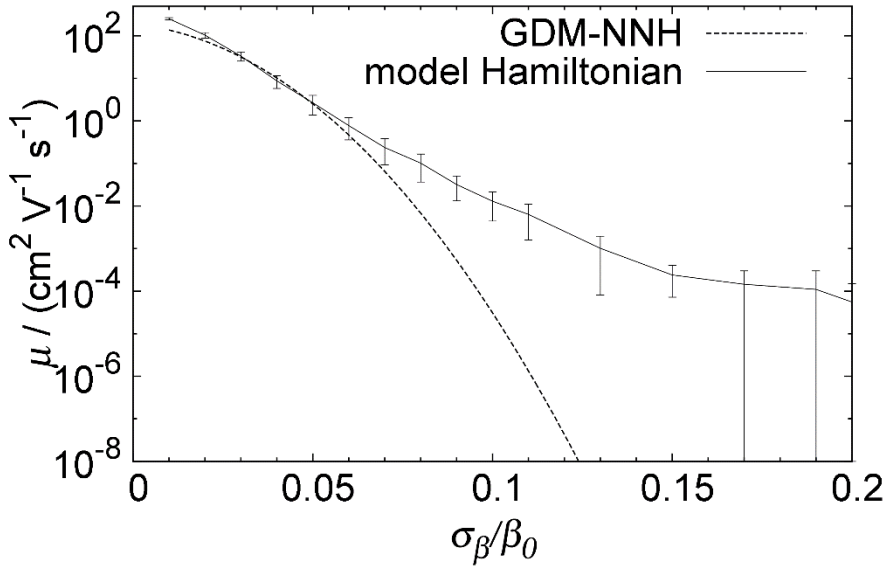

Figure 5.5. Mobility along a 1024 monomer chain obtained from our model (solid line) in the limit of weak electrical field (F = 100 V/cm) as a function of the static disorder σ_β for T = 300 K. Each point is obtained by averaging the mobilities of 10 realizations of the model with 10 charges per chain. The dashed line is the analytical solution given by ref. [252], eq. 30, with σ_β = 0.1 eV and prefactor $\upsilon_0 = 2 \cdot 10^{14}$ s^{-1}.

The data plotted in Figure 5.6 show that increasing the charge density yields higher mobilities. In GDM models this is a result of the transport level being in a region of higher density of states. In this case we have additionally the effect that higher energy states are more delocalized and therefore more likely to promote longer range hopping (the distribution of hopping distances is discussed in the next section).

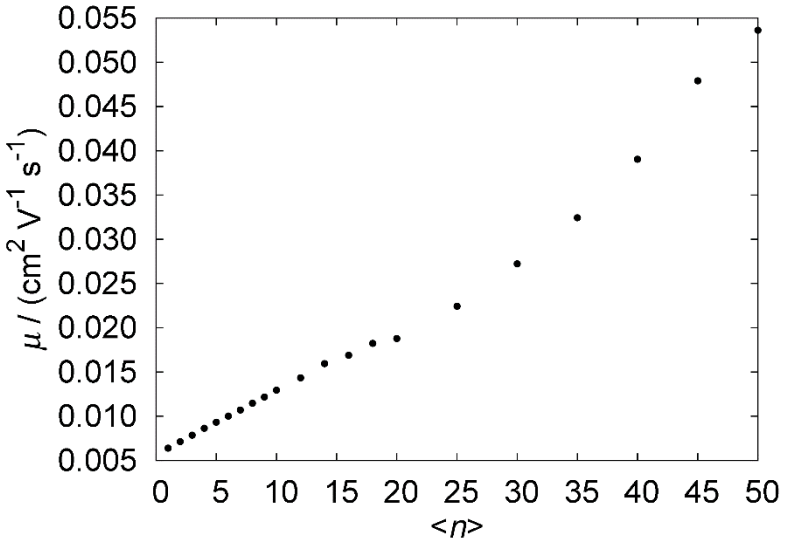

Figure 5.6. Dependence of mobility on the average number of charges for $\sigma_\beta = 0.1\beta_0$, using the same parameters as in Figure 5.5. These calculations have been performed setting the Fermi level at different values in the range between −2.19 and −2.01 β_0, i.e. the band tail region (see Figure 5.1).

The study of the mobility in this highly idealized system starting from the model Hamiltonian does not show radical qualitative difference with respect to analytical models built directly from a simplified master equation and the advantage of this formulation is possibly more evident only when the connection between specific polymers and experimental mobility are sought.

5.2.3 Hopping distance distribution and limit of validity

In order to investigate the role of more delocalized states included in our models, we analysed the distributions of hopping distances at the steady state for different amounts of disorder, see Figure 5.7(a). Each distribution is obtained considering all possible hopping distances $|R_{ij}|$ weighted by the corresponding particle currents $k_{ij} p_i (1 - p_j)$. We have considered the limit of vanishing field and fixed the Fermi level at $-2.1\beta_0$ (the results are qualitatively similar for different Fermi levels). The probability of hopping decreases exponentially with increasing hopping distance at short and medium distances, up to 50-100 monomer units. The overall distribution, including also very large distances and highly unlikely hops, is bi-exponential but the rarest events are unlikely to have any role as they are many orders of magnitude less frequent. As the disorder is decreased, longer hops become more likely. By fitting the distribution with the function $A\exp(-|R|/R_0)$ in the short-medium hopping range, it

is possible to quantify the typical hopping range via the parameter R_0. Figure 5.7 (b-c) reports the value of R_0 for different values of disorder. For $\sigma_\beta / \beta_0 = 0.1$ (a level of disorder common to many polymers) the typical hopping distance R_0 is close to 10 monomers and this distance changes very slowly as the disorder in the polymer chain is increased. Very interestingly, for disorders just below $\sigma_\beta / \beta_0 = 0.1$ we observe a very rapid increase of long range hopping with decreased disorder until a point, close to $\sigma_\beta / \beta_0 \sim 0.01$, where the results of the model are not reliable because the hopping distances become comparable with the size of the system itself (2048 monomers for this analysis). Therefore, it is maybe possible to speculate that what characterizes high mobility polymers is the increased occurrence of long range hopping. Figure 5.7(b-c) also reports the same analysis for different temperatures and values of reorganization energy. Expectedly, the hopping range is not much affected by these parameters that otherwise influence very strongly the hopping rate. This is because, according to the assumptions of the model, the hopping range is determined by the coupling $V_{ij}(t)$, which, as follows from its definition in eq. (5.6), is only dependent on the electronic part of the Hamiltonian, i.e. on σ_β, β_0 and M.

While we are unable to compute mobilities in the presence of too little disorder, we can observe the transition between a mechanism where carriers hop between localized states and a mechanism where localized carriers hop into relatively delocalized states and then back into localized states, illustrated qualitatively in Figure 5.2. The latter is akin to mobility edge (ME) models,[103,104] where one assumes that all states below an energy threshold are localized and static and all states above the threshold have a very high mobility. While VRH and ME models are normally considered alternative to one another, we see that our model built from the microscopic Hamiltonian incorporates elements of both.

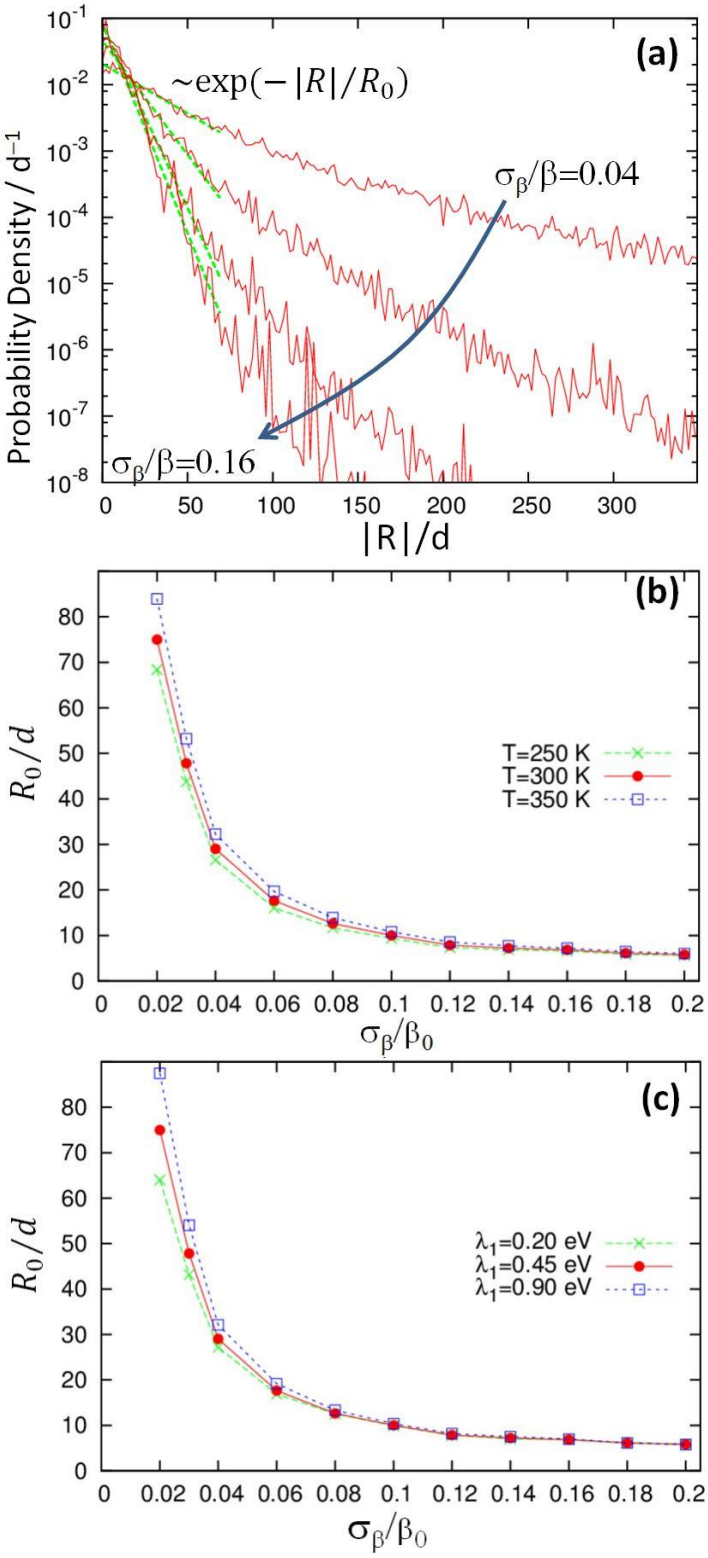

Figure 5.7. (a) Distribution of the hopping distances for different values of static disorder. An exponential fitting of this distribution at short and medium hopping distances is also shown in dashed lines. (b-c) Dependence of the hopping range R_0 (defined from fitting the hopping range distribution) on the static disorder of the chain. Panel (b) reports results for λ_1 = 0.45 eV and different temperatures and panel (c) for T = 300 K and different values of λ_1.

Finally, it is important to establish the limit of validity of the non-adiabatic hopping mechanism. The hopping rates should be slower than the vibrational relaxation rate in order for the hopping rate to be properly defined.[256] This condition seems to be always verified for the parameter range considered here where the fastest rates are typically below 10^{11} s^{-1} (corresponding to 10 ps or longer timescales), while the vibrational relaxation time in the solid is closer to 1 ps. A related condition for the validity of the proposed approach is that the charge hopping process is indeed inelastic, i.e. the electron decoherence time is shorter than the hopping time. A number of authors have investigated the opposite limit of ultra-fast dynamics studying fully coherent dynamics in polymer chains, which should be valid for up to few picoseconds.[257–260] These two approaches are therefore valid in opposite limits and cannot be directly compared. However, as the disorder of the chain is decreased (or the dynamic fluctuation *M* is increased) the hopping rate increases and, at some point, the assumptions of our model will break down and, instead, the methods developed to study coherent dynamics become more useful.

To establish a quantitative relation for the breakdown of the non-adiabatic hopping limit we consider the condition that the coupling between electronic states should be substantially smaller than the reorganization energy (otherwise one cannot easily define a transition between two distinct diabatic states [261]). The condition

$$\left\langle V_{ij}^{\,2} \right\rangle \ll \lambda_{ij}^{\,2} \tag{5.26}$$

considering eqs. (5.5) and (5.8) becomes

$$M^2 \sum_n \left(c_{ni} c_{nj} \right)^2 \ll \lambda_1 \sum_n \left| c_{ni} \right|^4 + \left| c_{nj} \right|^4 \tag{5.27}$$

$$\frac{M}{\lambda_1} \ll \frac{\sum_n \left| c_{ni} \right|^4 + \left| c_{nj} \right|^4}{\left(\sum_n \left(c_{ni} c_{nj} \right)^2 \right)^{1/2}} \tag{5.28}$$

The right hand side ratio of eq. (5.28) can be evaluated for all pairs of states *i* and *j* and for different values of static disorder σ_β / β_0. In Figure 5.8 we report the *minimum* value of this ratio observed for many replicas of the system at a given value of static disorder and the numerical value is actually very close to the ratio σ_β / β_0. The condition of validity of hopping can be therefore stated more simply in terms of the parameters of the model as

$$M / \lambda_1 \ll \sigma_\beta / \beta_0 \tag{5.29}$$

As expected, the condition of validity of hopping mechanism becomes more stringent as the system becomes more ordered. For the parameter choice made here (M = $0.005\beta_0$, λ_1 = $0.45\beta_0$) the hopping mechanism becomes invalid only at very low disorder but it is certainly possible that, in some case (e.g. polymers with very low reorganization energy per monomer), the above condition is not satisfied and, in such a case, the charge dynamics cannot be considered fully incoherent. This limit is not considered explicitly in this work, but it is worth noticing that only by formulating the transport model from the Hamiltonian it is possible to correctly identify the validity range for a given model.

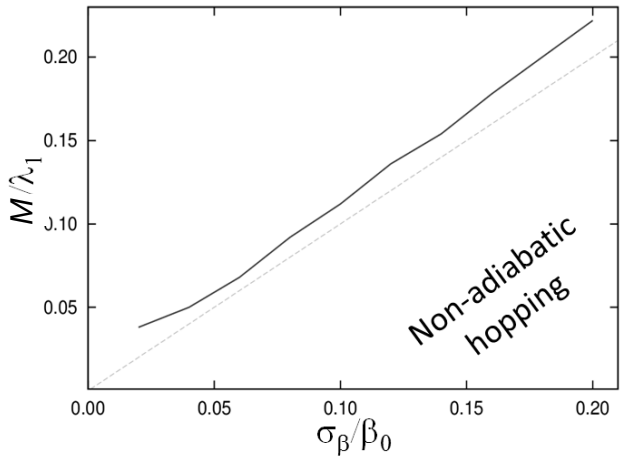

Figure 5.8. (solid line) Upper limit of M / λ_1 for which, at a given value of static disorder σ_β / β_0, the model based on non-adiabatic hopping is valid according to eq. (5.28). The dashed line represents the function $M / \lambda_1 = \sigma_\beta / \beta_0$.

5.2.4 The case of alternating copolymers: why a donor-acceptor electronic structure is not detrimental for charge transport

In the previous sections we have seen how the degree of disorder makes the difference between good and bad polymers. One of the most surprising observations in this field is that polymers with an extremely simple structure and a wide band like PPV (poly(*p*-phenynelene vinylene)) [15] are orders of magnitude worse in terms of charge mobility compared to recently introduced donor-acceptor copolymers that display a very complex chemical structure and, apparently, a lower degree of electronic conjugation (and narrower bandwidths) due to their greater flexibility. Although the charge transport does not take place via band transport, narrow bandwidths are considered detrimental to transport in the most common models of transport used for polymeric semiconductors. In VRH models narrower bands cause greater localization and slower hopping rate [101] and, in ME models, they cause the reduction of the mobility of carriers outside the traps.[104] In this section we discuss how a more complicated donor-acceptor electronic structure with narrower transport band can instead improve the mobility.

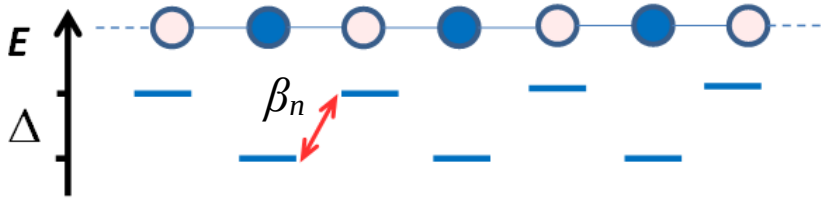

Figure 5.9. A cartoon representing the model Hamiltonian with an energy difference Δ between odd and even sites.

To represent a copolymer structure with alternating sites of different energy (see Figure 5.9), we start from the electronic Hamiltonian in eq. (5.1), where we set the site energies $\alpha_n = \Delta/2$ for odd values of *n* and $\alpha_n = -\Delta/2$ for even values of *n*. We have chosen to consider only the disorder σ_β in the off-diagonal terms β_n, following the indications from atomistic studies[110] that this is the main term determining charge localization and DOS. The results, however, remain similar if a realistic on-site (diagonal) disorder is added to the model, as shown in Figure 5.14. The average coupling between monomers β (previously named β_0) determines the energy scale in the remainder of this section.

Using different realizations of disorder and a chain of 1000 sites, we have computed DOS(E) and LL(E) (see eqs. (5.21)-(5.23)) for different values of the parameters Δ/β and σ_β/β. The results are shown in Figure 5.10. In the absence of disorder ($\sigma_\beta/\beta = 0$) and for the homo-polymer (i.e. when all monomers have the same energy and $\Delta/\beta = 0$) the DOS is obviously that of a one-dimensional chain and the states are fully delocalized (as previously shown in the top panel of Figure 5.1). For $\Delta/\beta \neq 0$ the system develops two bands which for $|\Delta| > \frac{1}{2}|\beta|$ contain states in two separate energy regions. The wavefunctions in the low energy band have their probability density concentrated on the sites corresponding to the low energy monomer and vice-versa. Each of these bands is similar to that of a one-dimensional chain with a smaller effective coupling: two donors separated by an acceptor are not directly coupled but their wavefunctions are mixed because they are both coupled to the same acceptor. The effective coupling between two degenerate sites mediated by another bridge site at different energy (known as superexchange [262]) decreases with increasing the energy gap Δ between the sites that are coupled and the site that mediates the coupling. The parameter controls both the energy separation between the bands and their narrowing. In the absence of disorder, the eigenfunctions are fully delocalized, i.e. LL(E) are of the order of the size of the system. Introducing disorder, i.e. when $\sigma_\beta/\beta_0 > 0$, few expected changes occur regardless of Δ: the DOS is broadened and the localization decreases. Importantly, as noted for example in ref. [110], the states at the band edge are more localized than the states deeper in the band. According to the mobility edge model, [103,104] charge mobility is thermally activated because very localized states in the tail of the band are not mobile while states deeper in the band have higher mobility and the measured thermal activation is the typical energy required to de-trap the carrier from the band tail. Actual calculations of model Hamiltonians [263] do not display a sharp cut-off between localized and delocalized states, but a similar principle may be in action, with higher temperatures increasing the population of charge carriers at more delocalized and therefore higher mobility energies. Our hypothesis is that the activation energy required to promote charge carriers from localized states in the band tail to delocalized states deeper in the band is *reduced for narrower bands*, simply because all states are closer in energy to each other and delocalized states are therefore closer to the band edge. This hypothesis

would explain why the activation energy for transport is reduced for copolymers (being everything else the same). Narrow bands, however, imply weaker coupling between localized states so one has to evaluate the combined effect of having more delocalized states closer to the band edge (which would increase the mobility) and a reduced coupling between these states (which would decrease the mobility).

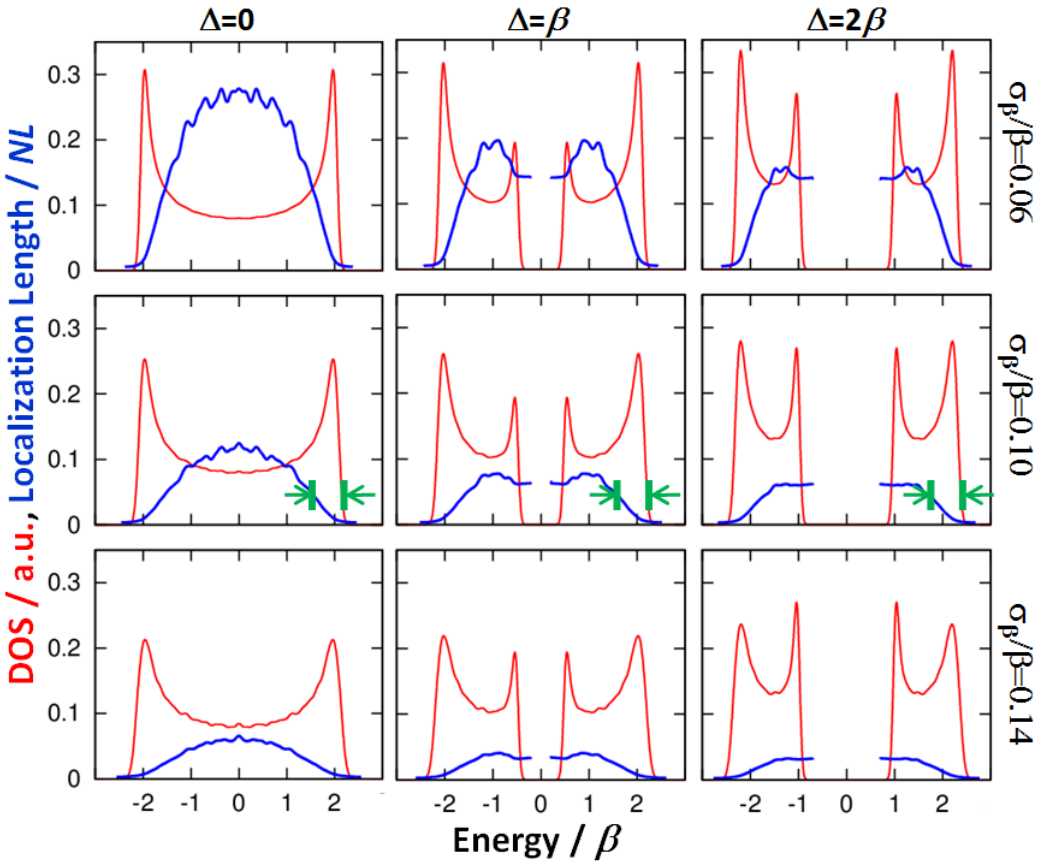

Figure 5.10. Nine panels representing the DOS and localization length of the model system for different combinations of disorder (σ_β / β) and difference of on-site energy (Δ / β). Arbitrary energy intervals shown in green in the central panels illustrate that the activation energy between localized states at the band edge and delocalized states within the band may be similar. A rigorous definition of the activation energy is discussed in the text (results shown in Figure 5.11).

To make the argument more quantitative, we compute the mobility along a copolymer chain using the model described in the previous sections, in the limit of vanishing field *F* applied along the chain and vanishing charge density. We consider explicitly only the intra-chain transport because only in this case the chemically controllable parameter Δ has two competing effects (reducing the intra-chain coupling but also the activation energy for transport). The inter-chain transport simply becomes less dispersive (faster) for larger values of Δ (narrower bands), which reduce the activation energy, and is determined by the inter-chain coupling, a parameter that is

much smaller than the polymer bandwidth and unrelated to it. The results are discussed as functions of the disorder (σ_β / β) and of the difference between on-site energies (Δ / β). The other parameters, which do not affect the conclusion of this work, are similar to those used in the previous sections. They have been set as follows: M = 0.01 eV, $k_B T$ = 0.025 eV, $g^2 / m\omega^2 = \lambda_1$ = 0.45 eV, β = 1.0 eV.

The model predicts a mobility that follows the simple Arrhenius law $\mu \approx \mu_0 \exp(-E_b / k_B T)$ as shown in Figure 5.11, which is used to define an empirical activation energy E_b. Figure 5.12(top) illustrates how the mobility increases moderately with increasing Δ, i.e., how band narrowing is not detrimental to mobility. Figure 5.12(bottom) shows how the activation energy decreases with the increase of Δ and that the decrease of the band width is responsible for the overall increase of mobility with increasing Δ. The effect can be visualized in Figure 5.13, where the highest particle currents $k_{ij} p_i (1 - p_j)$ are shown for systems with different values of Δ. When Δ is increased, the lower band gap and the smaller band width cause more delocalized states to be energetically closer to the band edge, allowing more long-range hopping. As the increase of mobility with Δ is not large compared to the variability in mobility that one can observe in these materials, a fair interpretation of the results is that an increase in Δ makes the material more insensitive to the local disorder: the same local disorder generates deeper traps in wider-band (small Δ) materials.

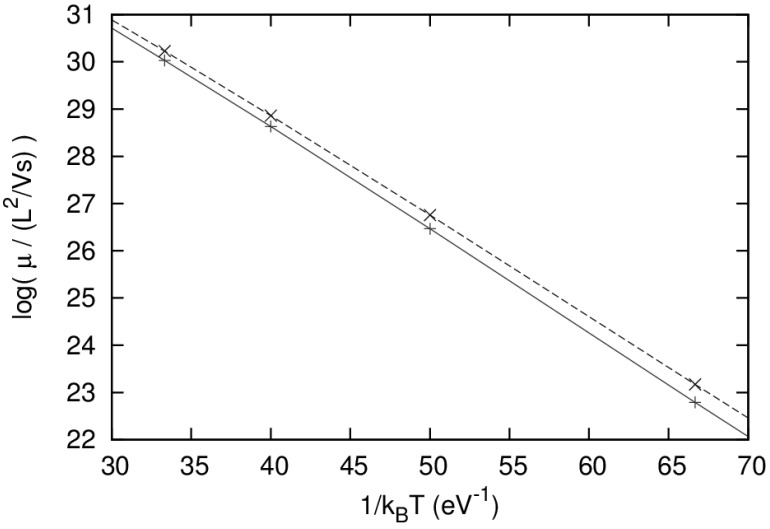

Figure 5.11. Arrhenius plot of the log of the average mobility plotted against the inverse temperature for σ_β / β = 0.10 and Δ / β = 0 (solid line) and 1 (dashed line).

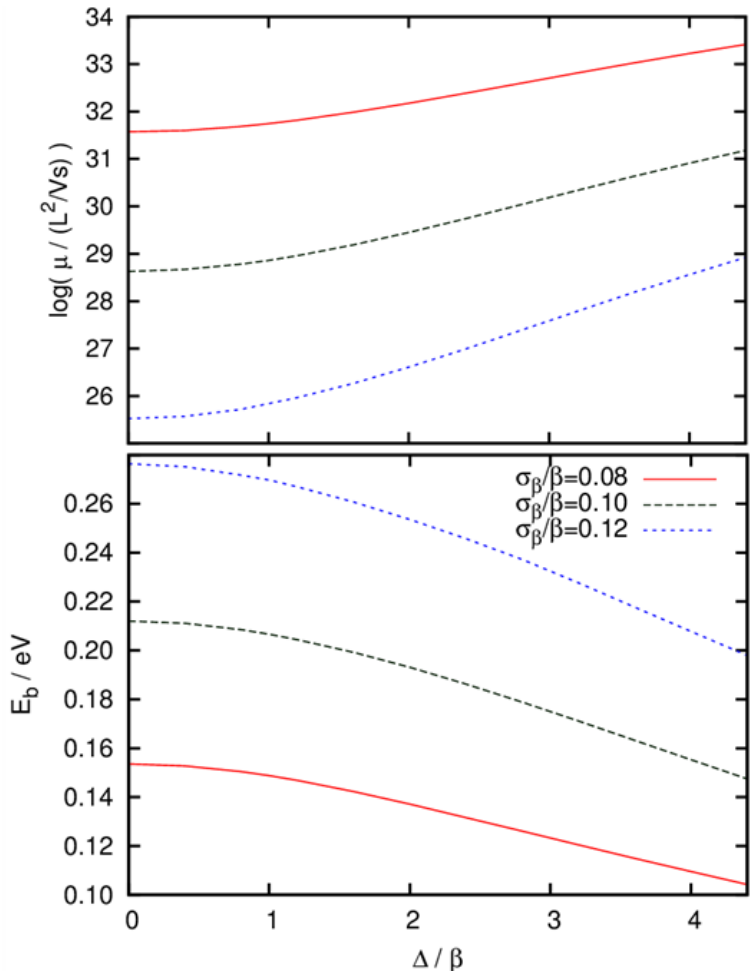

Figure 5.12. (Top) Increase of the mobility with increasing difference between on-site energies Δ for different values of static disorder. (Bottom) Corresponding decrease of the activation energy E_b computed from the temperature dependence of mobility (see Figure 5.11).

Figure 5.14 reports the mobility computed as in Figure 5.12(top) but with the addition of a variable amount of on-site disorder $f = \sigma_\alpha$. The computed mobility decreases only very slightly with the addition of a reasonable amount of on-site disorder (f < 0.5) and the general trend of mobility increasing with increasing Δ is maintained until very high (probably unreasonable) values of the relative on-site disorder (f ~ 1.0).

To make the results more easily comparable with other theories and experiments we note that a mobility $\log(\mu / (L^2/\mathrm{Vs})) = 29$, i.e. the centre of the mobility range in Figure 5.12(top), corresponds to an absolute mobility of 0.04 cm^2/Vs if the distance between monomers d is set to 10 Å and the vertical range of the figure would span between 10^{-3} and 6 cm^2/Vs. This model, by design, captures the experimental range between moderate and high mobilities because it does not include the possible effect

of extrinsic defects. It should not be forgotten that copolymers, having generally a smaller band gap, are less sensitive to the presence of extrinsic defects and this also contributes to their high mobility.[264]

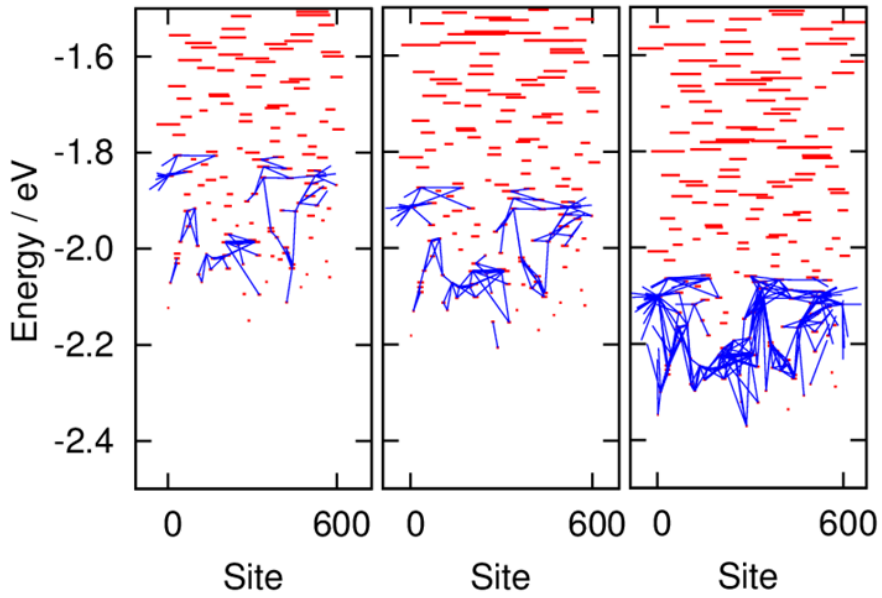

Figure 5.13. Diagram representing the energy levels (horizontal red segments) and their delocalization (length of the segment) for $\Delta / \beta = 0, 1, 2$ (left, centre, right panel) in a system with 600 sites. The blue segments connect sites with particle currents $k_{ij} p_i (1 - p_j)$ exceeding a common threshold. Increasing delocalization at higher energy is evident from the diagram. The larger total particle current for $\Delta / \beta = 2$ is due to the presence of more delocalized states near the bottom of the band.

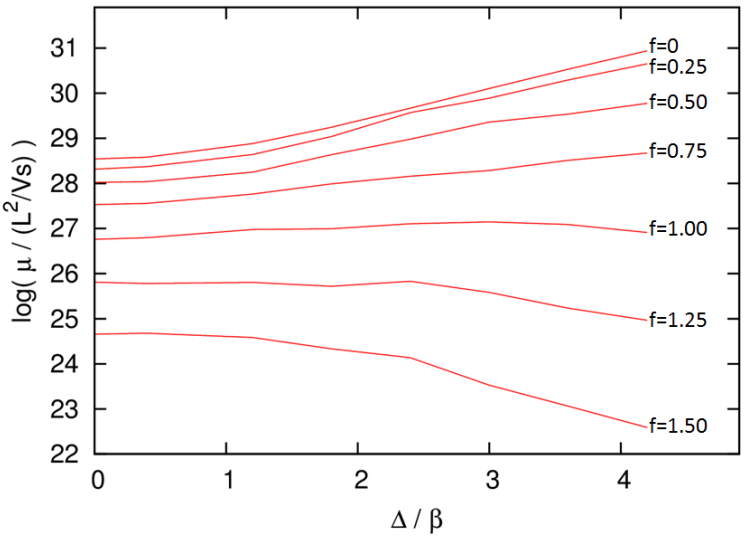

Figure 5.14. Effect of the inclusion of on-site disorder on the computed mobility as a function of the parameter Δ. In this plot $\beta = 1$ eV, $\sigma_\beta = 0.1$ eV and f is the strength (width) of the on-site disorder relative to the off-diagonal disorder σ_β. The data for $f = 0$ is the same as the dashed line in Figure 5.12.

Having started from a model Hamiltonian, rather than assuming localized charges and the shape of the DOS, it is also possible to establish the limit of validity of our result. If we increase indefinitely Δ, the bandwidth will eventually vanish and the assumption that the charge localization is mainly due to the polymer disorder becomes invalid. With vanishing bandwidth the system will form small polarons, localized on a single monomer.[127] When the bandwidth is of the order of the polaron formation energy of a single monomer (typically between 0.1 and 0.5 eV [265]) the transport is more appropriately described by small polaron hopping and is likely to be less efficient than the transport involving delocalized states. One can therefore argue that the electronic structure of the copolymer is beneficial to charge transport as long as the bandwidth remains larger than the polaron formation energy. Even more intriguingly, it is possible that the highest possible mobility achievable for disordered polymers is found for those materials whose band is narrow enough to minimize the activation energy for transport but not as narrow to promote the formation of very stable small polarons. To illustrate this in figures, we can consider the case where $\Delta / \beta = 2$, the bandwidth is close to β (Figure 5.10), and $\lambda \sim \beta$ would be a situation where this maximum mobility can be achieved and that corresponds to the plausible value of $\beta \sim$ 0.4 eV. While still not fully conclusive, there is some computational and experimental evidence that the highest mobility amorphous polymers are found in a transport regime where small polarons start becoming important.[144]

5.3 Conclusions

In this chapter we have presented a model for incoherent charge transport along a polymer chain starting from the Hamiltonian of the system instead of starting from a plausible DOS with arbitrary localization. We followed this route as the essential intermediate step to link detailed atomistic calculations of realistic polymers with the evaluation of charge mobility in models of devices, but we focused in this study on the general properties of the model rather than the description of a specific realistic system. In essence, in this hopping model the initial and final states are determined by static disorder and the coupling between them is due to the residual dynamic disorder. Such a model seems to be the best idealization of several large-scale calculations of polymers that have recently appeared in literature.

When looked at from the point of view of analytical models, our model does not lead to major qualitative differences in the dependence of the mobility on the disorder or the charge density. In principle, one can build a suitable variable range hopping model that incorporates all the specific features identified in our microscopic model. Specifically, the hopping range (the hopping rate as a function of inter-site distance) should not be defined independently from the disorder as the two are indeed coupled, i.e. smaller disorder is associated with higher rates of long-distance hops. Moreover, the hopping range should possibly derive from a statistical distribution instead of being set at the same level for all states. In fact, the most interesting effect displayed by our model is that larger charge displacements take place by hopping into a relatively delocalized state and then back into a localized state. Such "bridging" states are more often encountered in the discussions concerning long-range electron transfer in molecular or biological systems.[266] In summary, this model creates a natural link between variable range hopping theories (where all states are assumed to be equally localized) and mobility edge theories (where one assumes there is a threshold energy where the states become delocalized).

Moreover, we have shown that, at a constant level of disorder in the electronic Hamiltonian, the narrower bands present in a semiconducting donor-acceptor copolymer are overall beneficial to transport, i.e. the weaker coupling between states is more than compensated by a lower activation energy for transport. This is true until the band is so narrow that small polarons are formed on each monomer. It is essentially impossible to predict the level of disorder of any new polymer but it is relatively easy to compute and predict the bandwidth and the electron-phonon coupling for a given compound. The proposed model suggests that it is possible to select the parameters that can be controlled (coupling and electron-phonon coupling) to place the polymer in a region of the parameter space where the disorder (uncontrollable) plays a lesser role. In the perspective of going toward more realistic models, it is also easy to avoid some of the simplifications introduced in this model (presence of a single classical nuclear mode, a single electronic state per monomer) when the additional needed parameters can be derived from atomistic models.

6. A universal temperature dependence of charge mobility in polymeric semiconductors*

Summary: In this chapter we investigate how the temperature dependence of mobility in semiconducting polymers depends on the system parameters. The results are obtained from the charge transport model described in chapter 5: the disorder in the model Hamiltonian determines the electronic structure. To minimize the number of implicit assumptions we have used the very general hopping rate expression presented in chapter 2. In such a general model, charge mobility depends in principle on tens of parameters, reflecting the wide range of chemical structures encountered in these materials. Here we demonstrate that the steady state charge mobility in the limit of low charge density and low fields ultimately depends on only two parameters: an effective structural disorder (determining the activation energy for transport) and an effective electron-phonon coupling, weighted by the size of the monomer. The results support the experimental observation [113,114] that the mobility in a broad range of (not only polymeric) semiconductors follows a universal behaviour, insensitive to the chemical detail.

6.1 Motivation

The structural complexity of polymeric materials makes it difficult to rationalize the dependence of mobility on the chemical structure. Modest changes in the chemistry can cause large variations in measured mobility and the space of possible parameters that can be explored (including molecular weight and processing) defied any attempt at truly predictive modelling. On the other hand, the essence of charge transport (temperature, field and charge carrier dependence) can be captured by fairly simple models depending on just a few parameters as discussed in section 1.3.

The starting point of our analysis is a set of experimental measurements reported in refs. [113,114] which show that, for a large number of materials, the low-field and low-charge-density mobility μ obeys a simple temperature dependence $\mu = \mu_0 \exp\left(-E_a / k_{\mathrm{B}} T\right)$, where the parameter μ_0 is universal for all materials and the only material-dependent parameter is the activation energy E_a ($k_{\mathrm{B}} T$ is the thermal

* The content of this chapter is published in R. P. Fornari, P. W. M. Blom and A. Troisi, *Phys. Rev. Lett.*, 2017, **118**, 86601.

energy). It is certainly surprising that the chemical and morphological complexity [267] of organic semiconductors can be reduced to a single effective parameter for each material.

In this chapter we consider a rather general model that should mimic the large parameter space encountered in realistic polymers and study how many distinct effective parameters actually affect the charge mobility, through a parameter space exploration. This approach is somewhat opposite with respect to the most common strategies that *start* with a less general model that already contains a limited number of parameters (as in Gaussian disordered models [99] or mobility edge models [103,104] with four and two parameters, respectively). More specifically, we allow (i) for a more general (and realistic) electronic structure and (ii) for a more general hopping rate expression.

6.2 Charge transport model

The main assumptions are that the disorder in the one-dimensional electronic Hamiltonian determines the localization of the carrier states (chapter 5) and that the electron-phonon coupling interactions determine the hopping rates between these states (chapter 2).

6.2.1 Parameters determining the electronic structure

Rather than assuming a density of states (DOS) and an independent constant localization length we generate the one-electron states involved in the transport by computing the eigenstates $\left|\psi_i\right\rangle = \sum_n c_{ni} \left|n\right\rangle$ (and energies E_i) of a random electronic Hamiltonian (eq. (5.1)) as described in section 5.1.1. To illustrate the results we consider 14 models of random Hamiltonian, which are different combinations of the average (α_0 and β_0) and standard deviation (σ_α and σ_β) of the site energies α_n and couplings β_n, assumed to be normally distributed. They are summarized in
Table 6.1 and chosen to reproduce the range of charge mobility observed experimentally (see below).

Table 6.1. Hamiltonian parameters in eV for different models of disorder labelled 1-14. α_0 is always 0.0 eV and defines the zero of our energy scale.

Disorder model	average coupling β_0	diagonal disorder σ_α	off-diagonal disorder σ_β
1	0.25	0.0	0.05
2	1.0	0.0	0.1
3	0.5	0.0	0.1
4	1.5	0.0	0.1
5	1.0	0.1	0.1
6	1.0	0.1	0.15
7	0.5	0.1	0.1
8	1.5	0.1	0.1
9	1.0	0.2	0.1
10	1.5	0.0	0.15
11	1.0	0.1	0.2
12	1.0	0.2	0.2
13	1.5	0.2	0.2
14*	1.0	0.2	0.2

*with a 1 eV gap between odd and even sites

6.2.2 Parameters entering the hopping rate

For the rate of hopping between any two eigenstates *i* and *j* of the Hamiltonian we adopt the most general expression derived in chapter 2. More specifically, we use here the expression given in eq. (2.16) with the function $\rho_{\mathrm{FCTW},ij}\left(E\right)$ given in eqs. (2.6) and (2.7):

$$k_{i\to j}=\frac{\pi}{\hbar}\sum_k\left|M_{ij,k}\right|^2\Big[\left(N(\hbar\omega_k^{\mathrm{I}})+1\right)\rho_{\mathrm{FCTW},ij}\left(\Delta E_{ij}+\hbar\omega_k^{\mathrm{I}}\right) +N(\hbar\omega_k^{\mathrm{I}})\rho_{\mathrm{FCTW},ij}\left(\Delta E_{ij}-\hbar\omega_k^{\mathrm{I}}\right)\Big]. \tag{6.1}$$

In summary, the transition between localized electronic states is caused by electron-phonon coupling terms. For an intuitive picture we can imagine that a displacement from the equilibrium position along one of these modes *k* with energy $\hbar\omega_k^{\mathrm{I}}$ linearly couples any two electronic states *i* and *j* with a coupling strength $M_{ij,k}$. The transition between states *i* and *j* can be therefore induced by mode *k*, which we call *inducing* mode. We also incorporate the effect of the distance between initial and final states by parametrizing the coupling as $\left|M_{ij,k}\right|^2=M_k^2\sum_n\left(c_{ni}c_{nj}\right)^2$, i.e. states are coupled more if they overlap more (see eq. (5.8)). Considering only the inducing modes, the only allowed transitions would be those between states whose energy difference is $\hbar\omega_k^{\mathrm{I}}$

because one phonon is always created or destroyed in the hopping process. However, transitions between states with larger energy difference are possible via the exchange of multiple phonons with the system. These are the phonons associated with the relaxation of the nuclear geometry following the transition between states *i* and *j*, i.e. in the language of Marcus theory [16], those associated with the reorganization energy λ_{ij} for the hopping process. We have called these modes *accepting* as they can make up for larger energy difference between initial and final states; they are also the modes associated with *polaronic* effects. The total reorganization energy λ_{ij} depends on the single monomer reorganization energy, λ_1, and on the delocalization of both states *i* and *j* through the relation in eq. (5.5). The analytical expression for $\rho_{\mathrm{FCTW},ij}(E)$ given in eqs. (2.6) and (2.7) is more manageable if one makes the customary assumption that $\lambda_{ij}=\lambda_{ij}^{(\mathrm{C})}+\lambda_{ij}^{(\mathrm{Q})}$, i.e. that the reorganization energy is the sum of a classical component due to low frequency modes $\lambda_{ij}^{(\mathrm{C})}=(1-f_{\mathrm{Q}})\lambda_{ij}$, and a quantum component $\lambda_{ij}^{(\mathrm{Q})}=f_{\mathrm{Q}}\lambda_{ij}$, due to one effective *accepting* mode with energy $\hbar\omega^{\mathrm{A}}$. Note that, in the limit $\lambda_1 \to 0$ of hopping between delocalised states, the rate becomes identical to eq. (2.17) as explained in section 2.3.1.

6.2.3 Evaluation of mobility

Given a set of states and hopping rates, the mobility can be computed in several ways. Here we use the method described in section 5.1.5, based on evaluating the steady state solution of the master equation in the limit of low field and low carrier density (i.e. ignoring inter-carrier Coulombic interactions [115]). We will compare the results with experimental data extrapolated to the same limit, while generalizations, including to non-equilibrium situations, would be possible within the model but are not considered here. To evaluate the mobility, one needs to introduce the distance between monomers *d* as an additional model parameter, which we initially set to a value of the correct order of magnitude, 1 nm, while the role of this parameter is further discussed below.

The mobilities obtained from many realizations of the disordered Hamiltonian are normally distributed in the log scale (see Figure 6.1). Therefore, each of the

mobility values reported in this chapter is calculated as $\langle \log \mu \rangle$ (geometric mean) and the corresponding error bar is the standard deviation $\sigma_{\log \mu}$ of the distribution.

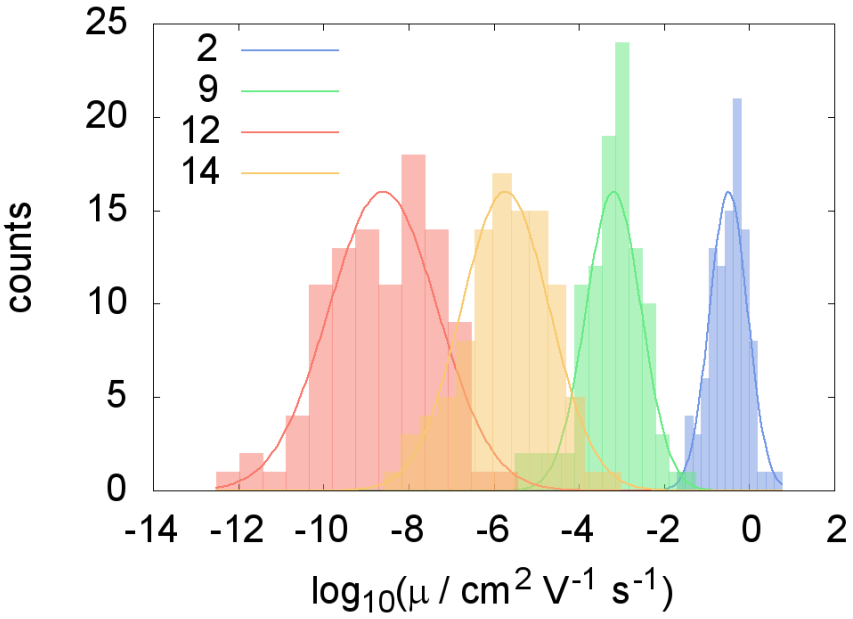

Figure 6.1. Distributions of mobilities obtained from four different disorder models (parameters given in Table 6.1) for 100 realizations of disorder for each model. The solid lines are Gaussian curves with the mean and standard deviation of the distribution.

6.2.4 Summary of the system parameters

To summarize, the model incorporates (i) parameters of the electronic Hamiltonian that determine DOS and localization characteristics (β_0, σ_α, σ_β), (ii) parameters determining the local electron phonon coupling (λ_1, $\hbar\omega^{\mathrm{A}}$, f_{Q}), (iii) parameters determining the non-local electron phonon coupling (the set of $\hbar\omega_k^{\mathrm{I}}$ and M_k), (iv) the inter-monomer distance d. In the next section we will analyse their relative importance attempting to understand which ones actually affect mobility.

6.3 Results and discussion

6.3.1 Role of local electron-phonon coupling

The effect of λ_1 on the mobility is virtually negligible on the $\mu(T)$ curves, as shown in Figure 6.2 for the electronic Hamiltonian models 5 and 12. The result is due to the fact that polaronic effects are negligible when the transport is mediated by fairly delocalized states (which have a negligible reorganization energy), an assumption

implicit in many of the models proposed so far, which is therefore validated by our more general model. This observation is in contrast with the extremely important role attributed to λ_1 in works considering the hopping rate between small molecules.[268] The limited importance of polaronic effects makes completely unimportant also the parameters that control their detail, i.e. $\hbar\omega^A$ and f_Q (see middle and bottom panels of Figure 6.2). For the remainder of this work, we have set the relevant parameters to realistic values: λ_1 = 0.45 eV [141,251], $\hbar\omega^A$ = 0.198 eV, f_Q = 0.4 [142]).

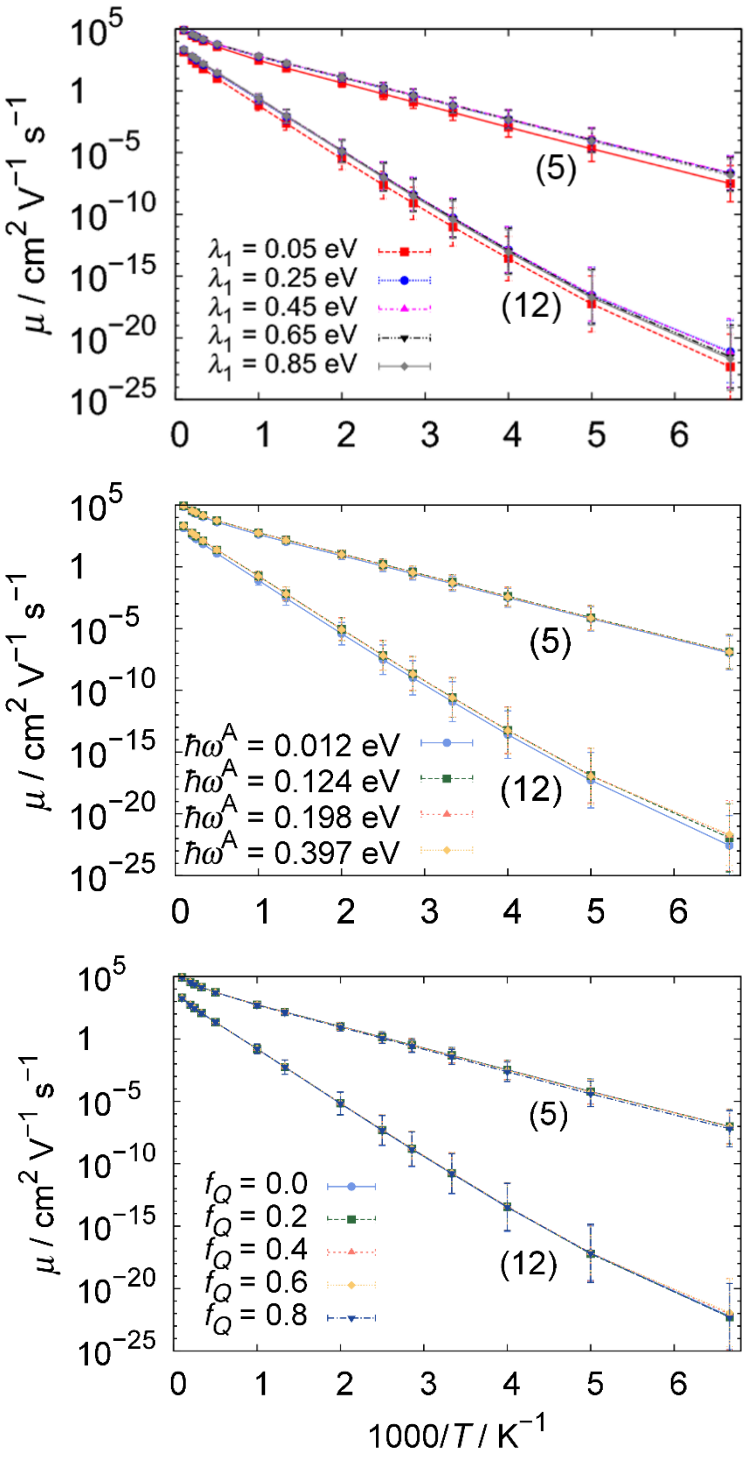

Figure 6.2. Mobility as a function of temperature computed using different values for the reorganization energy of the single site λ_1 (top), energies of the accepting mode $\hbar\omega^A$ (middle), and fractions f_Q of reorganization energy treated quantum mechanically (bottom). Results are shown for disorder models 5 and 12 (but are similar for any disorder model). They are computed using model (a) (see caption of Figure 6.3) for the inducing modes (non-local electron-phonon coupling).

6.3.2 Role of non-local electron-phonon coupling

The inducing modes participate to the rate expression in eq. (6.1) through the mode frequencies $\hbar\omega_k^{\mathrm{I}}$ and coupling strengths M_k^2 and there are in principle many conceivable possibilities. However, we show in Figure 6.3 that the $\mu(T)$ curves do not change much if we consider different combinations of low and high frequency inducing modes, provided that $\sum_k M_k^2$ is kept constant. In particular, the differences between the results obtained from different distributions of $\hbar\omega_k^{\mathrm{I}}$ values are negligible if one excludes the very unphysical model where there is a single high frequency inducing mode. The numerical results suggest that one can capture the variability between chemical systems simply by considering only one low frequency inducing mode (model (a) in Figure 6.3), and therefore a single parameter M^2 (now dropping the suffix *k*) that is essentially a measure of how effectively the nuclear motions mix the electronic states. The parameter M^2 is ultimately just a pre-factor multiplying each rate (see eq. 2). As the mobility obviously scales as the squared distance between sites d^2, the product d^2M^2 can be taken as one single effective parameter directly proportional to the mobility and the only relevant parameter beside those defining the electronic Hamiltonian in eq. (5.1). To obtain realistic ranges of mobilities with the choice of *d* equal to 1 nm, the results are presented with *M* set to $2.0 \cdot 10^{-2}$ eV. However, the conclusions do not depend on this pair of choices.

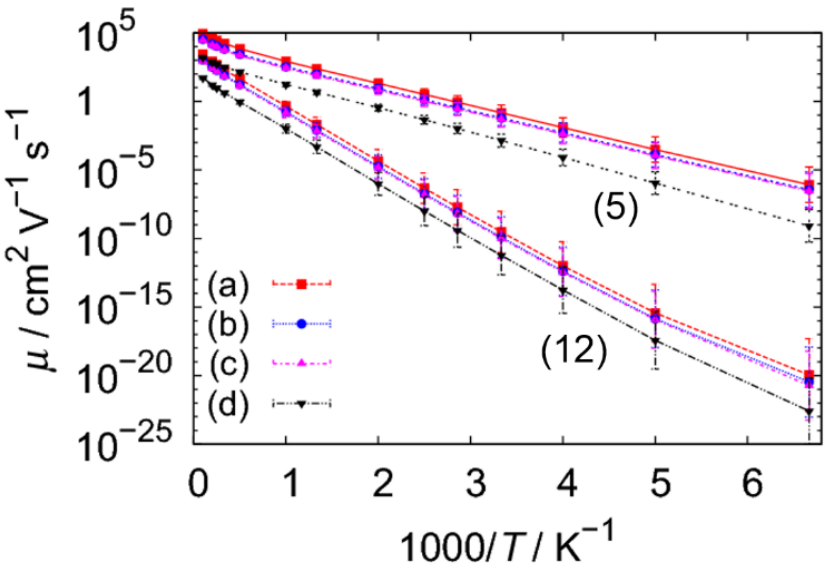

Figure 6.3. Mobility as a function of temperature for disorder models 5 and 12 computed using four different models for the inducing modes. The inducing mode frequencies $\hbar\omega_k^{\mathrm{I}}$ and coupling strengths M_k^2 have been set as follows. Model (a): one low energy mode (6.2 meV); model (b): four modes from low to intermediate energy (6.2, 12.4, 37.2, 49.6 meV); model (c): five modes from low to high energy (6.2, 12.4, 37.2, 49.6, 186 meV); model (d): one high energy mode (186 meV). The values of M_k^2 have been chosen to be identical for all inducing modes with strength such that $\sum_k M_k^2 = 4.0 \cdot 10^{-4}$ eV^2 to reproduce the experimental range of mobilities.

6.3.3 Temperature dependence of mobility

To evaluate the role of the type and magnitude of disorder we have computed the temperature dependent mobility for the range of models reported in Table 6.1 and reported the results in Figure 6.4. The first key observation is that the $\mu(T)$ curves are non-intersecting, i.e. the effects of different types of disorder (diagonal, off-diagonal, combined), different inter-monomer coupling, and different on-site energy alternation can be combined together into *just one* effective disorder parameter that differentiates the various systems. As the log (μ) vs 1/T plot is well fitted by a straight line, each $\mu(T)$ curve can be associated with an activation energy, which can offer a natural measure of the combined effect of all types of disorder. In the infinite temperature limit the mobility seems to converge to a very limited range of values (100-4000 cm^{2}V^{-1}s^{-1} with our choice of d^2M^2).

The results of the model are strikingly similar to the experimental results reported by Blom et al. [113,114] for a broad range of chemically different organic

semiconductors and also reported in Figure 6.4. All experimental data can be fitted by an Arrhenius temperature dependence $\mu = \mu_0 \exp\left(-E_a / k_B T\right)$ at low field and low charge density. There seems to be a common infinite temperature mobility μ_0 = 30 $cm^2V^{-1}s^{-1}$ valid for all materials considered. It was therefore proposed that there is a single material-specific parameter determining the temperature dependent mobility in all organic semiconductors. A $1/T$ dependence seems to contradict the $1/T^2$ dependence predicted from models based on hopping in a Gaussian DOS. It has been argued that in organic diodes the average charge carrier density in a device at zero bias exceeds 1×10^{21} m^{-3} due to the diffusion of charges from the contacts.[113] The presence of such a finite carrier density would then cause the mobility to follow a $\log(\mu) \propto 1/T$ temperature dependence over the temperature range where *J–V* measurements are usually carried out.[114] However, the model calculations presented here demonstrate that an Arrhenius-like temperature dependence is a fundamental property of transport along polymer chains.

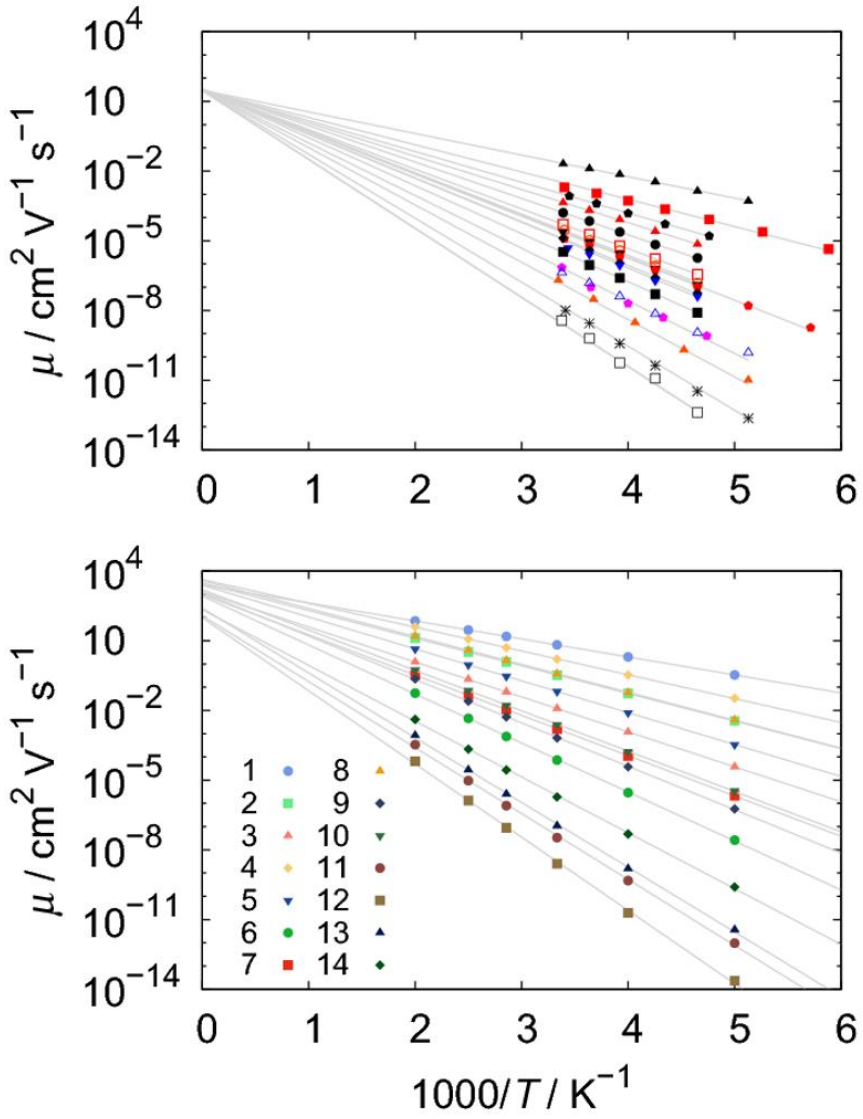

Figure 6.4. (Top) experimental hole mobility vs. 1/*T* for a range of organic semiconductors, adapted from ref. [113] and augmented with additional data points.[114] (Bottom) mobility vs. 1/*T* from various models of chains of 1000 monomers with a variety of disorder parameters (see Table 6.1), including an alternating copolymer (model 14). The lines are obtained from least squares linear fitting of log μ vs. 1000/*T*.

According to our model, $\mu(T)$ only depends on *two* parameters, a combined effect of disorder (which determines the activation energy) and the weighted strength of the electron-phonon coupling, d^2M^2, acting as a pre-factor for our computed mobility. To fully account for the experimental observation we can speculate that the parameter d^2M^2 is approximately a constant for this class of materials. The scaling of *d* and *M* supports this idea. One can partition the polymer into nearest neighbour interacting sites in different ways, e.g. considering a smaller or larger unit to take as "the monomer", and this partition defines the other parameters of the model.

According to the definition of M, the product dM should remain constant in order to have consistent models with different definitions of the monomer length, e.g. if we consider larger monomers, the effect of inducing modes will be weaker. As we have noted when we discussed the negligible importance of reorganization energy, the most effective charge hopping events involve fairly delocalized states (tens of monomers) and it is therefore not surprising that the electron-phonon coupling terms, being averaged over a large portion of the material, become weakly dependent on the chemical detail for similar classes of compounds.

6.4 Conclusion

In this chapter we performed a parameter space exploration of a generic charge transport model suitable for realistic polymers in the limit of low charge density and electric field. We have found that the temperature dependence of the mobility of conjugated polymers is determined by just two effective parameters, even though the model itself depends in principle on many tens of parameters. Remarkably, we find that polaronic effects, very different from system to system, are irrelevant for the computed mobility. The model helps explaining the experimental observation of a universal temperature dependence of the mobility determined by a single experimental parameter. To fully account for the experimental observation we have tentatively speculated that the strength of the mixing between electronic states due to the inducing modes is similar across all materials considered.

7. Effect of chain rigidity and inter-chain hopping on charge transport in 3D disordered polymer networks

Summary: In this chapter the single-chain charge transport model presented in the previous chapters is generalised by adding the ability to model the three-dimensional (3D) conformation of the polymer chains and the possibility of hopping between chains. The disordered 3D structures of the chains, whose rigidity is determined by the persistence length, are generated with a worm-like chain model. Their disordered electronic structures are obtained from a tight binding Hamiltonian such as that in eq. (5.1). After determining the correct form of the rates for hopping along the chains and to other chains, the ratio between them is set to a value which makes mobility independent of the chain length. Charge mobility as a function of the parameters of the model is computed from kinetic Monte Carlo simulations. The influence of persistence length on mobility is evaluated independently from the effect of electronic disorder. The mobility is linearly dependent on the persistence length, but the activation energy obtained from the temperature dependence is found to be independent from the persistence length, i.e. it is determined only by electronic disorder.

7.1 Introduction

The relationship between morphology and charge transport in semiconducting polymers is not as straightforward as it may appear. As mentioned in section 1.3, the simple and intuitive notion that more disorder determines lower charge mobility, supported by the success of the highly crystalline regioregular P3HT compared to amorphous polymers, [79,80] led the research community to design new polymers or improve existing ones with the goal of increasing long-range order and crystallinity. This design strategy was partly successful, resulting in an order of magnitude increase in mobility in the decade 2000-2010.[81] At the present day, the understanding of structure-property relationships semiconducting polymers has changed considerably. The discovery of donor-acceptor polymers, which are often weakly ordered but outperform the more ordered ones, has led to a new set of design rules which embrace disorder and deal with it rather than trying to remove it.[90] By enunciating these design rules, it is possible to summarise the characteristics of an ideal high-mobility semiconducting polymer, going from the microscopic to the macroscopic scale:

i) *Resilience to disorder* of the electronic structure ensures efficient transport along the polymer chains.[90] The backbone is rather planar[87] and torsion-free,[88] and/or the couplings between monomers are insensitive to dihedral angle rotations,[86] resulting in lower electronic disorder. Dynamical self-healing of electronic traps can also induce tolerance to disorder.[85] An alternating donor-acceptor structure causes a narrower transport band which can improve mobility if the effect of lower activation energy compensates for the reduced inter-monomer coupling (section 1.1.1).

ii) *Presence of non-crystalline short-range aggregates*.[83][84] Their function is to ensure that charges can hop to other chains. Aggregates can be small and disordered but need to be well-interconnected to form a continuous network of charge transport pathways. The connections between aggregates are ensured by transport along chains in disordered regions, which need to be long enough for this purpose.

iii) *Absence of big crystallites* which would make the material less uniform,[91,92] making processing more difficult. Crystallites are also subject to paracrystalline disorder which creates localized trap states,[269] therefore slowing down the charges crossing large ordered regions.

The motion of charges in polymeric materials can be essentially described as one-dimensional (1D) hopping[270] along three-dimensional (3D) chains with an occasional transfer to other chains (inter-chain hopping).[105] The charge transport model presented in chapter 5 was shown to correctly describe the relationship between mobility and electronic disorder. Its validity was further confirmed in chapter 6 by showing that it qualitatively reproduces the universal temperature dependence of mobility experimentally measured in a wide range of disordered polymers (see Figure 6.4). However, the model described in chapters 5 and 6, valid for 1D transport, was based on a few (reasonable) approximations. The role of inter-chain hopping was neglected, an assumption valid in the limit of very rigid (straight) chains.[246] Accordingly, the polymer chains were assumed to be completely straight and aligned with the applied electric field, thereby neglecting the 3D conformation of realistic chains. Finally, periodic boundary conditions (PBC) were applied along the chains, effectively making them of infinite length, in order to make the results independent of the chain length and to ensure the existence of a steady state, useful to compute the mobility analytically from the hopping rates.

The aim of this chapter is to generalise this model by removing these approximations. To this end, new features are introduced into the theoretical model described in chapter 5 in order to understand how they affect the charge transport mechanism. The role of disordered 3D conformations of the polymer chains and the interplay between intra- and inter-chain hopping have been studied by the Spakowitz group in a series of papers.[105–107] Their results highlighted the multiscale character of charge transport in polymers, with high on-chain mobility at short timescales and much lower macroscopic mobility (limited by inter-chain hopping) at longer timescales. In their model, the charge motion is described as a series of intra-chain hopping events with occasional inter-chain hopping, but charge transfer only takes places between states localized on neighbouring monomers, i.e. the electronic disorder of the chains (due to variations in couplings between monomers) is neglected. In our model, described in this chapter, we will generate the 3D conformations with a worm-like chain (WLC) model implemented as in ref. [105], a well-established simplified model describing the geometric structure of semiflexible polymer chains. The rigidity of the chains is determined by just one parameter: the persistence length in units of the distance between monomers. The main innovation introduced here is to associate to this disordered WLC geometric structure an electronic structure obtained from a tight binding model Hamiltonian, which was shown in the previous chapters to correctly describe a realistic density of states with variable delocalization. The kinetic rates for intra- and inter-chain hopping are given by the very general expression derived in chapter 2. The appropriate form of the inter-chain hopping rate will be discussed in section 7.2.4, and the relative frequency of intra- and inter-chain hopping will be set to a value which makes mobility independent from the chain length. A kinetic Monte Carlo method will then be used to simulate charge transport in a disordered 3D network of polymer chains: after hopping along the chain, the charge is allowed to escape from the chain and continue the trajectory on another chain with a different structure and random orientation. Finally, the dependence of mobility on the system parameters in the limit of low charge density is investigated and discussed.

7.2 Methodology

7.2.1 Worm-like chain conformation

The worm-like chain (WLC) model, first introduced by Kratky and Porod [271] to compute the persistence length of polymers in solution from X-ray scattering data, has often been used to describe the dynamical behaviour of semi-flexible polymer chains, especially in its continuous formulation.[272–274] Here we adopt a discretized version of the continuous WLC model and implement it as described in ref. [105]. The fundamental unit of our model is the monomer, or repeating unit, constituting the polymer. The rigidity of the polymer chain is determined by the reduced persistence length $\varepsilon_{\mathrm{b}} = l_{\mathrm{p}} / d$ (also called bending modulus) where l_{p} is the persistence length and *d* is the distance between repeating units (monomers), which is set to an arbitrary but realistic value of 1.0 nm as in chapters 5 and 6, in accordance with previous works. The segment connecting the first two monomers is randomly oriented with uniform distribution in 3D space, thus making the system isotropic, and the relative position of each successive monomer is determined as follows. The bending angle $0 \le \theta \le \pi$ between three successive monomers (see Figure 7.1) is randomly chosen from the probability distribution [105]

$$p(\theta) = \frac{\varepsilon_{\mathrm{b}} \sin\theta}{2 \sinh \varepsilon_{\mathrm{b}}} \exp\left(\varepsilon_{\mathrm{b}} \cos\theta\right). \tag{7.1}$$

The dihedral angle $0 \le \phi \le 2\pi$ (defined by four successive monomers) is randomly chosen from a uniform distribution. These steps are repeated until a chain of *N* monomers has been built.

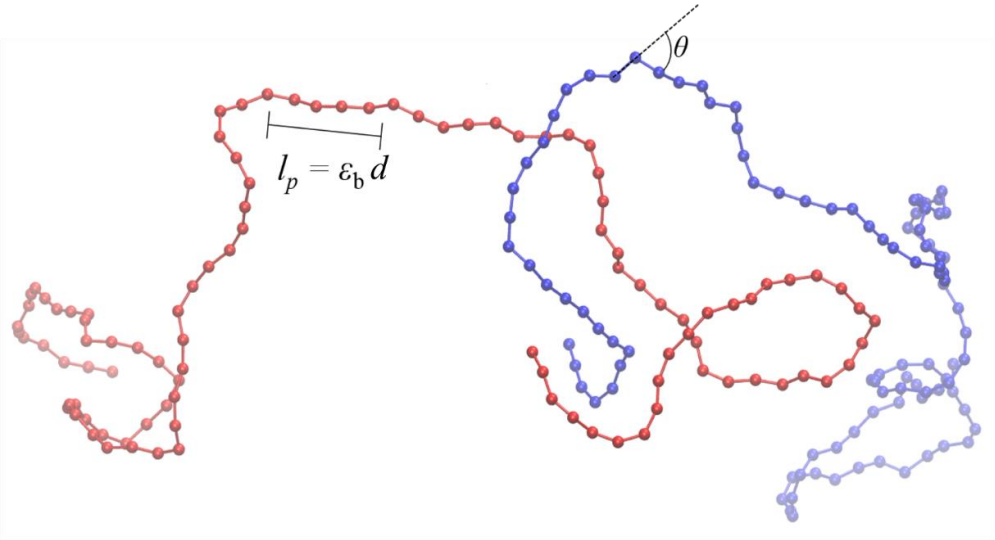

Figure 7.1. Representation of two worm-like polymer chain structures with reduced persistence length $\varepsilon_b = 5$. θ is the bending angle chosen according to eq. (7.1).

7.2.2 Electronic Hamiltonian

The adiabatic electronic states involved in charge transport in semiconducting polymers tend to delocalize along the conjugated backbone and can be localized by two distinct effects: polaronic effects (electron-phonon coupling) and static (structural) electronic disorder.[94] Since in polymers transport is mediated by fairly delocalized states,[110,254] the electron-phonon coupling is usually weak and the leading cause of localization is electronic disorder rather than polaronic effects, as discussed in section 5.1.2. Electronic disorder can in general be caused by variability of the diabatic site energies (diagonal disorder) and of the couplings between sites (off-diagonal disorder). A number of atomistic studies [85,110,122] have determined that the main cause of localization is off-diagonal disorder, since the couplings are strongly affected by the rotation angles between conjugated subunits. These angles are determined at the atomistic level and are related to the planarity of the conjugated backbone, but they are distinct from, and not necessarily correlated with the dihedral angles ϕ determining the chain conformation in the coarse-grained WLC description (see previous section). In other words, the off-diagonal disorder can more safely be assumed not to be correlated with the 3D conformation of the chain, in agreement with atomistic studies which found no evidence of such correlation.[110,122]

A realistic electronic energy landscape of a polymer chain can be easily obtained from the diagonalization of a disordered tight binding Hamiltonian identical to that in eq. (5.1), with the exception of the PBC term which will be removed as indicated in

the ensuing discussion. We include only one type of disorder (off-diagonal) since combinations of different types of disorder were previously shown to affect charge transport as just one effective parameter (see chapter 6). From the diagonalization of $\hat{H}_{\text{el}}$ we obtain N one-electron states with energies E_i and wavefunctions $\psi_i = \sum_n c_{ni} |n\rangle$, where E_i are the eigenvalues and c_{ni} are the eigenvectors. The position of the charge in state i is defined as $\mathbf{r}_i = \sum_n |c_{ni}|^2 \mathbf{s}_n$ where $\mathbf{s}_n$ is the position of monomer n. The degree of delocalization is expressed in terms of the inverse participation ratio $\text{IPR}_i = \left(\sum_n |c_{ni}|^4 \right)^{-1}$, a measure of how many monomers share the charge in state i.

7.2.3 Dynamics along a single chain: charge transfer rate

Charge transport along one polymer chain is described as incoherent hopping in a disordered electronic energy landscape of states obtained from the diagonalization of a Hamiltonian such as eq. (5.1). A general expression for the kinetic rate of charge transfer in semiconducting polymers was described in detail in chapter 2. We have established in chapter 6 that a limited number of parameters are necessary to describe the phenomenology of charge transport across many polymers. In this chapter, instead of exploring all possible parameters entering the rate, we use for the transition between any two states i and j a simplified expression that was proven to capture the physics of transport across many different materials:

$$\begin{aligned} k_{ij} = \frac{\pi}{\hbar} M^2 |S_{ij}|^2 \Big[& \left(N(\hbar\omega_I) + 1 \right) \rho_{\text{FCTW},ij} \left(\Delta E_{ij} + \hbar\omega_I \right) \\ & + N(\hbar\omega_I) \rho_{\text{FCTW},ij} \left(\Delta E_{ij} - \hbar\omega_I \right) \Big], \end{aligned} \tag{7.2}$$

where the non-local electron-phonon coupling strength M, defined in eq. (2.8), is set to 0.02 eV as discussed in section 6.3.2, and $|S_{ij}|^2 = \sum_n |c_{ni}|^2 |c_{nj}|^2$ is the spatial overlap between states i and j. $N(\hbar\omega_I)$ is the phonon occupation number (see eq. (2.14)) of a nuclear mode of energy $\hbar\omega_I$ = 6.2 eV (defined in eq. (2.8)). Following the discussion in section 6.3.1, we adopt the fully classical version of the Franck-Condon and temperature weighted density of states, which is identical to eq. (2.5):

$$\rho_{\text{FCTW},ij}(\Delta E) = \sqrt{\frac{1}{4\pi\lambda_{ij} k_{\text{B}} T}} \exp\left(-\frac{(\Delta E + \lambda_{ij})^2}{4\lambda_{ij} k_{\text{B}} T} \right), \tag{7.3}$$

where the reorganization energy λ_{ij} is defined in eq. (54) and (55) and λ_1 is set to 0.45 eV (see section 6.3.1). The energy difference ΔE_{ij} is modified by the applied electric field **F** as

$$\Delta E_{ij} = \Delta E_{ij}^0 - q\mathbf{F}\cdot\left(\mathbf{r}_j - \mathbf{r}_i\right), \tag{7.4}$$

where ΔE_{ij}^0 is the electronic energy difference in absence of the field and $\mathbf{r}_i$ is the position of the charge in state *i* as defined in section 7.2.2. The electric field **F** is applied along the direction *x* for simplicity in the remainder of this chapter.

7.2.4 Rate of escape from a polymer chain

The description of charge hopping in a disordered polymer solid is completed by including the possibility of hopping to different chains. We assume that the rate of hopping to different chains (escape rate) has the same form of the intra-chain hopping rate, but with a different (smaller) electronic coupling. The resulting expression is therefore identical to eq. (7.2), but M^2 is substituted with the average inter-chain coupling $|V|^2$. Consequently, the probability of escaping from the chain starting from any initial state *i* is

$$p_{\text{esc}} = \frac{\sum_j k_{ij}^{\text{escape}}}{\sum_j k_{ij}^{\text{escape}} + \sum_j k_{ij}} = \frac{|V|^2}{|V|^2 + M^2} \tag{7.5}$$

An alternative expression considered for the escape rate:

$$k_i^{\text{escape}} = \frac{2\pi}{\hbar}|V|^2\, LDOS(E_i), \tag{7.6}$$

which was derived assuming that it depends just on the local density of states $LDOS(E_i)$ of the material at the energy of the initial state E_i, resulted in a positive curvature of the $\log(\mu)$ vs. $1/T$ curve (see Figure 7.2) in disagreement with existing theoretical models and experiments. Eq. (7.5) is therefore adopted in the remainder of this chapter since it yields a linear temperature dependence which does not contradict experimental results such as those reported in Figure 6.4.[113,114]

7.2.5 Kinetic Monte Carlo simulation

The incoherent dynamics of a charge moving in a polymeric material is described as a series of hopping events between electronic states in a 3D network of chains. In chapters 5 and 6 we were able to compute the mobility analytically from the steady

state solution of the master equation of the system (see section 5.1.5), where the system was a single periodic chain. Here we cannot define a steady state since we consider finite chains and we are interested in the mobility of charges hopping along chains and between different chains. The kinetic Monte Carlo (kMC) technique is the most straightforward numerical method for simulating incoherent hopping and has been widely employed in studies of charge transport in disordered materials including polymers.[99,105,251,275] To study the charge mobility arising from a combination of intra- and inter-chain hopping we employ a simple kMC algorithm outlined below. We are considering the special case of low charge density with only one charge carrier present in the system. At each MC step, the charge can either hop to another state in the same chain with rate given by eq. (7.2) or it can escape from the chain with probability p_{esc} (eq. (7.5)) and continue moving along a different chain which has a different structure and random orientation in space. For convenience, a large number W of chains and random electronic Hamiltonians are generated and diagonalized before starting the simulation. W is chosen to be large enough not to affect the results. Each chain is characterized by a sequence of monomer coordinates, eigenvalues $\{E_i\}$ and eigenvectors, and average positions $\{\mathbf{r}_i\}$ of each eigenstate. The kMC algorithm for one trajectory is briefly outlined as follows:

(i) Randomly initialize the carrier on one initial state on one of the chains.

(ii) Compute the rates k_{ij} (for $j = 1 \ldots N, j \neq i$) from state i to all other states on the same chain (eq. (7.2)).

(iii) Randomly choose a hopping process to a state j with probability proportional to the relative rate. Update the time with time step $dt = \ln(1/u) \Big/ \left(\sum_{j \neq i} k_{ij} + p_{\text{esc}} k_{ij} \right)$, where u is a uniform random number in the interval $0 \leq u < 1$ and update the position as $\mathbf{R}(t) = \mathbf{R}(t - dt) + (\mathbf{r}_j - \mathbf{r}_i)$.

(iv) Randomly choose if the charge escapes from the chain with probability p_{esc}. In this case, the trajectory continues from step (ii) on a different chain, chosen randomly among those previously generated, and from a state with energy closest to the energy of the final state j in the original

chain. If the charge does not escape, the trajectory continues from step (ii) on the same chain.

The relevant observables saved at each timestep t (or at pre-determined time bins) are the position $\mathbf{R}$ (displacement from the origin of the trajectory) and the elements $R_\alpha F_\beta$ of the tensor $\mathbf{R}\times\mathbf{F}$ (outer product of displacement and field), where $\alpha, \beta = x, y, z$. From these tensor elements one can obtain the drift mobility tensor

$$\mu_{\alpha\beta}^{F}(t) = R_\alpha F_\beta \Big/ \left(t \cdot \|\mathbf{F}\|^2\right). \tag{7.7}$$

Each trajectory is considered to be converged when the xx component of the drift mobility $\mu = \mu_{xx}^{F}$ (with field applied along x) varies by less than 1% in 3 consecutive sampling points. The mobilities reported in this chapter are the geometric average $\langle \log(\mu) \rangle$ (see section 6.2.3) of the mobilities obtained from several trajectories, each starting from a different chain.

7.2.6 Parameter ranges considered in this study

The internal (chemical) parameters of the model are (i) the electronic disorder in the Hamiltonian σ_β, (ii) the reduced persistence length ε_b controlling the rigidity of the chain and (iii) the escape probability p_{esc}. The distance between monomers d sets the length scale of the system and is kept constant to 1.0 nm (see section 7.2.1). The charge displacement associated with the rather infrequent inter-chain hopping, expected to be very small, is assumed to be zero to avoid introducing new parameters with no effect on the final result. The external parameters are the electric field $\mathbf{F}$ (applied only along x for simplicity) and the temperature, both affecting the intra-chain hopping rates. As we did not want to consider the effect of finite polymer length we have set the length of the chains to a number sufficiently large that does not affect the results.

Table 7.1. Parameters of the model.

Description	Parameter	Value
number of monomers	N	$\rightarrow \infty$
number of chains	W	$\rightarrow \infty$
Spatial structure (WLC)		
distance between monomers	d	1.0 nm
adimensional persistence length	ε_b	2 - ∞
Electronic structure (Hamiltonian)		
mean coupling between monomers	β_0	1 eV
off-diagonal disorder	σ_β	0.08 - 0.12 eV
Intra-chain hopping rate		
temperature	T	150 - 500 K
electric field ($F = F_x$)	F	10^2 - 10^6 V/cm
Escape rate		
escape probability	p_{esc}	10^{-7} - 10^{-3}

7.3 Results and discussion

The charge transport model described in the previous section is used to compute mobility as a function of a range of parameters. The main innovations introduced here with respect to the model described in chapters 5 and 6 are the possibility of jumping to other chains (inter-chain hopping), the finite chain length and the 3D conformation of the chain. Furthermore, here the mobility is obtained numerically with the kinetic Monte Carlo (kMC) method rather than from the analytical steady-state solution of the master equation. To test the validity of the new method, we start from a 1D system identical to that described in chapter 6, then introduce the new features one by one. First, we will introduce inter-chain hopping and determine the correct form of the escape rate, then we will remove the PBC (making the chains finite) and set the frequency of escape events to a value making the finite chain effect irrelevant. Finally, we will introduce the 3D conformation of the chains to assess the role of chain rigidity and examine the dependence of mobility on electric field and temperature.

7.3.1 Transport along 1D rigid parallel chains with inter-chain hopping

A 1D system is built as a special case of the WLC model described in section 7.2.1 by generating straight chains with bending modulus $\varepsilon_b = \infty$ (all bending angles = 180°), all parallel and aligned with the *x* axis (no rotation is applied). We first verify that the kMC simulations correctly describe charge transport along a single chain with PBC (infinite chain): the temperature dependence of mobility obtained analytically in chapter 6 (Figure 6.4 (Bottom), model 2), is reproduced by the kMC simulations starting from the same parameters (results not shown).

We consider next the same 1D system of straight rigid chains with PBC, but we introduce the possibility of inter-chain hopping. The temperature dependence of mobility in the absence of escape (single chain) and with escape probability p_{esc} in the range 10^{-7} - 10^{-3} is shown in Figure 7.2. When $p_{esc} \leq 10^{-5}$ the $\log(\mu)$ vs. $1/T$ curves are almost identical to those obtained without escape, i.e. the system approaches the single chain limit. A slighly higher mobility at low temperature is attributable to the fact that the charge can explore other chains with different electronic structures and thereby avoid the electronic traps found along a single chain. This effect becomes dominant when $p_{esc} > 10^{-5}$, determining an almost constant increase of mobility across the whole temperature range. Figure 7.2 also shows that using the alternative escape rate in eq. (7.6), i.e. assuming a lower activation energy for inter-chain transport than for intra-chain transport, would result in a $\log(\mu)$ vs. $1/T$ curve with a strong positive curvature. Since this behaviour is not predicted by any model, nor has not been observed experimentally in any real polymer, where mobility is surely determined by both intra- and inter-chain transport, it can be concluded that the activation energy must be the same for intra- and inter-chain transport in order to explain the universal Arrhenius temperature dependence observed in a wide range of polymers (see Figure 6.4).[113,114] There is also some experimental evidence supporting the anisotropy of the activation energy in aligned polymer films.[276] The most straightforward way to interpret this behaviour is to assume that the intra- and inter-chain hopping rates must have the same dependence on energy and temperature, i.e. they have the same form but with a different prefactor as discussed in section 7.2.4. Therefore, we choose to adopt this assumption, rather than the alternative escape rate in eq. (7.6), since it is consistent with the experimental data.

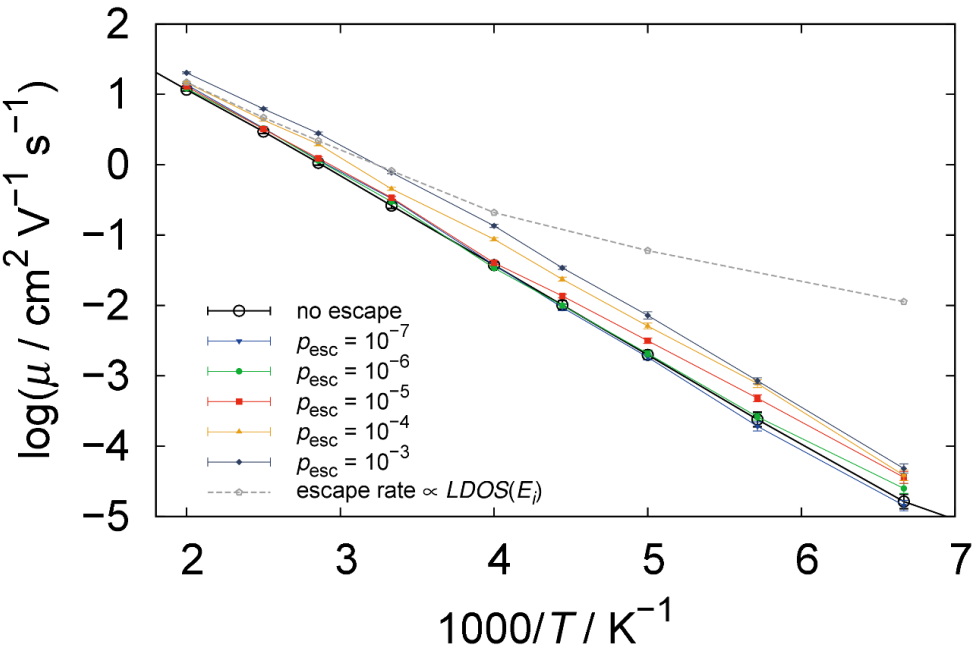

Figure 7.2. Temperature dependence of mobility in a 1D system of parallel straight chains of length N = 2000 monomers with PBC. Each curve is obtained with a different value of the escape probability p_{esc} shown in the legend. The blue data points are obtained using the rate in eq. (7.6) with $V = 5 \cdot 10^{-4}$ eV, which determines an observed escape probability in the range $4 \cdot 10^{-3}$ - $3 \cdot 10^{-4}$ going from low to high T. Electronic disorder σ_β = 0.1 eV. Electric field $F = 10^3$ V/cm. Each data point is averaged over 100 trajectories.

Since our final goal is to study mobility in a realistic morphology composed of finite chains, we need to assess the effect of finite chain length by comparing the temperature dependence of mobility of the 1D system with and without PBC. The results obtained for different values of the escape probability p_{esc} are shown in Figure 7.3. When $p_{esc} \leq 10^{-5}$, removing the PBC drastically reduces mobility, because the charge can rarely escape the chain and transport becomes limited by chain length. It should be noted that this effect also causes the $\log(\mu)$ vs. $1/T$ curves to bend down with increasing T as transport becomes increasingly dependent on long-range intra-chain hops mediated by more delocalized states at higher energies. This finite chain effect decreases when p_{esc} is increased and eventually disappears when $p_{esc} = 10^{-3}$, which is therefore chosen as the minimum escape probability for which the chain length N = 2000 does not affect mobility. Intuitively, in this regime the charges can hop to other chains before they hit the chain end. We choose this regime in order to study the effect of the chains' 3D geometry separately from the effect of chain length,

but the model is also suitable to compute mobility of polymers with shorter chains, i.e. when charge transport is affected by chain length.

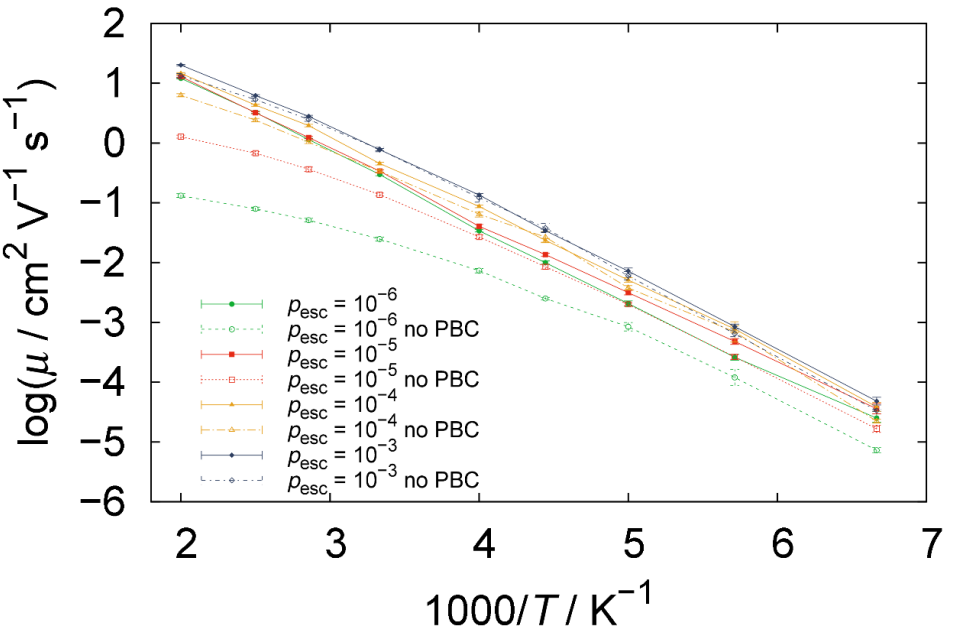

Figure 7.3. Temperature dependence of mobility in a 1D system of parallel straight chains of length N = 2000 monomers with and without PBC (solid and dashed lines respectively). Each curve is obtained with a different value of the escape probability p_{esc} shown in the legend. Electronic disorder σ_β = 0.1 eV. Electric field $F = 10^3$ V/cm. Each data point is averaged over 100 trajectories.

We examine next the dependence of mobility on the applied electric field in the same 1D systems considered so far, which is shown in Figure 7.4. At low to intermediate field strength ($F < 4{\cdot}10^3$ V/cm), μ is independent of the field (linear regime) in all systems. The introduction of inter-chain hopping causes μ to increase, and μ is independent of the chain length as previously observed in Figure 7.2. At higher fields ($4{\cdot}10^3 < F \leq 2{\cdot}10^4$ V/cm), in the periodic systems μ increases nonlinearly as long-range hops are activated by the field (see also Figure 5.4 in section 5.2.2). Since the same values of μ are observed in the periodic systems both with and without inter-chain hopping, we conclude that transport is dominated by intra-chain hopping in this regime. When the chain length is finite, however, μ remains almost constant and then decreases in the same field range, confirming that transport is limited by chain length and dominated by intra-chain hopping. Finally, when $F \geq 2{\cdot}10^4$ V/cm we observe the trivial high field regime where $\mu \propto 1/F$ as predicted by analytical GDM models.[252] For the purpose of this work, where we are interested in the low field

transport regime, this analysis confirms that $F = 10^3$ V/cm is a sufficiently low value for transport not to be affected by the field nor by the chain length.

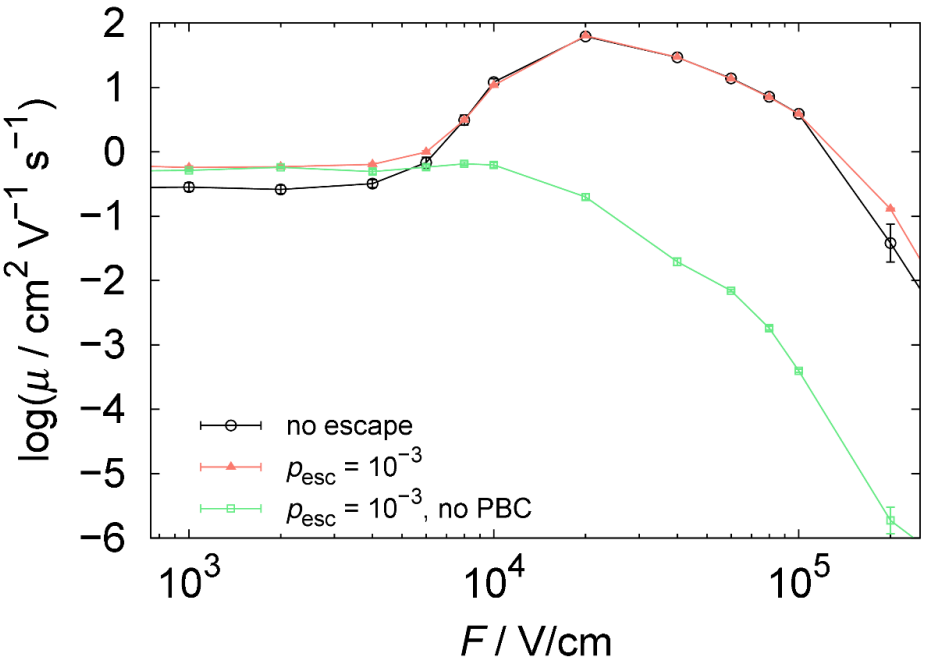

Figure 7.4. Field dependence of mobility in 1D systems of parallel straight chains of $N = 2000$ monomers. The systems shown in the legend are respectively: infinite chains without inter-chain hopping, infinite chains with inter-chain hopping and finite chains with inter-chain hopping. Electronic disorder σ_β = 0.1 eV. Escape probability $p_{esc} = 10^{-3}$, temperature 300 K. Each data point is averaged over 20 trajectories.

7.3.2 3D chains

Once the effects of inter-chain hopping and finite chain length on 1D transport are understood, we proceed to introduce the main feature of this model, i.e. the 3D spatial conformation of the chains, and study how the charge transport properties depend on the chain rigidity determined by the reduced persistence length ε_b. As explained in section 7.2.2, we do not assume any correlation between the electronic disorder σ_β and the 3D structure. Therefore, we investigate the effect of changing ε_b while keeping σ_β constant, which implies that the energy levels and the delocalization of the states along the polymer backbone (quantified by the IPR) will not change while the distances between states will decrease when ε_b is decreased, as the chains will become more coiled. In order to understand the limits of the model, we report results obtained from the largest possible range of chain rigidity: the chains with $\varepsilon_b = 2$ are

extremely coiled and those with $\varepsilon_b = \infty$ are perfectly straight but with random orientation in 3D space.

The field dependence of the mobility μ in systems of 3D chains with persistence length in the range ε_b = 2-∞ is reported in Figure 7.5 (the 1D system is shown for comparison). The results show that when ε_b is decreased μ also decreases. In the low field regime μ is independent of F, which we set to 10^3 V/cm in the remaining calculations. The high field regime where $\mu \propto 1/F$ is shifted to higher fields when ε_b is decreased, suggesting that polymers with more coiled chains can sustain higher fields without affecting mobility if the electronic disorder does not increase.

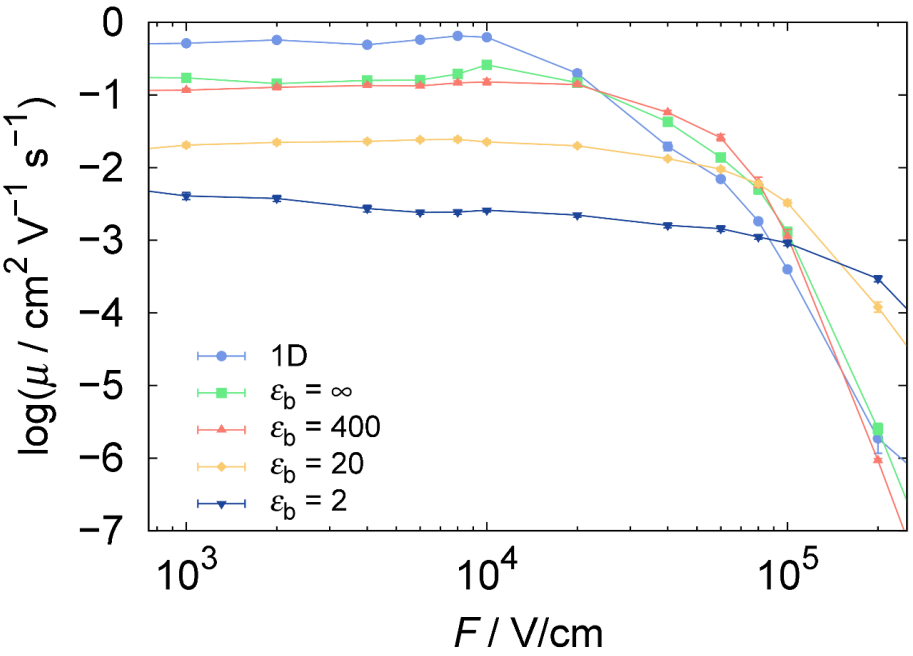

Figure 7.5. Field dependence of mobility in 3D systems with chain length N = 2000 monomers, with persistence length ε_b = 2-∞. 1D system shown for comparison. Escape probability $p_{esc} = 10^{-3}$, temperature 300 K, electronic disorder σ_β = 0.1 eV. Each data point is averaged over 20 trajectories.

The temperature dependence of mobility in the same systems is shown in Figure 7.6. The mobilities follow a linear temperature dependence as illustrated by the grey lines obtained by fitting the data in the range T = 150-250 K. The top panel shows the difference between the 1D and 3D systems and the effect of decreasing chain rigidity. Going from 1D to 3D and changing the parameter ε_b causes the log(μ) vs 1/T curves to shift vertically while the slopes remain almost unchanged. In other words, the spatial arrangement of the chains affects mobility but not the activation energy for

transport when the electronic disorder σ_β is constant. An examination of the log(μ) vs 1/T plots reported in the bottom panel of Figure 7.6, which are obtained from different combinations of σ_β and ε_b, confirms that ε_b acts as a scaling factor for μ and the activation energy is determined only by electronic disorder. For each value of ε_b, the curves with different amounts of electronic disorder σ_β do not intersect and converge to a narrow range of infinite temperature mobility μ_0 (as defined in section 6.3.3), but each value of ε_b seems to define a different value of μ_0. The effect of persistence length on the field and temperature dependence can be qualitatively explained by the fact that having more coiled (less rigid) 3D chain conformations reduces the distances between electronic states. Since mobility scales as the square of the average hopping distance, the persistence length affects mobility at all temperatures as observed in Figure 7.6 but does not add electronic disorder to the system. Similarly, the effect of persistence length on the field dependence (Figure 7.5) can also be explained by reduced distances between states: a larger field is required to match a given energy difference between two states when the distance between them is decreased (see eq. (7.4)).

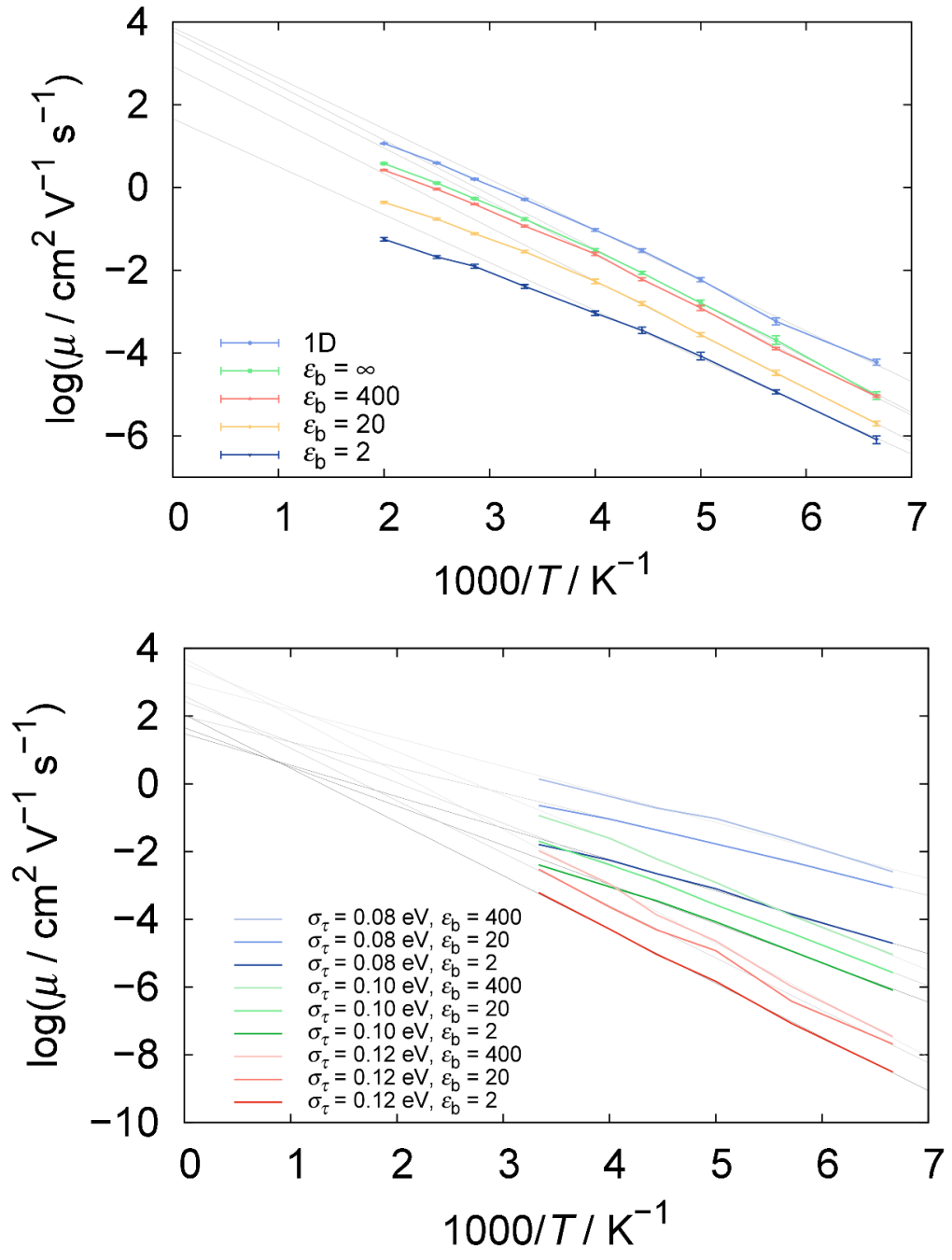

Figure 7.6. Temperature dependence of mobility in 3D systems with chain length N = 2000. The grey lines are obtained from linear fitting of the log(μ) vs 1/T data in the range T = 150-250 K. Escape probability $p_{esc} = 10^{-3}$, field $F = 10^3$ V/cm. Each data point is averaged over 20 trajectories. (Top) Mobility for different values of persistence length (ε_b = 2-∞) with constant electronic disorder σ_β = 0.1 eV. 1D system with and without PBC shown for comparison. (Bottom) Mobility for different combinations of electronic disorder and persistence length as shown in the legend.

The relationship between chain rigidity, hopping distance and mobility deserves to be investigated further by computing the distribution of hopping distances and the

values of mobility as a function of ε_b at constant temperature and field. The components of the hopping distances along the field's direction, R_x^{hop}, have been obtained from 20 trajectories of 10^5 MC steps each. The distributions of R_x^{hop}, shown in the top panel of Figure 7.7, are bi-exponential as observed in the 1D model (see Figure 5.7) and become wider for larger ε_b as the chains become more elongated. The typical hopping range R_0 for each value of ε_b was obtained as described in section 5.2.3 by fitting the distributions with the function $A\exp\left(-R_x^{hop}/R_0\right)$ in the range 0-30 *d* (the monomer-monomer distance *d* is set to 1.0 nm). In the bottom left panel of Figure 7.7 it can be clearly seen that R_0 is directly proportional to $\log(\varepsilon_b)$ when $\varepsilon_b \leq 40$. Remarkably, the effect on charge transport is straightforward: $\log(\mu)$ is also linearly dependent on $\log(\varepsilon_b)$ when $\varepsilon_b \leq 40$ (Figure 7.7, bottom right). Both quantities then reach a plateau for very rigid chains when $\varepsilon_b > 100$ in agreement with the analytical diffusion model proposed by Carbone et al.[246] This very clear linear relationship confirms the hypothesis formulated earlier that, with constant electronic disorder, the rigidity of the 3D chains predominantly affects charge transport by changing the distances between electronic states.

Although we started from a common assumptions about the worm-like chain morphology, there is a radical difference between the charge transport model presented here and the Spakowitz model presented in ref. [105] This difference is schematically illustrated in Figure 7.8. In the Spakowitz model (Figure 7.8a), all electronic states are localized on one monomer and they all have the same energy. A further assumption is that only hopping between neighbouring monomers is allowed. For this reason, when the charge carrier reaches a kink or loop aligned with the electric field, it becomes trapped and the only ways out of the trap are escaping to another chain or keeping moving along the chain against the direction of the field. In our model we do not observe this morphological trapping because we do not assume localized electronic states and, most importantly, we do not restrict hopping to nearest neighbours: each state is connected to several others, so the kinks in the chains do not act as morphological traps (Figure 7.8b). The variable delocalization of the states along the polymer backbone is another characteristic of our model essential for intra-chain connectivity and long-range hopping (Figure 7.8c), since the hopping rates (eq.

(7.2)) are directly proportional to the spatial overlap between electronic wavefunctions.

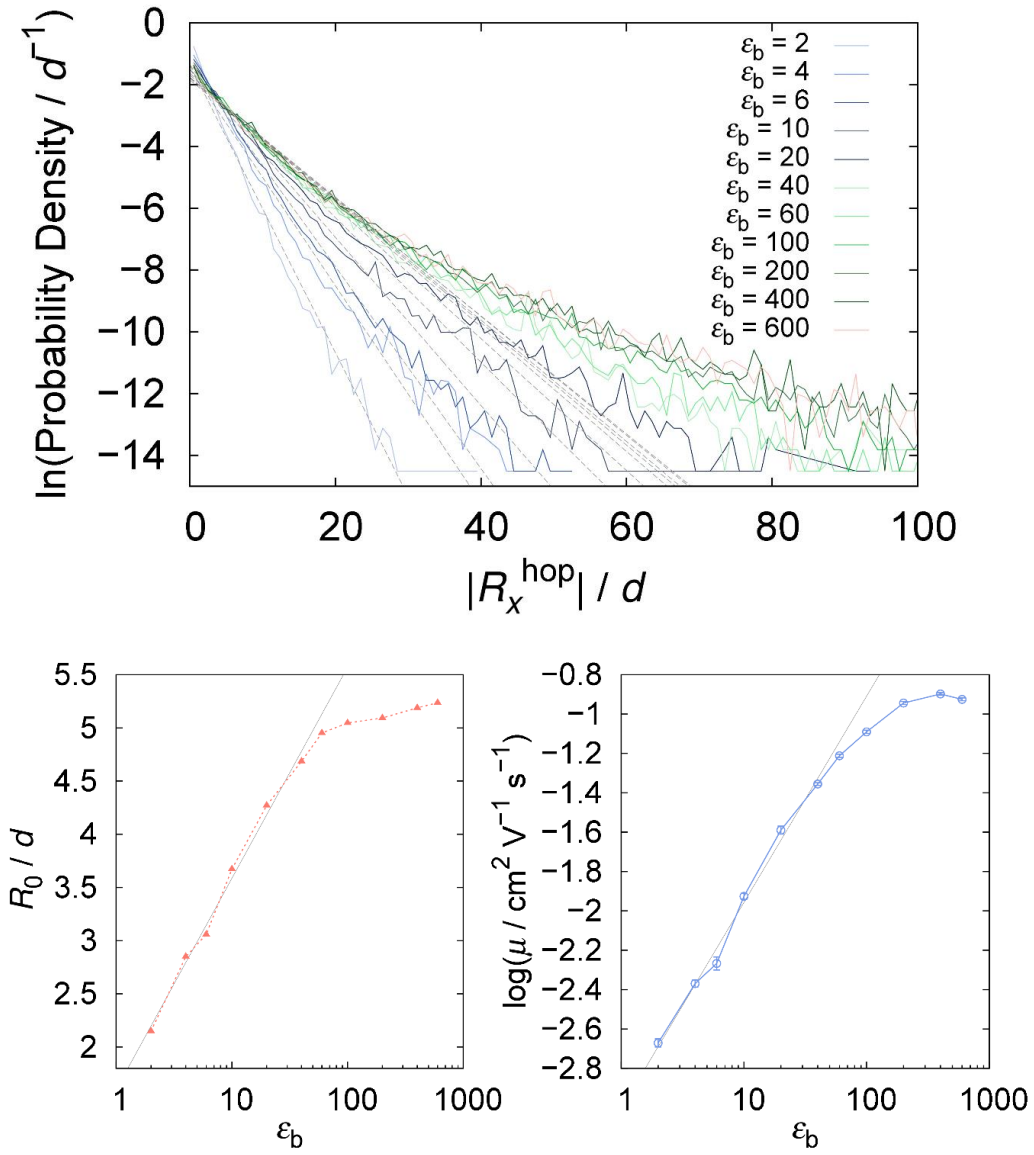

Figure 7.7. (Top) Distributions of hopping distances, from 20 trajectories of 10^5 MC steps each, in 3D systems with chain length N = 2000, electronic disorder σ_β = 0.1 eV, ε_b = 2-600, T = 300 K and F = 10^3 V/cm. The distributions are fitted to the function $A\exp\left(-R_x^{hop}/R_0\right)$ (dashed lines) in the range 0-30 d. (Bottom) Left: Typical hopping range R_0 as a function of ε_b obtained from fitting the distributions above. Right: Mobility as a function of ε_b at 300 K and F = 10^3 V/cm. The straight lines are obtained from linear fitting in the range ε_b = 2-40.

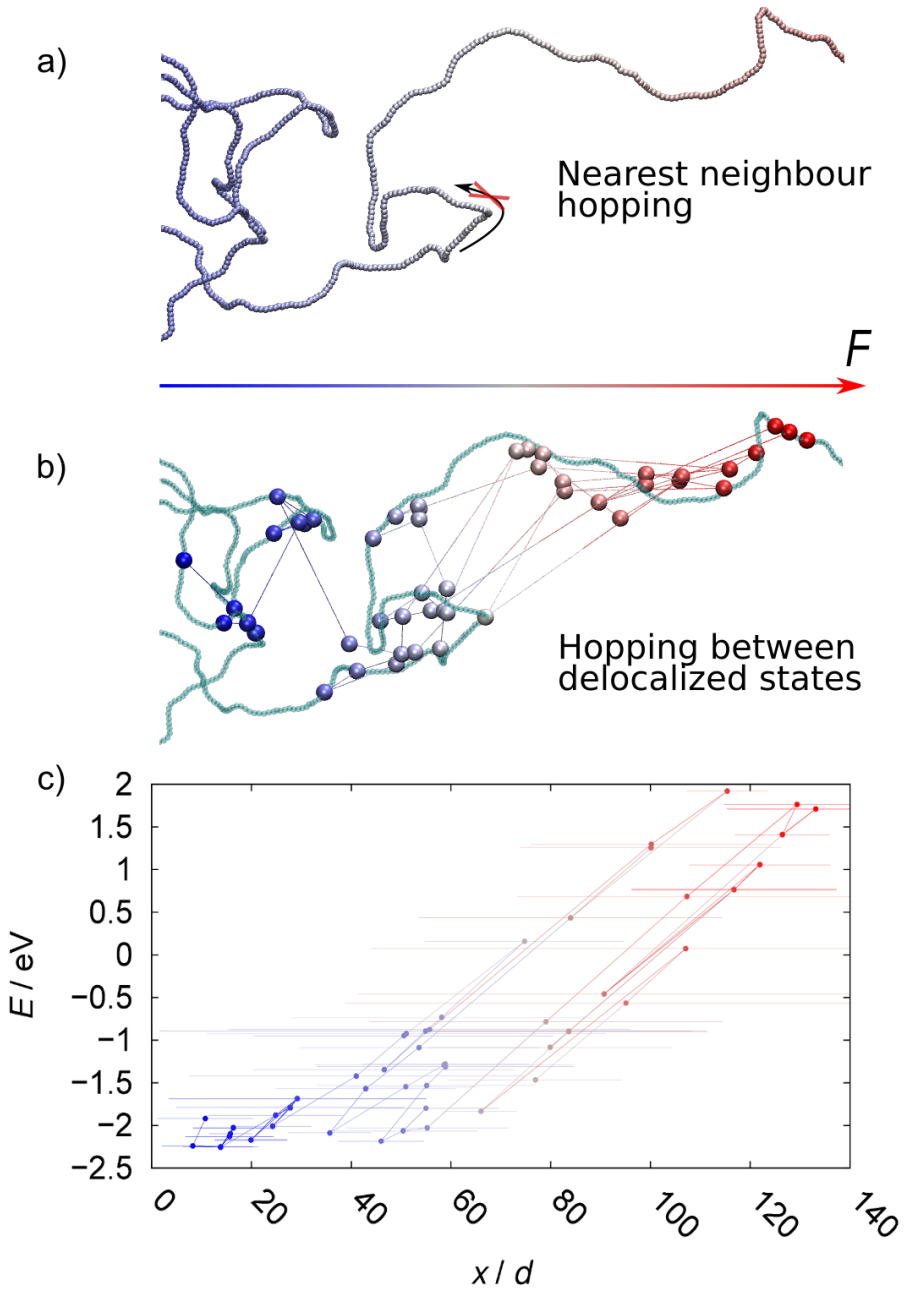

Figure 7.8. A segment of a 3D chain with $\varepsilon_b = 2$ and $\sigma = 0.20$ eV. (a) When hopping is allowed only between neighbouring monomers, the kinks in the chain can act as morphological traps. (b) Spheres are drawn at the mean positions $\mathbf{r}_i$ of the states visited during a trajectory of 250 MC steps. The network of hops connecting the states (represented by segments) allows the kinks to be easily bypassed. (c) Energy landscape of the states shown in (b): the dots are drawn at the mean positions r_x. The width of each horizontal bar is the IPR (number of monomers sharing the charge), representing the delocalization of the state along the backbone (not along x). Electric field $F_x = 5 \cdot 10^5$ V/cm. In (a), (b) and (c) the electronic states are coloured according to the position along x.

7.4 Conclusion

In this chapter we presented a generalisation of the charge transport model described in chapters 5 and 6 with the aim of establishing a relationship between chain rigidity and charge transport. The only additional assumptions regard the 3D conformation of the polymer chains and the rate of hopping to other chains. The 3D structures were generated with a discrete worm-like chain model and the electronic structure of each chain was obtained from a tight binding Hamiltonian such as that in eq. (5.1) without assuming correlations between geometric and electronic disorder. The mobility resulting from a combination of intra- and inter-chain hopping at low field and low charge density was computed from kinetic Monte Carlo simulations as a function of the system parameters.

Charge transport was found to be limited by the chain length in chains of 2000 monomers when the ratio between the inter- and intra-chain hopping rate is smaller than 10^{-3}, or in other words inter-chain hopping needs to occur rather frequently to achieve high mobilities. This observation confirms the importance of the presence of many short-range aggregates in disordered polymeric materials since it is believed that inter-chain hopping taking place in these aggregates, which provide high-mobility pathways by ensuring sufficient connectivity between chains.[90]

The relationship between chain rigidity and charge mobility was found to be more straightforward than expected. Decreasing the persistence length of the chains at constant electronic disorder was found to cause a linear decrease of mobility simply because the distances between the states are reduced. Surprisingly, changes in persistence length were found not to change the activation energy for transport, i.e. they do not affect the effective electronic disorder. Instead, the reduced persistence length ε_b acts as a scaling factor directly proportional to mobility when $\varepsilon_b \leq 40$. This behaviour apparently contrasts with the model described in refs. [105–107] where kinks in the chain parallel to the field were found to act as morphological traps. We suggest that this effect is observed only if nearest neighbour hopping is assumed, while in our model each state is connected to many others allowing the charge to escape the trap.

The results of our generalised transport model confirm the validity of some of the design strategies, outlined in the introduction, aimed at improving mobility in disordered polymers. Reducing the amount of effective electronic disorder was shown

in chapters 5 and 6 to increase mobility and reduce the activation energy for transport. In this chapter it was found that increasing chain rigidity improves mobility but does not reduce activation energy at constant electronic disorder. The universal temperature dependence of experimental mobility in a range of disordered materials, shown in Figure 6.4, suggests that only one parameter, the effective electronic disorder, affects the activation energy. Therefore, to account for these experimental observations, one should either assume that the chain rigidity is rather constant across different polymers, or that chain rigidity and electronic disorder are indeed correlated. In the latter case, the model presented in this chapter should be improved to include such correlation.

8. Summary and Outlook

The main themes discussed in this thesis are exciton dynamics in molecular aggregates and charge transport in polymers. Some of the fundamental theoretical aspects in these two very active research fields were addressed with simplified models and various computational techniques. Chapter 1 includes a review of the rapidly evolving field of organic electronics, followed by an overview of the methods most commonly used to describe exciton and charge transport in organic materials. The methods used in this thesis were discussed in greater detail.

When appropriate conditions are met, the charge or exciton transport mechanism can be assumed to be incoherent and one can define a hopping rate between electronic states localized by static disorder. In chapter 2 a very general kinetic rate of hopping between electronic states in the incoherent regime was derived. This derivation considered both local and non-local electron-phonon coupling (polaronic effects and dynamic disorder). The resulting rate expression bridges among existing theories, i.e. it can be reduced to the rates most commonly used in the literature (Miller-Abrahams, Marcus, Marcus-Levich-Jortner, Vukmirović) when the appropriate limits are taken. This expression was employed in the charge transport model described in chapters 5 and 6 of this thesis and, thanks to its generality, can be applied to a large number of incoherent dynamics problems.

The properties of excited states in biological and artificial molecular aggregates depend of the strength of the interactions between the localized excitations (excitonic couplings). In chapters 3 and 4, using a combination of molecular dynamics and quantum chemical calculations, a large number of excitonic couplings in artificial and biological molecular aggregates were computed. The full excitonic couplings, including both the Coulombic and the short-range (non-Coulombic) contributions, which can be captured by diabatization techniques, were considered to fully account for the interaction also in presence of thermal fluctuation of the coupling (dynamic disorder). The short-range contributions were found to be of non-negligible magnitude in some closely spaced chromophores in light-harvesting complexes, and very large in closely packed disordered and ordered phthalocyanine aggregates. The results also suggest that, when the first two excited states are quasi-degenerate, both states and all the couplings between them, as well as their thermal fluctuation, should be taken into account to correctly describe exciton dynamics.

The findings reported in chapters 3 and 4 represent a useful benchmark for future studies of exciton dynamics in molecular aggregates. Depending on the morphology and the nature of the aggregate (biological or artificial, disordered or ordered), selecting a method for the evaluation of the excitonic interactions between chromophores with the desired level of accuracy is a crucial step in the construction of excitonic Hamiltonians such as eq. (1.1). For example, in order to investigate the role of coherence in the exciton dynamics of a photosynthetic complex containing chlorophyll one would need to take into account both lowest excited states and the dynamic fluctuation of the couplings. On the basis of our findings, however, the short-range components of the couplings should be included only for chromophore pairs in close contact, while for the others the computationally cheaper Coulombic couplings would be accurate enough.

Charge transport in disordered semiconducting polymers is challenging to rationalize due to the large variety of chemical structures and material morphologies. A very general but simple model for charge transport, which should mimic the large parameter space of realistic polymers, was presented in chapter 5. Starting from a model Hamiltonian depending on just a few parameters, it was shown how a detailed disordered electronic structure with variable localization of the electronic states can be obtained. The hopping rates between the electronic states were determined by the expression derived in chapter 2. Starting from the hopping rates, the charge mobility along single polymer chains was computed as a function of the parameters of the model. The proposed model provides a detailed description of charge transport in a disordered energy landscape and can therefore bridge between variable range hopping (VRH) and mobility edge (ME) models, but it was derived starting from fewer assumptions and therefore is more general. The narrower transport band of donor-acceptor alternating copolymers was surprisingly found to enhance mobility since it results in lower activation energy, providing a possible explanation for their high mobility despite their disordered morphology.

From an exploration of the large parameter space of this model, performed in chapter 6, the Arrhenius temperature dependence of mobility was found to be a universal property of polymeric semiconductors in agreement with experimental observations. The activation energy for transport was found to depend essentially on the effective amount of static disorder affecting the couplings between monomers,

which depends on the static conformation of the polymer chain, while all other parameters were found to be of negligible importance. The squared non-local electron phonon coupling strength, scaled by the squared distance between monomers, was found to act as a scaling factor directly proportional to mobility.

In chapter 7 the transport model was generalised to take into account the 3D structure of the polymer chains and inter-chain hopping. Random chain conformations were generated with a discrete worm-like chain model where the rigidity of the chain is determined by the persistence length. The rates for inter-chain hopping were assumed to have the same form as the intra-chain hopping rates (defined in chapter 2) but much smaller in magnitude. The mobility was found to be directly proportional to the persistence length since it depends on the average hopping distance, which becomes larger for more rigid chains. However, the persistence length was found not to affect the activation energy, which therefore was confirmed to depend only on the effective electronic disorder. These results have been obtained with a set of parameters that makes mobility independent of the chain length since the aim was to study the effect of chain rigidity. However, many reports indicate that mobility is strongly dependent on molecular weight. [277–281] A future application of this model is therefore investigating how charge mobility depends on the interplay between chain length and the ratio between inter- and intra-chain hopping rates.

In summary, the simple but very general charge transport model presented in this thesis provides a new way of thinking about the energy landscape that charges need to cross when moving in a disordered polymeric material. The results confirm that the fundamental characteristics of high mobility polymers are resilience to electronic disorder, rigid chains, and well-interconnected aggregates to allow frequent inter-chain hopping. This model was discussed using realistic ranges of parameters, but it can also act as a link between atomistic modelling and macroscopic charge transport properties: for example, parameters obtained from molecular dynamics and electronic structure calculations can be fed into the model to predict the mobility of yet-to-be-synthesized polymers in order to accelerate materials discovery driven by design. Additionally, this model could be used in conjunction with specially designed experiments to achieve a deeper understanding of the charge transport mechanism and its relationship with electronic structure and morphology. For example, such a combined theoretical-experimental setup could be employed to further investigate the

dependence of mobility and activation energy on electronic disorder, chain rigidity, chain length and connectivity between chains.

The theoretical and computational studies presented in this thesis attempt to answer some fundamental questions regarding charge and exciton transport in organic semiconducting materials. A common theme emerging from the results is the important role played by static and dynamic disorder which affect the electronic structure and the dynamic behaviour of excited states. Considering the technological importance of efficient charge and exciton transport, we can conclude that this thesis contains some significant contributions to the field of organic electronics which can be useful for future theoretical and experimental investigations aimed at designing new high-performance materials.

References

[1] G. Ciamician, The photochemistry of the future, *Science*, 1912, **26**, 385–394.

[2] S. Beaupré and M. Leclerc, PCDTBT: en route for low cost plastic solar cells, *J. Mater. Chem. A*, 2013, **1**, 11097.

[3] S. Gélinas, A. Rao, A. Kumar, S. L. Smith, A. W. Chin, J. Clark, T. S. Van Der Poll, G. C. Bazan and R. H. Friend, Ultrafast Long-Range Charge Separation in Organic Semiconductor Photovoltaic Diodes, *Science*, 2014, **343**, 512–517.

[4] Y. Zhang, E. Bovill, J. Kingsley, A. R. Buckley, H. Yi, A. Iraqi, T. Wang and D. G. Lidzey, PCDTBT based solar cells: One year of operation under real-world conditions, *Sci. Rep.*, 2016, **6**, 4–11.

[5] G. Malliaras and R. H. Friend, An organic electronics primer, *Phys. Today*, 2005, **58**, 53–58.

[6] D. D. Eley, Phthalocyanines as Semiconductors, *Nature*, 1948, **162**, 819.

[7] D. D. Eley and G. D. Parfitt, The semiconductivity of organic substances. Part 1, *Trans. Faraday Soc.*, 1953, **49**, 79–86.

[8] D. D. Eley and G. D. Parfitt, The semiconductivity of organic substances. Part 2, *Trans. Faraday Soc.*, 1955, **51**, 1529–1539.

[9] H. Mette and H. Pick, Elektronenleitfähigkeit von Anthracen-Einkristallen, *Zeitschrift für Phys.*, 1953, **134**, 566–575.

[10] H. Akamatu, H. Inokuchi and Y. Matsunaga, Electrical Conductivity of the Perylene–Bromine Complex, *Nature*, 1954, **173**, 168.

[11] A. Bernanose, Electroluminescence of Organic Compounds, *Br. J. Appl. Phys.*, 1955, **paper 9**, 54.

[12] M. Pope, H. P. Kallmann and P. Magnante, Electroluminescence in Organic Crystals, *J. Chem. Phys.*, 1963, **38**, 2042–2043.

[13] C. W. Tang and S. A. VanSlyke, Organic electroluminescent diodes, *Appl. Phys. Lett.*, 1987, **51**, 913–915.

[14] H. Shirakawa, E. J. Louis, A. G. MacDiarmid, C. K. Chiang and A. J. Heeger, Synthesis of electrically conducting organic polymers: halogen derivatives of polyacetylene, (CH)x, *J. Chem. Soc. Chem. Commun.*, 1977, 578–580.

[15] J. H. Burroughes, D. D. C. Bradley, A. R. Brown, R. N. Marks, K. Mackay, R. H. Friend, P. L. Burns and A. B. Holmes, Light-emitting diodes based on

conjugated polymers, *Nature*, 1990, **347**, 539–541.

[16] C. Sekine, Y. Tsubata, T. Yamada, M. Kitano and S. Doi, Recent progress of high performance polymer OLED and OPV materials for organic printed electronics, *Sci. Technol. Adv. Mater.*, 2014, **15**, 34203.

[17] F. Ebisawa, T. Kurokawa and S. Nara, Electrical properties of polyacetylene/polysiloxane interface, *J. Appl. Phys.*, 1983, **54**, 3255–3259.

[18] K. Kudo, M. Yamashina and T. Moriizumi, Field Effect Measurement of Organic Dye Films, *Jpn. J. Appl. Phys.*, 1984, **23**, 130.

[19] H. Sirringhaus, 25th Anniversary Article: Organic Field-Effect Transistors: the Path Beyond Amorphous Silicon., *Adv. Mater.*, 2014, **26**, 1319–1335.

[20] X. Guo, Y. Xu, S. Ogier, T. N. Ng, M. Caironi, A. Perinot, L. Li, J. Zhao, W. Tang, R. A. Sporea, A. Nejim, J. Carrabina, P. Cain and F. Yan, Current Status and Opportunities of Organic Thin-Film Transistor Technologies, *IEEE Trans. Electron Devices*, 2017, **64**, 1906–1921.

[21] G. A. A. Chamberlain, Organic solar cells: A review, *Sol. Cells*, 1983, **8**, 47–83.

[22] C. W. Tang, Two-layer organic photovoltaic cell, *Appl. Phys. Lett.*, 1986, **48**, 183–185.

[23] N. S. Sariciftci, L. Smilowitz, A. J. Heeger and F. Wudl, Photoinduced electron transfer from a conducting polymer to buckminsterfullerene., *Science*, 1992, **258**, 1474–1476.

[24] A. J. Heeger, 25th anniversary article: Bulk heterojunction solar cells: Understanding the mechanism of operation, *Adv. Mater.*, 2014, **26**, 10–28.

[25] G. Yu, J. Gao, J. C. Hummelen, F. Wudl and A. J. Heeger, Polymer Photovoltaic Cells: Enhanced Efficiencies via a Network of Internal Donor-Acceptor Heterojunctions, *Science*, 1995, **270**, 1789–1791.

[26] L. Dou, J. You, Z. Hong, Z. Xu, G. Li, R. a. Street and Y. Yang, 25th anniversary article: A decade of organic/polymeric photovoltaic research, *Adv. Mater.*, 2013, **25**, 6642–6671.

[27] Heliatek sets new Organic Photovoltaic world record efficiency of 13.2%, http://www.heliatek.com/en/press/press-releases/details/heliatek-sets-new-organic-photovoltaic-world-record-efficiency-of-13-2, (accessed 19 September 2017).

[28] R. Steim, T. Ameri, P. Schilinsky, C. Waldauf, G. Dennler, M. Scharber and C. J. Brabec, Organic photovoltaics for low light applications, *Sol. Energy Mater. Sol. Cells*, 2011, **95**, 3256–3261.

[29] H. K. H. Lee, Z. Li, J. R. Durrant and W. C. Tsoi, Is organic photovoltaics promising for indoor applications?, *Appl. Phys. Lett.*, 2016, **108**, 253301.

[30] C. L. Cutting, M. Bag and D. Venkataraman, Indoor Light Recycling: A New Home for Organic Photovoltaics, *J. Mater. Chem. C*, 2016, **4**, 10367–10370.

[31] F. C. Krebs, N. Espinosa, M. Hösel, R. R. Søndergaard and M. Jørgensen, 25th anniversary article: Rise to power - OPV-based solar parks, *Adv. Mater.*, 2014, **26**, 29–39.

[32] P. Sullivan, S. Schumann, R. Da Campo, T. Howells, A. Duraud, M. Shipman, R. A. Hatton and T. S. Jones, Ultra-high voltage multijunction organic solar cells for low-power electronic applications, *Adv. Energy Mater.*, 2013, **3**, 239–244.

[33] M. Jacoby, The future of low-cost solar cells, *Chem. Eng. News*, 2016, **94**, 30–35.

[34] C. Kittel, *Introduction To Solid State Physics*, John Wiley & Sons, Hoboken, NJ, USA, 8th edn., 2005.

[35] J. Frenkel, On the Transformation of Light into Heat in Solids. II, *Phys. Rev.*, 1931, **37**, 1276.

[36] M. Pope and C. E. Swenberg, *Electronic Processes in Organic Crystals and Polymers*, Oxford University Press, New York, 2nd edn., 1999.

[37] T. Förster, Zwischenmolekulare Energiewanderung und Fluoreszenz, *Ann. Phys.*, 1948, **2**, 55–75.

[38] R. McWeeny, *Methods of Molecular Quantum Mechanics*, Academic Press, London, 2nd edn., 1992.

[39] B. P. Krueger, G. D. Scholes and G. R. Fleming, Calculation of Couplings and Energy-Transfer Pathways between the Pigments of LH2 by the ab Initio Transition Density Cube Method, *J. Phys. Chem. B*, 1998, **102**, 5378–5386.

[40] C. Hsu, The Electronic Couplings in Electron Transfer and Excitation Energy Transfer, *Acc. Chem. Res.*, 2009, **42**, 509–518.

[41] J. C. Chang, Monopole effects on electronic excitation interactions between large molecules. I. Application to energy transfer in chlorophylls, *J. Chem.*

Phys., 1977, **67**, 3901–3909.

[42] H. Yamagata, J. Norton, E. Hontz, Y. Olivier, D. Beljonne, J. Brédas, R. J. Silbey and F. C. Spano, The nature of singlet excitons in oligoacene molecular crystals, *J. Chem. Phys.*, 2011, **134**, 204703.

[43] R. D. Harcourt, G. D. Scholes and K. P. Ghiggino, Rate expressions for excitation transfer. II. Electronic considerations of direct and through–configuration exciton resonance interactions, *J. Chem. Phys.*, 1994, **101**, 10521.

[44] G. D. Scholes and K. P. Ghiggino, Electronic Interactions and Interchromophore Excitation Transfer, *J. Phys. Chem.*, 1994, **98**, 4580–4590.

[45] G. D. Scholes, R. D. Harcourt and K. P. Ghiggino, Rate expressions for excitation transfer. III. An ab initio study of electronic factors in excitation transfer and exciton resonance interactions, *J. Chem. Phys.*, 1995, **102**, 9574.

[46] J. Aragó and A. Troisi, Dynamics of the Excitonic Coupling in Organic Crystals, *Phys. Rev. Lett.*, 2015, **114**, 26402.

[47] J. Aragó and A. Troisi, Regimes of Exciton Transport in Molecular Crystals in the Presence of Dynamic Disorder, *Adv. Funct. Mater.*, 2016, **26**, 2316–2325.

[48] T. Pacher, L. S. Cederbaum and H. Köppel, Approximately diabatic states from block diagonalization of the electronic Hamiltonian, *J. Chem. Phys.*, 1988, **89**, 7367–7381.

[49] H. Nakamura and D. G. Truhlar, The direct calculation of diabatic states based on configurational uniformity, *J. Chem. Phys.*, 2001, **115**, 10353.

[50] J. Aragó and A. Troisi, Excitonic couplings between molecular crystal pairs by a multistate approximation, *J. Chem. Phys.*, 2015, **142**, 164107.

[51] P. H. Schönemann, A generalized solution of the orthogonal procrustes problem, *Psychometrika*, 1966, **31**, 1–10.

[52] G. S. Engel, T. R. Calhoun, E. L. Read, T.-K. Ahn, T. Mancal, Y.-C. Cheng, R. E. Blankenship and G. R. Fleming, Evidence for wavelike energy transfer through quantum coherence in photosynthetic systems., *Nature*, 2007, **446**, 782–786.

[53] A. Chenu and G. D. Scholes, Coherence in energy transfer and photosynthesis, *Annu. Rev. Phys. Chem.*, 2015, **66**, 69–96.

[54] I. Kassal, J. Yuen-Zhou and S. Rahimi-Keshari, Does coherence enhance

transport in photosynthesis?, *J. Phys. Chem. Lett.*, 2013, **4**, 362–367.

[55] E. Collini and G. D. Scholes, Coherent Intrachain Energy Migration in a Conjugated Polymer at Room Temperature, *Science*, 2009, **323**, 369–373.

[56] J. Yuen-Zhou, D. H. Arias, D. M. Eisele, C. P. Steiner, J. J. Krich, M. G. Bawendi, K. A. Nelson and A. Aspuru-Guzik, Coherent Exciton Dynamics in Nanotubes Revealed by Ultrafast Quantum Process Tomography, *ACS Nano*, 2014, **8**, 5527–5534.

[57] S. M. Falke, C. A. Rozzi, D. Brida, M. Maiuri, M. Amato, E. Sommer, A. De Sio, A. Rubio, G. Cerullo, E. Molinari and C. Lienau, Coherent ultrafast charge transfer in an organic photovoltaic blend., *Science*, 2014, **344**, 1001–1005.

[58] J. Sung, P. Kim, B. Fimmel, F. Würthner and D. Kim, Direct observation of ultrafast coherent exciton dynamics in helical π-stacks of self-assembled perylene bisimides, *Nat. Commun.*, 2015, **6**, 8646.

[59] G. D. Scholes, G. R. Fleming, A. Olaya-Castro and R. van Grondelle, Lessons from nature about solar light harvesting, *Nat. Chem.*, 2011, **3**, 763–774.

[60] S. Verma and H. N. Ghosh, Exciton Energy and Charge Transfer in Porphyrin Aggregate/Semiconductor (TiO2) Composites, *J. Phys. Chem. Lett.*, 2012, **3**, 1877–1884.

[61] D. Hayes, G. B. Griffin and G. S. Engel, Engineering Coherence Among Excited States in Synthetic Heterodimer Systems, *Science*, 2013, **340**, 1431–1434.

[62] S. Tanaka, K. Miyata, T. Sugimoto, K. Watanabe, T. Uemura, J. Takeya and Y. Matsumoto, Enhancement of the Exciton Coherence Size in Organic Semiconductor by Alkyl Chain Substitution, *J. Phys. Chem. C*, 2016, **120**, 7941–7948.

[63] J.-L. Brédas, E. H. Sargent and G. D. Scholes, Photovoltaic concepts inspired by coherence effects in photosynthetic systems, *Nat. Mater.*, 2017, **16**, 35–44.

[64] N. Renaud and F. C. Grozema, Intermolecular Vibrational Modes Speed Up Singlet Fission in Perylenediimide Crystals, *J. Phys. Chem. Lett.*, 2015, **6**, 360–365.

[65] M. H. Lee and A. Troisi, Vibronic enhancement of excitation energy transport: Interplay between local and non-local exciton-phonon interactions, *J. Chem. Phys.*, 2017, **146**, 75101.

[66] G. D. Scholes, X. J. X. J. Jordanides and G. R. Fleming, Adapting the Förster Theory of Energy Transfer for Modeling Dynamics in Aggregated Molecular Assemblies, *J. Phys. Chem. B*, 2001, **105**, 1640–1651.

[67] A. Ishizaki and G. R. Fleming, On the adequacy of the Redfield equation and related approaches to the study of quantum dynamics in electronic energy transfer, *J. Chem. Phys.*, 2009, **130**, 234110.

[68] H. D. Meyer, U. Manthe and L. S. Cederbaum, The multi-configurational time-dependent Hartree approach, *Chem. Phys. Lett.*, 1990, **165**, 73–78.

[69] S. Nakajima, On Quantum Theory of Transport Phenomena, *Prog. Theor. Phys.*, 1958, **20**, 948–959.

[70] R. Zwanzig, Approximate Eigenfunctions of the Liouville Operator in Classical Many-Body Systems, *Phys. Rev.*, 1966, **144**, 170.

[71] Y. Tanimura, Stochastic Liouville, Langevin, Fokker–Planck, and Master Equation Approaches to Quantum Dissipative Systems, *J. Phys. Soc. Japan*, 2006, **75**, 82001.

[72] A. Ishizaki and G. R. Fleming, Unified treatment of quantum coherent and incoherent hopping dynamics in electronic energy transfer: Reduced hierarchy equation approach, *J. Chem. Phys.*, 2009, **130**, 234111.

[73] M.-L. Zhang, B. J. Ka and E. Geva, Nonequilibrium quantum dynamics in the condensed phase via the generalized quantum master equation, *J. Chem. Phys.*, 2006, **125**, 44106.

[74] M. H. Lee and A. Troisi, Quantum dynamics of a vibronically coupled linear chain using a surrogate Hamiltonian approach, *J. Chem. Phys.*, 2016, **144**, 214106.

[75] S. Fratini, D. Mayou and S. Ciuchi, The Transient Localization Scenario for Charge Transport in Crystalline Organic Materials, *Adv. Funct. Mater.*, 2016, **26**, 2292–2315.

[76] J. C. Tully, Molecular dynamics with electronic transitions, *J. Chem. Phys.*, 1990, **93**, 1061–1071.

[77] L. Wang, A. E. Sifain and O. V. Prezhdo, Fewest Switches Surface Hopping in Liouville Space, *J. Phys. Chem. Lett.*, 2015, **6**, 3827–3833.

[78] A. Troisi and G. Orlandi, Charge-Transport Regime of Crystalline Organic Semiconductors: Diffusion Limited by Thermal Off-Diagonal Electronic

Disorder, *Phys. Rev. Lett.*, 2006, **96**, 86601.

[79] Z. Bao, A. Dodabalapur and A. J. Lovinger, Soluble and processable regioregular poly(3-hexylthiophene) for thin film field-effect transistor applications with high mobility, *Appl. Phys. Lett.*, 1996, **69**, 4108–1210.

[80] H. Sirringhaus, P. J. Brown, R. H. Friend, M. M. Nielsen, K. Bechgaard, B. M. W. Langeveld-Voss, A. J. H. Spiering, R. A. J. Janssen, E. W. Meijer, P. Herwig and D. M. De Leeuw, Two-dimensional charge transport in self-organized, high-mobility conjugated polymers, *Nature*, 1999, **401**, 685–688.

[81] A. Nawaz, M. S. Meruvia, D. L. Tarange, S. P. Gopinathan, A. Kumar, A. Kumar, H. Bhunia, A. J. Pal and I. A. Hümmelgen, High mobility organic field-effect transistors based on defect-free regioregular poly(3-hexylthiophene-2,5-diyl), *Org. Electron.*, 2016, **38**, 89–96.

[82] W. Li, K. H. Hendriks, M. M. Wienk and R. A. J. Janssen, Diketopyrrolopyrrole Polymers for Organic Solar Cells, *Acc. Chem. Res.*, 2015, **49**, 78–85.

[83] R. Noriega, J. Rivnay, K. Vandewal, F. P. V. Koch, N. Stingelin, P. Smith, M. F. Toney and A. Salleo, A general relationship between disorder, aggregation and charge transport in conjugated polymers, *Nat. Mater.*, 2013, **12**, 1038–1044.

[84] S. Y. Son, Y. Kim, J. Lee, G. Y. Lee, W. T. Park, Y. Y. Noh, C. E. Park and T. Park, High-Field-Effect Mobility of Low-Crystallinity Conjugated Polymers with Localized Aggregates, *J. Am. Chem. Soc.*, 2016, **138**, 8096–8103.

[85] T. Liu and A. Troisi, Understanding the microscopic origin of the very high charge mobility in PBTTT: Tolerance of thermal disorder, *Adv. Funct. Mater.*, 2014, **24**, 925–933.

[86] A. Troisi and A. Shaw, Very Large π-Conjugation Despite Strong Nonplanarity: A Path for Designing New Semiconducting Polymers, *J. Phys. Chem. Lett.*, 2016, **7**, 4689–4694.

[87] X. Zhang, H. Bronstein, A. J. Kronemeijer, J. Smith, Y. Kim, R. J. Kline, L. J. Richter, T. D. Anthopoulos, H. Sirringhaus, K. Song, M. Heeney, W. Zhang, I. McCulloch and D. M. DeLongchamp, Molecular origin of high field-effect mobility in an indacenodithiophene- benzothiadiazole copolymer, *Nat. Commun.*, 2013, **4**, 2238.

[88] D. Venkateshvaran, M. Nikolka, A. Sadhanala, V. Lemaur, M. Zelazny, M. Kepa, M. Hurhangee, A. J. Kronemeijer, V. Pecunia, I. Nasrallah, I. Romanov, K. Broch, I. McCulloch, D. Emin, Y. Olivier, J. Cornil, D. Beljonne and H. Sirringhaus, Approaching disorder-free transport in high-mobility conjugated polymers, *Nature*, 2014, **515**, 384–388.

[89] S. Wang, S. Fabiano, S. Himmelberger, S. Puzinas, X. Crispin, A. Salleo and M. Berggren, Experimental evidence that short-range intermolecular aggregation is sufficient for efficient charge transport in conjugated polymers., *Proc. Natl. Acad. Sci. U. S. A.*, 2015, **112**, 10599–10604.

[90] S. Himmelberger and A. Salleo, Engineering semiconducting polymers for efficient charge transport, *MRS Commun.*, 2015, **5**, 383–395.

[91] J. M. Verilhac, M. Benwadih, A. L. Seiler, S. Jacob, C. Bory, J. Bablet, M. Heitzman, J. Tallal, L. Barbut, P. Frère, G. Sicard, R. Gwoziecki, I. Chartier, R. Coppard and C. Serbutoviez, Step toward robust and reliable amorphous polymer field-effect transistors and logic functions made by the use of roll to roll compatible printing processes, *Org. Electron.*, 2010, **11**, 456–462.

[92] M. Nikolka, I. Nasrallah, B. Rose, M. K. Ravva, K. Broch, A. Sadhanala, D. Harkin, J. Charmet, M. Hurhangee, A. Brown, S. Illig, P. Too, J. Jongman, I. McCulloch, J. Brédas and H. Sirringhaus, High operational and environmental stability of high-mobility conjugated polymer field-effect transistors through the use of molecular additives, *Nat. Mater.*, 2017, **16**, 356–362.

[93] Y. Yamashita, F. Hinkel, T. Marszalek, W. Zajaczkowski, W. Pisula, M. Baumgarten, H. Matsui, K. Müllen and J. Takeya, Mobility exceeding 10 cm 2 /Vs in donor-acceptor polymer transistors with band-like charge transport, *Chem. Mater.*, 2015, **28**, 420−424.

[94] H. Sirringhaus, Device physics of solution-processed organic field-effect transistors, *Adv. Mater.*, 2005, **17**, 2411–2425.

[95] N. Mott, M. Pepper, S. Pollitt, R. H. Wallis and C. J. Adkins, The Anderson Transition, *Proc. R. Soc. A*, 1975, **345**, 169–205.

[96] E. H. Magin and P. M. Borsenberger, Electron transport in N,N'-bis(2-phenethyl)-perylene-3,4: 9,10-bis(dicarboximide), *J. Appl. Phys.*, 1993, **73**, 787–791.

[97] N. Vukmirović and L.-W. Wang, Density of States and Wave Function

Localization in Disordered Conjugated Polymers : A Large Scale Computational Study, *J. Phys. Chem. B*, 2011, **115**, 1792–1797.

[98] M. Mladenović and N. Vukmirović, Charge Carrier Localization and Transport in Organic Semiconductors: Insights from Atomistic Multiscale Simulations, *Adv. Funct. Mater.*, 2015, **25**, 1915–1932.

[99] H. Bässler, Charge Transport in Disordered Organic Photoconductors, *Phys. Status Solidi B*, 1993, **15**, 15–55.

[100] N. F. Mott, Conduction in non-crystalline materials, *Philos. Mag.*, 1969, **19**, 835–852.

[101] M. C. J. M. Vissenberg and M. Matters, Theory of the field-effect mobility in amorphous organic transistors, *Phys. Rev. B*, 1998, **57**, 964–967.

[102] G. Horowitz, R. Hajlaoui and P. Delannoy, Temperature Dependence of the Field-Effect Mobility of Sexithiophene. Determination of the Density of Traps, *J. Phys. III*, 1995, **5**, 355–371.

[103] R. A. Street, J. E. Northrup and A. Salleo, Transport in polycrystalline polymer thin-film transistors, *Phys. Rev. B*, 2005, **71**, 165202.

[104] A. Salleo, T. W. Chen, A. R. Völkel, Y. Wu, P. Liu, B. S. Ong and R. A. Street, Intrinsic hole mobility and trapping in a regioregular poly(thiophene), *Phys. Rev. B*, 2004, **70**, 115311.

[105] R. Noriega, A. Salleo and A. J. Spakowitz, Chain conformations dictate multiscale charge transport phenomena in disordered semiconducting polymers., *Proc. Natl. Acad. Sci. U. S. A.*, 2013, **110**, 16315–16320.

[106] S. A. Mollinger, B. A. Krajina, R. Noriega, A. Salleo and A. J. Spakowitz, Percolation, Tie-Molecules, and the Microstructural Determinants of Charge Transport in Semicrystalline Conjugated Polymers, *ACS Macro Lett.*, 2015, **4**, 708–712.

[107] S. A. Mollinger, A. Salleo and A. J. Spakowitz, Anomalous Charge Transport in Conjugated Polymers Reveals Underlying Mechanisms of Trapping and Percolation, *ACS Cent. Sci.*, 2016, **2**, 910–915.

[108] S. D. Baranovskii, Theoretical description of charge transport in disordered organic semiconductors, *Phys. Status Solidi B*, 2014, **251**, 487–525.

[109] D. L. Cheung, D. P. McMahon and A. Troisi, A realistic description of the charge carrier wave function in microcrystalline polymer semiconductors, *J.*

Am. Chem. Soc., 2009, **131**, 11179–11186.

[110] T. Qin and A. Troisi, Relation between structure and electronic properties of amorphous MEH-PPV polymers, *J. Am. Chem. Soc.*, 2013, **135**, 11247–11256.

[111] S. M. Gali, G. D'Avino, P. Aurel, G. Han, Y. Yi, T. A. Papadopoulos, V. Coropceanu, J.-L. Brédas, G. Hadziioannou, C. Zannoni and L. Muccioli, Energetic fluctuations in amorphous semi-conducting polymers: impact on charge-carrier mobility, *J. Chem. Phys.*, 2017, **147**, 134906.

[112] S. L. M. Van Mensfoort, S. I. E. Vulto, R. A. J. Janssen and R. Coehoorn, Hole transport in polyfluorene-based sandwich-type devices: Quantitative analysis of the role of energetic disorder, *Phys. Rev. B*, 2008, **78**, 85208.

[113] N. I. Craciun, J. Wildeman and P. W. M. Blom, Universal Arrhenius temperature activated charge transport in diodes from disordered organic semiconductors, *Phys. Rev. Lett.*, 2008, **100**, 56601.

[114] M. Kuik, G.-J. A. H. Wetzelaer, H. T. Nicolai, N. I. Craciun, D. M. De Leeuw and P. W. M. Blom, 25th anniversary article: charge transport and recombination in polymer light-emitting diodes., *Adv. Mater.*, 2014, **26**, 512–531.

[115] A. Miller and E. Abrahams, Impurity Conduction at Low Concentrations, *Phys. Rev.*, 1960, **120**, 745.

[116] R. A. Marcus, On the Theory of Oxidation-Reduction Reactions Involving Electron Transfer. I, *J. Chem. Phys.*, 1956, **24**, 966.

[117] M. Kasha, Characterization of electronic transitions in complex molecules, *Discuss. Faraday Soc.*, 1950, **9**, 14.

[118] R. Englman and J. Jortner, The energy gap law for radiationless transitions in large molecules, *Mol. Phys.*, 1970, **18**, 145–164.

[119] R. P. Fornari and A. Troisi, Theory of charge hopping along a disordered polymer chain, *Phys. Chem. Chem. Phys.*, 2014, **16**, 9997–10007.

[120] L.-W. Wang and N. Vukmirović, Charge carrier motion in disordered conjugated polymers: a multiscale Ab initio study, *Nano Lett.*, 2009, **9**, 3996–4000.

[121] N. Vukmirović and L.-W. Wang, Carrier hopping in disordered semiconducting polymers: How accurate is the Miller–Abrahams model?, *Appl. Phys. Lett.*, 2010, **97**, 43305.

[122] N. Vukmirović and L.-W. Wang, Electronic structure of disordered conjugated polymers: polythiophenes, *J. Phys. Chem. B*, 2009, **113**, 409–15.

[123] N. Vukmirović, A comparative study of electronic properties of disordered conjugated polymers, *Phys. Chem. Chem. Phys.*, 2013, **15**, 3543–3551.

[124] A. Nitzan, *Chemical Dynamics in Condensed Phases*, Oxford University Press, Oxford, 1st edn., 2006.

[125] V. May and O. Kühn, *Charge and Energy Transfer Dynamics in Molecular Systems*, Wiley-VCH, Weinheim, Germany, 3rd edn., 2011.

[126] P. F. Barbara, T. J. Meyer and M. A. Ratner, Contemporary Issues in Electron Transfer Research, *J. Phys. Chem.*, 1996, **3654**, 13148–13168.

[127] T. Holstein, Studies of polaron motion: Part I. The molecular-crystal model, *Ann. Phys. (N. Y).*, 1959, **8**, 325–342.

[128] D. Emin, Phonon-Assisted Jump Rate in Noncrystalline Solids, *Phys. Rev. Lett.*, 1974, **32**, 303–307.

[129] S. S. Skourtis, Electron transfer through time-dependent bridges: tunneling by virtual transitions that break the Born–Oppenheimer approximation, *Chem. Phys. Lett.*, 2003, **372**, 224–231.

[130] J. Birks, *Organic molecular photophysics*, John Wiley & Sons, New York, 1975.

[131] R. W. Munn and R. Silbey, Theory of electronic transport in molecular crystals. II. Zeroth order states incorporating nonlocal linear electron–phonon coupling, *J. Chem. Phys.*, 1985, **83**, 1843–1853.

[132] D. C. Harris and M. D. Bertolucci, *Symmetry and spectroscopy: an introduction to vibrational and electronic spectroscopy*, Oxford University Press, New York, 1978.

[133] H. Gerischer, Über den Ablauf von Redoxreaktionen an Metallen und an Halbleitern, *Zeitschrift für Phys. Chemie*, 1960, **26**, 223–247.

[134] A. Devos and M. Lannoo, Electron-phonon coupling for aromatic molecular crystals: Possible consequences for their superconductivity, *Phys. Rev. B*, 1998, **58**, 8236–8239.

[135] A. G. Redfield, On the Theory of Relaxation Processes, *IBM J. Res. Dev.*, 1957, **1**, 19–31.

[136] E. S. Medvedev and A. A. Stuchebrukhov, Inelastic tunneling in long-distance

biological electron transfer reactions, *J. Chem. Phys.*, 1997, **107**, 3821.

[137] A. Troisi, A. Nitzan and M. a. Ratner, A rate constant expression for charge transfer through fluctuating bridges, *J. Chem. Phys.*, 2003, **119**, 5782.

[138] S. S. Skourtis, I. A. Balabin, T. Kawatsu and D. N. Beratan, Protein dynamics and electron transfer: electronic decoherence and non-Condon effects., *Proc. Natl. Acad. Sci. U. S. A.*, 2005, **102**, 3552–3557.

[139] T. R. Prytkova, I. V Kurnikov and D. N. Beratan, Coupling coherence distinguishes structure sensitivity in protein electron transfer, *Science*, 2007, **315**, 622–625.

[140] K. Senthilkumar, F. C. Grozema, C. Fonseca Guerra, F. M. Bickelhaupt, F. D. Lewis, Y. A. Berlin, M. A. Ratner and L. D. A. Siebbeles, Absolute Rates of Hole Transfer in DNA, *J. Am. Chem. Soc.*, 2005, **127**, 14894–14903.

[141] S. S. Zade and M. Bendikov, Study of Hopping Transport in Long Oligothiophenes and Oligoselenophenes: Dependence of Reorganization Energy on Chain Length, *Chem. - A Eur. J.*, 2008, **14**, 6734–6741.

[142] T. Liu and A. Troisi, Absolute rate of charge separation and recombination in a molecular model of the P3HT/PCBM interface, *J. Phys. Chem. C*, 2011, **115**, 2406–2415.

[143] S. V Novikov, D. H. Dunlap, V. M. Kenkre, P. E. Parris and a V Vannikov, Essential role of correlations in governing charge transport in disordered organic materials, *Phys. Rev. Lett.*, 1998, **81**, 4472–4475.

[144] A. Luzio, D. Fazzi, D. Natali, E. Giussani, K.-J. J. Baeg, Z. Chen, Y.-Y. Y. Noh, A. Facchetti and M. Caironi, Synthesis, electronic structure, and charge transport characteristics of naphthalenediimide-based co-polymers with different oligothiophene donor units, *Adv. Funct. Mater.*, 2014, **24**, 1151–1162.

[145] Y. Yamashita, J. Tsurumi, F. Hinkel, Y. Okada, J. Soeda, W. Zajaczkowski, M. Baumgarten, W. Pisula, H. Matsui, K. Müllen and J. Takeya, Transition between band and hopping transport in polymer field-effect transistors, *Adv. Mater.*, 2014, **26**, 8169–8173.

[146] G. D. Scholes and G. Rumbles, Excitons in nanoscale systems, *Nat. Mater.*, 2006, **5**, 683–696.

[147] G. D. Scholes, T. Mirkovic, D. B. Turner, F. Fassioli and A. Buchleitner, Solar light harvesting by energy transfer: from ecology to coherence, *Energy*

Environ. Sci., 2012, **5**, 9374.

[148] S. M. Menke and R. J. Holmes, Exciton diffusion in organic photovoltaic cells, *Energy Environ. Sci.*, 2014, **7**, 499.

[149] O. V. Mikhnenko, P. W. M. Blom and T.-Q. T. Nguyen, Exciton Diffusion in Organic Semiconductors, *Energy Environ. Sci.*, 2015, **8**, 1867–1888.

[150] A. T. Haedler, K. Kreger, A. Issac, B. Wittmann, M. Kivala, N. Hammer, J. Köhler, H.-W. Schmidt and R. Hildner, Long-range energy transport in single supramolecular nanofibres at room temperature, *Nature*, 2015, **523**, 196–199.

[151] H. Park, N. Heldman, P. Rebentrost, L. Abbondanza, A. Iagatti, A. Alessi, B. Patrizi, M. Salvalaggio, L. Bussotti, M. Mohseni, F. Caruso, H. C. Johnsen, R. Fusco, P. Foggi, P. F. Scudo, S. Lloyd and A. M. Belcher, Enhanced energy transport in genetically engineered excitonic networks, *Nat. Mater.*, 2015, **15**, 211–216.

[152] G. Bottari, G. de la Torre and T. Torres, Phthalocyanine–Nanocarbon Ensembles: From Discrete Molecular and Supramolecular Systems to Hybrid Nanomaterials, *Acc. Chem. Res.*, 2015, **48**, 900–910.

[153] G. Bottari, O. Trukhina, M. Ince and T. Torres, Towards artificial photosynthesis: Supramolecular, donor–acceptor, porphyrin- and phthalocyanine/carbon nanostructure ensembles, *Coord. Chem. Rev.*, 2012, **256**, 2453–2477.

[154] C. G. Claessens, U. Hahn and T. Torres, Phthalocyanines: From outstanding electronic properties to emerging applications, *Chem. Rec.*, 2008, **8**, 75–97.

[155] A. Satake and Y. Kobuke, Artificial photosynthetic systems: assemblies of slipped cofacial porphyrins and phthalocyanines showing strong electronic coupling., *Org. Biomol. Chem.*, 2007, **5**, 1679–1691.

[156] L. D. a. Siebbeles, A. Huijser and T. J. Savenije, Effects of molecular organization on exciton diffusion in thin films of bioinspired light-harvesting molecules, *J. Mater. Chem.*, 2009, **19**, 6067.

[157] F. Fassioli, R. Dinshaw, P. C. Arpin and G. D. Scholes, Photosynthetic light harvesting: excitons and coherence, *J. R. Soc. Interface*, 2014, **11**, 20130901.

[158] J. Tant, Y. H. Geerts, M. Lehmann, V. De Cupere, G. Zucchi, B. W. Laursen, T. Bjørnholm, V. Lemaur, V. Marcq, A. Burquel, E. Hennebicq, F. Gardebien, P. Viville, D. Beljonne, R. Lazzaroni and J. Cornil, Liquid crystalline metal-

free phthalocyanines designed for charge and exciton transport, *J. Phys. Chem. B*, 2005, **109**, 20315–20323.

[159] M. Yoneya, A. Miyamoto, Y. Shimizu, A. Fujii and M. Ozaki, Origin of the High Carrier Mobilities of Nonperipheral Octahexyl Substituted Phthalocyanine, *J. Phys. Chem. C*, 2015, **119**, 23852–23858.

[160] D. A. Da Silva Filho, V. Coropceanu, N. E. Gruhn, P. H. de Oliveira Neto and J.-L. Brédas, Intramolecular reorganization energy in zinc phthalocyanine and its fluorinated derivatives: a joint experimental and theoretical study, *Chem. Commun.*, 2013, **49**, 6069–6071.

[161] A. Huijser, T. J. Savenije, S. C. J. Meskers, M. J. W. Vermeulen and L. D. A. Siebbeles, The Mechanism of Long-Range Exciton Diffusion in a Nematically Organized Porphyrin Layer, *J. Am. Chem. Soc.*, 2008, **130**, 12496–12500.

[162] Y. Gao, Y. Chen, R. Li, Y. Bian, X. Li and J. Jiang, Nonperipherally octa(butyloxy)-substituted phthalocyanine derivatives with good crystallinity: Effects of metal-ligand coordination on the molecular structure, internal structure, and dimensions of self-assembled nanostructures, *Chem. - A Eur. J.*, 2009, **15**, 13241–13252.

[163] N. Rawat, Z. Pan, L. W. Manning, C. J. Lamarche, I. Cour, R. L. Headrick, R. Waterman, A. R. Woll and M. I. Furis, Macroscopic Molecular Ordering and Exciton Delocalization in Crystalline Phthalocyanine Thin Films, *J. Phys. Chem. Lett.*, 2015, **6**, 1834–1840.

[164] A. S. Davydov, *Theory of Molecular Excitons*, Springer US, Boston, MA, 1971.

[165] E. Orti, J. Brédas and C. Clarisse, Electronic structure of phthalocyanines: Theoretical investigation of the optical properties of phthalocyanine monomers, dimers, and crystals, *J. Chem. Phys.*, 1990, **92**, 1228.

[166] M. Rust, J. Lappe and R. J. Cave, Multistate effects in calculations of the electronic coupling element for electron transfer using the generalized Mulliken-Hush method, *J. Phys. Chem. A*, 2002, **106**, 3930–3940.

[167] J. E. Subotnik, S. Yeganeh, R. J. Cave and M. A. Ratner, Constructing diabatic states from adiabatic states: Extending generalized Mulliken–Hush to multiple charge centers with Boys localization, *J. Chem. Phys.*, 2008, **129**, 244101.

[168] R. J. Cave and M. D. Newton, Multistate Treatments of the Electronic Coupling

in Donor–Bridge–Acceptor Systems: Insights and Caveats from a Simple Model, *J. Phys. Chem. A*, 2014, **118**, 7221–7234.

[169] G. D. Scholes, Long-Range Resonance Energy Transfer in Molecular Systems, *Annu. Rev. Phys. Chem.*, 2003, **53**, 57–87.

[170] C. Hsu, Z. You and H. Chen, Characterization of the Short-Range Couplings in Excitation Energy Transfer, *J. Phys. Chem. C*, 2008, **112**, 1204–1212.

[171] N. J. Hestand, R. Tempelaar, J. Knoester, T. L. C. Jansen and F. C. Spano, Exciton mobility control through sub − Å packing modifications in molecular crystals, *Phys. Rev. B*, 2015, **91**, 195315.

[172] K. A. Kistler, F. C. Spano and S. Matsika, A benchmark of excitonic couplings derived from atomic transition charges, *J. Phys. Chem. B*, 2013, **117**, 2032–2044.

[173] J. W. Ponder and F. M. Richards, An efficient Newton-like method for molecular mechanics energy minimization of large molecules, *J. Comput. Chem.*, 1987, **8**, 1016–1024.

[174] N. L. Allinger, Y. H. Yuh and J. H. Lii, Molecular mechanics. The MM3 force field for hydrocarbons. 1, *J. Am. Chem. Soc.*, 1989, **111**, 8551–8566.

[175] J. H. Lii and N. L. Allinger, Molecular mechanics. The MM3 force field for hydrocarbons. 2. Vibrational frequencies and thermodynamics, *J. Am. Chem. Soc.*, 1989, **111**, 8566–8575.

[176] J. H. Lii and N. L. Allinger, Molecular mechanics. The MM3 force field for hydrocarbons. 3. The van der Waals' potentials and crystal data for aliphatic and aromatic hydrocarbons, *J. Am. Chem. Soc.*, 1989, **111**, 8576–8582.

[177] O. A. Vydrov and G. E. Scuseria, Assessment of a long-range corrected hybrid functional, *J. Chem. Phys.*, 2006, **125**, 234109.

[178] M. M. Francl, W. J. Pietro, W. J. Hehre, J. S. Binkley, M. S. Gordon, D. J. DeFrees and J. A. Pople, Self-consistent molecular orbital methods. XXIII. A polarization-type basis set for second-row elements, *J. Chem. Phys.*, 1982, **77**, 3654–3665.

[179] M. A. Rohrdanz, K. M. Martins and J. M. Herbert, A long-range-corrected density functional that performs well for both ground-state properties and time-dependent density functional theory excitation energies, including charge-transfer excited states, *J. Chem. Phys.*, 2009, **130**, 54112.

[180] M. Valiev, E. J. Bylaska, N. Govind, K. Kowalski, T. P. Straatsma, H. J. J. Van Dam, D. Wang, J. Nieplocha, E. Apra, T. L. Windus and W. A. de Jong, NWChem: A comprehensive and scalable open-source solution for large scale molecular simulations, *Comput. Phys. Commun.*, 2010, **181**, 1477–1489.

[181] A. Troisi and G. Orlandi, Dynamics of the Intermolecular Transfer Integral in Crystalline Organic Semiconductors, *J. Phys. Chem. A*, 2006, **110**, 4065–4070.

[182] M. Malagoli, V. Coropceanu, D. A. Da Silva Filho and J. Brédas, A multimode analysis of the gas-phase photoelectron spectra in oligoacenes, *J. Chem. Phys.*, 2004, **120**, 7490–7496.

[183] H. Van Mingroot, S. De Backer, J. van Stam, M. Van Der Auweraer and F. C. De Schryver, The emission at 669 nm of metal free phthalocyanine in toluene and 1-bromonaphthalene solutions, *Chem. Phys. Lett.*, 1996, **253**, 397–402.

[184] Y. Baeten, E. Fron, C. Ruzié, Y. H. Geerts and M. Van Der Auweraer, Investigation of the Qx-Qy Equilibrium in a Metal-Free Phthalocyanine, *ChemPhysChem*, 2015, **16**, 3992–3996.

[185] T. Elsaesser and W. Kaiser, Vibrational and Vibronic Relaxation of Large Polyatomic Molecules in Liquids, *Annu. Rev. Phys. Chem.*, 1991, **42**, 83–107.

[186] D. P. McMahon and A. Troisi, Evaluation of the external reorganization energy of polyacenes, *J. Phys. Chem. Lett.*, 2010, **1**, 941–946.

[187] N. G. Martinelli, J. Idé, R. S. Sánchez-Carrera, V. Coropceanu, J. Brédas, L. Ducasse, F. Castet, J. Cornil and D. Beljonne, Influence of structural dynamics on polarization energies in anthracene single crystals, *J. Phys. Chem. C*, 2010, **114**, 20678–20685.

[188] M. Schröter and O. Kühn, Interplay Between Nonadiabatic Dynamics and Frenkel Exciton Transfer in Molecular Aggregates: Formulation and Application to a Perylene Bismide Model, *J. Phys. Chem. A*, 2013, **117**, 7580–7588.

[189] L. Wang, A. V. Akimov, L. Chen and O. V. Prezhdo, Quantized Hamiltonian dynamics captures the low-temperature regime of charge transport in molecular crystals, *J. Chem. Phys.*, 2013, **139**, 174109.

[190] A. V. Akimov, R. Long and O. V. Prezhdo, Coherence penalty functional: A simple method for adding decoherence in Ehrenfest dynamics, *J. Chem. Phys.*, 2014, **140**, 194107.

[191] R. Tempelaar, F. C. Spano, J. Knoester and T. L. C. Jansen, Mapping the Evolution of Spatial Exciton Coherence through Time-Resolved Fluorescence, *J. Phys. Chem. Lett.*, 2014, **5**, 1505–1510.

[192] T. Wang and W.-L. Chan, Dynamical Localization Limiting the Coherent Transport Range of Excitons in Organic Crystals, *J. Phys. Chem. Lett.*, 2014, **5**, 1812–1818.

[193] S. Kakade, R. Ghosh and D. K. Palit, Excited State Dynamics of Zinc − Phthalocyanine Nanoaggregates in Strong Hydrogen Bonding Solvents, *J. Phys. Chem. C*, 2012, **116**, 15155–15166.

[194] O. V. Mikhnenko, P. W. M. Blom and T.-Q. T. Nguyen, Exciton Diffusion in Organic Semiconductors, *Energy Environ. Sci.*, 2015, **8**, 1867.

[195] C. Curutchet and B. Mennucci, Quantum Chemical Studies of Light Harvesting, *Chem. Rev.*, 2017, **117**, 294−343.

[196] T. Mirkovic, E. E. Ostroumov, J. M. Anna, R. van Grondelle, Govindjee and G. D. Scholes, Light Absorption and Energy Transfer in the Antenna Complexes of Photosynthetic Organisms, *Chem. Rev.*, 2017, **117**, 249–293.

[197] T. Stangl, P. Wilhelm, D. Schmitz, K. Remmerssen, S. Henzel, S. S. Jester, S. Höger, J. Vogelsang and J. M. Lupton, Temporal fluctuations in excimer-like interactions between π-conjugated chromophores, *J. Phys. Chem. Lett.*, 2015, **6**, 1321–1326.

[198] C. Olbrich, T. L. C. Jansen, J. Liebers, M. Aghtar, J. Strümpfer, K. Schulten, J. Knoester and U. Kleinekathöfer, From atomistic modeling to excitation transfer and two-dimensional spectra of the FMO light-harvesting complex, *J. Phys. Chem. B*, 2011, **115**, 8609–8621.

[199] S. Shim, P. Rebentrost, S. Valleau and A. Aspuru-Guzik, Atomistic study of the long-lived quantum coherences in the Fenna-Matthews-Olson complex, *Biophys. J.*, 2012, **102**, 649–660.

[200] S. Jurinovich, C. Curutchet and B. Mennucci, The fenna-matthews-olson protein revisited: A fully polarizable (TD)DFT/MM description, *ChemPhysChem*, 2014, **15**, 3194–3204.

[201] L. Cupellini, S. Jurinovich, M. Campetella, S. Caprasecca, C. A. Guido, S. M. Kelly, A. T. Gardiner, R. J. Cogdell and B. Mennucci, An ab initio Description of the Excitonic Properties of LH2 and their Temperature Dependence, *J. Phys.*

Chem. B, 2016, **8**, 11348−11359.

[202] M. Aghtar, U. Kleinekathöfer, C. Curutchet and B. Mennucci, Impact of electronic fluctuations and their description on the exciton dynamics in the light-harvesting complex PE545, *J. Phys. Chem. B*, 2017, **121**, 1330–1339.

[203] F. Haverkort, A. Stradomska, A. H. de Vries and J. Knoester, First-principles calculation of the optical properties of an amphiphilic cyanine dye aggregate., *J. Phys. Chem. A*, 2014, **118**, 1012–1023.

[204] C. P. van der Vegte, J. D. Prajapati, U. Kleinekathöfer, J. Knoester and T. L. C. Jansen, Atomistic modeling of two-dimensional electronic spectra and excited-state dynamics for a Light Harvesting 2 complex, *J. Phys. Chem. B*, 2015, **119**, 1302–1313.

[205] J. R. Durrant, J. Knoester and D. A. Wiersma, Local energetic disorder in molecular aggregates probed by the one-exciton to two-exciton transition, *Chem. Phys. Lett.*, 1994, **222**, 450–456.

[206] J. Clark, C. Silva, R. H. Friend and F. C. Spano, Role of intermolecular coupling in the photophysics of disordered organic semiconductors: Aggregate emission in regioregular polythiophene, *Phys. Rev. Lett.*, 2007, **98**, 206406.

[207] T. E. Dykstra, E. Hennebicq, D. Beljonne, J. Gierschner, G. Claudio, E. R. Bittner, J. Knoester and G. D. Scholes, Conformational disorder and ultrafast exciton relaxation in PPV-family conjugated polymers, *J. Phys. Chem. B*, 2009, **113**, 656–667.

[208] W. Barford and D. Trembath, Exciton localization in polymers with static disorder, *Phys. Rev. B*, 2009, **80**, 165418.

[209] X. Zhang, Z. Li and G. Lu, First-principles simulations of exciton diffusion in organic semiconductors, *Phys. Rev. B*, 2011, **84**, 235208.

[210] S. K. Saikin, A. Eisfeld, S. Valleau and A. Aspuru-Guzik, Photonics meets excitonics: Natural and artificial molecular aggregates, *Nanophotonics*, 2013, **2**, 21–38.

[211] P. C. Tapping, S. N. Clafton, K. N. Schwarz, T. W. Kee and D. M. Huang, Molecular-Level Details of Morphology-Dependent Exciton Migration in Poly(3-hexylthiophene) Nanostructures, *J. Phys. Chem. C*, 2015, **119**, 7047–7059.

[212] S. M. Vlaming and R. J. Silbey, Correlated intermolecular coupling

fluctuations in photosynthetic complexes, *J. Chem. Phys.*, 2012, **136**, 55102.

[213] P. Huo and D. F. Coker, Influence of environment induced correlated fluctuations in electronic coupling on coherent excitation energy transfer dynamics in model photosynthetic systems, *J. Chem. Phys.*, 2012, **136**, 115102.

[214] G. D. Scholes, I. R. Gould, R. J. Cogdell and G. R. Fleming, Ab initio molecular orbital calculations of electronic couplings in the LH2 bacterial light-harvesting complex of Rps-acidophila, *J. Phys. Chem. B*, 1999, **103**, 2543–2553.

[215] R. Hildner, D. Brinks, J. B. Nieder, R. J. Cogdell and N. F. van Hulst, Quantum Coherent Energy Transfer over Varying Pathways in Single Light-Harvesting Complexes, *Science*, 2013, **340**, 1448–1451.

[216] H. W. Kim, A. Kelly, J. W. Park and Y. M. Rhee, All-Atom Semiclassical Dynamics Study of Quantum Coherence in Photosynthetic Fenna − Matthews − Olson Complex, *J. Am. Chem. Soc.*, 2012, **134**, 11640–11651.

[217] J. M. Olson, in *Discoveries in Photosynthesis*, eds. Govindjee, J. T. Beatty, H. Gest and J. F. Allen, Springer, Dordrecht, The Netherlands, 2005, pp. 421–427.

[218] G. McDermott, S. M. Prince, A. A. Freer, A. M. Hawthornthwaite-Lawless, M. Z. Papiz, R. J. Cogdell and N. W. Isaacs, Crystal structure of an integral membrane light-harvesting complex from photosynthetic bacteria, *Nature*, 1995, **374**, 517–521.

[219] E. Hofmann, P. M. Wrench, F. P. Sharples, R. G. Hiller, W. Welte and K. Diederichs, Structural basis of light harvesting by carotenoids: peridinin-chlorophyll-protein from Amphidinium carterae., *Science*, 1996, **272**, 1788.

[220] A. Ishizaki and G. R. Fleming, Theoretical examination of quantum coherence in a photosynthetic system at physiological temperature., *Proc. Natl. Acad. Sci. U. S. A.*, 2009, **106**, 17255–17260.

[221] R. J. Cogdell, A. Gall and J. Köhler, The architecture and function of the light-harvesting apparatus of purple bacteria: from single molecules to in vivo membranes, *Q. Rev. Biophys.*, 2006, **39**, 227.

[222] R. Jimenez, S. N. Dikshit, S. E. Bradforth and G. R. Fleming, Electronic Excitation Transfer in the LH2 Complex of Rhodobacter sphaeroides, *J. Phys. Chem.*, 1996, **100**, 6825–6834.

[223] W. P. Bricker and C. S. Lo, Efficient Pathways of Excitation Energy Transfer from Delocalized S2 Excitons in the Peridinin–Chlorophyll a –Protein

Complex, *J. Phys. Chem. B*, 2015, **119**, 5755–5764.

[224] S. Wo, R. L. Headrick and J. E. Anthony, Fabrication and characterization of controllable grain boundary arrays in solution-processed small molecule organic semiconductor films, *J. Appl. Phys.*, 2012, **111**, 73716.

[225] J. Rivnay, S. C. B. Mannsfeld, C. E. Miller, A. Salleo and M. F. Toney, Quantitative Determination of Organic Semiconductor Microstructure from the Molecular to Device Scale with Quantitative X-ray Scattering and Absorption Analyses, *Chem. Rev.*, 2012, **112**, 5488–5519.

[226] Z. Pan, N. Rawat, I. Cour, L. Manning, R. L. Headrick and M. I. Furis, Polarization-resolved spectroscopy imaging of grain boundaries and optical excitations in crystalline organic thin films, *Nat. Commun.*, 2015, **6**, 8201.

[227] W. Humphrey, A. Dalke and K. Schulten, VMD: Visual molecular dynamics, *J. Mol. Graph.*, 1996, **14**, 33–38.

[228] A. Ben-Shem, F. Frolow and N. Nelson, Evolution of photosystem I - from symmetry through pseudosymmetry to asymmetry, *FEBS Lett.*, 2004, **564**, 274–280.

[229] M. Z. Papiz, S. M. Prince, T. Howard, R. J. Cogdell and N. W. Isaacs, The structure and thermal motion of the B800-850 LH2 complex from Rps. acidophila at 2.0 Å resolution and 100 K: New structural features and functionally relevant motions, *J. Mol. Biol.*, 2003, **326**, 1523–1538.

[230] E. P. Kenny and I. Kassal, Benchmarking Calculations of Excitonic Couplings between Bacteriochlorophylls, *J. Phys. Chem. B*, 2016, **120**, 25–32.

[231] M. J. Abraham, T. Murtola, R. Schulz, S. Páll, J. C. Smith, B. Hess and E. Lindah, Gromacs: High performance molecular simulations through multi-level parallelism from laptops to supercomputers, *SoftwareX*, 2015, **1**–**2**, 19–25.

[232] P. J. Dwyer, R. J. Vander Valk, V. Caltaldo, D. Demianicz and S. P. Kelty, All-Atom CHARMM Force Field and Bulk Properties of Perfluorozinc Phthalocyanines, *J. Phys. Chem. A*, 2014, **118**, 11583.

[233] W. R. Scheidt and W. Dow, Molecular stereochemistry of phthalocyanatozinc (II), *J. Am. Chem. Soc.*, 1977, **99**, 1101–1104.

[234] A. Olaya-Castro and G. D. Scholes, Energy transfer from Förster–Dexter theory to quantum coherent light- harvesting, *Int. Rev. Phys. Chem.*, 2011, **30**,

49–77.

[235] B. P. Krueger, G. D. Scholes, R. Jimenez and G. R. Fleming, Electronic Excitation Transfer from Carotenoid to Bacteriochlorophyll in the Purple Bacterium Rhodopseudomonas acidophila, *J. Phys. Chem. B*, 1998, **102**, 2284–2292.

[236] S. Tretiak, C. Middleton, V. Chernyak and S. Mukamel, Bacteriochlorophyll and Carotenoid Excitonic Couplings in the LH2 System of Purple Bacteria, *J. Phys. Chem. B*, 2000, **104**, 9540–9553.

[237] Y. Wan, A. Stradomska, S. Fong, Z. Guo, R. D. Schaller, G. P. Wiederrecht, J. Knoester and L. Huang, Exciton Level Structure and Dynamics in Tubular Porphyrin Aggregates, *J. Phys. Chem. C*, 2014, **118**, 24854–24865.

[238] P. T. Kiss, M. Sega and A. Baranyai, Efficient handling of gaussian charge distributions: An application to polarizable molecular models, *J. Chem. Theory Comput.*, 2014, **10**, 5513–5519.

[239] C. Curutchet, J. Kongsted, A. Muñoz-Losa, H. Hossein-Nejad, G. D. Scholes and B. Mennucci, Photosynthetic Light-Harvesting Is Tuned by the Heterogeneous Polarizable Environment of the Protein, *J. Am. Chem. Soc.*, 2011, **133**, 3078–3084.

[240] B. Mennucci and C. Curutchet, The role of the environment in electronic energy transfer: a molecular modeling perspective., *Phys. Chem. Chem. Phys.*, 2011, **13**, 11538–11550.

[241] A. M. Rosnik and C. Curutchet, Theoretical Characterization of the Spectral Density of the Water-Soluble Chlorophyll-Binding Protein from Combined Quantum Mechanics/Molecular Mechanics Molecular Dynamics Simulations, *J. Chem. Theory Comput.*, 2015, **11**, 5826–5837.

[242] D. Padula, S. Jurinovich, L. Di Bari and B. Mennucci, Simulation of Electronic Circular Dichroism of Nucleic Acids: From the Structure to the Spectrum, *Chem. - A Eur. J.*, 2016, **22**, 17011–17019.

[243] J. Adolphs, F. Müh, M. E. A. Madjet and T. Renger, Calculation of pigment transition energies in the FMO protein: From simplicity to complexity and back, *Photosynth. Res.*, 2008, **95**, 197–209.

[244] T. Renger and F. Müh, Understanding photosynthetic light-harvesting: a bottom up theoretical approach., *Phys. Chem. Chem. Phys.*, 2013, **15**, 3348–

3371.

[245] M. E. Madjet, A. Abdurahman and T. Renger, Intermolecular coulomb couplings from ab initio electrostatic potentials: Application to optical transitions of strongly coupled pigments in photosynthetic antennae and reaction centers, *J. Phys. Chem. B*, 2006, **110**, 17268–17281.

[246] P. Carbone and A. Troisi, Charge Diffusion in Semiconducting Polymers: Analytical Relation between Polymer Rigidity and Time Scales for Intrachain and Interchain Hopping, *J. Phys. Chem. Lett.*, 2014, **5**, 2637–2641.

[247] D. H. Dunlap and V. M. Kenkre, Disordered polaron transport: a theoretical description of the motion of photoinjected charges in molecularly doped polymers, *Chem. Phys.*, 1993, **178**, 67–75.

[248] J. F. Chang, H. Sirringhaus, M. Giles, M. Heeney and I. McCulloch, Relative importance of polaron activation and disorder on charge transport in high-mobility conjugated polymer field-effect transistors, *Phys. Rev. B*, 2007, **76**, 205204.

[249] M. Van Der Auweraer, F. C. De Schryver, P. M. Borsenberger and H. Bässler, Disorder in Charge-Transport in Doped Polymers, *Adv. Mater.*, 1994, **6**, 199–213.

[250] S. Stafström, Electron localization and the transition from adiabatic to nonadiabatic charge transport in organic conductors, *Chem. Soc. Rev.*, 2010, **39**, 2484–2499.

[251] C. Poelking, E. Cho, A. Malafeev, V. Ivanov, K. Kremer, C. Risko, J. Brédas and D. Andrienko, Characterization of charge-carrier transport in semicrystalline polymers: Electronic couplings, site energies, and charge-carrier dynamics in poly(bithiophene-alt-thienothiophene) [PBTTT], *J. Phys. Chem. C*, 2013, **117**, 1633–1640.

[252] H. Cordes, S. D. Baranovskii, K. Kohary, P. Thomas, S. Yamasaki, F. Hensel and J.-H. Wendorff, One-dimensional hopping transport in disordered organic solids. I. Analytic calculations, *Phys. Rev. B*, 2001, **63**, 94201.

[253] J. J. M. Van Der Holst, PhD thesis, Technische Universiteit Eindhoven, 2010.

[254] D. P. McMahon, D. L. Cheung, L. J. Goris, J. Dacuña, A. Salleo and A. Troisi, Relation between microstructure and charge transport in polymers of different regioregularity, *J. Phys. Chem. C*, 2011, **115**, 19386–19393.

[255] W. F. Pasveer, P. A. Bobbert and M. a. J. Michels, Temperature and field dependence of the mobility in 1D for a Gaussian density of states, *Phys. Status Solidi C*, 2004, **1**, 164–167.

[256] A. Troisi, The speed limit for sequential charge hopping in molecular materials, *Org. Electron.*, 2011, **12**, 1988–1991.

[257] E. Mozafari and S. Stafström, Polaron dynamics in a two-dimensional Holstein-Peierls system, *J. Chem. Phys.*, 2013, **138**, 184104.

[258] M. Hultell and S. Stafström, Impact of ring torsion on the intrachain mobility in conjugated polymers, *Phys. Rev. B*, 2007, **75**, 104304.

[259] P. Prins, F. C. Grozema, J. M. Schins, T. J. Savenije, S. Patil, U. Scherf and L. D. A. Siebbeles, Effect of intermolecular disorder on the intrachain charge transport in ladder-type poly (p-phenylenes), *Phys. Rev. B*, 2006, **73**, 45204.

[260] P. Prins, F. C. Grozema, F. Galbrecht, U. Scherf and L. D. A. Siebbeles, Charge transport along coiled conjugated polymer chains, *J. Phys. Chem. C*, 2007, **111**, 11104–11112.

[261] R. A. Marcus, Chemical and Electrochemical Electron-Transfer Theory, *Annu. Rev. Phys. Chem.*, 1964, **15**, 155–196.

[262] S. S. Skourtis and D. N. Beratan, in *Advances in Chemical Physics: Electron Transfer - from Isolated Molecules to Biomolecules. Part 1, Volume 106*, eds. I. Prigogine and S. A. Rice, John Wiley & Sons, Hoboken, NJ, USA, 1999, pp. 377–452.

[263] S. Fratini and S. Ciuchi, Bandlike motion and mobility saturation in organic molecular semiconductors, *Phys. Rev. Lett.*, 2009, **103**, 266601.

[264] H. T. Nicolai, M. Kuik, G. A. H. Wetzelaer, B. de Boer, C. Campbell, C. Risko, J. Brédas and P. W. M. Blom, Unification of trap-limited electron transport in semiconducting polymers, *Nat. Mater.*, 2012, **11**, 882–887.

[265] Y. Zhang, X. Cai, Y. Bian, X. Li and J. Jiang, Heteroatom Substitution of Oligothienoacenes: From Good p-Type Semiconductors to Good Ambipolar Semiconductors for Organic Field-Effect Transistors, *J. Phys. Chem. C*, 2008, **112**, 5148–5159.

[266] Y. A. Berlin, A. L. Burin and M. A. Ratner, Elementary steps for charge transport in DNA: thermal activation vs. tunneling, *Chem. Phys.*, 2002, **275**, 61–74.

[267] D. Mendels and N. Tessler, A Comprehensive study of the Effects of Chain Morphology on the Transport Properties of Amorphous Polymer Films, *Sci. Rep.*, 2016, **6**, 29092.

[268] J. Brédas, D. Beljonne and V. Coropceanu, Charge-Transfer and Energy-Transfer Processes in π-Conjugated Oligomers and Polymers: A Molecular Picture, *Chem. Rev.*, 2004, **104**, 4971–5003.

[269] J. Rivnay, R. Noriega, J. E. Northrup, R. J. Kline, M. F. Toney and A. Salleo, Structural origin of gap states in semicrystalline polymers and the implications for charge transport, *Phys. Rev. B*, 2011, **83**, 121306(R).

[270] J. D. Yuen, R. Menon, N. E. Coates, E. B. Namdas, S. Cho, S. T. Hannahs, D. Moses and A. J. Heeger, Nonlinear transport in semiconducting polymers at high carrier densities, *Nat. Mater.*, 2009, **8**, 572–575.

[271] O. Kratky and G. Porod, Röntgenuntersuchung gelöster Fadenmoleküle, *Recl. des Trav. Chim. des Pays-Bas*, 1949, **68**, 1106–1122.

[272] R. A. Harris and J. E. Hearst, On Polymer Dynamics, *J. Chem. Phys.*, 1966, **44**, 2595–2602.

[273] N. Saitô, K. Takahashi and Y. Yunoki, The Statistical Mechanical Theory of Stiff Chains, *J. Phys. Soc. Japan*, 1967, **22**, 219–226.

[274] Andrew J. Spakowitz and Z.-G. Wang, Exact Results for a Semiflexible Polymer Chain in an Aligning Field, *Macromolecules*, 2004, **37**, 5814–5823.

[275] A. Devižis, A. Serbenta, K. Meerholz, D. Hertel and V. Gulbinas, Ultrafast dynamics of carrier mobility in a conjugated polymer probed at molecular and microscopic length scales, *Phys. Rev. Lett.*, 2009, **103**, 27404.

[276] C. Tanase, E. J. Meijer, P. W. M. Blom and D. M. De Leeuw, Unification of the hole transport in polymeric field-effect transistors and light-emitting diodes, *Phys. Rev. Lett.*, 2003, **91**, 216601.

[277] R. J. Kline, M. D. McGehee, E. N. Kadnikova, J. Liu and J. M. J. Fréchet, Controlling the field-effect mobility of regioregular polythiophene by changing the molecular weight, *Adv. Mater.*, 2003, **15**, 1519–1522.

[278] A. Zen, J. Pflaum, S. Hirschmann, W. Zhuang, F. Jaiser, U. Asawapirom, J. P. Rabe, U. Scherf and D. Neher, Effect of molecular weight and annealing of poly(3-hexylthiophene)s on the performance of organic field-effect transistors, *Adv. Funct. Mater.*, 2004, **14**, 757–764.

[279] H. N. Tsao, D. M. Cho, I. Park, M. R. Hansen, A. Mavrinskiy, D. Y. Yoon, R. Graf, W. Pisula, H. W. Spiess and K. Müllen, Ultrahigh mobility in polymer field-effect transistors by design, *J. Am. Chem. Soc.*, 2011, **133**, 2605–2612.

[280] J. Li, Y. Zhao, H. S. Tan, Y. Guo, C.-A. Di, G. Yu, Y. Liu, M. Lin, S. H. Lim, Y. Zhou, H. Su and B. S. Ong, A stable solution-processed polymer semiconductor with record high-mobility for printed transistors, *Sci. Rep.*, 2012, **2**, 754.

[281] A. Katsouras, N. Gasparini, C. Koulogiannis, M. Spanos, T. Ameri, C. J. Brabec, C. L. Chochos and A. Avgeropoulos, Systematic Analysis of Polymer Molecular Weight Influence on the Organic Photovoltaic Performance, *Macromol. Rapid Commun.*, 2015, **36**, 1778–1797.